

# EFFECT OF ION TEMPERATURE ON THE DYNAMICS OF ANALYTICAL SOLITARY WAVE SOLUTION OF THE DUST ION ACOUSTIC WAVES FOR THE DAMPED FORCED KdV EQUATION IN $q$ -NONEXTENSIVE PLASMAS

 Sarbamon Tokbi<sup>1\*</sup>,  Satyendra Nath Barman<sup>2</sup>

<sup>1</sup>Department of mathematics, Gauhati University, Guwahati-781014, Assam, India

<sup>2</sup>B. Borooah College, Guwahati-781007, Assam, India

\*Corresponding Author e-mail: [tokbimon828@gmail.com](mailto:tokbimon828@gmail.com)

Received September 7, 2025; revised October 19, 2025; accepted November 2, 2025

This paper examines the dynamical properties of the analytical solitary wave solution of dust ion acoustic (DIA) solitary waves induced by the damped forced Korteweg-de Vries (DFKdV) equation in an unmagnetized collisional dusty plasma that contains neutral particles,  $q$ -nonextensive electrons, positively charged ions, and negatively charged dust grains in the presence of an external periodic force. To obtain the damped forced Korteweg-de Vries (DFKdV) equation, the reductive perturbation approach was developed. It is observed that both the compressive and rarefactive dust-ion acoustic (DIA) solitary-wave solutions are possible for this plasma model. The effects of a number of physical parameters are taken into account: the entropic index ( $q$ ), dust ion collisional frequency ( $\nu_{id0}$ ), traveling wave speed ( $M$ ), periodic force frequency ( $\omega$ ), ion-to-electron temperature ratio ( $\sigma$ ), the parameter that is the ratio between the unperturbed densities of the dust ions and electrons ( $\mu$ ), the strength and frequency of the external periodic force ( $f_0$ ). It is observed that those parameters have significant effects on the structures of the damped forced dust-ion acoustic solitary waves. The implication of the outcomes of this investigation may be relevant for understanding the dynamics of dust-ionacoustic (DIA) solitary waves in laboratory plasma as well as in space plasma environment.

**Keywords:** *Ion-acoustic soliton, Solitary wave, Dusty plasma, Reductive perturbation method, nonextensive electron, Damped forced KdV equation*

**PACS:** 52.35.Fp, 52.35.Sb, 52.25.Vy

**AMS Classification 2020:** 35C08, 35Q51, 35Q53

## 1. INTRODUCTION

In plasmas, ions are able to exchange vibrations with one another due to their charge despite the absence of collisions. As the movement of large numbers of ions is included, these vibrations take the form of low-frequency oscillations, referred to as Ion-Acoustic (IA) waves [1]. One of the most exciting features of IA waves is that they can occur as types of waves similar to electron solitary waves [2, 3, 4, 5, 6, 7]. The solitary waves are localised waves which are seen from a mutual balance between the effects of dispersion and nonlinearity in a medium. A solitary wave is referred to as a soliton if it has two characteristics: it moves for a long period without changing its shape or speed, and it undergoes further phase shifts when it interacts with other waves while retaining its identities and stabilities [8]. The word "soliton" was first used by Zabusky and Kruskal [9] to describe the numerical solution of the Korteweg-de Vries (KdV) problem. Solitary waves have been thoroughly investigated both theoretically and experimentally as a significant non-linear topic (Shukla [10]; Verheest [12]; Tian and Gao [13]; Misra and Bhowmik [11]). Many writers have examined ion-acoustic solitons using the reductive perturbation approach (Bharuthram and Shukla[14]; Yadav and Sharma[15]). It has been noted that nonlinear waves in plasmas with extra components, such as positrons, behave differently from those in plasmas that are composed of electrons and positive ions (Rizzato[16]). Propagation of ion-acoustic solitons in magnetised and unmagnetised plasmas has been studied theoretically (Washimi and Taniuti[20]; Ostrovoski et al.[23]; Boldyrev et al.[24]; Kadomstev and Karpman[21]; Gresillon and Doveil[22]) and experimentally by Ludwig et al.[28]; Cooney et al.[29]; Okutsu et al.[27]; Ikezi et al.[25]; Ikezi[26] in the past, and interesting results have been obtained.

Dusty plasma is an ionised gas that contains huge solid charged dust grains that are micrometres in size, as well as electrons, positive ions, and neutral atoms. The dusty plasma has become one of the prominent matters of research during the last five decades because of its great presence in the universe. This is the most astounding and fascinating matter of fact: over ninety-nine percent of the known universe is in the form of plasma, and the remaining one percent or less which includes our earth, is not in the form of plasma. It may be found in a wide range of astrophysical objects, such as pulsar magnetospheres [18, 19], planetary rings, comet tails, the interstellar medium, noctilucent clouds, the solar atmosphere [30, 47], active galactic nuclei [17], and more [32, 33, 34]. Besides its application in astrophysical studies, nowadays investigation of the plasma becomes a promising topic because of its important role in the semiconductor processing industry, nanoparticle production, and film deposition reactors, etc.,[35, 36].

During the last three decades, physicists have become quite interested in observing DIAW in a dusty plasma system. Tonks et al. made the first theoretical prediction that ion-acoustic waves (IAW) would be present in ionised gas [37], while

Rewans made the first practical observation of IAW in gas-discharge plasma in [38]. Sazdeev [39] studied theoretically these types of waves in plasma systems, and Ikezi et.al. [40] observed the same experimentally. Subsequently, numerous experimental and theoretical studies had been conducted in various plasma fields, and it was found that dust grains generate a variety of new wave features, viz., dust ion acoustic mode, dust acoustic mode [41, 42], dust drift mode [43], dust lattice mode [44], Shukla–Varma mode [45], dust cyclotron mode [46], dust Bernstein–Green–Kruskal mode [47], etc. Shukla and Silin [49] predicted theoretically DIAWs in dusty plasma consisting of negatively charged static dust grains for the first time, and Barken et al. [50] observed the existence of DIAWs experimentally. Linear and nonlinear DIAWs had also been experimentally investigated by Nakamura et al. [51] in a homogeneous unmagnetized dusty plasma. They observed that the phase velocity of the wave increases and the wave endures heavy damping with increasing dust density in the linear regime. Recently, Jharna et al. [48] studied the DIAWs in an unmagnetized collisional nonextensive dusty plasma. They showed that characteristic of the wave affected by the nonextensive parameter and dust ion collisional frequency. Renyi [52] first introduced the nonextensive generalisation of BGS entropy for statistical equilibrium. Liyan and Du [53] studied ion acoustic solitary waves (IASWs) in the plasma with power-law  $q$ -distribution in non-extensive statistics, and they suggested that Tsallis [54] statistics are suitable for the system being the non-equilibrium stationary state with inhomogeneous temperature and containing a huge supply of the superthermal low-velocity particles. Saha et al. [55, 56, 57] studied the dynamical behaviour of DIAWs in the presence of an external periodic force. L. Mandi, K.K. Mondal and P. Chatterjee studied the Analytical solitary wave solution of the dust ion acoustic waves for the damped forced modified Korteweg–de Vries equation in  $q$ -nonextensive plasmas [56]. Considering the external periodic perturbation, Saha et al. [57] observed the quasiperiodic, periodic, and chaotic structures of DIAWs. Shalini and Saini [58] studied the properties of DIA rogue waves in an unmagnetised collisionless plasma system composed of charged dust grains, superthermal electrons, and warm ions. It is noteworthy that the external periodic perturbation has a significant effect in many real physical situations [59, 60]. P. Chatterjee, R. Ali, A. Saha [61] studied the analytical solitary wave solution of the dust ion acoustic (DIA) waves in the framework of the damped forced Korteweg–de Vries (DFKdV) equation in superthermal collisional dusty plasmas, but they did not take the ion temperature effect and  $q$ -nonextensive electron into account in their investigation. This inspired us to investigate how solitary wave structure forms in a dusty plasma system with warm fluid ions and  $q$ -nonextensive electrons. As far as we are aware, there has never been an attempt to investigate the characteristics of DIA solitary waves in this kind of plasma model.

Our objective in this work is to derive the analytical DIA solitary wave of the damped force KdV (DFKdV) equation in an unmagnetized collisional dusty plasma with  $q$ -nonextensive electrons, neutral particles, positively charged ions, and negatively charged dust grains in the presence of an external periodic force. Furthermore, the effect of the entropic index  $q$ , dust ion collisional frequency  $\nu_{id0}$ , the speed of the travelling wave  $M$ , ion-to-electron temperature ratio  $\sigma$ , strength  $f_0$ , and frequency  $\omega$ , of the periodic force and the parameter  $\mu$ , which is the ratio between the unperturbed densities of the dust ions and electrons, are studied on the analytical solution of DIA solitary waves. The rest of the paper is organized as follows. The basic governing equations are provided in Section 2. In sections 3 and 4, we have derived the damped forced Korteweg–de Vries equation (DFKdV) and the solitary wave solution for non-linear propagation of dust ion acoustic solitary waves. Section 5 presents the result and discusses the effect of the different parameters on the analytical solitary wave solution of DFKdV. Section 6 states the conclusions. At the end, the 'references' are included.

## 2. BASIC PLASMA MODEL EQUATIONS

In this article, we consider an unmagnetized collisional dusty plasma which is composed of  $q$ -nonextensive electrons, stationary dust with negative charge, and hot inertial ions. The normalized ion fluid equations, which comprise the equation of continuity, equation of momentum balance and Poisson equation, governing the dynamics of DIA waves in such a plasma system are as follows:

$$\frac{\partial n}{\partial t} + \frac{\partial(nu)}{\partial x} = 0 \quad (1)$$

$$\frac{\partial u}{\partial t} + u \frac{\partial u}{\partial x} + \frac{\sigma}{n} \frac{\partial n}{\partial x} = -\frac{\partial \phi}{\partial x} - \nu_{id} u \quad (2)$$

$$\frac{\partial^2 \phi}{\partial x^2} = (1 - \mu)n_e - n + \mu \quad (3)$$

Where  $n$ ,  $u$  and  $\phi$  indicate the number density of ions, ion fluid velocity, electrostatic wave potential respectively normalised to its equilibrium value  $n_0$ , ion acoustic speed  $C_s = \sqrt{\frac{K_B T_e}{m_i}}$ , with  $T_e$  as electron temperature,  $K_B$  as Boltzmann constant and  $m_i$  as mass of ions and  $\frac{K_B T_e}{e}$ , with  $e$  as magnitude of electron charge. Also, the space variable  $x$  and time  $t$  are normalized to the Debye length  $\lambda_D = \sqrt{\frac{T_e}{4\pi n_{e0} e^2}}$  and  $\omega_{pi}^{-1} = \sqrt{\frac{m_i}{4\pi n_{e0} e^2}}$ , with  $\omega_{pi}$  as ion-plasma frequency. Here  $\nu_{id}$  is the dust-ion collisional frequency and  $\mu = \frac{z_d n_{d0}}{n_0}$  (dust-to-ion number density ratio). Here  $z_d$  are the charge number of dust particle. Also we define  $\sigma = \frac{T_i}{T_e}$  (ion-to-electron temperature ratio)

To explain the  $q$ -nonextensive electron, we take into account the distribution function[62] that follows.

$$f_e(v) = C_q \left\{ 1 + (q-1) \left[ \frac{m_e v^2}{2K_B T_e} - \frac{e\phi}{K_B T_e} \right] \right\}^{\frac{1}{q-1}} \quad (4)$$

Where  $\phi$  indicates the electrostatic potential and other variables or parameter have their typical meaning. It is important to note that this particular distribution function  $f_e(v)$  maximizes the Tsallis entropy and hence complies the principles of thermodynamics. Then, the constant of normalization is given by

$$C_q = n_{e0} \frac{\Gamma\left(\frac{1}{1-q}\right)}{\Gamma\left(\frac{1}{1-q} - \frac{1}{2}\right)} \sqrt{\frac{m_e(1-q)}{2\pi k_B T_e}}, \quad \text{for } -1 < q < 1 \quad (5)$$

$$C_q = n_{e0} \frac{1 + q\Gamma\left(\frac{1}{1-q} + \frac{1}{2}\right)}{2\Gamma\left(\frac{1}{1-q}\right)} \sqrt{\frac{m_e(1-q)}{2\pi k_B T_e}}, \quad \text{for } q > 1 \quad (6)$$

Integrating the distribution function  $f_e(v)$  after normalization across the velocity space, the  $q$ -nonextensive electron number density may be found as

$$n_e = n_{e0} \left\{ 1 + (q-1) \frac{e\phi}{k_B T_e} \right\}^{\frac{q+1}{2(q-1)}} \quad (7)$$

As a result, the normalized  $q$ -nonextensive electron number density is expressed as

$$n_e = \{1 + (q-1)\phi\}^{\frac{q+1}{2(q-1)}} \quad (8)$$

### 3. DERIVATION OF DAMPED FORCED KORTEWEG-de VRIES (DFKdV) EQUATION

In order to examine the nonlinear wave propagation of DIA solitary wave in unmagnetised collisional dusty plasma, we proceed to derive the damped forced KdV (DFKdV) equation from the set of governing equation by utilizing standard reductive perturbation technique (RPT). According to the RPT, the independent variables are stretched as

$$\xi = \epsilon^{\frac{1}{2}}(x - Ut), \quad \tau = \epsilon^{\frac{3}{2}}t \quad (9)$$

Where  $\epsilon$  is a dimensionless parameter indicating the amplitude of the perturbation and  $U$  indicate the phase velocity of the DIA solitary wave to be determined from the lowest order of  $\epsilon$ . Now, the expression of the dependent variables  $n, u, \phi, v$ , are as follows:

$$\left. \begin{aligned} n &= 1 + \epsilon n_1 + \epsilon^2 n_2 + \epsilon^3 n_3 + \dots \\ u &= 0 + \epsilon u_1 + \epsilon^2 u_2 + \epsilon^3 u_3 + \dots \\ \phi &= 0 + \epsilon \phi_1 + \epsilon^2 \phi_2 + \epsilon^3 \phi_3 + \dots \\ V_{id} &\sim \epsilon^{\frac{3}{2}} v_{id0} \end{aligned} \right\} \quad (10)$$

Substituting the above transformation (10) along with stretching coordinate (9) into the set of governing equations (1)-(3) then collecting the coefficient of lowest order terms in  $\epsilon$ , and after integration with the boundary conditions:  $n_1 = 0, u_1 = 0, \phi_1 = 0$  at  $|\xi| \rightarrow \infty$ , we obtain the first order perturbed terms as

$$\left. \begin{aligned} n_1 &= \frac{\phi_1}{E} \\ u_1 &= \frac{\phi_1 U}{E} \\ n_1 &= a(1 - \mu)\phi_1 \end{aligned} \right\} \quad (11)$$

Where  $a = \frac{q+1}{2}$  and  $E = U^2 - \sigma$  also found the dispersion relation is obtained as

$$U = \sqrt{\frac{1}{a(1-\mu)}} + \sigma \quad (12)$$

Again, taking the coefficient of next higher order of  $\epsilon$  (i.e the coefficient of  $\epsilon^{\frac{5}{2}}$  from equation (1) and (2) and coefficient of  $\epsilon^2$  from equation (3)), we obtain the following equations

$$\frac{\partial n_1}{\partial \tau} - U \frac{\partial n_2}{\partial \xi} + \frac{\partial u_2}{\partial \xi} + \frac{\partial(n_1 u_1)}{\partial \xi} = 0 \quad (13)$$

$$\frac{\partial u_1}{\partial \tau} - U \frac{\partial u_2}{\partial \xi} - n_1 U \frac{\partial u_1}{\partial \xi} + u_1 \frac{\partial u_1}{\partial \xi} + \sigma \frac{\partial n_2}{\partial \xi} + \frac{\partial \phi_2}{\partial \xi} + n_1 \frac{\partial \phi_1}{\partial \xi} + V_{id0} u_1 = 0 \quad (14)$$

$$a(1 - \mu)\phi_1 - n_1 = 0 \quad (15)$$

Now eliminating  $n_2, u_2$  from equation (13)-(15), then using equation (11) and equation (12), we get the DKdV equation

$$\frac{\partial \phi_1}{\partial \tau} + P \phi_1 \frac{\partial \phi_1}{\partial \xi} + Q \frac{\partial^3 \phi_1}{\partial \xi^3} + R \phi_1 = 0 \quad (16)$$

Where  $P = \frac{U}{E} + \frac{1-2E^2b(1-\mu)}{2U}$ ,  $Q = \frac{E^2}{2U}$  and  $R = \frac{V_{id0}}{2}$  with  $b = \frac{(q+1)(3-q)}{8}$ .

The damped KdV equation (16) is a nonlinear partial differential equation. Here  $P$  is the nonlinear coefficient, which determines the steepness/sharpness of the solitary excitation,  $Q$  is the dispersion coefficient, which measures the broadening of the solitary waves, and  $R$  is the dissipation/damping coefficient, which measures the decay of the solitary wave over time while propagating. It has been shown that the existence of an external periodic force significantly changes the behaviour of nonlinear waves. In the presence of an external magnetic force, resistive wall modes of the plasma have been discussed and it has been demonstrated that a flexible, high-speed waveform generator may generate such a force. When an external periodic force  $f_0 \cos(\omega\tau)$  is taken into account, the damped KdV has the following form:

$$\frac{\partial \phi_1}{\partial \tau} + P \phi_1 \frac{\partial \phi_1}{\partial \xi} + Q \frac{\partial^3 \phi_1}{\partial \xi^3} + R \phi_1 = f_0 \cos(\omega\tau) \quad (17)$$

Which is termed as the damped forced KdV equation.

#### 4. SOLITARY WAVE SOLUTION OF DAMPED FORCED KORTEWEG-de VRIES (DFKdV) EQUATION

In the absence of  $R$  and  $f_0$ , that is,  $R = 0$  and  $f_0 = 0$ , of the damped forced KdV equation (17) takes the form of the well-known KdV equation

$$\frac{\partial \phi_1}{\partial \tau} + P \phi_1 \frac{\partial \phi_1}{\partial \xi} + Q \frac{\partial^3 \phi_1}{\partial \xi^3} = 0 \quad (18)$$

with the solitary wave solution

$$\phi_1 = \phi_m \operatorname{sech}^2 \left( \frac{\xi - M\tau}{W} \right) \quad (19)$$

Where  $\phi_m = \frac{3M}{P}$  is the amplitude and  $W = 2\sqrt{\frac{Q}{M}}$  is the width of the DIA solitary wave with  $M$  consist the speed of the DIA solitary wave. In this case, it is well established that

$$\int_{-\infty}^{\infty} \phi_1^2 d\xi \quad (20)$$

is a conserved quantity.

For small values of  $R$  and  $f_0$ , let us assume that amplitude, width and velocity of the DIA solitary waves are dependent on  $\tau$  and the approximate solution of equation (17) is of the form

$$\phi_1 = \phi_m(\tau) \operatorname{sech}^2 \left( \frac{x - M(\tau)\tau}{W(\tau)} \right) \quad (21)$$

Where  $M(\tau)$  is an unknown function of  $\tau$  and  $\phi_m(\tau) = \frac{3M(\tau)}{P}$  and  $W(\tau) = 2\sqrt{\frac{Q}{M(\tau)}}$ .

Differentiating (19) with respect to  $\tau$  and using (17), one can obtain

$$\frac{dI}{d\tau} + 2CI = 2f_0 \cos(\omega\tau) \int_{-\infty}^{\infty} \phi_1 d\xi, \quad (22)$$

$$\frac{dI}{d\tau} + 2CI = \frac{24f_0\sqrt{Q}}{P} \sqrt{M(\tau)} \cos(\omega\tau). \quad (23)$$

Again

$$I = \int_{-\infty}^{\infty} \phi_1^2 d\xi, \quad (24)$$

$$I = \int_{-\infty}^{\infty} \phi_m^2(\tau) \operatorname{sech}^4 \left( \frac{\xi - M(\tau)\tau}{W(\tau)} \right) d\xi, \quad (25)$$



$$I = \frac{24\sqrt{Q}}{P^2} M^{\frac{3}{2}}(\tau) \quad (26)$$

From (21) and (25), the expression of  $M(\tau)$  is obtained as

$$M(\tau) = \left( M - \frac{8PCf_0}{16C^2 + 9\omega^2} \right) e^{\frac{4}{3}C\tau} + \frac{6Pf_0}{16C^2 + 9\omega^2} \left( \frac{4}{3}C \cos(\omega\tau) + \omega \sin(\omega\tau) \right) \quad (27)$$

Therefore, the analytical solitary wave solution of the DIA solitary waves for the damped forced KdV (17) is

$$\phi_1 = \phi_m(\tau) \operatorname{sech}^2 \left( \frac{\xi - M(\tau)\tau}{W(\tau)} \right), \quad (28)$$

Where  $M(\tau)$  is given by equation (27), and the amplitude and width are as follows:

$$\phi_m(\tau) = \frac{3 \left( M - \frac{8PCf_0}{16C^2 + 9\omega^2} \right) e^{\frac{4}{3}C\tau} + \frac{18Pf_0}{16C^2 + 9\omega^2} \left( \frac{4}{3}C \cos(\omega\tau) + \omega \sin(\omega\tau) \right)}{P} \quad (29)$$

$$W(\tau) = \frac{2\sqrt{Q}}{\sqrt{\left( M - \frac{8PCf_0}{16C^2 + 9\omega^2} \right) e^{\frac{4}{3}C\tau} + \frac{6Pf_0}{16C^2 + 9\omega^2} \left( \frac{4}{3}C \cos(\omega\tau) + \omega \sin(\omega\tau) \right)}} \quad (30)$$

## 5. RESULTS AND DISCUSSION

In this manuscript, we have explored the impact of various physical parameters, such as the dust-ion collisional frequency ( $\nu_{id0}$ ), frequency ( $\omega$ ), strength of the external periodic force ( $f_0$ ), ion-to-electron temperature ratio ( $\sigma$ ) and entropic index ( $q$ ) on the formation and existence of DIA solitary wave by the DIA solitary wave solution of the damped forced KdV equation (17) using numerical computations.

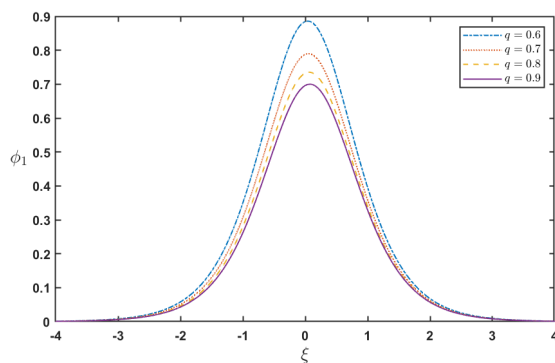


**Figure 1.** Profile of solitary wave potential  $\phi_1$  with  $\xi$  for different values of  $q$  and fixed values of  $\mu = 0.2$ ,  $\sigma = 0.1$ ,  $\nu_{id0} = 0.01$ ,  $\omega = 0.5$ ,  $f_0 = 0.05$ ,  $M = 0.1$ , and  $\tau = 2$ .

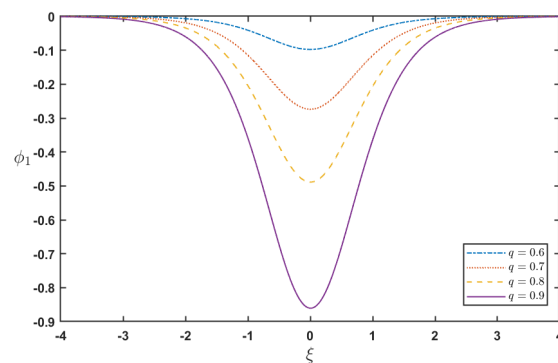
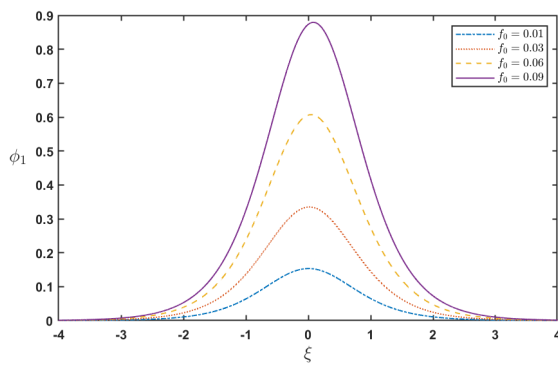


**Figure 2.** Profile of solitary wave potential  $\phi_1$  with  $\xi$  for different values of  $q$  and fixed values of  $\mu = 0.5$ ,  $\sigma = 0.1$ ,  $\nu_{id0} = 0.01$ ,  $\omega = 0.5$ ,  $f_0 = 0.05$ ,  $M = 0.1$ , and  $\tau = 2$ .

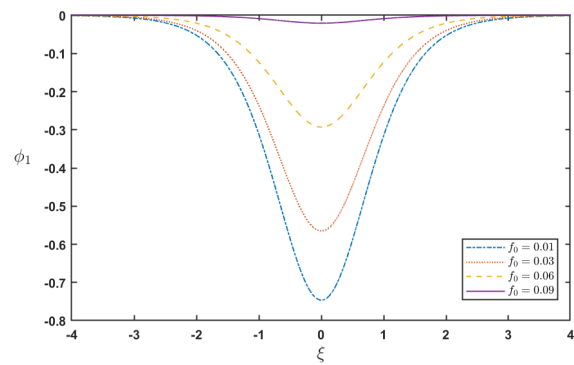
Figure (1) depict the graph of the variation of compressive solitary wave profile  $\phi_1$  versus  $\xi$  of the damped forced KdV equation (17) for the different values of the entropic index  $q = 0.6, 0.7, 0.8, 0.9$  where  $q$  is taken from the interval  $(0.6, 0.9)$  with special values of the other fixed parameter  $M = 0.1$ ,  $\sigma = 0.1$ ,  $\mu = 0.2$ ,  $\nu_{id0} = 0.01$ ,  $\omega = 0.5$ ,  $f_0 = 0.05$  and  $\tau = 2$ . It is observed that the amplitude of the compressive solitary wave decreases and width also decreases as the value of entropic index  $q$  increases. A right hand shifting of the DIA solitary wave solution is also observed as  $q$  increases.

Figure (2) represent the variation of the rarefactive solitary wave profile for the DIA solitary wave corresponding to the damped forced KdV equation (17) for different entropic index  $q = 0.6, 0.7, 0.8, 0.9$  with dust-to-ion number density ratio  $\mu = 0.5$ , and the other parameters are the same as in Figure (1). In this figure we observed that the amplitude and width of the rarefactive solitary wave increases as the value of entropic index  $q$  increases. Thus the DIA rarefactive solitary wave flourishes as the entropic index  $q$  grows rapidly. Here we also observed from Figure (1) and Figure (2), and it is interesting to note that the reverse effect happened after changing the value of dust-to-ion number density ratio ( $\mu$ ) from 0.2 to 0.5. that means the value of dust-to-ion number density ratio  $\mu$  has a significant effect on the dynamics of the DIA solitary wave of the damped forced KdV equation.

Figure (3) depict the variation of the compressive solitary wave profile  $\phi_1$  versus  $\xi$  of the damped forced KdV equation (17) for varying values of the strength of the external periodic force  $f_0 = 0.01, 0.03, 0.06, 0.09$ , here  $f_0$  is taken from the interval  $(0.01, 0.09)$  with special fixed values of the other parameters  $\sigma = 0.1$ ,  $\mu = 0.2$ ,  $M = 0.1$ ,  $\nu_{id0} =$



**Figure 3.** Profile of solitary wave potential  $\phi_1$  with  $\xi$  for different values of  $f_0$  and fixed values of  $\mu = 0.2$ ,  $\sigma = 0.1$ ,  $\nu_{id0} = 0.01$ ,  $\omega = 0.5$ ,  $q = 0.8$ ,  $M = 0.1$ , and  $\tau = 2$ .



**Figure 4.** Profile of solitary wave potential  $\phi_1$  with  $\xi$  for different values of  $f_0$  and fixed values of  $\mu = 0.5$ ,  $\sigma = 0.1$ ,  $\nu_{id0} = 0.01$ ,  $\omega = 0.5$ ,  $q = 0.8$ ,  $M = 0.1$ , and  $\tau = 2$ .

0.01,  $\omega = 0.5$ ,  $q = 0.8$  and  $\tau = 2$ . We observed that as the strength of the external periodic force  $f_0$  rises, it is found that the compressive DIA solitary wave's amplitude and breadth also increase.

Figure (4) shows a graph of the variation of the rarefactive solitary wave profile  $\phi_1$  versus  $\xi$  of the damped forced KdV equation (17) for varying values of the strength of the external periodic force  $f_0 = 0.01, 0.03, 0.06, 0.09$  with dust-to-ion number density ratio  $\mu = 0.5$ . All other parameters are the same as in Figure (3). Here, we found that when the external periodic force  $f_0$  becomes stronger, the rarefactive DIA solitary wave's amplitude and width decrease. Figure (3) and Figure (4) also showed us that the behaviour of the DIA solitary wave completely changes when the dust-to-ion number density ratio ( $\mu$ ) is changed from 0.2 to 0.5. It is interesting to note that Figure (3) shows compressive and right hand shifting of the DIA solitary wave and Figure (4) shows rarefactive and not right hand shifting.

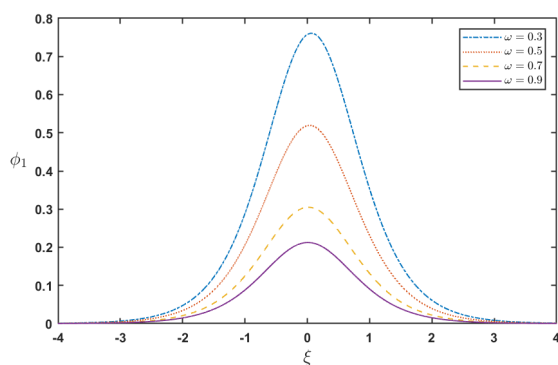


**Figure 5.** Profile of solitary wave potential  $\phi_1$  with  $\xi$  for different values of  $\omega$  and fixed values of  $\mu = 0.2$ ,  $\sigma = 0.1$ ,  $\nu_{id0} = 0.01$ ,  $f_0 = 0.05$ ,  $q = 0.8$ ,  $M = 0.05$ , and  $\tau = 2$ .

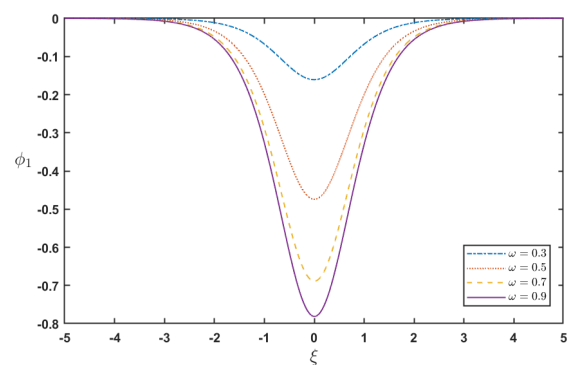
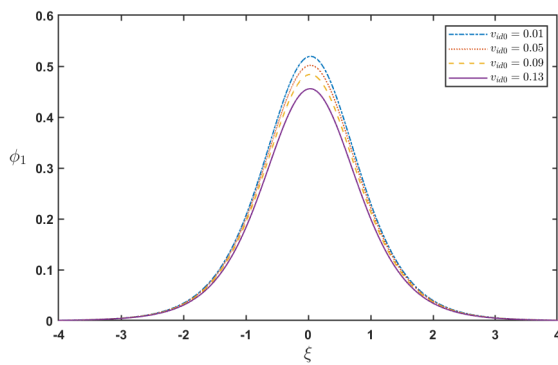


**Figure 6.** Profile of solitary wave potential  $\phi_1$  with  $\xi$  for different values of  $\omega$  and fixed values of  $\mu = 0.5$ ,  $\sigma = 0.1$ ,  $\nu_{id0} = 0.01$ ,  $f_0 = 0.05$ ,  $q = 0.8$ ,  $M = 0.05$ , and  $\tau = 2$ .

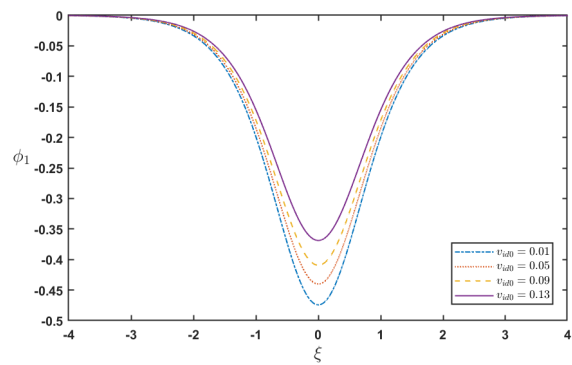
Figure (5) also shows the variation of the compressive DIA solitary wave profile  $\phi_1$  versus  $\xi$  of the damped forced KdV equation (17) for different values of the frequencies  $\omega = 0.3, 0.5, 0.7, 0.9$ , here  $\omega$  is taken from the interval (0.3, 0.9) with special fixed values of the other parameters  $\sigma = 0.1$ ,  $\mu = 0.2$ ,  $M = 0.05$ ,  $\nu_{id0} = 0.01$ ,  $f_0 = 0.05$ ,  $q = 0.8$  and  $\tau = 2$ . It is observed from the graph that the amplitude and width of the compressive DIA solitary wave decreases with the value of the frequencies  $\omega$  increases.

Figure (6) depict the graph of the variation of the rarefactive solitary wave profile  $\phi_1$  versus  $\xi$  of the damped forced KdV equation (17) for different values of the frequencies  $\omega = 0.3, 0.5, 0.7, 0.9$ , here  $\omega$  is taken from the interval (0.3, 0.9) with dust-to-ion number density ratio  $\mu = 0.5$  and other parameter are the same as in Figure (5). Figure (5) and Figure (6) are shown different behaviour compressive right hand shifting and rarefactive not right hand shifting after changing the parameter dust-to-ion number density ratio  $\mu$  value from 0.2 to 0.5.

Figure (7) reflects the variation of the compressive solitary wave profile  $\phi_1$  versus  $\xi$  of the damped forced KdV equation (17) for the different values of dust ion collisional frequencies  $\nu_{id0} = 0.01, 0.05, 0.09, 0.13$ , with special values of the other parameters  $\sigma = 0.1$ ,  $\mu = 0.2$ ,  $M = 0.05$ ,  $\omega = 0.4$ ,  $f_0 = 0.05$ ,  $q = 0.8$ ,  $\tau = 2$  and Figure (8) reflects the variation of the rarefactive solitary wave profile  $\phi_1$  versus  $\xi$  of the damped forced KdV equation (17) for the different values of dust ion collisional frequencies  $\nu_{id0} = 0.01, 0.05, 0.09, 0.13$ ,  $\mu = 0.5$  and other parameter are the same as in Figure (7) and  $\nu_{id0}$  is taken from the interval (0.01, 0.13) and to discuss the changes, we observed from Figure (7) that the amplitude and width decreases as the value of dust ion collisional frequencies  $\nu_{id0}$  increases and from Figure (8) we observed that



**Figure 7.** Profile of solitary wave potential  $\phi_1$  with  $\xi$  for different values of  $\nu_{ido}$  and fixed values of  $\mu = 0.2$ ,  $\sigma = 0.1$ ,  $\omega = 0.5$ ,  $f_0 = 0.05$ ,  $q = 0.8$ ,  $M = 0.05$ , and  $\tau = 2$ .



**Figure 8.** Profile of solitary wave potential  $\phi_1$  with  $\xi$  for different values of  $\nu_{ido}$  and fixed values of  $\mu = 0.5$ ,  $\sigma = 0.1$ ,  $\omega = 0.5$ ,  $f_0 = 0.05$ ,  $q = 0.8$ ,  $M = 0.05$  and  $\tau = 2$ .

the amplitude and width of the rarefactive solitary wave decreases as the values of dust ion collisional frequencies  $\nu_{ido}$  increases. Here from both the graph we also observed that Figure (7) and Figure (8) shows the compressive and rarefactive DIA solitary wave behaviour after changing the only one parameter value  $\mu$  from 0.2 to 0.5.

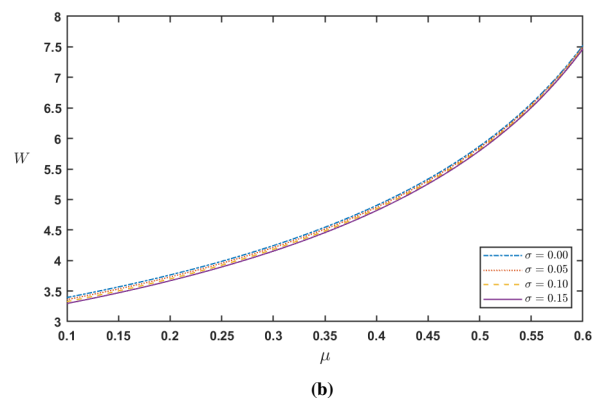
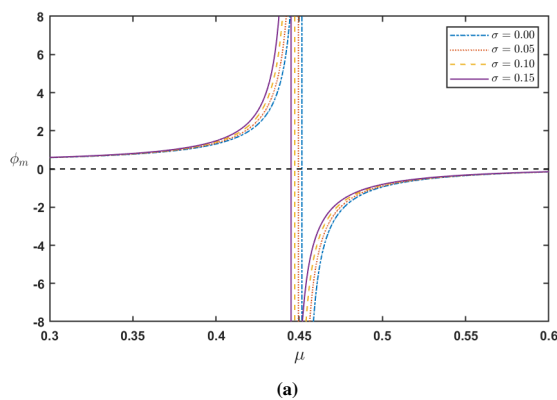


**Figure 9.** (a) Soliton amplitude  $\phi_m$  and (b) Soliton width  $W$  with  $\mu$  for different values of  $\sigma$  and fixed values of  $\omega = 0.5$ ,  $f_0 = 0.05$ ,  $q = 0.8$ ,  $M = 0.1$  and  $\tau = 2$ .



Figure (9a) shows the graph amplitude  $\phi_m$  versus  $\mu$  of compressive and rarefactive damped forced KdV solitons for different values of  $\sigma = 0.00, 0.05, 0.10, 0.15$  and fixed values of  $\omega = 0.5$ ,  $f_0 = 0.05$ ,  $q = 0.8$ ,  $M = 0.1$  and  $\tau = 2$ . Here we observed that an increase of the amplitudes of compressive DIA KdV solitons suddenly shows a rapid and convex increase within a very small interval of  $\mu$ , but their rarefactive counter parts sharply decrease concavely for each increasing value of  $\sigma$  in a similar but opposite pattern. Figure (9b) shows the graph the variation of width  $W$  of the rarefactive solitary wave solution of the damped forced KdV with respect to  $\mu$  for different values of  $\sigma = 0.00, 0.05, 0.10, 0.15$  with fixed values of  $\omega = 0.5$ ,  $f_0 = 0.05$ ,  $q = 0.8$ ,  $M = 0.1$  and  $\tau = 2$ . The width of DIA solitary waves is seen to increase as the dust-to-ion number density ratio  $\mu$  increases. Also, at the same time, it is observed that the width of the solitary wave increases rapidly with the different increase in values of the ion-to-electron temperature ratio  $\sigma$ .

## 6. CONCLUSIONS

In this study, we examined DIA solitary waves in a dusty plasma containing immobile dust particles, non-extensive electrons, and negatively charged ions. We derive the damped forced KdV equation using the reductive perturbation approach. An analytical solitary wave solution has been derived for the damped forced KdV equation in the presence of a small damped and externally applied periodic force. The effect of parameters  $q$ ,  $f_0$ ,  $M$ ,  $\sigma$  and  $\omega$  on the acoustic solitary wave solution of dust ions with fixed values of the other physical parameters  $\mu$ ,  $\tau$  has been presented. The parameters  $q$ ,  $f_0$ ,  $M$ ,  $\nu_{ido}$ ,  $\sigma$  and  $\omega$  have played an important role in the nonlinear structure of the DIA solitary wave in a collisional dusty plasma.

The present theoretical finding should be crucial for understanding how nonlinear DIA solitary waves behave in a variety of plasma environments, such as the Earth's magnetosphere in space plasma, the pulsar magnetosphere of astrophysical plasmas, and laboratory plasmas that contain the plasma under consideration.

## ORCID

 Sarbamon Tokbi, <https://orcid.org/0009-0002-8917-7373>;  Satyendra Nath Barman, <https://orcid.org/0000-0003-1136-8364>

## REFERENCES

- [1] F.F. Chen, *Introduction to Plasma Physics and Controlled Fusion*, 3rd edition, (Springer, 2016).
- [2] H. Schamel, and V.I. Maslov, "Adiabatic growth of electron holes in current-carrying plasmas", *Physica Scripta*, **T50**, 42 (1994). <https://doi.org/10.1088/0031-8949/t50/006>
- [3] V.I. Maslov, and H.Schamel, "Growing electron holes in drifting plasmas", *Physics Letters A*, **178**, 171 (1993). <https://doi.org/10.1088/0031-8949/1994/t50/006>
- [4] H. Schamel, and V. Maslov, "Langmuir Wave Contraction Caused by Electron Holes," *Physica Scripta*, **82**, 122 (1999). <https://doi.org/10.1238/physica.topical.082a00122>
- [5] D. Batani, V. Maslov, and D. Bondar, *et al.* "Smoothing of transverse nonuniformities at the critical density in laser interaction with nonuniform plasmas," *Laser and Particle Beams*, **43**, (e3) (2025). <https://doi.org/10.1017/lpb.2025.10003>
- [6] V.I. Maslov, "Electron beam excitation of a potential well in a magnetized plasma waveguide," *Physics Letters A*, **165**(1), 63–68 (1992). [https://doi.org/10.1016/0375-9601\(92\)91055-v](https://doi.org/10.1016/0375-9601(92)91055-v)
- [7] V.I. Maslov, I.N.Onishchenko, I.P.Yarovaya, *et al.* "Excitation and properties of large amplitude soliton near foil at laser pulse interaction with it," *Problems of Atomic Science and Technology*, (1), 324–327 (2012).
- [8] A. Scott, *Encyclopedia of nonlinear science*, 1st edition, (Routledge, 2006).
- [9] N.J. Zabusky, and M.D. Kruskal, "Interaction of solitons in a collisionless plasma and the recurrence of initial states," *Physical review letters*, **15**(6), 240 (1965). <https://doi.org/10.1103/physrevlett.15.240>
- [10] P.K. Shukla, "Nonlinear waves and structures in dusty plasmas," *Physics of Plasmas*, **10**(5), 1619-1627 (2003). <https://doi.org/10.1063/1.1557071>
- [11] A.P. Misra, and C. Bhowmik, "Nonplanar ion-acoustic waves in a quantum plasma," *Physics Letters A*, **369**(1-2), 90-97 (2007). <https://doi.org/10.1016/j.physleta.2007.04.066>
- [12] F. Verheest, "Waves and instabilities in dusty space plasmas," *Space Science Reviews*, **77**(3), 267-302 (1996). <https://doi.org/10.1007/bf00226225>
- [13] B. Tian, and Y.T. Gao, "Symbolic computation on cylindrical-modified dust-ion-acoustic nebulons in dusty plasmas," *Physics Letters A*, **362**(4), 283-288 (2007). <https://doi.org/10.1016/j.physleta.2006.10.094>
- [14] R. Bharuthram, and P.K. Shukla, "Large amplitude ion-acoustic double layers in a double Maxwellian electron plasma," *The Physics of fluids*, **29**(10), 3214-3218 (1986). <https://doi.org/10.1063/1.865839>
- [15] L.L. Yadav, and S.R. Sharma, "Obliquely propagating ion-acoustic double layers in a multicomponent magnetized plasma," *Physica scripta*, **43**(1), 106 (1991). <https://doi.org/10.1088/0031-8949/43/1/018>
- [16] F.B. Rizzato, "Weak nonlinear electromagnetic waves and low-frequency magnetic-field generation in electron-positron-ion plasmas," *Journal of plasma physics*, **40**(2), 289-298 (1988). <https://doi.org/10.1017/s0022377800013283>
- [17] H.R. Miller, and P.J. Wiita, *Active galactic nuclei*, vol. 30, (1988).
- [18] V.S. Beskin, A.V. Gurevich, and Y.N. Istomin, *Physics of the pulsar magnetosphere*, (Cambridge university press, 1993).
- [19] F.C. Michel, "Theory of pulsar magnetospheres," *Reviews of Modern Physics*, **54**(1), 1 (1982). <https://doi.org/10.1103/revmodphys.54.1>
- [20] H. Washimi, and T. Taniuti, "Propagation of ion-acoustic solitary waves of small amplitude," *Physical Review Letters*, **17**(19), 996 (1966). <https://doi.org/10.1103/physrevlett.17.996>
- [21] B.B. Kadomtsev, and V.I. Karpman, "Nonlinear waves," *Soviet Physics Uspekhi*, **14**(1), 40 (1971).
- [22] D. Gresillon, and F. Doveil, "Normal modes in the ion-beam-plasma system," *Physical Review Letters*, **34**(2), 77 (1975). <https://doi.org/10.1103/physrevlett.34.77>
- [23] B.C. Kalita, and S.N. Barman, "Fully nonlinear ion-acoustic solitary waves in a warm magnetized plasma with electron inertia," *Astrophysics and Space Science*, **330**, 311-316 (2010). <https://doi.org/10.1007/s10509-010-0394-y>
- [24] S.A. Boldyrev, S.V. Vladimirov, and V.N. Tsytovich, "Coupled Langmuir and ion-acoustic solitons," *Soviet Journal of Plasma Physics*, **18**(11), 727-732 (1992).
- [25] H. Ikezi, R.J. Taylor, and D.R. Baker, "Formation and interaction of ion-acoustic solitons," *Physical Review Letters*, **25**(1), 11 (1970). <https://doi.org/10.1103/physrevlett.25.11>
- [26] H. Ikezi, Experiments on ion-acoustic solitary waves. Research Report: (IPPI, 1973).
- [27] Y. Nakamura, and T. Ogino, "Numerical and laboratory experiments on spherical ion-acoustic solitons," *Plasma Physics*, **24**(10), 1295 (1982). <https://doi.org/10.1088/0032-1028/24/10/007>
- [28] G.O. Ludwig, J.L. Ferreira, and Y. Nakamura, "Observation of ion-acoustic rarefaction solitons in a multicomponent plasma with negative ions," *Physical review letters*, **52**(4), 275 (1984). <https://doi.org/10.1103/physrevlett.52.275>

- [29] J.L. Cooney, M.T. Gavin, and K.E. Lonngren, "Experiments on Korteweg–de Vries solitons in a positive ion–negative ion plasma," *Physics of Fluids B: Plasma Physics*, **3**(10), 2758-2766 (1991). <https://doi.org/10.1063/1.859912>
- [30] W.H. Julian, and P. Goldreich, "Pulsar electrodynamics," *Astrophys. J.*, **157**, 869 (1969). <https://doi.org/10.1086/150119>
- [31] E. Tandberg-Hanssen, and A.G. Emslie, *The physics of solar flares*, vol. 14, (Cambridge University Press, 1988).
- [32] C.K. Goertz, "Dusty plasmas in the solar system. Reviews of Geophysics," **27**(2), 271-292 (1989). <https://doi.org/10.1029/rg027i002p00271>
- [33] O. Havnes, T. Aslaksen, F. Melandsø, and T. Nitter, "Collisionless braking of dust particles in the electrostatic field of planetary dust rings," *Physica Scripta*, **45**(5), 491 (1992). <https://doi.org/10.1088/0031-8949/45/5/012>
- [34] E.C. Whipple, T.G. Northrop, and D.A. Mendis, "The electrostatics of a dusty plasma," *Journal of Geophysical Research: Space Physics*, **90**(A8), 7405-7413 (1985). <https://doi.org/10.1029/ja090ia08p07405>
- [35] P.K. Shukla, and A.A. Mamun, *Introduction to dusty plasma physics*, 1st edn. (IOP, London, 2002).
- [36] F. Verheest, "Waves and instabilities in dusty space plasmas," *Space Science Reviews*, **77**(3), 267-302 (1996). <https://doi.org/10.1007/bf00226225>
- [37] L. Tonks, and I. Langmuir, "Oscillations in ionized gases," *Physical Review*, **33**(2), 195 (1929). <https://doi.org/10.1103/physrev.33.195>
- [38] R.W. Revans, "The transmission of waves through an ionized gas," *Physical Review*, **44**(10), 798 (1933). <https://doi.org/10.1103/physrev.44.798>
- [39] M.A. Leontovich, editor, *Reviews of Plasma Physics*, (Springer Science & Business Media, (2012).
- [40] H. Ikezi, R.J. Taylor, and D.R. Baker, "Formation and interaction of ion-acoustic solitons," *Physical Review Letters*, **25**(1), 11 (1970). <https://doi.org/10.1103/physrevlett.25.11>
- [41] A.A. Mamun, "Arbitrary amplitude dust-acoustic solitary structures in athree-component dusty plasma," *Astrophysics and Space Science*, **268**, 443-454 (1999). <https://doi.org/10.1023/a:1002031022895>
- [42] N.N. Rao, P.K. Shukla, and M.Y. Yu, "Dust-acoustic waves in dusty plasmas," *Planetary and space science*, **38**(4), 543-546 (1990). [https://doi.org/10.1016/0032-0633\(90\)90147-i](https://doi.org/10.1016/0032-0633(90)90147-i)
- [43] P.K. Shukla, M.Y. Yu, and R. Bharuthram, "Linear and nonlinear dust drift waves," *Journal of Geophysical Research: Space Physics*, **96**(A12), 21343-21346 (1991). <https://doi.org/10.1029/91ja02331>
- [44] F. Melandsø, "Lattice waves in dust plasma crystals," *Physics of Plasmas*, **3**(11), 3890-3901 (1996). <https://doi.org/10.1063/1.871577>
- [45] P.K. Shukla, and R.K. Varma, "Convective cells in nonuniform dusty plasmas," *Physics of Fluids B: Plasma Physics*, **5**(1), 236-237 (1993). <https://doi.org/10.1063/1.860864>
- [46] R.L. Merlino, A. Barkan, C. Thompson, and N. D'angelo, "Laboratory studies of waves and instabilities in dusty plasmas," *Physics of Plasmas*, **5**(5), 1607-1614 (1998). <https://doi.org/10.1063/1.872828>
- [47] M. Tribeche, and T.H. Zerguini, "Small amplitude Bernstein–Greene–Kruskal solitary waves in a thermal charge-varying dusty plasma," *Physics of Plasmas*, **11**(8), 4115-4122 (2004). <https://doi.org/10.1063/1.1768957>
- [48] J. Tamang, K. Sarkar, and A. Saha, "Solitary wave solution and dynamic transition of dust ion acoustic waves in a collisional nonextensive dusty plasma with ionization effect," *Physica A: Statistical Mechanics and its Applications*, **505**, 18-34 (2018). <https://doi.org/10.1016/j.physa.2018.02.213>
- [49] P.K. Shukla, and V.P. Silin, "Dust ion-acoustic wave," *Physica Scripta*, **45**(5), 508 (1992). <https://doi.org/10.1088/0031-8949/45/5/015>
- [50] A. Barkan, N. D'angelo, and R.L. Merlino, "Experiments on ion-acoustic waves in dusty plasmas," *Planetary and Space Science*, **44**(3), 239-242 (1996). [https://doi.org/10.1016/0032-0633\(95\)00109-3](https://doi.org/10.1016/0032-0633(95)00109-3)
- [51] Y. Nakamura, H. Bailung, and P.K. Shukla, "Observation of ion-acoustic shocks in a dusty plasma," *Physical review letters*, **83**(8), 1602 (1999). <https://doi.org/10.1103/physrevlett.83.1602>
- [52] A. Rényi, "On a new axiomatic theory of probability," *Acta Mathematica Academiae Scientiarum Hungarica*, **6**, 285-335 (1955). <https://doi.org/10.1007/bf02024393>
- [53] L. Liyan, and D. Jiulin, "Ion acoustic waves in the plasma with the power-law q-distribution in nonextensive statistics," *Physica A: Statistical Mechanics and its Applications*, **387**(19-20), 4821-4827 (2008). <https://doi.org/10.1016/j.physa.2008.04.016>
- [54] C. Tsallis, "Nonadditive entropy and nonextensive statistical mechanics-an overview after 20 years," *Brazilian Journal of Physics*, **39**, 337-356 (2009). <https://doi.org/10.1590/s0103-97332009000400002>
- [55] A. Saha, "Bifurcation, periodic and chaotic motions of the modified equal width-Burgers (MEW-Burgers) equation with external periodic perturbation," *Nonlinear Dynamics*, **87**(4), 2193-2201 (2017). <https://doi.org/10.1007/s11071-016-3183-5>
- [56] L. Mandi, K.K. Mondal, and P. Chatterjee, "Analytical solitary wave solution of the dust ion acoustic waves for the damped forced modified Korteweg–de Vries equation in q-nonextensive plasmas," *The European Physical Journal Special Topics*, **228**(12), 2753-2768 (2019). <https://doi.org/10.1140/epjst/e2019-900047-4>
- [57] A. Saha, and P. Chatterjee, "Solitonic, periodic and quasiperiodic behaviors of dust ion acoustic waves in superthermal plasmas," *Brazilian Journal of Physics*, **45**, 419-426 (2015). <https://doi.org/10.1007/s13538-015-0329-8>

- [58] N.S. Saini, "Dust ion acoustic rogue waves in superthermal warm ion plasma," *Journal of Plasma Physics*, **81**(3), 905810316 (2015). <https://doi.org/10.1017/s0022377815000082>
- [59] K. Nozaki, and N. Bekki, "Chaos in a perturbed nonlinear Schrödinger equation," *Physical review letters*, **50**(17), 1226 (1983). <https://doi.org/10.1103/physrevlett.50.1226>
- [60] W. Beiglbock, J.P. Eckmann, H. Grosse, M. Loss, S. Smirnov, *et al. Concepts and Results in Chaotic Dynamics*, (Springer, Berlin 2000).
- [61] P. Chatterjee, R. Ali, and A. Saha, "Analytical solitary wave solution of the dust ion acoustic waves for the damped forced Korteweg–de Vries equation in superthermal plasmas," *Zeitschrift für Naturforschung A*, **73**(2), 151-159 (2018). <https://doi.org/10.1515/zna-2017-0358>
- [62] A.S. Bains, M. Tribeche, and T.S. Gill, "Modulational instability of ion-acoustic waves in a plasma with a q-nonextensive electron velocity distribution," *Physics of Plasmas*, **18**(2), (2011). <https://doi.org/10.1063/1.3554658>

# ВПЛИВ ТЕМПЕРАТУРИ ІОНІВ НА ДИНАМІКУ АНАЛІТИЧНОГО РІШЕННЯ ВІДОКРЕМЛЕНОЇ ХВИЛІ ДЛЯ ПИЛОВИХ ІОННИХ АКУСТИЧНИХ ХВИЛЬ ДЛЯ ЗАГАСАЮЧОГО РІВНЯННЯ КОРТЕВЕГА-ДЕ ФРІЗА В Q-НЕЕКСТЕНСИВНІЙ ПЛАЗМІ

Сарбамон Токбі<sup>1\*</sup>, Сатъєндра Натх Барман<sup>2</sup>

<sup>1</sup>Кафедра математики, Університет Гаухаті, Гувахаті-781014, Ассам, Індія


<sup>2</sup>Б. Коледж Боруа, Гувахаті-781007, Ассам, Індія

У цій статті досліджуються динамічні властивості аналітичного розв'язку одиночних хвиль пилово-іонної акустики (DIA), індукованих затухаючим вимушеним рівнянням Кортевега-де Фріза (DFKdV) у ненамагніченій зіткнувальній пиловій плазмі, що містить нейтральні частинки,  $q$ -неекстенсивні електрони, позитивно заряджені іони та негативно заряджені пилові частинки за наявності зовнішньої періодичної сили. Для отримання затухаючого вимушеного рівняння Кортевега-де Фріза (DFKdV) було розроблено підхід редукувальних збурень. Помічено, що для цієї моделі плазми можливі як стискаючі, так і розріджені одиночні хвильові розв'язки пилово-іонної акустики (DIA). Враховується вплив низки фізичних параметрів: ентропійного індексу ( $q$ ), частоти зіткнень іонів пилу ( $\nu_{id0}$ ), швидкості біжучої хвилі ( $M$ ), частоти періодичної сили ( $\omega$ ), співвідношення температур іонів до електронів ( $\sigma$ ), параметра, що є співвідношенням між незбуреними густинами іонів пилу та електронів ( $\mu$ ), сили та частоти зовнішньої періодичної сили ( $f_0$ ). Спостерігається, що ці параметри мають значний вплив на структури затухаючих вимушених акустичних одиночних хвиль іонів пилу. Результати цього дослідження можуть бути важливими для розуміння динаміки одиночних хвиль пил-іонів (DIA) у лабораторній плазмі, а також у космічному плазмовому середовищі.

**Ключові слова:** іонно-акустичний солітон, одиночна хвиля, пилова плазма, метод редукувальних збурень, неекстенсивний електрон, затухаюче вимушене рівняння KdV



## THIRD HARMONIC GENERATION OF Q-GAUSSIAN LASER BEAM IN COLLISIONLESS PLASMA

Kulkaran Singh,  Keshav Walia\*, Taranjot Singh

Department of Physics, DAV University Jalandhar, Punjab-144012, India

\*Corresponding Author Email: [keshavwalia86@gmail.com](mailto:keshavwalia86@gmail.com)

Received September 13, 2025; revised October 26, 2025; accepted October 27, 2025

In the current study, third-harmonic generation (THG) of a q-Gaussian laser beam propagating through a collisionless plasma is investigated. This nonlinear beam profile induces density gradients in the plasma due to the ponderomotive force. These density gradients excite electron plasma waves (EPW) at twice the pump wave frequency via  $\vec{V} \times \vec{B}$  mechanism. The fundamental pump wave and the EPW interact nonlinearly to produce third-harmonic radiation. The nonlinear ODE for the beam waist of the pump beam and the THG conversion efficiency expressions are obtained by employing WKB and paraxial approaches. The influence of key laser-plasma parameters, including plasma density, beam width, intensity, and q-parameter, on the self-focusing of the main beam and the 3<sup>rd</sup> harmonic efficiency is also analyzed. The results indicate that q-Gaussian beams, due to their higher field amplitudes and broader wings than conventional Gaussian beams, can significantly enhance THG in collisionless plasmas. These findings provide insights into optimizing harmonic generation in structured laser beams for applications in ultrafast optics, particle acceleration, and plasma-based radiation sources.

**Keywords:** Collisionless Plasma; Density Gradients; Pump Wave; Electron Plasma Wave; Self-focusing; Third harmonic Generation

**PACS:** 52.38.Hb, 52.35.Mw, 52.38.Dx

### 1. INTRODUCTION

Lasers interaction with plasma medium is an important research topic amongst theoretical/experimental researchers in recent decades, owing to their crucial role in inertial confinement fusion (ICF), charged particle acceleration and radiation sources [1-6]. During laser-plasma interaction, a wide variety of nonlinear processes, including self-focusing, parametric instabilities, self-phase modulation, and harmonic generation, are produced [6-15]. Harmonic generation has received significant attention due to its fundamental significance and technological applications. The propagation dynamics of the laser beam is strongly influenced by harmonic generation. Harmonic generation facilitates beam propagation in overdense regions and supports mode conversion processes. The generation of harmonics has been extensively studied in laser-plasma systems [16-21]. Third harmonics generation becomes an important nonlinear process for ultra-relativistic laser intensities and structured beams. Mostly the work on harmonic generation was explored by considering uniform plane waves. However, actual laser beams have non-uniform spatial irradiance profiles and nonlinear processes are greatly triggered by such spatial profiles. Such non-uniform profiles exhibit self-focusing/Self-defocusing phenomena. So, they modify overall electric field strength and hence enhance efficiency of harmonic production. q-Gaussian beams have higher field amplitude across the wave front in comparison to ordinary Gaussian profiles. So, this motivates us to explore third harmonic radiation from q-Gaussian beam in plasmas. Researchers interest in laser-plasma interaction extends beyond plasma optics. Because, electron plasma wave (EPW) is excited at high frequency during this process. This high frequency plasma wave may result in to production of energetic electrons, which can preheat the fusion target and could cause degradation of implosion performance. Similarly, high frequency plasma wave transfers energy to charged particles through wave-particle interaction. In this process, charged particles acquire extremely high energy thereby causing ultrahigh acceleration gradients. So, in actual practice, nonlinear plasma response that generates harmonic radiation also plays key part in such processes.

Experimental/Theoretical researchers have explored higher harmonic radiations in plasma. Schifano et al. [22] explored generation of harmonics in plasma through filamentation process.

Esarey et al. [23] explored relativistic harmonic radiations in plasma and further the discussed the effect of diffraction in forward harmonic emission. The production of harmonics in forward direction has also been explored in underdense plasma [24-25]. Ganeev et al. [26] explored production of higher harmonics in plasma plumes and Gupta et al. [27] explored third harmonic generation at ultrarelativistic intensities. The use of wiggler magnetic field has been shown to significantly enhance THG efficiency by satisfying phase matching conditions [28-31]. Azad et al. explored that Raman-enhanced nonlinear effects in Hermite-cosh Gaussian beam are found to increase harmonic efficiency in magnetized plasmas [32]. Ganeev et al. explored that higher harmonic generation in boron carbide plasmas are found to show enhancement over carbon and boron plasmas [33]. Laser pulse critically influences harmonic yield, increasing linearly below and decreasing near saturation [34]. R.A. Ganeev explored enhancement of higher harmonics in laser induced plasmas [35]. Furthermore, pulse slippage and density transitions have been identified as critical factors influencing THG

efficiency [37-39]. It is already quite clear from these observations that third harmonic generations in plasmas are sensitive to beam structure, plasma profile, and nonlinear interaction geometry. Recently, a new class of lasers i.e. q-Gaussian lasers has been invented. Such beams have intensity irradiance in the form,  $f(r) = f(0) \left(1 + \frac{r^2}{qr_0^2}\right)^{-q}$ . Setting  $q \rightarrow \infty$  changes it to conventional Gaussian beam. There is greater flexibility linked with q-Gaussian profiles on account of tunable q-parameter. This q-parameter helps them to change their profiles from Gaussian like to Super-Gaussian like forms. Such beams also exhibit less divergence thereby enabling improved confinement of optical energy. q-Gaussian beam profiles also exhibit reduced power content and broader wings, which makes them suitable candidate in advanced nonlinear plasma studies. The researchers have explored numerous plasma instabilities using q-Gaussian laser beams in laser-plasma interaction studies, due to their strong nonlinear coupling characteristics [40-44]. The aim of present study is to explore THG of q-Gaussian laser beam propagating through collisionless plasma, with particular focus on understanding the roles of plasma density gradients and EPW in enhancing THG efficiency. It analyzes how q-parameter, beam width, intensity and plasma density affect self-focusing and THG efficiency optimization. The plasma electrons get redistributed as a result of ponderomotive force, thereby creating density gradients in plasma. They produce EPW at twice frequency of fundamental wave. The nonlinear interaction of EPW excited at  $2\omega$  with fundamental wave having frequency  $\omega$  produces third harmonic generation. The paper is organized as follows: In Section 2, wave equation for q-Gaussian beam in collisionless has been derived using paraxial theory. In Section 3, we derived the amplitude of electron plasma wave at  $2\omega$  starting from the fluid equations and further using perturbation analysis and process of linearization. In Section 4, we derived the efficiency of 3<sup>rd</sup> harmonics. Sections 5 & 6 are devoted to discussion of results and conclusion respectively.

## 2. SOLUTION OF WAVE EQUATION FOR PUMP BEAM

The current study explores transition of q-Gaussian beam in plasma in z-direction. The beam's intensity at plane  $z = 0$  is represented as

$$E \cdot E^*|_{z=0} = E_0^2 \left(1 + \frac{r^2}{qr_0^2}\right)^{-q} \quad (1)$$

In Eq. (1),  $E_0$  and  $r_0$  denote field amplitude and beam radius at  $z = 0$ . q-Gaussian beam profiles form more generalized concept of normal Gaussian profile through q value. Increasing q values make them closer to Gaussian beam profiles. If we keep the values of q very low, then we are in a position to produce broader/flatter profiles. For  $z > 0$ , the beam irradiance takes the form

$$E \cdot E^* = \frac{E_0^2}{f^2} \left(1 + \frac{r^2}{qr_0^2 f^2}\right)^{-q} \quad (2)$$

In Eq. (2),  $f$  is a parameter telling us about the contraction/divergence of the beam as it transits through plasma. This parameter, known as the beam waist, is related to the equilibrium beam radius. The Wave equation for the pump beam is expressed as

$$\nabla^2 E + \frac{\omega^2}{c^2} \varepsilon E = 0 \quad (3)$$

In writing Eq. (3), we just ignored  $\nabla(\nabla \cdot E)$  term. When we are having transverse waves then,  $\nabla \cdot E = k \cdot E = 0$ , where  $k$  is wave vector. Then term  $\nabla(\nabla \cdot E)$  has also been neglected in present problem considering  $\frac{c^2}{\omega^2} \left| \frac{1}{\varepsilon} \nabla^2 \ln \varepsilon \right| \leq 1$ . The alteration in plasma's dielectric response is observed in course of laser propagation within plasma. The Plasma's total dielectric function is comprising of two parts, i.e.

$$\varepsilon = \varepsilon_0 + \Phi(E \cdot E^*) \quad (4)$$

In Eq. (4), there are two contributions on RHS, ' $\varepsilon_0$ ' being linear contribution while ' $\Phi(E \cdot E^*)$ ' being nonlinear contribution. Both these terms are expressed mathematically as

$$\varepsilon_0 = 1 - \frac{\omega_p^2}{\omega^2} \quad (5)$$

$$\Phi(E \cdot E^*) = \frac{\omega_p^2}{\omega^2} \left[ 1 - \frac{N_{0e}}{N_0} \right] \quad (6)$$

In the above Eqs. (5) and (6),  $\omega_p = \sqrt{\frac{4\pi n e^2}{m}}$  is plasma frequency. ' $N_{0e}$ ' and ' $N_0$ ' denote the concentrations of plasma electrons in presence/absence of beams. Suppose a beam profile with angular frequency  $\omega$  and wave vector  $k$  is transiting along the z-axis in a hot collisionless plasma. During the transition of the laser beam through plasma, the nonlinear ponderomotive force induces density variations in plasma. This further changes the plasma density profile in the transverse direction as

$$\frac{N_{0e}}{N_0} = \exp\left(-\frac{3}{4}\beta \frac{m}{M} E \cdot E^*\right) \quad (7)$$



In Eq. (7),  $\beta = \frac{e^2 M}{6K_B T_0 \gamma \omega^2 m^2}$ ; Where,  $e$ ,  $m$ ,  $M$ ,  $T_0$  and  $K_B$  correspond to electronic charge, electronic mass, ionic mass, plasma temperature and Boltzmann constant respectively. So, on using Eq. (7), we can write the nonlinear portion for collisionless plasma as

$$\Phi(E \cdot E^*) = \frac{\omega_p^2}{\omega^2} \left[ 1 - \exp\left(-\frac{3}{4}\beta \frac{m}{M} E \cdot E^*\right) \right] \quad (8)$$

Now, we will make use of the approach [45-46] to obtain a solution of Eq. (3)

$$E = E_0(r, z) \exp[i(\omega t - k(S + z))] \quad (9)$$

$$E_0 \cdot E_0^* = \frac{E_{00}^2}{f^2} \left( 1 + \frac{r^2}{qr_0^2 f^2} \right)^{-q} \quad (10)$$

$$S = \frac{1}{2} r^2 \frac{1}{f} \frac{df}{dz} + \Phi_0(z) \quad (11)$$

$$k = \frac{\omega}{c} \sqrt{\epsilon_0} \quad (12)$$

Here,  $f$  is a parameter describing beam waist of q-Gaussian beam and it satisfies 2<sup>nd</sup> order differential equation as

$$\frac{d^2 f}{d\eta^2} = \frac{q+4}{qf^3} - \left( \frac{\omega p r_0}{c} \right)^2 \left( \frac{3}{4} \beta \frac{m}{M} E_{00}^2 \right) \exp\left[-\frac{3}{4} \beta \frac{m}{M} \frac{E_{00}^2}{f^2}\right] \frac{1}{f^3} \quad (13)$$

Eq. (13) denotes variation in beam waist with normalized propagation distance as laser beam transition in hot collisionless plasma take place. The boundary conditions are  $f = 1$  &  $\frac{df}{d\eta} = 0$  at  $\eta = 0$ .

### 3. EXCITATION OF ELECTRON PLASMA WAVE

We have considered the dynamics of plasma electrons in exploring excitation mechanism of EPW. Since, mass of ions is almost 2000 times mass of electrons. So, they will not react to large frequency field and will be treated as fixed in their respective position. Moreover, ions don't play any role in excitation mechanism of EPW. The nonlinear ponderomotive force produces density gradients in collisionless plasma, which act as source for EPW. We will start from the following Fluid equations in order to derive source term for THZ.

$$\frac{\partial N_e}{\partial t} + \nabla \cdot (N_e V) = 0 \quad (14)$$

$$\nabla \cdot E = 4\pi(ZN_{oi} - N_e)e \quad (15)$$

$$\frac{P}{N_e} = \text{Constant} \quad (16)$$

$$m \left[ \frac{\partial V}{\partial t} + (V \cdot \nabla)V \right] = -e \left[ E + \frac{1}{c} V \times B \right] - 2\Gamma m V - \frac{\gamma}{N_e} \nabla P_e \quad (17)$$

Using perturbation analysis and further linearizing the equations, amplitude term in case of EPW is obtained as

$$n_{2\omega}(r) = \frac{en_0 E_{00}}{m f} \left( 1 + \frac{r^2}{qr_0^2 f^2} \right)^{-\frac{q}{2}} \left\{ \frac{r}{r_0^2 f^2} \right\} \frac{1}{\left\{ 4\omega^2 - k^2 v_{th}^2 - \omega_p^2 \left( \exp\left[-\frac{3}{4}\beta \frac{m}{M} \frac{E_{00}^2}{f^2}\right] \right)^2 \right\}} \quad (18)$$

### 4. EFFICIENCY OF THIRD HARMONICS

Third harmonic radiation is produced through coupling of interaction of amplitude term for EPW  $n_{2\omega}$  with fundamental beam.

$$J_3^{NL} = -en_{2\omega} v_0 \quad (19)$$

In presence of input field, an electron oscillatory velocity is

$$v_0 = -\frac{eE_0}{mi\omega} \quad (20)$$

$$\text{Hence, } J_3^{NL} = \frac{e^2}{mi\omega} n_{2\omega} E_0 \quad (21)$$

The field vector  $E_3$  of THG obeys wave equation

$$\nabla^2 E_3 + \frac{\omega_3^2}{c^2} \epsilon_3(\omega_3) E_3 = -\frac{8\pi i \omega_3}{c^2} J_3^{NL} \quad (22)$$

On substituting value of  $J_3^{NL}$  from Eq. (21) in Eq. (22), one can obtain

$$\nabla^2 E_3 + \frac{\omega_3^2}{c^2} \varepsilon_3(\omega_3) E_3 = \frac{\omega_p^2}{c^2} \frac{n_2 \omega}{n_0} E_0 \quad (23)$$

In Eq. (23),  $\omega_3 = 3\omega$  and  $\varepsilon_3$  are for 3<sup>rd</sup> harmonic frequency and 3<sup>rd</sup> harmonic dielectric function respectively. We can easily solve Eq. (23) to obtain

$$E_3 = \frac{\omega_p^2}{c^2} \frac{n_2 \omega}{n_0} \frac{E_{00}}{f} \left(1 + \frac{r^2}{qr_0^2 f^2}\right)^{-\frac{q}{2}} \frac{1}{(k_3^2 - 9k^2)} \quad (24)$$

Now, the power of 3<sup>rd</sup> harmonics is

$$P_3 = \iint |E_3|^2 dx dy \quad (25)$$

The power of fundamental beam is

$$P_0 = \iint |E_0|^2 dx dy \quad (26)$$

The efficiency of 3<sup>rd</sup> harmonics is expressed as

$$Y_3 = \frac{\iint \left( \frac{\omega_p^2}{c^2} \frac{e}{m} \left( \frac{E_{00}}{f} \left(1 + \frac{r^2}{qr_0^2 f^2}\right)^{-\frac{q}{2}} \right) \left\{ \frac{r}{r_0^2 f^2} \right\} \frac{1}{4\omega^2 - k^2 v_{th}^2 - \omega_p^2 \left( \exp \left[ -\frac{3}{4} \beta \frac{m E_{00}^2}{M f^2} \right] \right)^2} \right)^2 \frac{1}{(k_3^2 - 9k^2)} r dr d\theta}{\iint \left( \frac{E_{00}}{f} \left(1 + \frac{r^2}{qr_0^2 f^2}\right)^{-\frac{q}{2}} \right)^2 r dr d\theta} \quad (27)$$

## 5. DISCUSSION

The Eqs. (13) and (27) don't have analytical solution on account of their nonlinear and coupled character. So, numerical simulations of these equations are performed by taking established laser and plasma parameters;

$$\alpha \left( = \frac{3}{4} \beta \frac{m}{M} \right) E_{00}^2 = 3.0, 4.0, 5.0 ; \frac{\omega_p^2}{\omega^2} = 0.3, 0.5, 0.7 ; r_0 = 15 \mu\text{m}, 20 \mu\text{m}, 25 \mu\text{m}, q = 1, 2, 3$$

Eq. (13) contains two contributions on RHS with each contribution has fundamental physical effect. The first term causes spreading of beam as it transits through medium. The second term causes nonlinear self-focusing of beam. So, the overall beam response in plasma is decided through interplay between these two opposite mechanisms. If first term is stronger, then beam divergence takes place. If second term is stronger, then contraction of beam takes place. When these two opposing mechanisms exactly balance each other in magnitude, then beam neither contracts nor diverges. On the other hand, beam's radius remains almost fixed during its transition through plasma medium. This equilibrium state so obtained is known as self-trapping, where beam transits through plasma medium without spreading or collapsing.

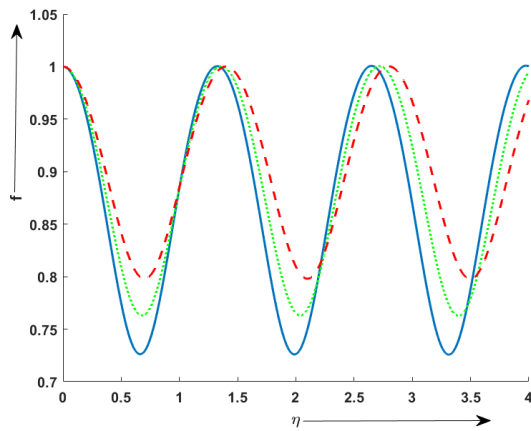
Figure 1 illustrates variation of  $f$  with  $\eta$  for three different beam intensities i.e.  $\alpha E_{00}^2 = 3.0, 4.0, 5.0$ . The curves corresponding to  $\alpha E_{00}^2 = 3.0$ ,  $\alpha E_{00}^2 = 4.0$ , and  $\alpha E_{00}^2 = 5.0$  are shown in blue, green and red respectively. It is clear from results that increment in  $\alpha E_{00}^2$  parameter reduces tendency of beam to focus. This behavior arises due to reason that divergence term becomes more dominant than convergence term at higher  $\alpha E_{00}^2$  parameter. So, there is weakening of self-focusing at higher  $\alpha E_{00}^2$ .

Figure 2 illustrates variation of  $f$  with  $\eta$  for three different plasma densities i.e.  $\frac{\omega_p^2}{\omega^2} = 0.3, 0.5, 0.7$ . The curves corresponding to  $\frac{\omega_p^2}{\omega^2} = 0.3$ ,  $\frac{\omega_p^2}{\omega^2} = 0.5$ , and  $\frac{\omega_p^2}{\omega^2} = 0.7$  are shown in blue, green and red respectively. It is clear from results that increment in  $\frac{\omega_p^2}{\omega^2}$  parameter enhances tendency of beam to focus. This behavior arises due to reason that refractive term becomes more dominant than diffraction term at higher  $\frac{\omega_p^2}{\omega^2}$  values. So, there is strengthening of self-focusing at higher  $\frac{\omega_p^2}{\omega^2}$  values.

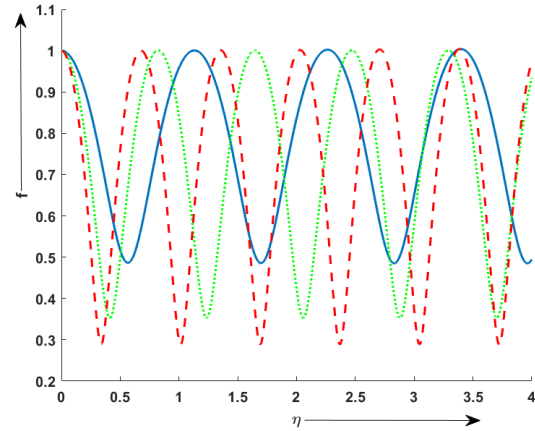
Figure 3 illustrates variation of  $f$  with  $\eta$  for three different beam radii i.e.  $r_0 = 15\mu\text{m}, 20\mu\text{m}, 25\mu\text{m}$ . The curves corresponding to  $r_0 = 15\mu\text{m}$ ,  $r_0 = 20\mu\text{m}$ , and  $r_0 = 25\mu\text{m}$  are shown in Blue, Green and Red respectively. It is clear from results that increment in  $r_0$  parameter enhances tendency of beam to focus. This behavior arises due to reason that refractive term becomes more dominant than diffraction term at higher  $r_0$  value. So, there is strengthening of self-focusing at higher  $r_0$ .

Figure 4 illustrates variation of  $f$  with  $\eta$  for three different  $q$ -values i.e.  $q = 1, 2, 3$ , and  $\infty$ . The curves corresponding to  $q = 1$ ,  $q = 2$ ,  $q = 3$ , and  $q = \infty$  shown in Blue, Green, Red and Black respectively. It is clear from figures that increment in  $q$  parameter enhances tendency of beam to focus. This is due to increase in intensity

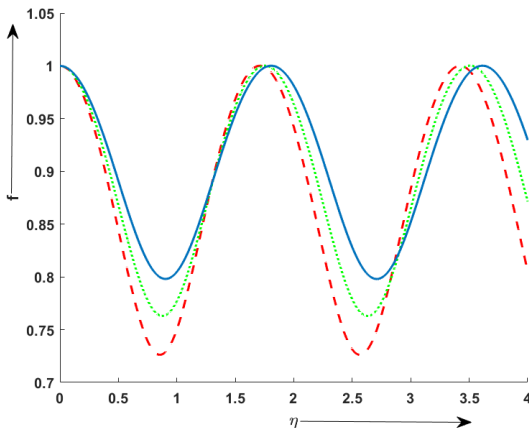
localization along axis of beam with rapid increase in  $q$  values. So, axial rays start undergoing focusing earlier than off-axial rays, thereby improving focusing characteristics of beam. For  $q \rightarrow \infty$ , the beam profile changes to ordinary Gaussian beam, and has less sharply localized intensity thereby reducing nonlinear focusing effect, hence decreasing self-focusing compared to finite  $q$  values.



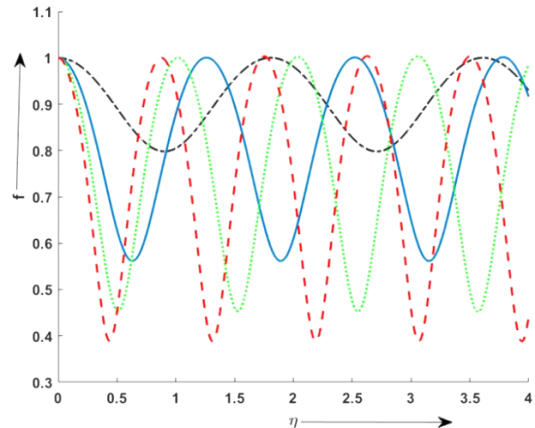
**Figure 1.** Variation of  $f$  with  $\eta$  for three different beam intensities i.e.  $\alpha E_{00}^2 = 3.0, 4.0, 5.0$ . The curves corresponding to  $\alpha E_{00}^2 = 3.0$ ,  $\alpha E_{00}^2 = 4.0$ , and  $\alpha E_{00}^2 = 5.0$  are shown in blue, green and red respectively



**Figure 2.** Variation of  $f$  with  $\eta$  for three different plasma densities i.e.  $\frac{\omega_p^2}{\omega^2} = 0.3, 0.5, 0.7$ . The curves corresponding to  $\frac{\omega_p^2}{\omega^2} = 0.3$ ,  $\frac{\omega_p^2}{\omega^2} = 0.5$ , and  $\frac{\omega_p^2}{\omega^2} = 0.7$  are shown in blue, green and red respectively



**Figure 3.** Variation of  $f$  with  $\eta$  for three different beam radii i.e.  $r_0 = 15\mu m, 20\mu m, 25\mu m$ . The curves corresponding to  $r_0 = 15\mu m$ ,  $r_0 = 20\mu m$ , and  $r_0 = 25\mu m$  are shown in Blue, Green and Red respectively



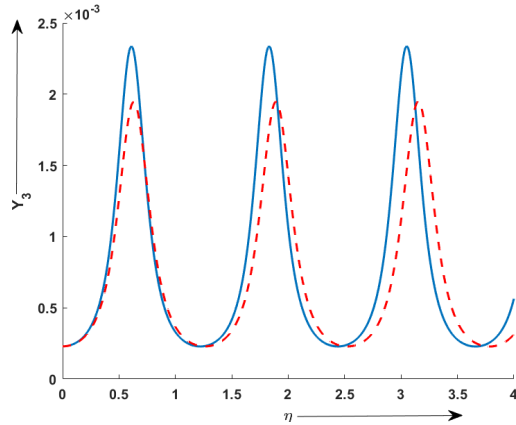
**Figure 4.** Variation of  $f$  with  $\eta$  for three different  $q$ -values i.e.  $q = 1, 2, 3, \infty$ . The curves corresponding to  $q = 1$ ,  $q = 2$ ,  $q = 3$ , and  $q = \infty$  shown in Blue, Green, Red and Black respectively

Figure 5 illustrates variation of  $Y_3$  with  $\eta$  for two different beam intensities i.e.  $\alpha E_{00}^2 = 4.0, 5.0$ . The curves corresponding to  $\alpha E_{00}^2 = 4.0$ , and  $\alpha E_{00}^2 = 5.0$  are shown in Blue, and Red respectively. It is clear from results that there is decrease in magnitude of  $Y_3$  with enhancement in  $\alpha E_{00}^2$  parameter. This reduction is directly connected with focusing characteristics of pump beam. Since, focusing ability of pump beam is found to get weakened by increasing  $\alpha E_{00}^2$  parameter. So, amplitude of EPW and hence yield of 3<sup>rd</sup> harmonics are decreased accordingly.

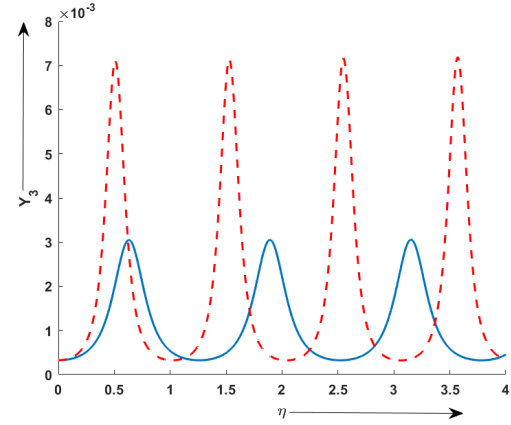
Figure 6 illustrates variation of  $Y_3$  with  $\eta$  for two different plasma densities i.e.  $\frac{\omega_p^2}{\omega^2} = 0.5, 0.7$ . The curves corresponding to  $\frac{\omega_p^2}{\omega^2} = 0.5$ , and  $\frac{\omega_p^2}{\omega^2} = 0.7$  are shown in Blue, and Red respectively. It is clear from the results that there is increase in magnitude of  $Y_3$  with enhancement in  $\frac{\omega_p^2}{\omega^2}$  parameter. This amplification is directly connected with focusing characteristics of pump beam. Since, focusing ability of pump beam is found to get strengthened by increasing  $\frac{\omega_p^2}{\omega^2}$  parameter. So, amplitude of EPW and hence yield of 3<sup>rd</sup> harmonics are enhanced accordingly.

Figure 7 illustrates variation of  $Y_3$  with  $\eta$  for two different beam radii i.e.  $r_0 = 20\mu m, 25\mu m$ . The curves corresponding to  $r_0 = 20\mu m$ , and  $r_0 = 25\mu m$  are shown in Blue, and Red respectively. It is clear from the results that there is increase in magnitude of  $Y_3$  with enhancement in  $r_0$  parameter. This amplification is directly connected with focusing characteristics of pump beam. Since, focusing ability of pump beam is found to get strengthened by increasing  $r_0$  parameter. So, amplitude of EPW and hence yield of 3<sup>rd</sup> harmonics are enhanced accordingly.

Figure 8 illustrates variation of  $Y_3$  with  $\eta$  for two different  $q$ -values i.e.  $q = 1, 2$  and  $\infty$ . The curves corresponding to  $q = 1, q = 2$  and  $q = \infty$  are shown in Blue, Red and Black respectively. It is clear from results that magnitude of  $Y_3$  is amplified with enhancement in  $q$  values. This is on account of reason that increase in  $q$  value enhances axial self-focusing of pump beam thereby amplifying nonlinear interaction that produces third harmonics. So, dominant role is played by  $q$ -parameter in optimizing THG output. For  $q \rightarrow \infty$ , the beam profile changes to ordinary Gaussian beams and has less localized intensity, reducing axial self-focusing and thus lowering the efficiency of 3<sup>rd</sup> harmonics.



**Figure 5.** Variation of  $Y_3$  with  $\eta$  for two different beam intensities i.e.  $\alpha E_{00}^2 = 4.0, 5.0$ . The curves corresponding to  $\alpha E_{00}^2 = 4.0$ , and  $\alpha E_{00}^2 = 5.0$  are shown in Blue, and Red respectively



**Figure 6.** Variation of  $Y_3$  with  $\eta$  for two different plasma densities i.e.  $\frac{\omega_p^2}{\omega^2} = 0.5, 0.7$ . The curves corresponding to  $\frac{\omega_p^2}{\omega^2} = 0.5$ , and  $\frac{\omega_p^2}{\omega^2} = 0.7$  are shown in Blue, and Red respectively

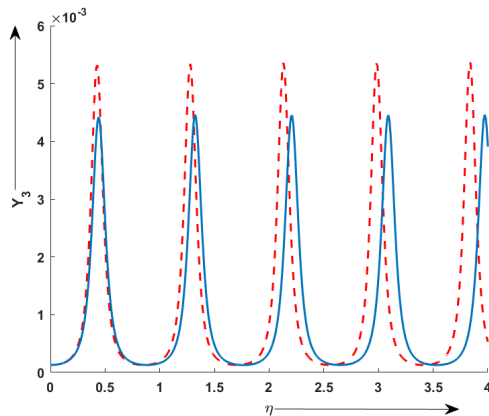


**Figure 7.** Variation of  $Y_3$  with  $\eta$  for two different beam radii i.e.  $r_0 = 20\mu m, 25\mu m$ . The curves corresponding to  $r_0 = 20\mu m$ , and  $r_0 = 25\mu m$  are shown in Blue, and Red respectively

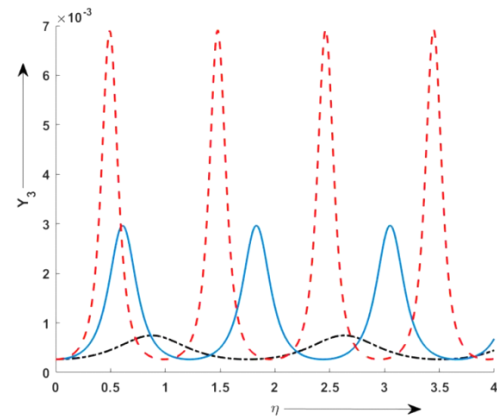


**Figure 8.** Variation of  $Y_3$  with  $\eta$  for two different  $q$ -values i.e.  $q = 1, 2$  and  $\infty$ . The curves corresponding to  $q = 1, q = 2$  and  $q = \infty$  are shown in Blue, Red and Black respectively

## 6. CONCLUSIONS

The present study explores third-harmonic generation of a  $q$ -Gaussian beam in a Collisionless plasma using the paraxial approach. The analysis reveals two key outcomes:

1. **Beam Focusing:** The beam's self-focusing capability is strengthened with enhancement in plasma density, beam radius,  $q$ -parameter, and with a decrease in beam intensity. To optimize self-focusing, we need careful control of beam and plasma parameters.
2. **THG Efficiency:** The efficiency of 3<sup>rd</sup> harmonics is amplified with enhancement in plasma density, beam radius,  $q$ -parameter, and with reduction in beam intensity. So, to optimize THG efficiency, we need to have careful control of beam and plasma parameters

These results are highly crucial for applications in laser-driven fusion and other laser-plasma interaction schemes, where the production of 3<sup>rd</sup> harmonics plays an important role.

## ORCID

●Keshav Walia, <https://orcid.org/0000-0001-9547-3027>

## REFERENCES

- [1] H. Hora, "New aspects for fusion energy using inertial confinement," *Laser Part. Beams*, **25**, 37–45 (2007). <https://doi.org/10.1017/s0263034607070073>

- [2] T. Feder, "Petawatt laser probes nature at Texas University," *Phys. Today*, **61**, 27 (2008). <https://doi.org/10.1063/1.3001859>
- [3] R. Singh, A. Sharma, and V. Tripathi, "Relativistic self-distortion of a laser pulse and ponderomotive acceleration of electrons in an axially inhomogeneous plasma," *Laser Part. Beams*, **28**, 299 (2010). <https://doi.org/10.1017/s0263034610000200>
- [4] E. Esarey, C.B. Schroeder, and W.P. Leemans, "Physics of laser-driven plasma-based electron accelerators," *Rev. Mod. Phys.*, **81**, 1229 (2009). <https://doi.org/10.1103/revmodphys.81.1229>
- [5] R. Bingham, J.T. Mendonca, and P.K. Shukla, "Topical review: plasma based charged-particle accelerators," *Plasma Phys. Controlled Fusion*, **46**, R1 (2004). <https://doi.org/10.1088/0741-3335/46/1/r01>
- [6] Z. Zeng, Y. Cheng, X. Song, R. Li, and Z. Xu, "Generation of an extreme ultraviolet supercontinuum in a two color laser field," *Phys. Rev. Lett.* **98**, 203901 (2007). <https://doi.org/10.1103/physrevlett.98.203901>
- [7] K. Walia, "Propagation characteristics of a high-power beam in weakly relativistic-ponderomotive thermal quantum plasma," *Commun. Theor. Phys.*, **75**, 095501 (2023). <https://doi.org/10.1088/1572-9494/accf82>
- [8] K. Walia, "Nonlinear interaction of high power beam in weakly relativistic and ponderomotive cold quantum plasma," *Optik*, **219**, 165040 (2020). <https://doi.org/10.1016/j.ijleo.2020.165040>
- [9] K. Walia, "Nonlinear Interaction of High Power Elliptical Laser Beam with Cold Collisionless Plasma," *J. Fusion Energ.* **35**, 446 (2016). <https://doi.org/10.1007/s10894-016-0059-0>
- [10] T. Singh, and K. Walia, "Impact of High-Power Cosh-Gaussian Beam on Second Harmonic Generation in Collisionless Magnetoplasma," *J. Contemp. Phys.* **59**, 254 (2024). <https://doi.org/10.1134/s106833722470049x>
- [11] K. Walia, "Self-focusing of high power beam in unmagnetized plasma and its effect on Stimulated Raman scattering process," *Optik*, **225**, 165592 (2021). <https://doi.org/10.1016/j.ijleo.2020.165592>
- [12] K. Walia, "Stimulated Brillouin Scattering of high power beam in unmagnetized plasma: Effect of relativistic and ponderomotive nonlinearities," *Optik*, **221**, 165365 (2020). <https://doi.org/10.1016/j.ijleo.2020.165365>
- [13] K.M. Gavade, T.U. Urunkar, B.D. Vhanmore, A.T. Valkunde, M.V. Takale, and S.D. Patil, "Self-focusing of Hermite cosh Gaussian laser beams in a plasma under a weakly relativistic and ponderomotive regime," *J. Appl. Spectrosc.* **87**, 499–504 (2020). <https://doi.org/10.1007/s10812-020-01030-1>
- [14] S. Chib, L.D. Essakali, and A. Belafhal, "Propagation properties of a novel generalized flattened Hermite-cosh-Gaussian light beam," *Opt. Quantum Electron.* **52**, 277 (2020). <https://doi.org/10.1007/s11082-020-02406-5>
- [15] M.A. Wani, and N. Kant, "Investigation of relativistic self-focusing of Hermite-cosine-Gaussian laser beam in collisionless plasma," *Optik*, **127**, 4705 (2016). <https://doi.org/10.1016/j.ijleo.2016.02.026>
- [16] K. Singh, and K. Walia, "Second Harmonic Generation of High Power Cosh-Gaussian Beam in Thermal Quantum Plasma: Effect of Relativistic and Ponderomotive Nonlinearity," *J. Contemp. Phys.* **59**, 244 (2024). <https://doi.org/10.1134/s1068337224700488>
- [17] K. Singh, and K. Walia, "Influence of Self-Focused Elliptical Laser Beam on Second Harmonic Generation in Cold Quantum Plasma," *J. Contemp. Phys.* **59**, 154 (2024). <https://doi.org/10.1134/s1068337224700300>
- [18] J. Wadhwa, and A. Singh, "Generation of second harmonics by a self-focused Hermite-Gaussian laser beam in collisionless plasma," *Phys. Plasmas*, **26**, 062118 (2019). <https://doi.org/10.1063/1.5086858>
- [19] R. Singh, and V.K. Tripathi, "Brillouin shifted third harmonic generation of a laser in a plasma," *J. Appl. Phys.* **107**, 113308 (2010). <https://doi.org/10.1063/1.3431402>
- [20] H.R. Askari, and M. Noroozi, "Effect of a wiggler magnetic field and the ponderomotive force on the second harmonic generation in laser-plasma interactions," *Turkish J. Phys.* **33**, 299 (2009). <https://doi.org/10.3906/fiz-0810-14>
- [21] M. Abedi-Varaki, and S. Jafari, "Second-harmonic generation of a linearly polarized laser pulse propagating through magnetized plasma in the presence of a planar magnetostatic wiggler," *Eur. Phys. J. Plus*, **133**, 1 (2018). <https://doi.org/10.1140/epjp/i2018-11975-2>
- [22] E. Schifano, S.D. Baton, C. Labaune, N. Renard, V. Biancalana, A. Giulietti, and D. Giulietti, "Second harmonic emission from laser-preformed plasmas as a diagnostic for filamentation in various interaction conditions," *Laser Part. Beams*, **12**, 435 (1994). <https://doi.org/10.1017/s0263034600008296>
- [23] E. Esarey, A. Ting, P. Sprangle, D. Umstadter, and X. Liu, "Nonlinear analysis of relativistic harmonic generation by intense lasers in plasmas," *IEEE Trans. Plasma Sci.* **21**, 95 (1993). <https://doi.org/10.1109/27.221107>
- [24] S.D. Baton, H.A. Baldis, T. Jalinaud, and C. Labaune, "Fine-Scale Spatial and Temporal Structures of Second-Harmonic Emission from an Underdense Plasma," *Europhys. Lett.* **23**, 191 (1993). <https://doi.org/10.1209/0295-5075/23/3/006>
- [25] F. Brandi, F. Giammanco, and W. Ubachs, "Spectral red shift in harmonic generation from plasma dynamics in laser focus," *Phys. Rev. Lett.* **96**, 123904 (2006). <https://doi.org/10.1103/physrevlett.96.123904>
- [26] R.A. Ganeev, M. Suzuki, M. Baba, and H. Kuroda, "Higher order harmonic generation from laser plasma produced by pulses of different duration," *Phys. Rev. A*, **76**, 023805 (2007). <https://doi.org/10.1103/physreva.76.023805>
- [27] M.K. Gupta, R.P. Sharma, and S.T. Mahmoud, "Generation of plasma wave and third harmonic generation at ultra-relativistic laser power," *Laser Part. Beams*, **25**, 211 (2007). <https://doi.org/10.1017/s0263034607000031>
- [28] H. Sharma, H. Jaloree, and J. Prashar, "Magnetic field wiggler assisted third harmonic generation of a Gaussian laser pulse in plasma," *Turk. J. Phys.* **37**, 368–374 (2013). <https://doi.org/10.3906/fiz-1212-12>
- [29] V. Sharma, V. Thakur, and N. Kant, "Third harmonic generation of a relativistic self-focusing laser in plasma in the presence of wiggler magnetic field," *High Energy Dens. Phys.* **32**, 51–55 (2019). <https://doi.org/10.1016/j.hedp.2019.04.007>
- [30] M. Abedi-Varaki, "Relativistic laser third-harmonic generation from magnetized plasmas under a tapered magnetostatic wiggler," *Phys. Plasmas*, **30**, 083102 (2023). <https://doi.org/10.1063/5.0155016>
- [31] M. Singh, and D.N. Gupta, "Relativistic third-harmonic generation of a laser in a self-sustained magnetized plasma channel," *IEEE J. Quantum Electron.* **50**, 491–496 (2014). <https://doi.org/10.1109/jqe.2014.2320763>
- [32] T. Azad, N. Kant, A. Paknezhad, et al. "Raman-enhanced nonlinear effects on third harmonic generation in plasma using Hermite cosh Gaussian laser beam," *Opt. Quant. Electron.* **57**, 239 (2025). <https://doi.org/10.1007/s11082-025-08143-x>
- [33] R.A. Ganeev, "High-order harmonic generation in boron carbide laser-induced plasma: comparison with carbon and boron plasmas, two-color-pumping-induced enhancement, quasi-phase-matching, and tuning of harmonics," *Optics Continuum*, **3**(12), 2272–2285 (2024). <https://doi.org/10.1364/optcon.540708>



- [34] S. Westerberg, M. Redon, A.-K. Raab, G. Beaufort, *et al.* "Influence of the laser pulse duration in high-order harmonic generation," APL Photonics, **10**, 096103 (2025). <https://doi.org/10.1063/5.0272968>
- [35] R.A. Ganeev, "High-order harmonics enhancement in laser-induced plasma," Sci. Rep. **13**, 13951 (2023). <https://doi.org/10.1038/s41598-023-41239-6>
- [36] V. Thakur, and N. Kant, "Effect of pulse slippage on density transition-based resonant third harmonic generation of short pulse laser in plasma," Front. Phys. **11**, 115202 (2016). <https://doi.org/10.1007/s11467-016-0563-8>
- [37] V. Sharma, V. Thakur, A. Singh, and N. Kant, "Third harmonic generation of a relativistic self-focusing laser in plasma under exponential density ramp," Z. Naturforsch. A, **77**, 323–328 (2022). <https://doi.org/10.1515/zna-2021-0266>
- [38] M.J. Basiry, M. Sharifian, M. Hashemzadeh, M. Borhani, and H. Alirezaie, "Influence of rippled density and laser profile on third harmonic generation using cosh–Gaussian laser pulses in inhomogeneous magnetized plasmas," Contrib. Plasma Phys. **63**, 202200196 (2023). <https://doi.org/10.1002/ctpp.202200196>
- [39] K.Y. Khandale, P.T. Takale, T.U. Urunkar, S.S. Patil, P.P. Nikam, M.B. Mane, V.S. Pawar, *et al.* "On the exploration of q parameter in propagation dynamics of q-Gaussian laser beam in underdense collisional plasma," Bulg. J. Phys. **49**, 375–385 (2022). <https://doi.org/10.55318/bgjp.2022.49.4.375>
- [40] D.N. Yadav, and S.C. Sharma, "Electron plasma wave excitation by a q-Gaussian laser beam and subsequent electron acceleration," Phys. Plasmas, **27**, 093106 (2020). <https://doi.org/10.1063/5.0007998>
- [41] A.S. Ahmed, H.A. Salih, and K.I. Hassoon, "Relativistic self-focusing of a q-Gaussian laser beam in plasma by the influence of magnetic field," Braz. J. Phys. **53**, 112 (2023). <https://doi.org/10.1007/s13538-023-01324-7>
- [42] D. Tripathi, S. Kaur, A. Vijay, and K. Walia, "Nonlinear Dynamics of q-Gaussian Laser Beam in Collisional Plasma: Effect of Linear Absorption," J. Contemp. Phys. **60**, 16 (2025). <https://doi.org/10.1134/s1068337225700409>
- [43] K. Walia, N. Mehra, and S. Pandit, "Propagation Characteristics of q-Gaussian Laser Beam in Cold Collisionless Plasma," J. Contemp. Phys. **59**, 378 (2024). <https://doi.org/10.1134/s1068337225700203>
- [44] K. Walia, "Self-focusing of q-Gaussian beam in unmagnetized plasma and its impact on second harmonic generation," Optik, **277**, 170681 (2023). <https://doi.org/10.1016/j.ijleo.2023.170681>
- [45] S.A. Akhmanov, A.P. Sukhorokov, and R.V. Kokhlov, "Self-focusing and diffraction of light in nonlinear medium," Sov. Phys. Uspekhi, **10**, 609 (1968).
- [46] M.S. Sodha, A.K. Ghatak, and V.K. Tripathi, "Self focusing of laser beams in plasmas and semiconductors," Prog. Opt. **13**, 169 (1976). [https://doi.org/10.1016/s0079-6638\(08\)70021-0](https://doi.org/10.1016/s0079-6638(08)70021-0)

## ГЕНЕРАЦІЯ ТРЕТЬОЇ ГАРМОНІКИ Q-ГАУСІВСЬКОГО ЛАЗЕРНОГО ПРОМЕНЯ У ПЛАЗМІ БЕЗ ЗІТКНЕНЬ

Кулкаран Сінгх, Кешав Валья, Таранджот Сінгх

Кафедра фізики, Університет DAV, Джаландхар, Пенджаб-144012, Індія

У цьому дослідженні досліджується генерація третьої гармоніки (ГТГ) q-гауссового лазерного променя, що поширюється через беззіткнювальну плазму. Цей нелінійний профіль променя індукує градієнти густини в плазмі через пондеромоторну силу. Ці градієнти густини збуджують електронні плазмові хвилі (ЕПХ) з подвоєною частотою хвилі накачування за допомогою механізму  $\vec{V} \times \vec{B}$ . Фундаментальна хвиля накачування та ЕПХ взаємодіють нелінійно, створюючи випромінювання третьої гармоніки. Нелінійне ЗДР для перетяжки променя накачування та вирази ефективності перетворення ГТГ отримані за допомогою методу ВКБ та параксiального підходів. Також проаналізовано вплив ключових параметрів лазерної плазми, включаючи густину плазми, ширину променя, інтенсивність та q-параметр, на самофокусування основного променя та ефективність третьої гармоніки. Результати показують, що q-гаусові пучки, завдяки своїм вищим амплітудам поля та ширшим крилам, ніж у звичайних гаусових пучках, можуть значно покращити генерацію гармонік у беззіткнювальній плазмі. Ці результати дають уявлення про оптимізацію генерації гармонік у структурованих лазерних променях для застосувань в надшвидкій оптиці, прискоренні частинок та джерелах випромінювання на основі плазми.

**Ключові слова:** беззіткнювальна плазма; градієнти густини; хвиля накачування; електронна плазмова хвиля; самофокусування; генерація третьої гармоніки

# IMPLICIT QUIESCENT OPTICAL SOLITON PERTURBATION HAVING NONLINEAR CHROMATIC DISPERSION AND LINEAR TEMPORAL EVOLUTION WITH KUDRYASHOV'S FORMS OF SELF-PHASE MODULATION STRUCTURE BY LIE SYMMETRY

 Abdullahi Rashid Adem<sup>1\*</sup>,  Ahmed H. Arnous<sup>2</sup>,  Hamlet Isakhanli<sup>3</sup>,  Oswaldo González-Gaxiola<sup>4</sup>,  
 Anjan Biswas<sup>5,6,7</sup>

<sup>1</sup>Department of Mathematical Sciences, University of South Africa, UNISA-0003, South Africa

<sup>2</sup>Department of Engineering Mathematics and Physics, Higher Institute of Engineering, El-Shorouk Academy, Cairo-11837, Egypt

<sup>3</sup>Department of Mathematics, Khazar University, Baku, AZ-1096, Azerbaijan

<sup>4</sup>Applied Mathematics and Systems Department, Universidad Autonoma Metropolitana-Cuajimalpa, Vasco de Quiroga 4871, Mexico City 05348, Mexico

<sup>5</sup>Department of Mathematics & Physics, Grambling State University, Grambling, LA 71245-2715, USA

<sup>6</sup>Department of Physics and Electronics, Khazar University, Baku, AZ-1096, Azerbaijan

<sup>7</sup>Department of Mathematics and Applied Mathematics, Sefako Makgatho Health Sciences University, Medunsa-0204, South Africa

\*Corresponding Author e-mail: [ademar@unisa.ac.za](mailto:ademar@unisa.ac.za) [ademarunisa@gmail.com](mailto:ademarunisa@gmail.com)

Received September 1, 2025; revised October 19, 2025; accepted November 4, 2025

The paper retrieves implicit quiescent optical solitons for the nonlinear Schrödinger's equation that is taken up with nonlinear chromatic dispersion and linear temporal evolution. Using a stationary or quiescent approach combined with Lie symmetry analysis, the study systematically examines six distinct self-phase-modulation structures proposed by Kudryashov. The analytical procedure reduces the governing equation to amplitude forms whose solutions are obtained through quadratures, leading to both implicit solitary-wave profiles and one explicit periodic case. The six forms of self-phase modulation structures, as proposed by Kudryashov, yielded solutions in terms of quadratures, periodic solutions as well as in terms of elliptic functions. The existence of each family of solutions is discussed in terms of the admissible parameter relations that ensure physically meaningful solitary profiles. The approach provides a unified framework compared with earlier methods based on direct elliptic-function expansions, highlighting how Lie symmetry facilitates a compact treatment of multiple nonlinear dispersion laws. The results are relevant to understanding stationary optical pulses in nonlinear fibers and photonic crystal fibers, and they establish a foundation for future numerical and experimental studies on nonlinear-dispersion-driven pulse propagation.

**Keywords:** Quiescent solitons; Chromatic dispersion; Quadratures; Parameter constraints

**PACS:** 02.30.Jr; 05.45.Yv; 02.30.Ik

## 1. INTRODUCTION

The key ingredients for the propagation of solitons through optical fibers across transcontinental and transoceanic distances is the the sustainment of the delicate balance between chromatic dispersion (CD) and self-phase modulation (SPM) [1–10]. Any loss of this balance would lead to the solitons getting stalled and/or wave collapse and this would trigger catastrophic consequences. Therefore it is of paramount importance to make sure that the balance is continuously maintained for the smooth propagation of such solitons across intercontinental distances around the planet. Nevertheless, it may so happen that this balance is compromised owing to various factors that are beyond control. One such factor is when the CD is rendered to be nonlinear due to random variations in the fiber diameter or due to the rough handling of fibers during its installation underground or along the ocean bed [2].

The current paper will address this situation. In particular the governing model, namely the nonlinear Schrödinger's equation (NLSE) with nonlinear CD and having six forms of SPM structures that are of non-Kerr type. It must be noted that the concept of quiescent solitons has been addressed for several other models, apart from NLSE, in the past. These include Fokas–Lenells equation, complex Ginzburg–Landau equation and several others [1–9, 12–14]. These six forms of SPM were proposed by Kudryashov during the past few years [3]. In fact, the retrieval of quiescent optical solitons with nonlinear CD and with the six forms of SPM structure have been addressed in the past by the Jacobi's elliptic function approach [3]. The current paper will revisit the model with the same six forms of SPM and the implicit quiescent solitons will be recovered by the aid of Lie symmetry analysis. The details of the mathematical analysis and the derivation mechanism are exhibited in the rest of the paper after a quick introduction to the model.

**Cite as:** A.R. Adem, A.H. Arnous, H. Isakhanli, O. González-Gaxiola, A. Biswas, East Eur. J. Phys. 4, 248 (2025), <https://doi.org/10.26565/2312-4334-2025-4-22>

© A.R. Adem, A.H. Arnous, H. Isakhanli, O. González-Gaxiola, A. Biswas, 2025; CC BY 4.0 license

### 1.1. GOVERNING MODEL

The dimensionless form of the governing NLSE in optical fibers and PCF with nonlinear CD and non-Kerr laws of SPM, as proposed by Kudryashov, is structured as:

$$iq_t + a(|q|^n q)_{xx} + F(|q|^2)q = i \left[ \lambda (|q|^{2m} q)_x + \theta_1 (|q|^{2m})_x q + \theta_2 |q|^{2m} q_x \right]. \quad (1)$$

Here in (1)  $q(x, t)$  represents the wave amplitude and is a complex-valued function. The independent variables are  $x$  and  $t$  that represent spatial and temporal variables respectively. The first term is the linear temporal evolution with its coefficient being  $i = \sqrt{-1}$ . The second term with its coefficient being a real-valued constant,  $a$  is the nonlinear CD where the nonlinearity factor is dictated by the exponent  $n$ . When  $n = 0$ , one collapses to linear CD. The third term is from SPM where the functional  $F$  accounts for the nonlinear structure of intensity dependent refractive index change. The right hand side comprises of the Hamiltonian perturbation terms with arbitrary intensity. The coefficient of  $\lambda$  is the self-steepening while the coefficients of  $\theta_j$  for  $j = 1, 2$  represents the self-frequency shift effect. The perturbation parameters  $\lambda$  and  $\theta_j$  are real-valued constants.

### 2. MATHEMATICAL ANALYSIS

This section will analyze equation (1) with linear temporal evolution for six forms of SPM structures as proposed by Kudryashov. Equation (1) does not support mobile solitons unless  $n = 0$  in the CD. Thus, the quiescent optical solitons supported by (1) is taken to be of the form:

$$q(x, t) = \phi(x) e^{i\omega t}, \quad (2)$$

where  $\phi(x)$  represents the amplitude portion of the soliton while the second factor is the phase component with  $\omega$  representing the wave number. Substituting (2) into (1) and decomposing into real and imaginary components, the real part yields the ordinary differential equation (ODE) for the amplitude component  $\phi(x)$  as

$$a(n+1)\phi(x)^{2m+n} \left[ n \{\phi'(x)\}^2 + \phi(x)\phi''(x) \right] + \phi^2(x) [F\{\phi^2(x)\} - \omega] = 0. \quad (3)$$

Then, the imaginary part gives the parameter constraints as

$$(2m+1)\lambda + 2m\theta_1 + \theta_2 = 0. \quad (4)$$

With these parameter constraints, the governing model (1) conveniently reduces to

$$iq_t + a(|q|^n q)_{xx} + F(|q|^2)q = i \left[ \lambda (|q|^{2m} q)_x + \theta_1 (|q|^{2m})_x q - \{(2m+1)\lambda + 2m\theta_1\} |q|^{2m} q_x \right]. \quad (5)$$

This ODE given by (3) will be addressed in details in the subsequent section with the six forms of SPM structures, as proposed by Kudryashov, corresponding to the functional  $F$ , that would yield a variety of solution structures.

#### 2.1. FORM-I

For Form-I, the law of SPM is given as

$$F(s) = \frac{b_1}{s^m} + \frac{b_2}{s^{\frac{m}{2}}} + b_3 s^{\frac{m}{2}} + b_4 s^m. \quad (6)$$

Thus, the corresponding NLSE reduces to

$$iq_t + a(|q|^n q)_{xx} + \left( \frac{b_1}{|q|^{2m}} + \frac{b_2}{|q|^m} + b_3 |q|^m + b_4 |q|^{2m} \right) q = i \left[ \lambda (|q|^{2m} q)_x + \theta_1 (|q|^{2m})_x q + \theta_2 |q|^{2m} q_x \right]. \quad (7)$$

Thus, substituting (2) into (7), the imaginary part relation gives (4) which transforms (7) to

$$iq_t + a(|q|^n q)_{xx} + \left( \frac{b_1}{|q|^{2m}} + \frac{b_2}{|q|^m} + b_3 |q|^m + b_4 |q|^{2m} \right) q = i \left[ \lambda (|q|^{2m} q)_x + \theta_1 (|q|^{2m})_x q - ([2m+1]\lambda + 2m\theta_1) |q|^{2m} q_x \right]. \quad (8)$$

For equation (8) to be integrable, one needs to choose  $n = 2m$ . Therefore, the real part equation modifies (3) to

$$a(n+1)\phi^{4m}(x) \left[ n \{\phi'(x)\}^2 + \phi(x)\phi''(x) \right] + \phi^2(x) (\phi^m(x) (\phi^m(x) (\phi^m(x) (b_4 \phi^m(x) + b_3) - \omega) + b_2) + b_1) = 0. \quad (9)$$

Equation (9) admits the translational Lie point symmetry, namely  $\partial/\partial x$  which integrates the ODE (9) to:

$$x = \pm \sqrt{-\frac{A}{B}} C, \quad (10)$$



where

$$A = 4a(1+m)(2+m)(1+2m)^2(2+3m)(\phi^m - \kappa_1)(\phi^m - \kappa_2)(\phi^m - \kappa_3)(\phi^m - \kappa_4), \quad (11)$$

$$\begin{aligned} B = & 12m^5 b_2 \kappa_1 \kappa_2 \phi^m + 26m^4 b_2 \kappa_1 \kappa_2 \phi^m + 18m^3 b_2 \kappa_1 \kappa_2 \phi^m + 4m^2 b_2 \kappa_1 \kappa_2 \phi^m - 12m^5 b_2 \kappa_2 \kappa_3 \phi^m \\ & - 26m^4 b_2 \kappa_2 \kappa_3 \phi^m - 18m^3 b_2 \kappa_2 \kappa_3 \phi^m - 4m^2 b_2 \kappa_2 \kappa_3 \phi^m - 12m^5 b_2 \kappa_1 \kappa_4 \phi^m \\ & - 26m^4 b_2 \kappa_1 \kappa_4 \phi^m - 18m^3 b_2 \kappa_1 \kappa_4 \phi^m - 4m^2 b_2 \kappa_1 \kappa_4 \phi^m + 12m^5 b_2 \kappa_3 \kappa_4 \phi^m \\ & + 26m^4 b_2 \kappa_3 \kappa_4 \phi^m + 18m^3 b_2 \kappa_3 \kappa_4 \phi^m + 4m^2 b_2 \kappa_3 \kappa_4 \phi^m - 6m^5 \omega \kappa_1 \kappa_2 \phi^{2m} - 19m^4 \omega \kappa_1 \kappa_2 \phi^{2m} \\ & - 16m^3 \omega \kappa_1 \kappa_2 \phi^{2m} - 4m^2 \omega \kappa_1 \kappa_2 \phi^{2m} + 6m^5 \omega \kappa_2 \kappa_3 \phi^{2m} + 19m^4 \omega \kappa_2 \kappa_3 \phi^{2m} + 16m^3 \omega \kappa_2 \kappa_3 \phi^{2m} \\ & + 4m^2 \omega \kappa_2 \kappa_3 \phi^{2m} + 6m^5 \omega \kappa_1 \kappa_4 \phi^{2m} + 19m^4 \omega \kappa_1 \kappa_4 \phi^{2m} + 16m^3 \omega \kappa_1 \kappa_4 \phi^{2m} + 4m^2 \omega \kappa_1 \kappa_4 \phi^{2m} \\ & - 6m^5 \omega \kappa_3 \kappa_4 \phi^{2m} - 19m^4 \omega \kappa_3 \kappa_4 \phi^{2m} - 16m^3 \omega \kappa_3 \kappa_4 \phi^{2m} - 4m^2 \omega \kappa_3 \kappa_4 \phi^{2m} + 4m^5 b_3 \kappa_1 \kappa_2 \phi^{3m} \\ & + 14m^4 b_3 \kappa_1 \kappa_2 \phi^{3m} + 14m^3 b_3 \kappa_1 \kappa_2 \phi^{3m} + 4m^2 b_3 \kappa_1 \kappa_2 \phi^{3m} - 4m^5 b_3 \kappa_2 \kappa_3 \phi^{3m} - 14m^4 b_3 \kappa_2 \kappa_3 \phi^{3m} \\ & - 14m^3 b_3 \kappa_2 \kappa_3 \phi^{3m} - 4m^2 b_3 \kappa_2 \kappa_3 \phi^{3m} - 4m^5 b_3 \kappa_1 \kappa_4 \phi^{3m} - 14m^4 b_3 \kappa_1 \kappa_4 \phi^{3m} - 14m^3 b_3 \kappa_1 \kappa_4 \phi^{3m} \\ & - 4m^2 b_3 \kappa_1 \kappa_4 \phi^{3m} + 4m^5 b_3 \kappa_3 \kappa_4 \phi^{3m} + 14m^4 b_3 \kappa_3 \kappa_4 \phi^{3m} + 14m^3 b_3 \kappa_3 \kappa_4 \phi^{3m} + 4m^2 b_3 \kappa_3 \kappa_4 \phi^{3m} \\ & + 3m^5 b_4 \kappa_1 \kappa_2 \phi^{4m} + 11m^4 b_4 \kappa_1 \kappa_2 \phi^{4m} + 12m^3 b_4 \kappa_1 \kappa_2 \phi^{4m} + 4m^2 b_4 \kappa_1 \kappa_2 \phi^{4m} - 3m^5 b_4 \kappa_2 \kappa_3 \phi^{4m} \\ & - 11m^4 b_4 \kappa_2 \kappa_3 \phi^{4m} - 12m^3 b_4 \kappa_2 \kappa_3 \phi^{4m} - 4m^2 b_4 \kappa_2 \kappa_3 \phi^{4m} - 3m^5 b_4 \kappa_1 \kappa_4 \phi^{4m} - 11m^4 b_4 \kappa_1 \kappa_4 \phi^{4m} \\ & - 12m^3 b_4 \kappa_1 \kappa_4 \phi^{4m} - 4m^2 b_4 \kappa_1 \kappa_4 \phi^{4m} + 3m^5 b_4 \kappa_3 \kappa_4 \phi^{4m} + 11m^4 b_4 \kappa_3 \kappa_4 \phi^{4m} + 12m^3 b_4 \kappa_3 \kappa_4 \phi^{4m} \\ & + 4m^2 b_4 \kappa_3 \kappa_4 \phi^{4m} + 6m^6 b_1 \kappa_1 \kappa_2 + 25m^5 b_1 \kappa_1 \kappa_2 + 35m^4 b_1 \kappa_1 \kappa_2 + 20m^3 b_1 \kappa_1 \kappa_2 + 4m^2 b_1 \kappa_1 \kappa_2 \\ & - 6m^6 b_1 \kappa_2 \kappa_3 - 25m^5 b_1 \kappa_2 \kappa_3 - 35m^4 b_1 \kappa_2 \kappa_3 - 20m^3 b_1 \kappa_2 \kappa_3 - 4m^2 b_1 \kappa_2 \kappa_3 - 6m^6 b_1 \kappa_1 \kappa_4 - 25m^5 b_1 \kappa_1 \kappa_4 \\ & - 35m^4 b_1 \kappa_1 \kappa_4 - 20m^3 b_1 \kappa_1 \kappa_4 - 4m^2 b_1 \kappa_1 \kappa_4 + 6m^6 b_1 \kappa_3 \kappa_4 + 25m^5 b_1 \kappa_3 \kappa_4 + 35m^4 b_1 \kappa_3 \kappa_4 \\ & + 20m^3 b_1 \kappa_3 \kappa_4 + 4m^2 b_1 \kappa_3 \kappa_4, \end{aligned} \quad (12)$$

and

$$\begin{aligned} C = & \Pi \left( \frac{\kappa_1 - \kappa_4}{\kappa_2 - \kappa_4}; \sin^{-1} \left( \sqrt{\frac{(\phi^m - \kappa_1)(\kappa_2 - \kappa_4)}{(\phi^m - \kappa_2)(\kappa_1 - \kappa_4)}} \right) \middle| \frac{(\kappa_2 - \kappa_3)(\kappa_1 - \kappa_4)}{(\kappa_1 - \kappa_3)(\kappa_2 - \kappa_4)} \right) (\kappa_1 - \kappa_2) \\ & + F \left( \sin^{-1} \left( \sqrt{\frac{(\phi^m - \kappa_1)(\kappa_2 - \kappa_4)}{(\phi^m - \kappa_2)(\kappa_1 - \kappa_4)}} \right) \middle| \frac{(\kappa_2 - \kappa_3)(\kappa_1 - \kappa_4)}{(\kappa_1 - \kappa_3)(\kappa_2 - \kappa_4)} \right) \kappa_2. \end{aligned} \quad (13)$$

Since the expression under the square root in Eq. (10) must be real, the existence of admissible solutions requires that  $AB < 0$ . This condition guarantees that the radicand remains non-negative, ensuring the physical realizability of the obtained solitary-wave profiles.

Here,  $\kappa_j$  for  $j = 1 \cdots 4$  is any solution of the quartic (fourth-degree) equation

$$\begin{aligned} & \left( 3b_4 m^3 + 11b_4 m^2 + 12b_4 m + 4b_4 \right) \kappa^4 + \left( 4b_3 m^3 + 14b_3 m^2 + 14b_3 m + 4b_3 \right) \kappa^3 - \left( 6m^3 \omega + 19m^2 \omega + 16m \omega + 4 \omega \right) \kappa^2 \\ & + \left( 12b_2 m^3 + 26b_2 m^2 + 18b_2 m + 4b_2 \right) \kappa + 20b_1 m + 4b_1 + 6b_1 m^4 + 25b_1 m^3 + 35b_1 m^2 = 0. \end{aligned} \quad (14)$$

This polynomial is referred to as quartic rather than biquadratic because it contains both odd and even powers of  $\kappa$ . The four roots  $\kappa_1, \dots, \kappa_4$  of this equation parameterize the elliptic-integral representation used in the subsequent analysis.

Here,  $\Pi(v; \psi|m)$  the incomplete elliptic integral that is defined as:

$$\Pi(v; \psi|m) = \int_0^\psi \frac{1}{(1 - v \sin^2 \theta) \sqrt{1 - \mu \sin^2 \theta}} d\theta, \quad (15)$$

for

$$-\frac{\pi}{2} < \psi < \frac{\pi}{2}, \quad (16)$$

$$\mu \sin^2(\psi) < 1, \quad (17)$$

and

$$v \sin^2(\psi) > 1. \quad (18)$$

Moreover,  $F(\psi|\mu)$  is elliptic integral of the first kind which is defined as:

$$F(\psi|\mu) = \int_0^\psi \frac{1}{\sqrt{1 - \mu \sin^2(\theta)}} d\theta, \quad (19)$$

where

$$-\frac{\pi}{2} < \psi < \frac{\pi}{2}, \quad (20)$$

and

$$\mu \sin^2(\psi) < 1. \quad (21)$$

From (10), the solutions will exist provided

$$AB < 0. \quad (22)$$

## 2.2. FORM-II

For Form-II, the law of SPM is given as

$$F(s) = \frac{b_1}{s^{2m}} + \frac{b_2}{s^{\frac{3m}{2}}} + \frac{b_3}{s^m} + \frac{b_4}{s^{\frac{m}{2}}} + b_5 s^{\frac{m}{2}} + b_6 s^m + b_7 s^{\frac{3m}{2}} + b_8 s^{2m}. \quad (23)$$

Thus the corresponding NLSE reduces to

$$\begin{aligned} & i q_t + a(|q|^n q)_{xx} + \left( \frac{b_1}{|q|^{4m}} + \frac{b_2}{|q|^{3m}} + \frac{b_3}{|q|^{2m}} + \frac{b_4}{|q|^m} + b_5 |q|^m + b_6 |q|^{2m} + b_7 |q|^{3m} + b_8 |q|^{4m} \right) q \\ & = i \left[ \lambda \left( |q|^{2m} q \right)_x + \theta_1 \left( |q|^{2m} \right)_x q + \theta_2 |q|^{2m} q_x \right] \end{aligned} \quad (24)$$

The starting hypothesis given by (2) when applied to (24) modifies it to:

$$\begin{aligned} & i q_t + a(|q|^n q)_{xx} + \left( \frac{b_1}{|q|^{4m}} + \frac{b_2}{|q|^{3m}} + \frac{b_3}{|q|^{2m}} + \frac{b_4}{|q|^m} + b_5 |q|^m + b_6 |q|^{2m} + b_7 |q|^{3m} + b_8 |q|^{4m} \right) q \\ & = i \left[ \lambda \left( |q|^{2m} q \right)_x + \theta_1 \left( |q|^{2m} \right)_x q - \{(2m+1)\lambda + 2m\theta_1\} |q|^{2m} q_x \right], \end{aligned} \quad (25)$$

by virtue of the imaginary part. The real part leads to the ODE for  $\phi(x)$ :

$$\begin{aligned} & a(n+1)\phi(x)^{4m+n} \left[ n \{\phi'(x)\}^2 + \phi(x)\phi''(x) \right] + \phi^2(x) \left\{ \phi^m(x) \left\{ \phi^m(x) \left\{ \phi^m(x) \left\{ \phi^m(x) \left\{ \phi^m(x) \left\{ \phi^m(x) \right\} \right\} \right\} \right\} \right\} \right\} \\ & \times \left\{ b_8 \phi^m(x) + b_7 \right\} + b_6 \left\{ + b_5 \right\} - \omega \left\{ + b_4 \right\} + b_3 \left\{ + b_2 \right\} + b_1 \left\} = 0. \end{aligned} \quad (26)$$

Next, the translational Lie symmetry that is supported by (26), integrates it to the implicit solution in terms of quadratures as:

$$x = \pm \int \sqrt{\frac{A}{B}} d\phi, \quad (27)$$

where

$$\begin{aligned} A &= a(n+1)(n+2)(m-n-2)(2m-n-2)(3m-n-2)(4m-n-2)(m+n+2) \times \\ &\times (2m+n+2)(3m+n+2)(4m+n+2)\phi^{4m+n}, \end{aligned} \quad (28)$$

and

$$\begin{aligned} B &= 2\phi^2 \left\{ (4m-n-2)\phi^m \left\{ b_2(n+2)(2m-n-2)(m-n-2)(m+n+2)(2m+n+2)(3m+n+2) \right. \right. \\ &\times \left. (4m+n+2) - (3m-n-2)\phi^m \left\{ (2m-n-2)\phi^m \left\{ (m-n-2)\phi^m \right. \right. \right. \end{aligned}$$

$$\begin{aligned}
 & \times \left\{ (n+2)\phi^m \left\{ (m+n+2)\phi^m \left\{ (2m+n+2)\phi^m \left\{ b_8(3m+n+2)\phi^m + b_7(4m+n+2) \right\} \right. \right. \right. \\
 & + \left. b_6(3m+n+2)(4m+n+2) \right\} + b_5(2m+n+2)(3m+n+2)(4m+n+2) \Big\} \\
 & - \omega(m+n+2)(2m+n+2)(3m+n+2)(4m+n+2) \Big\} \\
 & - b_4(n+2)(m+n+2)(2m+n+2)(3m+n+2)(4m+n+2) \Big\} \\
 & - b_3(n+2)(m-n-2)(m+n+2)(2m+n+2)(3m+n+2)(4m+n+2) \Big\} \Big\} \\
 & + b_1(n+2)(3m-n-2)(2m-n-2)(m-n-2)(m+n+2)(2m+n+2)(3m+n+2)(4m+n+2) \Big\}.
 \end{aligned} \tag{29}$$

This solution (29) would remain valid provided

$$AB > 0. \tag{30}$$

The condition  $AB > 0$  arises from the requirement that the expression inside the square root in Eq. (29) must be real and positive. This ensures that the radicand of  $\sqrt{A/B}$  is non-negative, leading to physically meaningful and admissible solitary-wave solutions. The sign difference from the previous case ( $AB < 0$ ) is due to the absence of the negative sign under the square root in the present formulation.

### 2.3. FORM-III

The SPM structure here is:

$$F(s) = b_1 s^{\frac{m}{2}} + b_2 s^m + b_3 \left( s^{\frac{m}{2}} \right)''. \tag{31}$$

The corresponding NLSE therefore gets structured as:

$$iq_t + a(|q|^n q)_{xx} + [b_1 |q|^m + b_2 |q|^{2m} + b_3 (|q|^m)_{xx}] q = i \left[ \lambda (|q|^{2m} q)_x + \theta_1 (|q|^{2m})_x q + \theta_2 |q|^{2m} q_x \right]. \tag{32}$$

The starting hypothesis to locate for quiescent optical solitons is (2) which when implemented, the imaginary part gives (4). The real part leads to the ODE:

$$\begin{aligned}
 & a(n+1)\phi^{2m+n}(x) \left[ n \{ \phi'(x) \}^2 + \phi(x)\phi''(x) \right] + 2b_3 m \phi^{2m}(x) \left[ \phi(x)\phi''(x) + (2m-1) \{ \phi'(x) \}^2 \right] \\
 & + b_1 \phi(x)^{m+2} + b_2 \phi(x)^{2m+2} - \omega \phi(x)^2 = 0.
 \end{aligned} \tag{33}$$

For (33) to be integrable, one must choose

$$n = -1, \tag{34}$$

which leads to the modification of the governing model to be modified to:

$$\begin{aligned}
 & iq_t + a \left( \frac{|q|}{q} \right)_{xx} + [b_1 |q|^m + b_2 |q|^{2m} + b_3 (|q|^m)_{xx}] q \\
 & = i \left[ \lambda (|q|^{2m} q)_x + \theta_1 (|q|^{2m})_x q - \{ (2m+1)\lambda + 2m\theta_1 \} |q|^{2m} q_x \right]
 \end{aligned} \tag{35}$$

Also by virtue of (34), the governing ODE for  $\phi(x)$  given by (33) condenses to

$$2b_3 m \phi^{2m}(x) \left[ \phi(x)\phi''(x) + (2m-1) \{ \phi'(x) \}^2 \right] + b_1 \phi(x)^{m+2} + b_2 \phi(x)^{2m+2} - \omega \phi(x)^2 = 0. \tag{36}$$

The translational Lie symmetry supported by (36) leads to the periodic solution given by

$$\phi(x) = \left( \frac{2}{3b_2} \right)^{\frac{1}{m}} \left[ \pm \sqrt{2(2b_1^2 + 9\omega b_2)} \left\{ 1 + \cos \left( \sqrt{\frac{b_2}{b_3}} x \right) \right\} \csc^2 \left( \sqrt{\frac{b_2}{b_3}} x \right) \sin^3 \left( \frac{1}{2} \sqrt{\frac{b_2}{b_3}} x \right) - b_1 \right]^{\frac{1}{m}}. \tag{37}$$

This solution (37) is valid provided

$$b_2 b_3 > 0, \tag{38}$$

and

$$2b_1^2 + 9\omega b_2 > 0. \tag{39}$$

## 2.4. FORM-IV

In this case, the law of SPM is:

$$F(s) = b_1 s^{\frac{m}{2}} + b_2 s^m + b_3 s^{\frac{3m}{2}} + b_4 s^{2m} + b_5 s^{\frac{5m}{2}} + b_6 s^{3m}, \quad (40)$$

which leads to the structure of NLSE to be

$$\begin{aligned} & i q_t + a (|q|^n q)_{xx} + \left( b_1 |q|^m + b_2 |q|^{2m} + b_3 |q|^{3m} + b_4 |q|^{4m} + b_5 |q|^{5m} + b_6 |q|^{6m} \right) q \\ & = i \left[ \lambda \left( |q|^{2m} q \right)_x + \theta_1 \left( |q|^{2m} \right)_x q + \theta_2 |q|^{2m} q_x \right] \end{aligned} \quad (41)$$

Substituting (2) into (41), the imaginary part gives (4) which leads to the governing model (41) being modified to:

$$\begin{aligned} & i q_t + a (|q|^n q)_{xx} + \left( b_1 |q|^m + b_2 |q|^{2m} + b_3 |q|^{3m} + b_4 |q|^{4m} + b_5 |q|^{5m} + b_6 |q|^{6m} \right) q \\ & = i \left[ \lambda \left( |q|^{2m} q \right)_x + \theta_1 \left( |q|^{2m} \right)_x q - \{ (2m+1)\lambda + 2m\theta_1 \} |q|^{2m} q_x \right]. \end{aligned} \quad (42)$$

The real part leads to the ODE for  $\phi(x)$  takes the form

$$\begin{aligned} & a(n+1)\phi(x)^{2m+n} \left[ n \{ \phi'(x) \}^2 + \phi(x) \phi''(x) \right] \\ & + \phi^2(x) (\phi^m(x) (\phi^m(x) (\phi^m(x) (\phi^m(x) (\phi^m(x) (\phi^m(x) (b_6 \phi^m(x) + b_5) + b_4) + b_3) + b_2) + b_1) - \omega) = 0. \end{aligned} \quad (43)$$

By the aid of the translational Lie symmetry supported by (43), it integrates in terms of quadratures as given below

$$x = \pm \int \sqrt{-\frac{A}{B}} d\phi, \quad (44)$$

where

$$A = a(n+1)\phi^{n-2}, \quad (45)$$

and

$$B = 2 \left( \frac{b_2 \phi^{2m}}{2m+n+2} + \frac{b_3 \phi^{3m}}{3m+n+2} + \frac{b_4 \phi^{4m}}{4m+n+2} + \frac{b_5 \phi^{5m}}{5m+n+2} + \frac{b_6 \phi^{6m}}{6m+n+2} + \frac{b_1 \phi^m}{m+n+2} - \frac{\omega}{n+2} \right). \quad (46)$$

The integrability condition given by (22) must be valid in this case too for the solution to exist.

## 2.5. FORM-V

The SPM structure for this form is:

$$F(s) = b_1 s^{\frac{m}{2}} + b_2 s^m + b_3 s^{\frac{3m}{2}} + b_4 s^{2m} + b_5 \left( s^{\frac{m}{2}} \right)'' + b_6 (s^m)''. \quad (47)$$

Therefore, the corresponding NLSE is written as:

$$\begin{aligned} & i q_t + a (|q|^n q)_{xx} + \left[ b_1 |q|^m + b_2 |q|^{2m} + b_3 |q|^{3m} + b_4 |q|^{4m} + b_5 (|q|^m)_{xx} + b_6 \left( |q|^{2m} \right)_{xx} \right] q \\ & = i \left[ \lambda \left( |q|^{2m} q \right)_x + \theta_1 \left( |q|^{2m} \right)_x q + \theta_2 |q|^{2m} q_x \right]. \end{aligned} \quad (48)$$

Substituting the hypothesis (2) into (48), the real part leads to the ODE for  $\phi(x)$  as:

$$\begin{aligned} & a(n+1)\phi^n(x) \left[ n \{ \phi'(x) \}^2 + \phi(x) \phi''(x) \right] + 2b_6 m \phi^{2m}(x) \left[ \phi(x) \phi''(x) + (2m-1) \{ \phi'(x) \}^2 \right] \\ & + b_5 m \phi^m(x) \left[ \phi(x) \phi''(x) + (m-1) \{ \phi'(x) \}^2 \right] + b_1 \phi^{m+2}(x) + b_2 \phi^{2m+2}(x) + b_3 \phi^{3m+2}(x) + b_4 \phi^{4m+2}(x) - \omega \phi^2(x) = 0. \end{aligned} \quad (49)$$

For integrability, one must choose:

$$n = 2, \quad (50)$$

and

$$m = 1. \quad (51)$$

The imaginary part leads to (4) and by virtue of (50) and (51), equation (5) simplifies to:

$$\begin{aligned} & i q_t + a \left( |q|^2 q \right)_{xx} + \left[ b_1 |q| + b_2 |q|^2 + b_3 |q|^3 + b_4 |q|^4 + b_5 (|q|)_{xx} + b_6 \left( |q|^2 \right)_{xx} \right] q \\ & = i \left[ \lambda \left( |q|^2 q \right)_x + \theta_1 \left( |q|^2 \right)_x q - (3\lambda + 2\theta_1) |q|^2 q_x \right]. \end{aligned} \quad (52)$$

By means of the translational Lie symmetry that is supported by (52), it integrates to

$$x = \pm \sqrt{\frac{A}{B}} F \left( \sin^{-1} \left( \sqrt{\frac{(3a\phi + b_5 + 2\phi b_6 - \kappa_1)(\kappa_2 - \kappa_4)}{(3a\phi + b_5 + 2\phi b_6 - \kappa_2)(\kappa_1 - \kappa_4)}} \right) \middle| \frac{(\kappa_2 - \kappa_3)(\kappa_1 - \kappa_4)}{(\kappa_1 - \kappa_3)(\kappa_2 - \kappa_4)} \right), \quad (53)$$

where

$$A = 24A_1 A_2, \quad (54)$$

$$A_1 = (2a + b_6) (3a + b_6) (5a + 2b_6) (9a + 4b_6) (21a + 10b_6), \quad (55)$$

$$A_2 = (3a\phi + b_5 + 2\phi b_6 - \kappa_1) (3a\phi + b_5 + 2\phi b_6 - \kappa_2) (3a\phi + b_5 + 2\phi b_6 - \kappa_3) (3a\phi + b_5 + 2\phi b_6 - \kappa_4), \quad (56)$$

$$B = B_1 + B_2 + 2B_3 + 4B_4 + B_5 + B_6, \quad (57)$$

$$\begin{aligned} B_1 &= 5670a^4\omega - 3240a^4\phi^3b_3 - 2835a^4\phi^4b_4 + 540a^3\phi^2b_3b_5 + 540a^3\phi^3b_4b_5 - 72a^2\phi b_3b_5^2 - 90a^2\phi^2b_4b_5^2 + 6ab_3b_5^3 \\ &+ 12a\phi b_4b_5^3 - b_4b_5^4, \end{aligned} \quad (58)$$

$$B_2 = \left\{ 9a^3 \left( 1147\omega - 604\phi^3b_3 - 521\phi^4b_4 \right) + 6a^2\phi^2 \left( 111b_3 + 106\phi b_4 \right) b_5 - 6a\phi \left( 10b_3 + 11\phi b_4 \right) b_5^2 + (3b_3 + 4\phi b_4) b_5^3 \right\} b_6, \quad (59)$$

$$B_3 = \left\{ 6a^2 \left( 586\omega - 283\phi^3b_3 - 241\phi^4b_4 \right) + a\phi^2 \left( 135b_3 + 124\phi b_4 \right) b_5 - 6\phi \left( b_3 + \phi b_4 \right) b_5^2 \right\} b_6^2, \quad (60)$$

$$B_4 = \left( 531a\omega + 9\phi^2b_3(-26a\phi + b_5) + \phi^3b_4(-197a\phi + 8b_5) \right) b_6^3, \quad (61)$$

$$B_5 = 16 \left( 15\omega - 6\phi^3b_3 - 5\phi^4b_4 \right) b_6^4 - b_1(2a + b_6)(9a + 4b_6)(21a + 10b_6)(-b_5 + 4\phi(3a + b_6)), \quad (62)$$

$$(63)$$

$$B_6 = -b_2(2a + b_6)(21a + 10b_6) \left( b_5^2 - 4\phi b_5(3a + b_6) + 6\phi^2(3a + b_6)(5a + 2b_6) \right) \quad (64)$$

where  $\kappa_i$   $i = 1 \cdots 4$  is any solution of

$$\begin{aligned} & -81a^4v_1 - 9a^3b_6v_2 - 6a^2b_6^2v_3 - 368256a^2b_6^6\omega - 4ab_6^3v_4 + b_2v_7(2a + b_6)(3a + 2b_6)^2(21a + 10b_6) \\ & - 57024ab_6^7\omega - 48b_6^5v_6 - 8b_6^4v_5 + b_1v_8 - 3840b_6^8\omega = 0, \end{aligned} \quad (65)$$

and

$$v_1 = 5670a^4\omega - 6ab_3 \left( -70b_5\kappa^2 + 84b_5^2\kappa - 35b_5^3 + 20\kappa^3 \right) + b_4 \left[ 2b_5 \left\{ 80\kappa^3 - 7b_5 \left( -16b_5\kappa + 5b_5^2 + 20\kappa^2 \right) \right\} - 35\kappa^4 \right] = 0, \quad (66)$$

$$\begin{aligned} v_2 &= 228987a^4\omega + 3ab_3 \left( 2994b_5\kappa^2 - 3660b_5^2\kappa + 1567b_5^3 - 844\kappa^3 \right) \\ &+ b_4 \left( 2416b_5\kappa^3 - 4308b_5^2\kappa^2 + 3536b_5^3\kappa - 1147b_5^4 - 521\kappa^4 \right), \end{aligned} \quad (67)$$

$$\begin{aligned} \nu_3 = & 670680a^4\omega - 9ab_3 \left( -1403b_5\kappa^2 + 1750b_5^2\kappa - 773b_5^3 + 390\kappa^3 \right) \\ & - 2b_4 \left( -1132b_5\kappa^3 + 2055b_5^2\kappa^2 - 1732b_5^3\kappa + 586b_5^4 + 241\kappa^4 \right), \end{aligned} \quad (68)$$

$$\begin{aligned} \nu_4 = & 1116261a^4\omega + 3ab_3 \left( 2919b_5\kappa^2 - 3720b_5^2\kappa + 1703b_5^3 - 800\kappa^3 \right) \\ & + b_4 \left( 936b_5\kappa^3 - 1728b_5^2\kappa^2 + 1496b_5^3\kappa - 531b_5^4 - 197\kappa^4 \right), \end{aligned} \quad (69)$$

$$\begin{aligned} \nu_5 = & 384858a^4\omega - 3ab_3 \left( 15\kappa - 23b_5 \right) \left( -13b_5\kappa + 9b_5^2 + 6\kappa^2 \right) \\ & - 2b_4 \left[ b_5 \left\{ 5b_5 \left( -8b_5\kappa + 3b_5^2 + 9\kappa^2 \right) - 24\kappa^3 \right\} + 5\kappa^4 \right], \end{aligned} \quad (70)$$

$$\nu_6 = 28143a^3\omega + b_3 \left( 5b_5 \left( 2b_5 (b_5 - 2\kappa) + 3\kappa^2 \right) - 4\kappa^3 \right), \quad (71)$$

$$\nu_7 = 6\kappa^2 (3a + b_6) (5a + 2b_6) - 8b_5\kappa (3a + b_6) (9a + 4b_6) + 3b_5^2 (5a + 2b_6) (9a + 4b_6), \quad (72)$$

$$\nu_8 = (2a + b_6) (3a + 2b_6)^3 (9a + 4b_6) (21a + 10b_6) \{ 4\kappa (3a + b_6) - 3b_5 (5a + 2b_6) \}. \quad (73)$$

Here,  $F(\psi|\mu)$  is elliptic integral of the first kind that has been defined in (19). The existence criteria for the solution is given by (30).

## 2.6. FORM-VI

The SPM structure for this form is:

$$F(s) = b_1 s^{\frac{m}{2}} + b_2 s^m + b_3 s^{\frac{3m}{2}} + b_4 s^{2m} + b_5 s^{\frac{5m}{2}} + b_6 s^{3m} + b_7 \left( s^{\frac{m}{2}} \right)'' + b_8 (s^m)''. \quad (74)$$

Therefore, the corresponding NLSE shapes up to be:

$$\begin{aligned} & iq_t + a (|q|^n q)_{xx} + \left[ b_1 |q|^m + b_2 |q|^{2m} + b_3 |q|^{3m} + b_4 |q|^{4m} + b_5 |q|^{5m} + b_6 |q|^{6m} + b_7 (|q|^m)_{xx} + b_8 (|q|^{2m})_{xx} \right] q \\ = & i \left[ \lambda (|q|^{2m} q)_x + \theta_1 (|q|^{2m})_x q + \theta_2 |q|^{2m} q_x \right]. \end{aligned} \quad (75)$$

Substituting (2) into (75) and splitting into real and imaginary parts, equation (5) by virtue of (4) simplifies to:

$$\begin{aligned} & iq_t + a (|q|^n q)_{xx} + \left[ b_1 |q|^m + b_2 |q|^{2m} + b_3 |q|^{3m} + b_4 |q|^{4m} + b_5 |q|^{5m} + b_6 |q|^{6m} + b_7 (|q|^m)_{xx} + b_8 (|q|^{2m})_{xx} \right] q \\ = & i \left[ \lambda (|q|^{2m} q)_x + \theta_1 (|q|^{2m})_x q - \{ (2m+1)\lambda + 2m\theta_1 \} |q|^{2m} q_x \right]. \end{aligned} \quad (76)$$

The real part equation (3) in this case, is:

$$\begin{aligned} & a(n+1)\phi^n(x) \left[ n \{ \phi'(x) \}^2 + \phi(x)\phi''(x) \right] + 2b_8 m \phi^{2m}(x) \left[ \phi(x)\phi''(x) + (2m-1) \{ \phi'(x) \}^2 \right] \\ & + b_7 m \phi^m(x) \left[ \phi(x)\phi''(x) + (m-1) \{ \phi'(x) \}^2 \right] + b_1 \phi^{m+2}(x) + b_2 \phi^{2m+2}(x) + b_3 \phi^{3m+2}(x) \\ & + b_4 \phi^{4m+2}(x) + b_5 \phi^{5m+2}(x) + b_6 \phi^{6m+2}(x) - \omega \phi^2(x) = 0. \end{aligned} \quad (77)$$

By the translational Lie symmetry, supported by (77), the integral is written in quadratures as:

$$x = \pm \int \sqrt{\frac{A}{2B}} d\phi, \quad (78)$$

where

$$A = \exp \left( -2 \int^\phi - \frac{m (2(2m-1)b_8 \tau_1^m + (m-1)b_7) \tau_1^m + a n(n+1) \tau_1^n}{\tau_1 (m (2b_8 \tau_1^m + b_7) \tau_1^m + a(n+1) \tau_1^n)} d\tau_1 \right), \quad (79)$$

and

$$B = \int^{\phi} \frac{\exp\left(-2 \int^{\tau_2} -\frac{m(2(2m-1)b_8\tau_1^m + (m-1)b_7)\tau_1^m + a(n+1)\tau_1^n}{\tau_1(m(2b_8\tau_1^m + b_7)\tau_1^m + a(n+1)\tau_1^n)} d\tau_1\right) \Gamma}{m(2b_8\tau_2^m + b_7)\tau_2^m + a(n+1)\tau_2^n} d\tau_2, \quad (80)$$

with

$$\Gamma = \tau_2 \left( \omega - \tau_2^m \left( \tau_2^m \left( \tau_2^m \left( \tau_2^m (b_6\tau_2^m + b_5) + b_4 \right) + b_3 \right) + b_2 \right) + b_1 \right). \quad (81)$$

The parameter constraint given by (30) must also be satisfied for the solution to exist.

### 3. CONCLUSIONS

The paper addressed the NLSE with nonlinear CD and linear temporal evolutions but with six forms of SPM structures that were proposed by Kudryashov during the past decade. By applying the Lie symmetry analysis, the study systematically derived implicit quiescent optical solitons and reduced the governing nonlinear partial differential equation to solvable amplitude equations expressed through quadratures. The Lie symmetry analysis is the integration tool that has been implemented to address the models that gave way to the solutions also in terms of quadratures. The results, recovered with the usage of Lie symmetry analysis, were in terms of quadratures and in one particular case, emerged in terms of periodic functions. Among the six Kudryashov SPM structures, five produced implicit solitary-wave profiles while one yielded an explicit periodic solution under well-defined parameter constraints. These constraints delineate the parameter space in which physically admissible stationary solitons can exist, clarifying the interplay among nonlinear chromatic dispersion, self-steepening, and self-frequency-shift effects.

The analytical complexity of the solutions are a far cry from the explicit quiescent soliton solutions that were recovered in 2021 [3]. Compared with the earlier results obtained via extended elliptic-function methods, the Lie symmetry approach offers a unified and transparent framework capable of handling multiple nonlinear dispersion and SPM laws within a single analytical setting. This framework also highlights integrability conditions (such as specific exponent relations) that make the reduced equations analytically tractable.

The results of this work are interesting and thus pave the way for further activities with the model with time. Future investigations will extend the present analysis to include generalized temporal evolution, dissipative terms, and higher-order nonlinearities. Numerical simulations and stability analyses will be performed to validate the analytical predictions and explore the robustness of the stationary profiles under perturbations. Later, these same models are going to be addressed with generalized temporal evolution and the results of those research activities will be presented in a different journal. Overall, this work provides a clear analytical foundation for exploring nonlinear-dispersion-driven pulse dynamics in optical fibers and photonic crystal fibers, serving as a stepping stone toward a comprehensive understanding of nonlinear wave propagation in advanced optical media. This is just a tip of the iceberg!






### Disclosure

The authors claim there is no conflict of interest.

### Acknowledgement

This work of the last author (AB) was funded by the budget of Grambling State University for the Endowed Chair of Mathematics. The author thankfully acknowledges this support.

### ORCID

 **Abdullahi Rashid Adem**, <https://orcid.org/0000-0001-8335-8072>;  **Ahmed H. Arnous**, <https://orcid.org/0000-0002-7699-7068>;  **Hamlet Isakhanli**, <https://orcid.org/0000-0002-6383-0883>;  **Oswaldo González-Gaxiola**, <https://orcid.org/0000-0003-3317-9820>;  **Anjan Biswas**, <https://orcid.org/0000-0002-8131-6044>

### REFERENCES

- [1] A.R. Adem, A. Biswas, and Y. Yildirim, "Implicit quiescent optical solitons for perturbed Fokas–Lenells equation with nonlinear chromatic dispersion and a couple of self-phase modulation structures by Lie symmetry," *Semiconductor Physics, Quantum Electronics & Optoelectronics*, **28**(1), 047–052 (2025). <https://doi.org/10.15407/spqeo28.01.047>
- [2] A. Biswas, M. Ekici, A. Sonmezoglu, and M. Belic, "Stationary optical solitons with nonlinear group velocity dispersion by extended trial function scheme," *Optik*, **171**, 529–542. (2018). <https://doi.org/10.1016/j.ijleo.2018.06.067>
- [3] M. Ekici, A. Sonomezogulu, and A. Biswas, "Stationary optical solitons with Kudryashov's laws of refractive index," *Chaos, Solitons & Fractals*, **151**, 111226 (2021). <https://doi.org/10.1016/j.chaos.2021.111226>
- [4] M. Ekici, "Stationary optical solitons with complex Ginzburg–Landau equation having nonlinear chromatic dispersion and Kudryashov's refractive index structure," *Physics Letters A*, **440**, 128146 (2022). <https://doi.org/10.1016/j.physleta.2022.128146>

- [5] M. Ekici, "Kinky breathers, W-shaped and multi-peak soliton interactions for Kudryashov's quintuple power-law coupled with dual form of non-local refractive index structure," *Chaos, Solitons & Fractals*, **159**, 112172 (2022). <https://doi.org/10.1016/j.chaos.2022.112172>
- [6] M. Ekici, "Optical solitons with Kudryashov's quintuple power-law coupled with dual form of non-local law of refractive index with extended Jacobi's elliptic function," *Optical and Quantum Electronics*, **54**(5), 279 (2022). <https://doi.org/10.1007/s11082-022-03657-0>
- [7] M. Ekici, "Stationary optical solitons with Kudryashov's quintuple power law nonlinearity by extended Jacobi's elliptic function expansion," *Journal of Nonlinear Optical Physics and Materials*, **32**(01), 2350008 (2023). <https://doi.org/10.1142/s021886352350008x>
- [8] T. Han, Z. Li, C. Li, and L. Zhao, "Bifurcations, stationary optical solitons and exact solutions for complex Ginzburg–Landau equation with nonlinear chromatic dispersion in non-Kerr law media," *Journal of Optics*, **52**, 831–844, (2023). <https://doi.org/10.1007/s12596-022-01041-5>
- [9] N.A. Kudryashov, "Stationary solitons of the generalized nonlinear Schrödinger equation with nonlinear dispersion and arbitrary refractive index," *Applied Mathematics Letters*, **128**, 107888 (2022). <https://doi.org/10.1016/j.aml.2021.107888>
- [10] A.J.M. Jawad, and M.J. Abu-AlShaer, "Highly dispersive optical solitons with cubic law and cubic–quintic–septic law nonlinearities by two methods," *Al-Rafidain Journal of Engineering Sciences*, **1**(1), 1–8. (2023). <https://doi.org/10.61268/sapgh524>
- [11] N. Jihad, and M.A.A. Almuhsan, "Evaluation of impairment mitigations for optical fiber communications using dispersion compensation techniques," *Al-Rafidain Journal of Engineering Sciences*, **1**(1), 81–92. (2023). <https://doi.org/10.61268/Odat0751>
- [12] A.M. Yalçı, and M. Ekici, "Stationary optical solitons with complex Ginzburg–Landau equation having nonlinear chromatic dispersion," *Optical and Quantum Electronics*, **54**(3), 167 (2022). <https://doi.org/10.1007/s11082-022-03557-3>
- [13] Z. Yan, "New families of exact solitary patterns solutions for the nonlinearly dispersive  $R(m, n)$  equations," *Chaos, Solitons & Fractals*, **15**(5), 891–896 (2003). [https://doi.org/10.1016/s0960-0779\(02\)00204-7](https://doi.org/10.1016/s0960-0779(02)00204-7)
- [14] Z. Yan, "Envelope compact and solitary pattern structures for the  $GNLS(m, n, p, q)$  equations," *Physics Letters A*, **357**(3), 196–203 (2006). <https://doi.org/10.1016/j.physleta.2006.04.032>
- [15] Z. Yan, "Envelope compactons and solitary patterns," *Physics Letters A*, **355**(3), 212–215 (2006). <https://doi.org/10.1016/j.physleta.2006.02.032>

## НЕЯВНЕ СПОКІЙНЕ ОПТИЧНЕ СОЛІТОНЕ ЗБУРЕННЯ З НЕЛІНІЙНОЮ ХРОМАТИЧНОЮ ДИСПЕРСІЄЮ ТА ЛІНІЙНОЮ ЧАСОВОЮ ЕВОЛЮЦІЄЮ З ФОРМАМИ САМОФАЗОВОЇ МОДУЛЯЦІЇ КУДРЯШОВА ЗА СИМЕТРІЄЮ ЛІ

Абдуллахі Рашид Адем<sup>1</sup>, Ахмед Х. Арнус<sup>2</sup>, Гамлет Ісаханлі<sup>3</sup>, Освальдо Гонсалес–Гаксіола<sup>4</sup>,  
Анджан Бісвас<sup>5,6,7</sup>

<sup>1</sup>Кафедра математичних наук, Університет Південної Африки, UNISA-0003, Південна Африка

<sup>2</sup>Кафедра інженерної математики та фізики, Вищий інженерний інститут, Академія Ель-Шорук, Каір-11837, Єгипет

<sup>3</sup>Кафедра математики, Університет Хазар, Баку, Аризона-1096, Азербайджан

<sup>4</sup>Кафедра прикладної математики та систем, Автономний столичний університет–Куахімальпа,  
Васко-де-Кірога 4871, Мехіко 05348, Мексика

<sup>5</sup>Кафедра математики та фізики, Державний університет Гремблінга, Гремблінг, Луїзіана 71245–2715, США

<sup>6</sup>Кафедра фізики та електроніки, Університет Хазар, Баку, Аризона-1096, Азербайджан

<sup>7</sup>Кафедра Математика та прикладна математика, Університет медичних наук Сефако Макгатхо,  
Медунса-0204, Південна Африка

У статті отримано неявні спокійні оптичні солітони для нелінійного рівняння Шредінгера, яке враховує нелінійну хроматичну дисперсію та лінійну часову еволюцію. Використовуючи стаціонарний або спокійний підхід у поєднанні з аналізом симетрії Лі, дослідження систематично розглядає шість різних структур самофазової модуляції, запропонованих Кудряшовим. Аналітична процедура зводить керівне рівняння до амплітудних форм, розв'язки яких отримуються через квадратури, що призводить як до неявних профілів одиночної хвилі, так і до одного явного періодичного випадку. Шість форм структур самофазової модуляції, запропонованих Кудряшовим, дали розв'язки в термінах квадратур, періодичних розв'язків, а також в термінах еліптичних функцій. Існування кожного сімейства розв'язків обговорюється з точки зору допустимих параметричних співвідношень, які забезпечують фізично значущі одиночні профілі. Цей підхід забезпечує єдину структуру порівняно з попередніми методами, заснованими на прямих розкладах еліптичних функцій, підкреслюючи, як симетрія Лі сприяє компактному обробленню кількох нелінійних законів дисперсії. Результати є актуальними для розуміння стаціонарних оптичних імпульсів у нелінійних волокнах та фотоннокристалічних волокнах, і вони закладають основу для майбутніх числових та експериментальних досліджень нелінійне поширення імпульсів, зумовлене дисперсією.

**Ключові слова:** спокійні солітони; хроматична дисперсія; квадратури; параметричні обмеження



## EFFECT OF ANISOTROPIC DUST PRESSURE ON THE FORMATION AND PROPAGATION OF ARBITRARY AMPLITUDE DUST ACOUSTIC SOLITARY WAVES (DASW) IN A MAGNETIZED DUST-ION-ELECTRON PLASMA

 **Mamani Choudhury**

*Department of Mathematics, Handique Girls' College, Guwahati 781001, India*

*Corresponding Author email: [mamani.choudhury@hgcollege.edu.in](mailto:mamani.choudhury@hgcollege.edu.in)*

*Received July 14, 2025; revised October 24, 2025; accepted November 5, 2025*

Arbitrary amplitude dust acoustic solitary waves (DASW) in a dusty magneto-plasma with anisotropic dust pressure and nonthermal distribution of ions and electrons has been investigated. Sagdeev pseudopotential technique is used to derive an energy balance equation and to analyze various properties of dust acoustic solitons. The effects of anisotropic dust pressure, dust number density ratio, non-thermality, etc., are investigated numerically for the propagation of DASWs. It is found that rarefactive solitons can exist for negatively charged dust, and compressive solitons can exist for positively charged dust. The present study could be useful for the understanding of DASWs in various astrophysical environments.

**Keywords:** *Dust acoustic wave; Dusty plasma; Anisotropic pressure; Sagdeev pseudopotential; Solitary waves; Magnetized plasma; Non-thermal electrons and ions*

**PACS:** 52.27.Lw; 52.25.Xz; 52.53-g.

### 1. INTRODUCTION

Dusty plasmas are abundant in various astrophysical situations, such as interstellar media, cometary tails, ionospheres, planetary rings, etc. [1-6]. These are also relevant in industrial context [7-9]. The propagation of nonlinear waves in multispecies plasmas consisting of electrons, ions and massive dust particles is a fertile research area. Dust particles that spread in plasma media, acquire either positive or negative charges according to different mechanisms. In most cases, dust particles become negatively charged due to higher mobility of electrons compared to ions. On the other hand, dust particles can gain positive charge by emission of electrons from surface of dust particles by photo-electron emission, secondary electron emission and radiation [8]. From various studies [9-19] it has been observed that the presence of charged dust particles in plasma not only modifies the properties of existing plasma wave modes but also introduces new modes. Many authors showed that the role of dust charge fluctuation cannot be ignored. But it is important to mention here that the nonlinear study of dusty plasmas become too complicated when the charging process are taken into account. Therefore, for simplicity I limit my investigation in a dusty plasma without considering the charging process. The fundamental nature of waves does not change when dust charging and other collisional processes are ignored [20].

Often, magnetic fields [21-23] are involved with dusty plasma. The investigations of linear and non-linear propagation of dust acoustic waves with external magnetic fields have been performed by various researchers [24-28]. The existence of a magnetic field in plasma causes pressure anisotropy, i.e. the pressure in the perpendicular direction to the magnetic field is different from pressure in the parallel direction. The pressure anisotropy can be found in pulsar winds, planetary magnetosphere and near earth's magnetosheaths etc. The effect of anisotropic pressure of ions on solitary waves has been studied by many researchers using Chew-Golberger-Low (CGL) description [29].

The influence of anisotropic ion pressure on dust ion acoustic solitary waves and double layers in a magnetized dusty plasma has been studied by Choi et al. [30] and Chatterjee et al. [31] using the Sagdeev potential method. But this theory is not limited to ion dynamics only. We can also use it to describe the pressure anisotropy of dust particles in the plasma. In many places, like earth's magnetosphere, the dust pressure may not be negligible, and it can play an important role in the formation of various nonlinear structures. We incorporate the anisotropy of dust pressure so that the study may help in understanding the behaviors of nonlinear coherent structures in plasma. Bashir et al. [32] investigated the effect of anisotropic dust pressure and superthermal electrons on propagation and stability of dust acoustic waves. They employed the Reductive-perturbation technique and derived ZK equation for dust acoustic solitary waves in magnetized plasma. They found that the DASW is rarefactive for negative dust and compressive for positive dust.

Various studies have pointed out that highly energetic electrons and ions are present in several astrophysical plasma environments. Among non-thermal distributions, one of the frequently encountered distributions is Cairns' distribution [33-36]. Mamun et al. [33] studied dust acoustic waves in unmagnetized dusty plasma with non-thermal ions. Berbri and Tribeche [36] have considered non-thermal electrons to investigate weakly nonlinear dust ion acoustic shock waves. Choudhury [28] discussed the propagation of DASW in a magnetized plasma with nonthermal electrons and ions using the Sagdeev potential method.

To study nonlinear solitary waves in plasmas, reductive perturbation technique (RPT) and Sagdeev pseudopotential method are mainly used. With RPT only small amplitude nonlinear waves can be studied while Sagdeev pseudopotential

method can handle arbitrary amplitude waves [37]. In Sagdeev pseudopotential method, fully nonlinearity of the system is considered. Various researchers have employed Sagdeev pseudopotential method to dusty plasma to study electrostatic nonlinear solitary modes.

To the best of our knowledge, the effect of anisotropic dust pressure on the formation and propagation of arbitrary amplitude dust acoustic solitary waves in a magnetized plasma has not been reported in the literature to date. The goal of the present work is, to study the effect of anisotropic dust pressure on the solitary dust acoustic waves in a three-component dusty plasma with nonthermal ions and electrons. Dust grains are assumed to be uniform in mass and charge and plasma is considered to be collisionless. The present study could be useful for the understanding of properties of DASWs in various astrophysical environments like Earth's magnetopause.

The manuscript is organized in the following way: in section I, the usual 'Introduction' is considered; 'Basic set of governing equations' is included in section II; 'Energy integral' is derived in section III; 'Condition of existence' of Dust Acoustic Waves are incorporated in section IV; 'Parametric Analysis' of the results are described in section V; and lastly 'Conclusions' are deduced in section VI which is followed by 'References'.

## 2. BASIC SET OF GOVERNING EQUATIONS

We consider the propagation of dust acoustic waves in a magnetized, collisionless, three component plasma consisting of non-thermal ions and electrons and dust fluids. The pressure tensor of dust fluid is assumed to be anisotropic and modelled by Chew-Goldberger-Low [27] description. The ambient magnetic field is assumed to be uniform and directed along  $z$ -axis, i.e.  $\mathbf{B} = B_0 \hat{z}$ . The equations of continuity and motion governing the dust dynamics in this plasma system are described by

$$\frac{\partial n_d}{\partial t} + \nabla \cdot (n_d \mathbf{v}_d) = 0 \quad (1)$$

$$\frac{\partial \mathbf{v}_d}{\partial t} + (\mathbf{v}_d \cdot \nabla) \mathbf{v}_d = \frac{j z_d e}{m_d} \nabla \phi - \mathbf{v}_d \times \frac{j z_d e}{c m_d} \mathbf{B} - \frac{1}{m_d n_d} \nabla \cdot \tilde{\mathbf{P}} \quad (2)$$

respectively. Here  $n_d$  is dust number density and  $\mathbf{v}_d$  is the dust fluid velocity.  $m_d$  is the dust mass,  $e$  is the magnitude of the electron charge,  $c$  is the speed of light in vacuum,  $z_d$  is dust charge and  $\phi$  is the electrostatic potential.  $j = 1$  for negatively charged dust and  $j = -1$  for positively charged dust.

The dust pressure tensor  $\tilde{\mathbf{P}}$  takes the form  $\tilde{\mathbf{P}} = p_{\perp} \hat{\mathbf{I}} + (p_{\parallel} - p_{\perp}) \hat{\mathbf{B}} \hat{\mathbf{B}}$  where  $\hat{\mathbf{I}}$  is unit dyad and  $\hat{\mathbf{B}} \hat{\mathbf{B}}$  is the dyad form of unit vector along the magnetic field. We can evaluate  $\nabla \cdot \tilde{\mathbf{P}}$  as

$$\nabla \cdot \tilde{\mathbf{P}} = \nabla p_{\perp} + (\mathbf{B} \cdot \nabla) \left[ (p_{\parallel} - p_{\perp}) \frac{\mathbf{B}}{B_0^2} \right] \quad (3)$$

Using Chew-Golberger-Low (CGL) description for constant magnetic field, the perpendicular and parallel pressure terms can be obtained as

$$p_{\perp} = p_{\perp 0} \left( \frac{n_d}{n_{d0}} \right) \text{ and } p_{\parallel} = p_{\parallel 0} \left( \frac{n_d}{n_{d0}} \right)^3 \quad (4)$$

where  $n_{d0}$  equilibrium number density of dust fluid.

The electrons and ions are assumed to be inertia less due to their lighter masses. The expression for nonthermal electron density and ion density are

$$n_e = n_{e0} \left[ 1 - \beta_e \frac{e\phi}{KT_e} + \beta_e \left( \frac{e\phi}{KT_e} \right)^2 \right] \text{Exp} \left[ \frac{e\phi}{KT_e} \right] \quad (5)$$

$$n_i = n_{i0} \left[ 1 + \beta_i \frac{e\phi}{KT_i} + \beta_i \left( \frac{e\phi}{KT_i} \right)^2 \right] \text{Exp} \left[ \frac{-e\phi}{KT_i} \right] \quad (6)$$

The symbols  $\beta_e$  and  $\beta_i$  are nonthermal parameters of electrons and ions respectively that characterize nonthermal effect and  $n_{e0}$  and  $n_{i0}$  are equilibrium number densities of electrons and ions.

The charge neutrality condition is

$$n_e - n_i + j z_d n_d = 0 \quad (7)$$

The wave is assumed to be evolve and propagate in  $x - z$  plane. We have normalized densities by corresponding equilibrium densities, velocities by dust acoustic velocity  $C_d = \left( \frac{KT_i z_d}{m_d} \right)^{\frac{1}{2}}$ , potential by  $\frac{KT_i}{e}$ , time by gyroperiod  $\Omega_d^{-1} = \frac{m_d c}{B_0 z_d e}$  and distances by gyroradius  $C_d \Omega_d^{-1}$ ,  $K$  being the Boltzmann constant. Then the normalized set of governing equations are given by

$$\frac{\partial n_d}{\partial t} + \frac{\partial(n_d v_{dx})}{\partial x} + \frac{\partial(n_d v_{dz})}{\partial z} = 0 \quad (8)$$

$$\frac{\partial v_{dx}}{\partial t} + v_{dx} \frac{\partial v_{dx}}{\partial x} + v_{dz} \frac{\partial v_{dx}}{\partial z} = j \frac{\partial \phi}{\partial x} - j v_{dy} - \frac{P_{\perp}}{n_d} \frac{\partial n_d}{\partial x} \quad (9)$$

$$\frac{\partial v_{dy}}{\partial t} + v_{dx} \frac{\partial v_{dy}}{\partial x} + v_{dz} \frac{\partial v_{dy}}{\partial z} = j v_{dx} \quad (10)$$

$$\frac{\partial v_{dz}}{\partial t} + v_{dx} \frac{\partial v_{dz}}{\partial x} + v_{dz} \frac{\partial v_{dz}}{\partial z} = j \frac{\partial \phi}{\partial z} - P_{\parallel} n_d \frac{\partial n_d}{\partial x} \quad (11)$$

where  $P_{\perp} = \frac{p_{\perp 0}}{KT_i n_{d0}}$  and  $P_{\parallel} = \frac{3 p_{\parallel 0}}{KT_i n_{d0}}$

and the normalized number densities of nonthermal electron and ions are given by

$$n_e = (1 - f)(1 - \beta_e \alpha \phi + \beta_e \alpha^2 \phi^2) e^{\alpha \phi} \quad (12)$$

$$n_i = (1 + \beta_i \phi + \beta_i \phi^2) e^{-\phi} \quad (13)$$

where  $f = \frac{z_d n_{d0}}{n_{i0}}$  and  $\alpha = \frac{T_i}{T_e}$

The normalized quasi-neutrality condition is

$$f j n_d + (1 - f) n_e = n_i \quad (14)$$

### 3. DERIVATION OF ENERGY INTEGRAL

To obtain the energy integral, we consider a wave propagating obliquely to the external magnetic field  $B_0 \hat{z}$  in moving frame defined by  $\xi = x k_x + z k_z - M t$  with  $M = \frac{V}{C_d}$ ,  $k_x^2 + k_z^2 = 1$  where  $M$  is the Mach Number (normalized soliton velocity) defined in terms of soliton velocity  $V$  and dust acoustic velocity  $C_d$  and  $k_x, k_z$  are direction cosines, so that

$$\frac{\partial}{\partial t} \rightarrow -M \frac{d}{d\xi}, \quad \frac{\partial}{\partial x} \rightarrow k_x \frac{d}{d\xi} \text{ and } \frac{\partial}{\partial z} \rightarrow k_z \frac{d}{d\xi}. \quad (15)$$

Using these equations, equations (8-11) can be reduced to a set of ordinary differential equations

$$\frac{d}{d\xi} (-M n_d + k_x n_d v_{dx} + k_z n_d v_{dz}) = 0 \quad (16)$$

$$-\frac{M}{n_d} \frac{dv_{dx}}{d\xi} = j \left( k_x \frac{d\phi}{d\xi} - v_{dy} \right) - \frac{P_{\perp}}{n_d} k_x \frac{dn_d}{d\xi} \quad (17)$$

$$-\frac{M}{n_d} \frac{dv_{dy}}{d\xi} = j v_{dx} \quad (18)$$

$$-\frac{M}{n_d} \frac{dv_{dz}}{d\xi} = j k_z \frac{d\phi}{d\xi} - P_{\parallel} n_d k_z \frac{dn_d}{d\xi} \quad (19)$$

After some lengthy but straightforward algebra, the set of equations (16)-(19), along with the equations (12)-(14), can be deduced to a single dimensionless nonlinear differential equation

$$\frac{1}{2} \left( \frac{d\phi}{d\xi} \right)^2 + S(\phi) = 0 \quad (20)$$

The boundary condition using in deriving the equation (20) are  $\phi \rightarrow 0, \frac{d\phi}{d\xi} \rightarrow 0, v_{dx} \rightarrow 0, v_{dy} \rightarrow 0, v_{dz} \rightarrow 0$  as  $\xi \rightarrow \infty$   
Here,

$$S(\phi) = \frac{1}{H^2} \left[ j G(\phi) - j \phi + \frac{k_z^2}{M^2} \frac{(G(\phi))^2}{2} - \frac{P_{\parallel}}{3} \frac{k_z^2}{M^2} (K(\phi) - G(\phi)) - M^2 \left( \frac{1}{n_d} - 1 \right) - P_{\perp} k_x^2 (n_d - 1) - \frac{P_{\parallel}}{3} k_z^2 (n_d^3 - 1) + \right. \\ \left. \frac{M^2}{2} \left( \frac{1}{n_d^2} - 1 \right) + P_{\perp} k_x^2 \log n_d + \frac{P_{\parallel}}{2} k_z^2 (n_d^2 - 1) - j k_z^2 \left( \frac{G(\phi)}{n_d} - \phi \right) - j \frac{k_z^2}{M^2} P_{\perp} k_x^2 (G(\phi) n_d - J(\phi)) - j \frac{k_z^2}{M^2} P_{\parallel} k_z^2 (n_d^3 G(\phi) - \right. \\ \left. K(\phi)) - \frac{P_{\parallel}}{3} \frac{k_z^2}{M^2} \left( \frac{M^2}{2} (n_d^2 - 1) + M^2 \left( \frac{1}{n_d} - 1 \right) - \frac{P_{\perp} k_x^2}{4} (n_d^4 - 1) + P_{\perp} k_x^2 (n_d - 1) - \frac{P_{\parallel} k_z^2}{6} (n_d^6 - 1) + \frac{P_{\parallel} k_z^2}{3} (n_d^3 - 1) \right) \right] \quad (21)$$

is the Sagdeev potential, where:

$$H = 1 + j \left( \frac{M^2}{n_d^3} - \frac{P_{\perp} k_x^2}{n_d} - P_{\parallel} k_z^2 n_d \right) \frac{\partial n_d}{\partial \phi},$$

$$n_d = \frac{1}{jf} [(1 + \beta_i \phi + \beta_i \phi^2) e^{-\phi} - (1 - jf)(1 - \beta_e \alpha \phi + \beta_e \alpha^2 \phi^2) e^{\alpha \phi}],$$

$$G(\phi) = \int_0^\phi n_d d\phi,$$

$$J(\phi) = \int_0^\phi n_d^2 d\phi,$$

$$K(\phi) = \int_0^\phi n_d^4 d\phi.$$

The values of  $H$ ,  $G(\phi)$ ,  $J(\phi)$  and  $K(\phi)$  are calculated using MATHEMATICA-11.

This result is in agreement with the expression forwarded by my earlier paper [28] when I consider only negatively charged ( $j = 1$ ) and cold dust ( $P_\parallel, P_\perp = 0$ ).

Choi et al. [30] and Chatterjee et al. [31] had considered negatively charged stationary dust particles forming only background plasma and used ion dynamics to derive Sagdeev potential. In our paper we have considered fully dynamic dust particles and used dust dynamics to derive the Sagdeev potential. So, our result is not directly comparable to these results.

The amplitude  $\phi_m$  of solitary waves is determined by assigning different values of the parameters  $\alpha, \beta_i, \beta_e, k_z, f, P_\parallel, P_\perp$  and  $M$  in the non-linear dispersion relation viz  $S(\phi) = 0$ .

#### 4. CONDITION OF EXISTENCE OF SOLITARY DUST ACOUSTIC WAVES

The existence criterion of solitary wave formation is that the Sagdeev potential  $S(\phi)$  must satisfy the following conditions,

$$S(\phi) = 0, \frac{dS(\phi)}{d\phi} = 0, \frac{d^2S(\phi)}{d\phi^2} < 0 \text{ at } \phi = 0$$

$S(\phi) = 0$  at  $\phi = \phi_m$  and  $S(\phi) < 0$  for  $\phi$  lying between 0 and  $\phi_m$ , where  $\phi_m$  is the maximum amplitude of the solitons. If  $\phi_m < \phi < 0$ , rarefactive solitary waves exists, and if  $0 < \phi < \phi_m$  compressive solitary waves exist.

From equation (21) it can be easily verified that the conditions  $S(\phi) = 0, \frac{dS(\phi)}{d\phi} = 0$  at  $\phi = 0$  are automatically satisfied. From the condition  $\frac{d^2S(\phi)}{d\phi^2} < 0$  at  $\phi = 0$  we find that the dust acoustic soliton solution may exist in the interval

$$k_z \sqrt{\frac{f}{(1-\beta_i)+(1-jf)(1-\beta_e)\alpha}} + P_\parallel < M < \sqrt{\frac{f}{(1-\beta_i)+(1-jf)(1-\beta_e)\alpha}} + P_\perp (1 - k_z^2) + P_\parallel k_z^2 \quad (22)$$

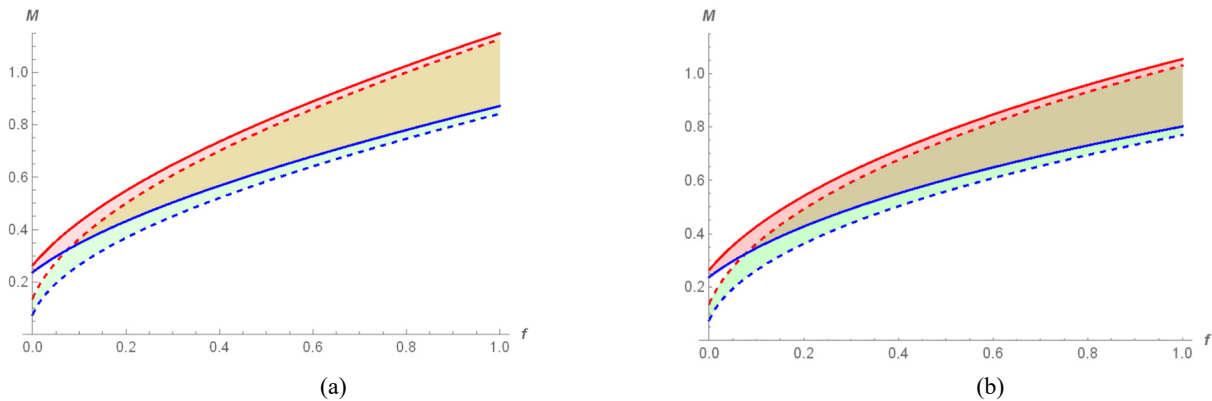
#### 5. PARAMETRIC ANALYSIS

To observe the existence of solitary wave, the range of Mach number for existence of DASWs and Sagdeev potential  $S(\phi)$  have been plotted against  $\phi$  for different values of plasma parameters. In this investigation, it is found that rarefactive waves travelling at both subsonic and supersonic speeds for negative dust and compressive waves travelling at subsonic speed for positive dust exist in this magnetized plasma. The effects of the parameters  $P_\parallel, P_\perp, f, \beta_i, M$  and  $k_z$  on the formation of dust acoustic solitons have also been studied.

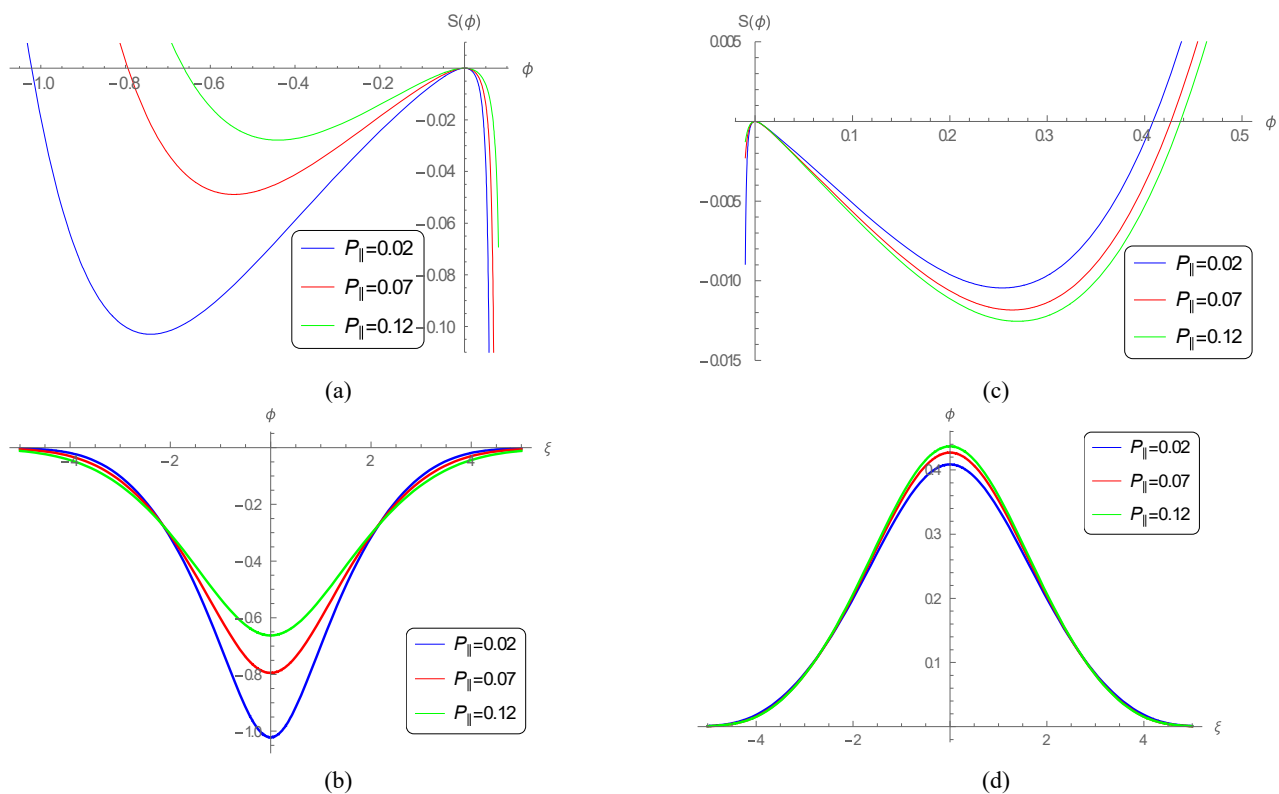
The range of Mach number for nonlinear arbitrary amplitude dust acoustic solitons is investigated numerically from equation (22). It was proven that  $\beta$  had an upper limit  $4/7$  [38]. When the values of  $\beta$  are above  $4/7$ , the Cairns distribution ceases to be monotonically decreasing. So, all present calculations were performed for values of  $\beta$  not exceeding  $4/7$ . For fixed plasma parameters  $\beta_i = 0.2, \beta_e = 0.2, \alpha = 0.1, k_z = 0.75$ , and  $P_\perp = 0.03$ , Fig 1 (a) and (b) show the Mach number  $M$  values versus dust-ion density ratio  $f$  that supports the existence of arbitrary amplitude dust acoustic solitons in a magnetized plasma with anisotropic dust pressure for two different values of  $P_\parallel = 0.1$  (solid) and  $0.01$  (dashed). In figure 1(a) we considered negative dust and in Figure 1(b) we considered positive dust. For both positive and negative dust, we get similar range (not exactly same) of Mach number for existence of solitons.

Figure 2(a) and (b) show the variation of the Sagdeev potential  $S(\phi)$  against the electrostatic potential  $\phi$  for different values of parallel dust pressure  $P_\parallel$  for negative and positive dust respectively. Other parameters are taken as fixed. From these figures it has been noted that the parallel pressure variation is quite effective for negative dust. As  $P_\parallel$  increases the amplitude of the rarefactive solitons decrease very fast. On the other hand, for positive dusts, the amplitude of the compressive soliton increases. In Figure 2(c) and (d) show the variation of  $\phi$  against  $\xi$  which has been computed numerically by integrating the Sagdeev potential for same parameters used in figure 2(a) and (b) respectively.

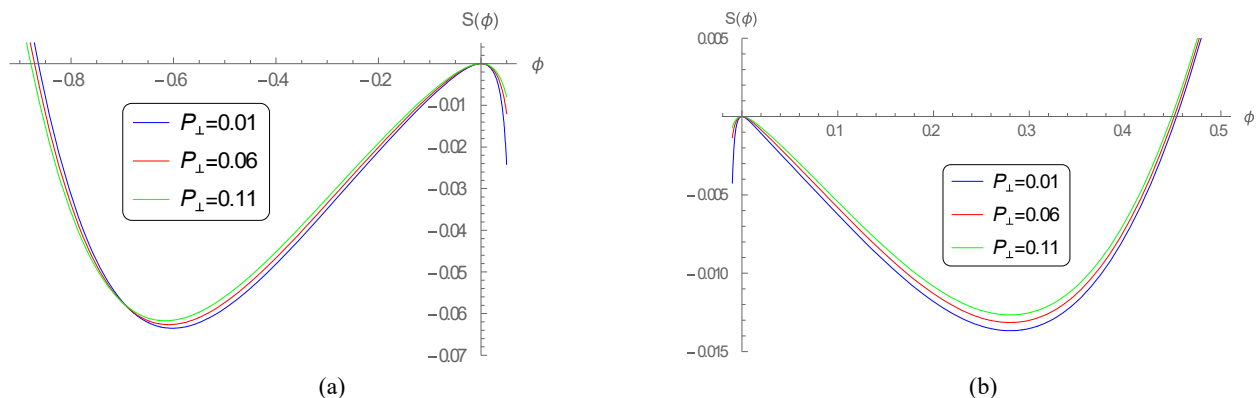
In figure 3(a) and (b), the variation of the Sagdeev potential  $S(\phi)$  against the electrostatic potential  $\phi$  for different values of perpendicular dust pressure  $P_\perp$  is plotted for negative and positive dust respectively. From these two figures, it can be seen that the increase of perpendicular dust pressure  $P_\perp$  increases(decreases) the amplitude of solitons very little for negative(positive) dust.



**Figure 1.** The range of Mach number for existence of dust acoustic waves against dust-ion density ratio  $f$  for  $P_{\parallel} = 0.1$  (solid curves) and  $0.01$  (dashed curves). The subfigure (a) for negative dust and (b) for positive dust



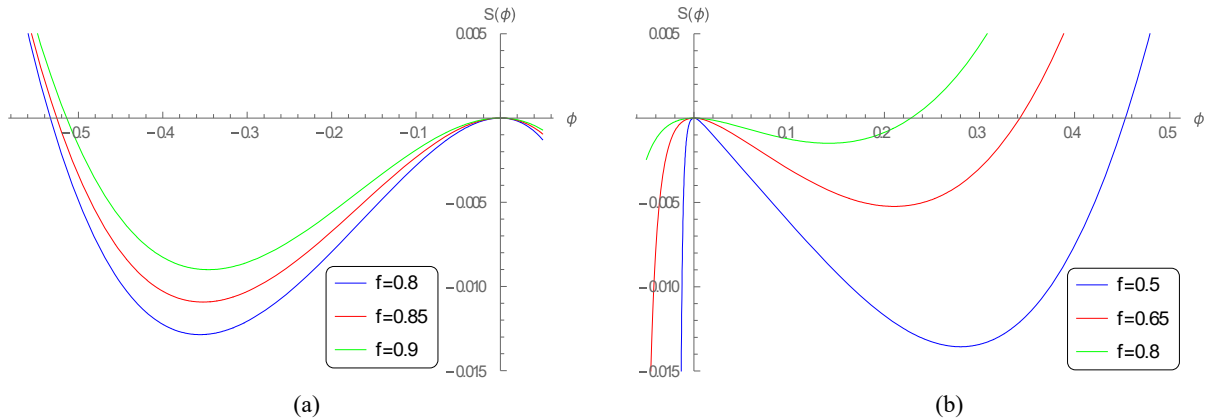
**Figure 2.** In panels: (a) Variation of Sagdeev potential  $S(\phi)$  against  $\phi$  and (b) the resulting soliton profile  $\phi$  are depicted for different  $P_{\parallel} = 0.02, 0.07, 0.12$  for negative dust, [Here  $M = 0.98, f = 0.75, k_z = 0.6, \alpha = 0.1, \beta_i = 0.3, \beta_e = 0.3$  and  $P_{\perp} = 0.02$ ]. Similarly, in panels (c) and (d) for positive dust [Here  $M = 0.77, f = 0.5, k_z = 0.7, \alpha = 0.1, \beta_i = 0.3, \beta_e = 0.3$  and  $P_{\perp} = 0.02$ .]



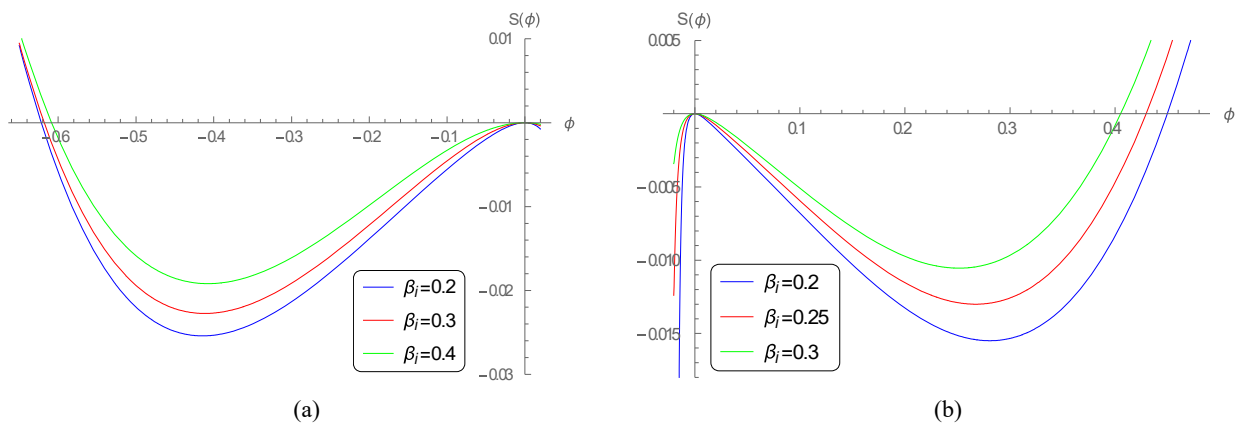
**Figure 3.** Variation of Sagdeev potential  $S(\phi)$  against  $\phi$  for different  $P_{\perp} = 0.01, 0.06, 0.11$  for (a)  $M = 0.98, f = 0.75, k_z = 0.6, \alpha = 0.1, j = 1$  (negative dust),  $\beta_i = 0.3, \beta_e = 0.3$  and  $P_{\parallel} = 0.05$ . (b)  $M = 0.78, f = 0.5, k_z = 0.7, \alpha = 0.1, j = -1$  (positive dust),  $\beta_i = 0.3, \beta_e = 0.3$  and  $P_{\perp} = 0.1$

Figure 4(a) and (b) displays variation of Sagdeev potential  $S(\phi)$  against  $\phi$  for different values of density ratio of dust to ions  $f$ . It can be seen that the increase of  $f$  leads to decrease in amplitude of solitary waves.

The effect of nonthermal parameter  $\beta_i$  of ions on the Sagdeev potential is shown in the Figure 5(a) and (b) by plotting Sagdeev potential  $S(\phi)$  against  $\phi$  for different values of  $\beta_i$ . As  $\beta_i$  increases the amplitude of the dust acoustic solitary waves decreases for both positive and negative dust.



**Figure 4.** Variation of Sagdeev potential  $S(\phi)$  against  $\phi$  (a) for different  $f = 0.8, 0.85, 0.9$  and  $M = 0.85, k_z = 0.6, \alpha = 0.1, j = 1$  (negative dust),  $\beta_i = 0.3, \beta_e = 0.3, P_\perp = 0.01$  and  $P_\parallel = 0.11$ . (b) for different  $f = 0.5, 0.65, 0.8$  and  $M = 0.78, k_z = 0.7, \alpha = 0.1, j = -1$  (positive dust),  $\beta_i = 0.3, \beta_e = 0.3, P_\perp = 0.02$  and  $P_\parallel = 0.1$



**Figure 5.** Variation of Sagdeev potential  $S(\phi)$  against  $\phi$  (a) for different  $\beta_i = 0.2, 0.3, 0.4$  and  $M = 0.93, k_z = 0.6, \alpha = 0.1, j = 1$  (negative dust),  $f = 0.75, \beta_e = 0.2, P_\perp = 0.02$  and  $P_\parallel = 0.11$ . (b) for different  $\beta_i = 0.2, 0.25, 0.3$  and  $M = 0.73, k_z = 0.68, \alpha = 0.1, j = -1$  (positive dust),  $f = 0.5, \beta_e = 0.3, P_\perp = 0.02$  and  $P_\parallel = 0.1$

Mach number is related to the speed of dust acoustic waves. Figure 6(a) and (b) show the variation of the Sagdeev potential  $S(\phi)$  against  $\phi$  for different values Mach number  $M$  for negative and positive dust respectively. From these figures it is shown that, for both positive and negative dust, increase of Mach number leads to increase in the amplitude of solitary waves.

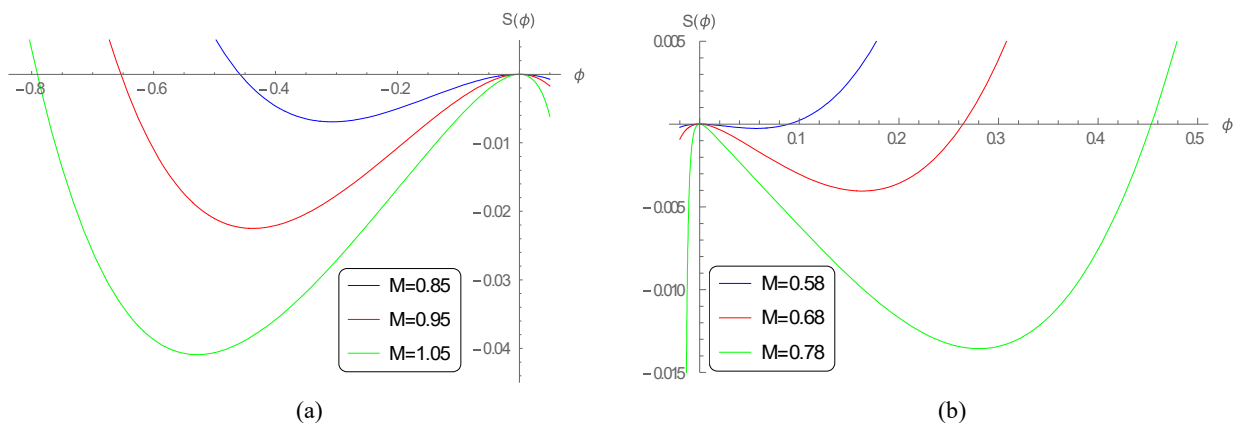


**Figure 6.** Variation of Sagdeev potential  $S(\phi)$  against  $\phi$  (a) for different  $M = 0.85, 0.95, 1.05$  and  $f = 0.85, k_z = 0.6, \alpha = 0.1, j = 1$  (negative dust),  $\beta_i = 0.3, \beta_e = 0.3, P_\perp = 0.01$  and  $P_\parallel = 0.11$ . (b) for different  $M = 0.58, 0.68, 0.78$  and  $f = 0.5, k_z = 0.7, \alpha = 0.1, j = -1$  (positive dust),  $\beta_i = 0.3, \beta_e = 0.3, P_\perp = 0.02$  and  $P_\parallel = 0.1$



In Figure 7(a) and (b) we have plotted the Sagdeev potential  $S(\phi)$  against  $\phi$  for different value of  $k_z$  for positive and negative dust respectively. We can see as  $k_z$  increases i.e. as direction of solitary waves approaches the direction of magnetic field, the amplitude of the solitary waves gradually decreases.

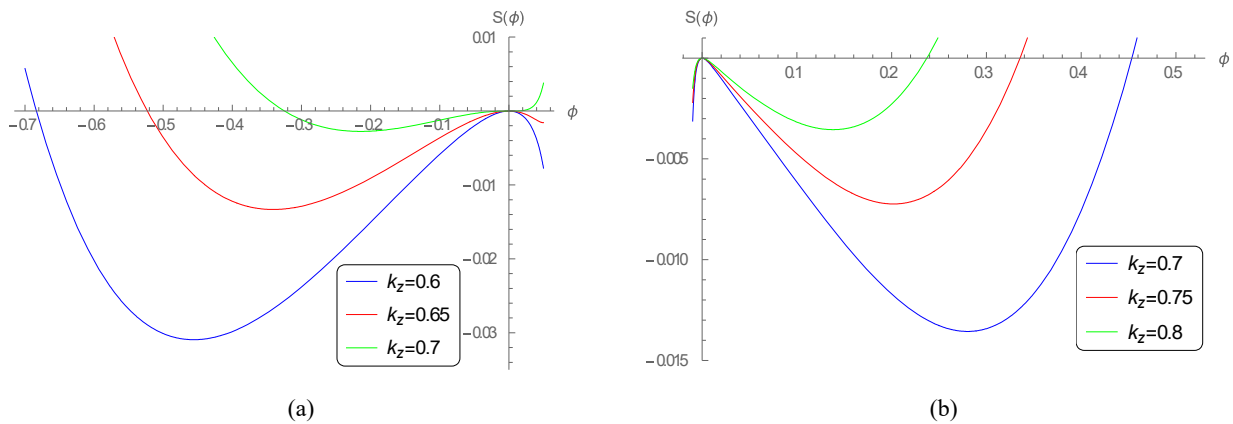


**Figure 7.** Variation of Sagdeev potential  $S(\phi)$  against  $\phi$  (a) for different,  $k_z = 0.6, 0.65, 0.7$  and  $f = 0.75, M = 0.98, \alpha = 0.1, j = 1$  (negative dust),  $\beta_i = 0.3, \beta_e = 0.3, P_\perp = 0.01$  and  $P_\parallel = 0.11$ . (b) for different  $k_z = 0.7, 0.75, 0.8$  and  $f = 0.5, M = 0.78, \alpha = 0.1, j = -1$  (positive dust),  $\beta_i = 0.3, \beta_e = 0.3, P_\perp = 0.02$  and  $P_\parallel = 0.1$

## 6. CONCLUSION

In this investigation, we have studied the effect of anisotropic dust pressure on the formation of dust acoustic solitary waves in a three-component magnetized plasma, consisting of dust fluid and nonthermal ions and electrons.

Although, Bashir et al. [32] studied the dusty plasma with anisotropic dust pressure as in this work but they used Reductive Perturbation Method. In our work we have used Sagdeev Potential Method which is more comprehensive method that accounts all nonlinearities and give more accurate results. Using Sagdeev pseudo-potential method, an energy integral has been derived for dust acoustic solitons. Bashir et al. [32] got very small amplitude solitons but we got solitons with larger amplitude. Also, we have calculated the range of Mach number for existence of solitary waves.

It is observed that, various parameters viz. parallel and perpendicular dust pressure, non-thermality of ions etc. significantly modify the arbitrary amplitude dust acoustic solitons. Some important findings are summarized as:

- As parallel dust pressure  $P_\parallel$  increases, for negative(positive) dust, the amplitude of the rarefactive(compressive) solitons decrease (increases).
- The increase of perpendicular dust pressure  $P_\perp$  increases(decreases) the amplitude of solitons very little for negative(positive) dust.
- The increase of density ratio  $f = \frac{z_d n_{d0}}{n_{i0}}$  leads to decrease in amplitude of solitary waves.
- As nonthermal parameter  $\beta_i$  increases the amplitude of the dust acoustic solitary waves decreases for both positive and negative dust.

Clusters of sub-micron and micron-sized dust particles within Earth's magnetosphere are detected by various satellites. Electrostatic solitary waves are also observed in various space and astrophysical plasma possessing the pressure anisotropy arising due to strong magnetic field [30, 39-40]. Theoretically, it is seen that in earth's magneto-tail region, electrostatic solitary waves exit [41-43], where the pressure anisotropy arises due to earth's magnetic field. Despite the theoretical plausibility and indirect evidence, the nature of dust particle swarms and associated DAWs in the magnetosheath remains an open question. The result of the present investigation may be effective to explore the various aspects of nonlinear structures of in those regions, where non-thermal electrons with pressure anisotropy can exist.

## ORCID

● Mamani Choudhury, <https://orcid.org/0000-0002-6480-4513>

## REFERENCES

- J.I. Vette, "Summary of Particle Populations in the Magnetosphere," *Particles and Fields in the Magnetosphere*. Astrophysics and Space Science Library, **17**, 305-318, (1970), [https://doi.org/10.1007/978-94-010-3284-1\\_30](https://doi.org/10.1007/978-94-010-3284-1_30)
- R.L. Toker, and S.P. Gary, "Electrostatic hiss and the beam driven electron acoustic instability in the dayside polar cusp," *Geophys. Res. Lett.* **11**(12), 1180-1183 (1984) <https://doi.org/10.1028/GL011i012p01180>
- P.K. Shukla, and V.P. Silin, "Dust ion-acoustic wave," *Phys. Scr.*, **45**, (5), 508 (1992) <https://doi.org/10.1088/0031-8949/45/5/015>
- V.W. Chow, D.A. Mendis, and M. Rosenberg, "Role of grain size and particle velocity distribution in secondary electron emission in space plasmas," *J. Geophys. Res.* **98**(A11), 19065-19076 (1993), <https://doi.org/10.1029/93JA02014>
- F. Verheest, *Waves in dusty space plasmas*, (Kluwer Academic, Dordrecht, Netherlands, 2000), <https://doi.org/10.1007/978-94-010-9945-5>
- P.K. Shukla, and A.A. Mamun, *Introduction to Dusty Plasma Physics*, (Bristol, U.K. 2000).
- A. Bouchoule, *Dusty plasmas: Physics, Chemistry, and Technological Impact in Plasma Processing*, (Wiley, Chichester, U. K. 1999).

- [8] D.A. Mendis, and M. Rosenberg, "Cosmic dusty plasma", *Annu. Rev. Astron. Astrophys.* **32**(1) 419-463 (1994). <https://doi.org/10.1146/annurev.aa.32.090194.002223>
- [9] L. Boufendi, M.C. Jouanny, E. Kovacevic, J. Berndt, and M. Mikikian, "Dusty plasma for nanotechnology," *J. Phys. D: Appl. Phys.* **44**, 174035 (2011). <https://doi.org/10.1088/0022-3727/44/17/174035>
- [10] U. Kortshagen, "Nonthermal Plasma Synthesis of Nanocrystals: Fundamentals, Applications, and Future Research Needs," *Plasma Chem. Plasma Process.* **36**, 73-84 (2016). <https://doi.org/10.1007/s11090-015-9663-4>
- [11] A.A. Mamun, "Arbitrary Amplitude Dust-acoustic Solitary Structures in a Three-component Dusty Plasma," *Astrophys. Space Sci.* **268**, 443-454 (1999). <https://doi.org/10.1023/A:1002031022895>
- [12] S. Ghosh, T.K. Chaudhuri, S. Sarkar, M. Khan, and M. R. Gupta, "Small Amplitude Nonlinear Dust Acoustic Wave Propagation in Saturn's F, G and E Rings," *Astrophys. Space Sci.* **278**, 463-477 (2001). <https://doi.org/10.1023/A:1013100707057>
- [13] S.K. El-Labany, W.F. El-Taibany, A.A. Mamun, and W.M. Moslem, "Dust acoustic solitary waves and double layers in a dusty plasma with two-temperature trapped ions," *Phys. Plasmas*, **11**, 926-933 (2004). <https://doi.org/10.1063/1.1643757>
- [14] A. Rahman, A.A. Mamun, and S.M.K. Alam, "Shock waves in a dusty plasma with dust of opposite polarities," *Astrophys. Space Sci.* **315**, 243-247 (2008). <https://doi.org/10.1007/s10509-008-9824-5>
- [15] F. Verheest, and S.R. Pillay, "Large amplitude dust-acoustic solitary waves and double layers in nonthermal plasmas," *Phys. Plasmas*, **15**, 013703 (2008). <https://doi.org/10.1063/1.2831025>
- [16] S.K. El-Labany, E.F. El-Shamy, R. Sabry, and M. Shokry, "Head-on collision of dust-acoustic solitary waves in an adiabatic hot dusty plasma with external oblique magnetic field and two-temperature ions," *Astrophys. Space Sci.* **325**, 201-207 (2010). <https://doi.org/10.1007/s10509-009-0192-6>
- [17] M. Shahmansouri, and M. Tribeche, "Dust acoustic localized structures in an electron depleted dusty plasma with two-suprathermal ion-temperature," *Astrophys. Space Sci.* **342**, 87-92 (2012). <https://doi.org/10.1007/s10509-012-1149-8>
- [18] T.K. Balaku, and M.A. Hellberg, "Dust acoustic solitons in plasmas with kappa-distributed electrons and/or ions," *Phys. Plasmas*, **15**, 123705 (2008), <https://doi.org/10.1063/1.3042215>
- [19] A. Paul, G. Mandal, A.A. Mamun, and M.R. Amin, "Nonlinear propagation of dust-acoustic waves in an unmagnetized dusty plasma with nonthermal electron and vortex-like ion distribution," *Phys. Plasmas*, **20**, 104505 (2013). <https://doi.org/10.1063/1.4826591>
- [20] N. Akhtar, S. Mahmood, and H. Saleem "Dust acoustic solitary waves in the presence of hot and cold dust" *Phys. Lett. A*, **361**, 126-132 (2007). <https://doi.org/10.1016/j.physleta.2006.09.017>
- [21] R.M. Crutcher, "Magnetic fields in molecular clouds," *Ann. Rev. Astron. Astrophys.* **50**(1), 29 (2012). <https://doi.org/10.1146/annurev-astro-081811-125514>
- [22] S. Reissl, A.M. Stutz, R.S. Klessen, D. Seifried, and S. Walch, "Magnetic fields in star-forming systems II: Examining dust polarization, the Zeeman effect, and the faraday rotation measure as magnetic field tracers," *Mon. Not. R. Astron. Soc.* **500**(1), 153-176 (2021). <https://doi.org/10.1093/mnras/staa3148>
- [23] H.B. Li, "Magnetic Fields in Molecular Clouds—Observation and Interpretation," *Galaxies*, **9**(2), 9020041 (2021). <https://doi.org/10.3390/galaxies9020041>
- [24] A.A. Mamun, "Nonlinear propagation of dust-acoustic waves in a magnetized dusty plasma with vortex-like ion distribution," *J. Plasma Phys.* **59**(3), 575-580 (1998). <http://dx.doi.org/10.1017/S002237789800645X>
- [25] A.A. Mamun, M.N. Alam, A.K. Das, Z. Ahmed, and T.K. Datta, "Obliquely Propagating Electrostatic Solitary Structures in a Hot Magnetized Dusty Plasma," *Phys. Scr.* **58**(1), 72 (1998). <https://doi.org/10.1088/0031-8949/58/1/010>
- [26] T. Farid, A.A. Mamun, P.K. Shukla, and A.M. Mirza, "Nonlinear electrostatic waves in a magnetized dust-ion plasma," *Phys. Plasmas*, **8**, 1529-1532 (2001). <https://doi.org/10.1063/1.1364512>
- [27] M. Shahmansouri, and H. Alinejad, "Dust acoustic solitary waves in a magnetized electron depleted superthermal dusty plasma," *Phys. Plasmas*, **20**, 033704 (2013). <https://doi.org/10.1063/1.4796195>
- [28] M. Choudhury, "Propagation of Arbitrary Amplitude Dust Acoustic (DA) Waves in a Magnetized Plasma with Non-thermal Electrons and Ions," *Braz. J. Phys.* **53**, 110 (2023). <https://doi.org/10.1007/s13538-023-01323-8>
- [29] G.F. Chew, M.L. Goldberger, and F.F. Low, "The Boltzmann equation and the one-fluid hydromagnetic equations in the absence of particle collisions," *Proc. R. Soc. London Ser.* **236**, 112-118 (1956). <https://doi.org/10.1098/rspa.1956.0116>
- [30] C.R. Choi, C.M. Ryu, D.Y. Lee, N.C. Lee, and Y.H. Kim, "Dust ion acoustic solitary waves in a magnetized dusty plasma with anisotropic ion pressure," *Phys. Lett. A*, **364**(3-4), 297 (2007). <https://doi.org/10.1016/j.physleta.2006.12.014>
- [31] P. Chatterjee, T. Saha, and C.M. Ryu, "Obliquely propagating ion acoustic solitary waves and double layers in a magnetized dusty plasma with anisotropic ion pressure," *Phys. Plasmas*, **15**, 123702 (2008). <https://doi.org/10.1063/1.2996114>
- [32] M.F. Bashir, E.E. Behary, and W.F. El-Taibany, "Effect of anisotropic dust pressure and superthermal electrons on propagation and stability of dust acoustic solitary waves," *Phys. Plasmas*, **22**, 062112 (2015). <https://doi.org/10.1063/1.4922750>
- [33] A.A. Mamun, R.A. Cairns, and P.K. Shukla, "Effects of vortex-like and non-thermal ion distributions on non-linear dust-acoustic waves," *Phys. Plasmas*, **3**, 2610-2614 (1996). <https://doi.org/10.1063/1.871973>
- [34] R. Roychoudhury, "Arbitrary-amplitude solitary kinetic Alfvén waves in a non-thermal plasma," *J. Plasma Phys.* **67**, 199-204(2-3), (2002). <https://doi.org/10.1017/S0022377801001544>
- [35] S. Ghosh, R. Bharuthram, M. Khan, and M.R. Gupta, "Instability of dust acoustic wave due to nonthermal ions in a charge varying dusty plasma," *Phys. Plasmas*, **11**, 3602-3609 (2004). <https://doi.org/10.1063/1.1760584>
- [36] A. Berbri, and M. Tribeche, "Weakly Nonlinear Dust-Ion-Acoustic Shock Waves in a Dusty Plasma with Nonthermal Electrons," *Phys. Plasmas*, **16**, 053701 (2009). <https://doi.org/10.1063/1.3124137>
- [37] R.Z. Sagdeev, *Rev. Plasma Phys.* **4**, 23 (1966).
- [38] A. Bahache, D. Bennaceur-Doumaz, and M. Djebli, "Effects of energetic electrons on ion acceleration in a quasi-static model", *Plasma Phys.* **24**, 083102 (2017). <https://doi.org/10.1063/1.4994706>
- [39] R.E. Denton, B.J. Anderson, S.P. Gary, and S.A. Fuselier, "Bounded anisotropy fluid model for ion temperatures," *J. Geophys. Res.* **99**, 11225-11241 (1994). <https://doi.org/10.1029/94ja00272>



- [40] M.S. Nakwacki, E.M. Gouveia Dal Pino, G. Kowal, and R. Santos-Lima, "The role of pressure anisotropy in the turbulent intracluster medium," J. Phys.: Conf. Ser. **370**, 012043 (2012). <https://doi.org/10.1088/1742-6596/370/1/012043>
- [41] R.E. Tolba, W.M. Moslem, and R. Sabry, "Modulated dust-ion-acoustic waves result from Earth's magnetosphere and lunar ionosphere interactions," Physics of Fluids, **36**, 037145 (2024). <https://doi.org/10.1063/5.0198213>
- [42] Y.N. Izvekova, T.I. Morozova, and S.I. Popel, "Interaction of the Earth's Magnetotail with Dusty Plasma Near the Lunar Surface: Wave Processes and Turbulent Magnetic Reconnection," IEEE Trans. **46**, 731-738 (2018). <https://doi.org/10.1109/tps.2017.2752084>
- [43] M.S. Afify, N.A. El-Shafeay, W.M. Moslem, W.F. El-Taibany, and S.K. El-Labany, "Structures of dust-ion acoustic waves in the lunar dark side induced by interaction with Earth's magnetosphere," Astrophys. Space Sci. **368**, 71 (2023). <https://doi.org/10.1007/s10509-023-04223-0>

**ВПЛИВ АНІЗОТРОПНОГО ТИСКУ ПИЛУ НА ФОРМУВАННЯ ТА ПОШИРЕННЯ ПИЛОВИХ АКУСТИЧНИХ  
ОДИНОКИХ ХВИЛЬ (DASW) ДОВІЛЬНОЇ АМПЛІТУДИ В НАМАГНІЧЕНІЙ  
ПИЛОВО-ІОННО-ЕЛЕКТРОННІЙ ПЛАЗМІ**

**Мамані Чоудхурі**

*Кафедра математики, коледж для дівчат Хандік, Гувахаті 781001, Індія*

Досліджено пилові акустичні одиночні хвилі (DASW) довільної амплітуди в запиленій магнітоплазмі з анізотропним тиском пилу та нетепловим розподілом іонів та електронів. Метод псевдопотенціалу Сагдеева використовується для виведення рівняння балансу енергії та аналізу різних властивостей пилових акустичних солітонів. Чисельно досліджуються анізотропний тиск пилу, коефіцієнт щільності пилу, нетеплові ефекти тощо при поширенні DASW. Встановлено, що розріджені солітони можуть існувати для негативно зарядженого пилу, а стискаючі солітони можуть існувати для позитивно зарядженого пилу. Це дослідження може бути корисним для розуміння DASW у різних астрофізичних середовищах.

**Ключові слова:** пилова акустична хвиля; пилова плазма; анізотропний тиск; псевдопотенціал Сагдеева; поодинокі хвилі; намагнічена плазма; нетеплові електрони та іони

## PROPAGATION OF AN AZIMUTHALLY POLARIZED TERAHERTZ LASER BEAMS WITH A PHASE SINGULARITY

 **Andrey V. Degtyarev**,  **Mykola M. Dubinin**,  **Vyacheslav A. Maslov\***,  **Konstantin I. Muntean**,  
 **Vladislav S. Senyuta**

*V.N. Karazin Kharkiv National University, 4 Svoboda Sq., Kharkiv 61022, Ukraine*

*\*Corresponding Author email: [v.a.maslov@karazin.ua](mailto:v.a.maslov@karazin.ua)*

Received June 30, 2025; revised October 14, 2025; accepted November 7. 2025

Analytical expressions are derived to describe the nonparaxial diffraction of modes in a dielectric waveguide resonator for a terahertz laser. The study examines the interaction between azimuthally polarized  $TE_{0m}$  ( $m = 1, 2, 3$ ) modes and a spiral phase plate (SPP), accounting for its different topological charges ( $n$ ). Using numerical modeling, the emerging physical properties of vortex beams are investigated when they propagate in free space. Vector integral Rayleigh-Sommerfeld transforms are used to study the propagation in the Fresnel zone of vortex laser beams excited by  $TE_{0m}$  modes of a dielectric waveguide quasi-optical resonator when they are incident on a phase plate. In the studied modes, in the absence of a phase plate, the field exhibits a ring-shaped transverse intensity distribution along the propagation axis. In this case, the number of rings in the cross-section corresponds to the azimuthal number of modes, and the phase distributions for the transverse components of these modes have opposite signs. The use of a SPP with a topological charge  $n = 1$  changes the structure of the beam field, forming an axial maximum in the transverse profile with an increase in the beam diameter at this maximum compared to the case without a phase plate. At the same time the phase structure of the field for transverse components acquires two-lobe symmetry. When using a SPP with a topological charge  $n = 2$  for the  $TE_{01}$  mode the restoration of the ring-like field structure is observed and for the  $TE_{02}$  and  $TE_{03}$  modes the formation of regions of increased intensity is observed. In this case, the phase distributions of the field components for the  $TE_{01}$  and  $TE_{02}$  modes acquire a three-lobe spiral structure, whereas those for the  $TE_{03}$  mode acquire a multi-lobe spiral configuration.

**Keywords:** *Terahertz laser; Dielectric waveguide resonator; Spiral phase plate; Vortex beams; Azimuthal polarization; Radiation propagation*

**PACS:** 42.55.Lt; 42.60.Da; 42.25.Bs; 47.32.C–

### 1. INTRODUCTION

In recent years, in addition to the development of efficient sources and detectors in the terahertz range [1 – 3], the development of terahertz optics is also necessary to ensure the possibility of specific control and manipulation of such radiation by changing its amplitude, phase, polarization, and even orbital angular momentum (OAM) [4 – 6]. Among various terahertz structured beams, vector beams with inhomogeneous phase and polarization states have shown significant practical value in many fields due to their unique light-field distribution characteristics [7 – 9]. The growing interest in terahertz vector vortex beams is due to the helical dislocations of the wavefront that arise in them. Such vortex beams combine the advantages of terahertz waves and OAM. In particular, terahertz waves have a highly coherent, non-ionizing nature and a high penetrating power, while OAM gives the radiation an additional degree of freedom [10 – 13].

The study of the propagation of vortex terahertz laser beams is of great importance for the development of modern science and technology. The unique polarization state and complex spatial structure of terahertz vortex beams provide a richer multiplexing space for information coding and encryption states. Studying the propagation of such beams allows us to better understand their interaction with various materials, particularly nonlinear media, which is crucial for developing new methods of visualization and diagnostics. In addition, these studies contribute to the development of higher-resolution technologies, which are essential for microelectronics and nanotechnology. In free space, vortices can exhibit a stable wavefront structure, allowing them to maintain their unique properties over large distances [14, 15].

Spiral phase plates (SPP),  $q$ -plates, achromatic polarization elements, diffraction optical elements, metasurfaces, polarization gratings are used to form vortex beams [9, 16]. SPPs are effective devices for the conversion of various types of beams into vortex beams due to their low fabrication cost, design simplicity and compactness [17, 18].

Optically pumped terahertz molecular lasers are among the first lasers developed in the terahertz range [19]. They have a narrow generation linewidth ( $\Delta\nu \approx 1$  kHz) and are among the most powerful tabletop terahertz sources available [20 – 22]. Most optically pumped lasers use waveguide resonators, enabling the generation of sufficiently high powers (up to 1 W) in continuous mode with relatively small cavity sizes [23 – 25]. Among the resonator modes with nonuniform polarization of radiation the  $TE_{0m}$  modes with azimuthal polarization have the lowest energy losses and can be effectively used in orbital angular momentum division multiplexing applications in wireless communications [26 – 28].

The present work is aimed to obtain analytical expressions for describing the nonparaxial diffraction of azimuthally polarized  $TE_{0m}$  modes of a dielectric waveguide resonator of a terahertz laser during their interaction with a spiral phase plate, as well as to investigate the spatial structure and evolution of the intensity and phase of the formed vortices.

## 2. THEORETICAL RELATIONSHIPS

The propagation of laser radiation in free space along the  $z$  axis is described by the well-known Rayleigh-Sommerfeld integrals. We use the following expressions of the field components for the cylindrical coordinate system in different diffraction zones [29–31]:

$$E_x(\rho, \beta, z) = -\frac{iz}{\lambda r_1^2} \exp(ikr_1) \int_0^\infty \int_0^{2\pi} E_x^0(\rho_0, \varphi) \exp\left(ik \frac{\rho_0^2}{2r_1}\right) \exp\left(-ik \frac{\rho \rho_0 \cos(\varphi - \beta)}{r_1}\right) \rho_0 d\rho_0 d\varphi, \quad (1.1)$$

$$E_y(\rho, \beta, z) = -\frac{iz}{\lambda r_1^2} \exp(ikr_1) \int_0^\infty \int_0^{2\pi} E_y^0(\rho_0, \varphi) \exp\left(ik \frac{\rho_0^2}{2r_1}\right) \exp\left(-ik \frac{\rho \rho_0 \cos(\varphi - \beta)}{r_1}\right) \rho_0 d\rho_0 d\varphi, \quad (1.2)$$

$$E_z(\rho, \beta, z) = \frac{i}{\lambda r_1^2} \exp(ikr_1) \int_0^\infty \int_0^{2\pi} \left[ E_x^0(\rho_0, \varphi)(\rho \cos \beta - \rho_0 \cos \varphi) + E_y^0(\rho_0, \varphi)(\rho \sin \beta - \rho_0 \sin \varphi) \right] \times \\ \times \exp\left(ik \frac{\rho_0^2}{2r_1}\right) \exp\left(-ik \frac{\rho \rho_0 \cos(\varphi - \beta)}{r_1}\right) \rho_0 d\rho_0 d\varphi, \quad (1.3)$$

where  $k = 2\pi / \lambda$  is the wave number,  $\lambda$  is the wavelength,  $(\rho_0, \varphi)$  are the polar coordinates in the area where the input field is specified,  $(\rho, \beta, z)$  are the cylindrical coordinates in the observation plane,  $E_x^0(\rho_0, \varphi)$  and  $E_y^0(\rho_0, \varphi)$  are the complex amplitudes  $x$  and  $y$  components of the input electric field, respectively,  $r_1 = \sqrt{\rho^2 + z^2}$ .

The modes of the studied dielectric resonator coincide with the modes of a hollow circular dielectric waveguide. Therefore, in the initial plane we define radiation in the form of symmetric azimuthally polarized  $TE_{0m}$  modes. The expressions for the Cartesian components of electromagnetic fields of these modes in the source plane  $z = 0$  have the following form [32]:

$$TE_{0m} \text{ mode } \begin{cases} E_x^0(\rho_0, \varphi) = -B_{01} J_1\left(U_{0m} \frac{\rho_0}{a}\right) \sin(\varphi), \\ E_y^0(\rho_0, \varphi) = B_{01} J_1\left(U_{0m} \frac{\rho_0}{a}\right) \cos(\varphi), \end{cases} \quad (2)$$

where  $a$  is the radius of the waveguide,  $J_1$  is the Bessel function of the first kind,  $U_{0m}$  are the first roots of the equations  $J_1(x) = 0$ ,  $B_{0m} = \frac{1}{a\sqrt{\pi}J_2(U_{0m})}$  are the normalizing factors for the  $TE_{0m}$  modes.

Consider the interaction of these modes with a spiral phase plate (SPP) with an arbitrary topological charge ( $n$ ) [33]. Let us place the SPP with an aperture of the same radius  $a$  at the output of a waveguide (Fig. 1).

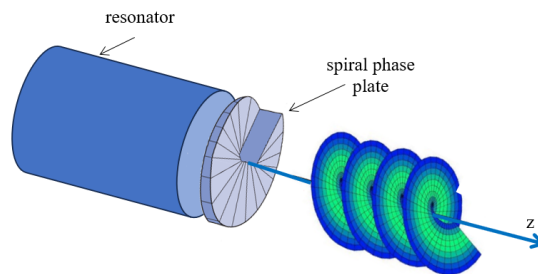


**Figure 1.** Theoretical scheme of the calculation model of laser beam propagation

The complex transmission function of this SPP in polar coordinates has the form [9]:

$$T_n(\rho_0, \varphi) = \text{circ}\left(\frac{\rho_0}{a}\right) \exp(in\varphi) = \begin{cases} \exp(in\varphi), & \rho_0 \leq a, \\ 0, & \rho_0 > a, \end{cases} \quad (3)$$

where  $\text{circ}(\cdot)$  is the circular function.

To simplify the calculations, integration over the angle  $\varphi$  in (1) can be performed with the known relationships for the integer  $\mu > 0$  from [34]

$$\begin{aligned} \int_0^{2\pi} \cos(\mu\varphi + \varphi_0) \exp[-ix \cos(\varphi - \theta)] d\varphi &= 2\pi (-i)^\mu J_\mu(x) \cos(\mu\theta + \varphi_0), \\ \int_0^{2\pi} \sin(\mu\varphi + \varphi_0) \exp[-ix \cos(\varphi - \theta)] d\varphi &= 2\pi (-i)^\mu J_\mu(x) \sin(\mu\theta + \varphi_0). \end{aligned}$$

Then from here we can get the following relation

$$\int_0^{2\pi} e^{-ix \cos(\varphi - \beta)} e^{in\varphi} d\varphi = 2\pi e^{in\beta} (-i)^n J_n(x). \quad (4)$$

Using Euler's formulas and taking into account Eq. (4), we obtain the expressions:

$$\int_0^{2\pi} e^{-ix \cos(\varphi - \beta)} e^{in\varphi} \sin \varphi d\varphi = -\pi e^{in\beta} (-i)^n [e^{i\beta} J_{n+1}(x) + e^{-i\beta} J_{n-1}(x)], \quad (5.1)$$

$$\int_0^{2\pi} e^{-ix \cos(\varphi - \beta)} e^{in\varphi} \cos \varphi d\varphi = \pi e^{in\beta} (-i)^{n+1} [e^{i\beta} J_{n+1}(x) - e^{-i\beta} J_{n-1}(x)]. \quad (5.2)$$

Then, using formulas (5.1) and (5.2), we obtain expressions for the field components that describe the nonparaxial diffraction of the  $TE_{0m}$  mode on the SPP. They look like this

$$E_x(\rho, \beta, z) = \frac{(-i)^{n+1} k z}{2r_1^2} \exp[i(n\beta + kr_1)] B_{0m} [\exp(i\beta) G_{2_{1n+1}}(\rho, z) + \exp(-i\beta) G_{2_{1n-1}}(\rho, z)], \quad (6.1)$$

$$E_y(\rho, \beta, z) = \frac{(-i)^{n+2} k z}{2r_1^2} \exp[i(n\beta + kr_1)] B_{0m} [\exp(i\beta) G_{2_{1n+1}}(\rho, z) - \exp(-i\beta) G_{2_{1n-1}}(\rho, z)], \quad (6.2)$$

$$E_z(\rho, \beta, z) = \frac{(-i)^{n+1} k \rho}{2r_1^2} \exp[i(n\beta + kr_1)] B_{0m} [G_{2_{1n+1}}(\rho, z) + G_{2_{1n-1}}(\rho, z)], \quad (6.3)$$

where the following notation is introduced

$$G_{2_{1n\pm 1}}(\rho, z) = \int_0^a J_1 \left( U_{0m} \frac{\rho_0}{a} \right) \exp \left( ik \frac{\rho_0^2}{2r_1} \right) J_{n\pm 1} \left( \frac{k \rho \rho_0}{r_1} \right) \rho_0 d\rho_0.$$

### 3. NUMERICAL RESULTS AND DISCUSSIONS

Using expressions (6), the longitudinal and transverse distributions of the total intensity of the electric field ( $I = |E_x|^2 + |E_y|^2 + |E_z|^2$ ) as well as the transverse distributions of the intensity ( $I_i = |E_i|^2$ ,  $i = x, y, z$ ) and phase  $\varphi_i = \arctg(\text{Im}(E_i) / \text{Re}(E_i))$  of individual field components were calculated. The study was performed for laser beams formed by modes of a dielectric waveguide resonator during their interaction with SPP. The calculations were performed for azimuthally polarized  $TE_{0m}$  modes (azimuthal number  $m = 1, 2, 3$ ) at a wavelength of  $\lambda = 432.6 \mu\text{m}$ , which corresponds to the generation line of a THz laser with optical pumping on the HCOOH molecule [35]. The waveguide diameter in the calculations was  $2a = 35 \text{ mm}$  and a phase plate with an identical diameter was installed at its output. In the work the spatial-energy properties of the field of the studied beams were compared for the values of the topological charge of the SPP  $n = 0, 1, 2$ .

Fig. 2 shows the longitudinal and transverse distributions of the field intensity of laser beams excited by  $TE_{01}$ ,  $TE_{02}$ ,  $TE_{03}$  modes in the Fresnel zone in three cases: in the absence of a phase plate ( $n = 0$ ) and with topological charge 1 and 2. The transverse intensity distributions are plotted in a plane that corresponds to the position of the maximum field intensity along the  $z$ -axis. For the studied modes in the absence of a phase plate the field is characterized by a ring transverse intensity distribution along the propagation axis. In this case the number of rings in the cross section corresponds to the azimuthal number of the mode. The introduction of a phase plate with a topological charge  $n = 1$  leads to the formation of an axial maximum in the transverse profile and its displacement toward the radiation source. A further increase in the topological charge to  $n = 2$  returns the beam profile to its initial annular shape, but a decrease in the beam energy localization region is observed.

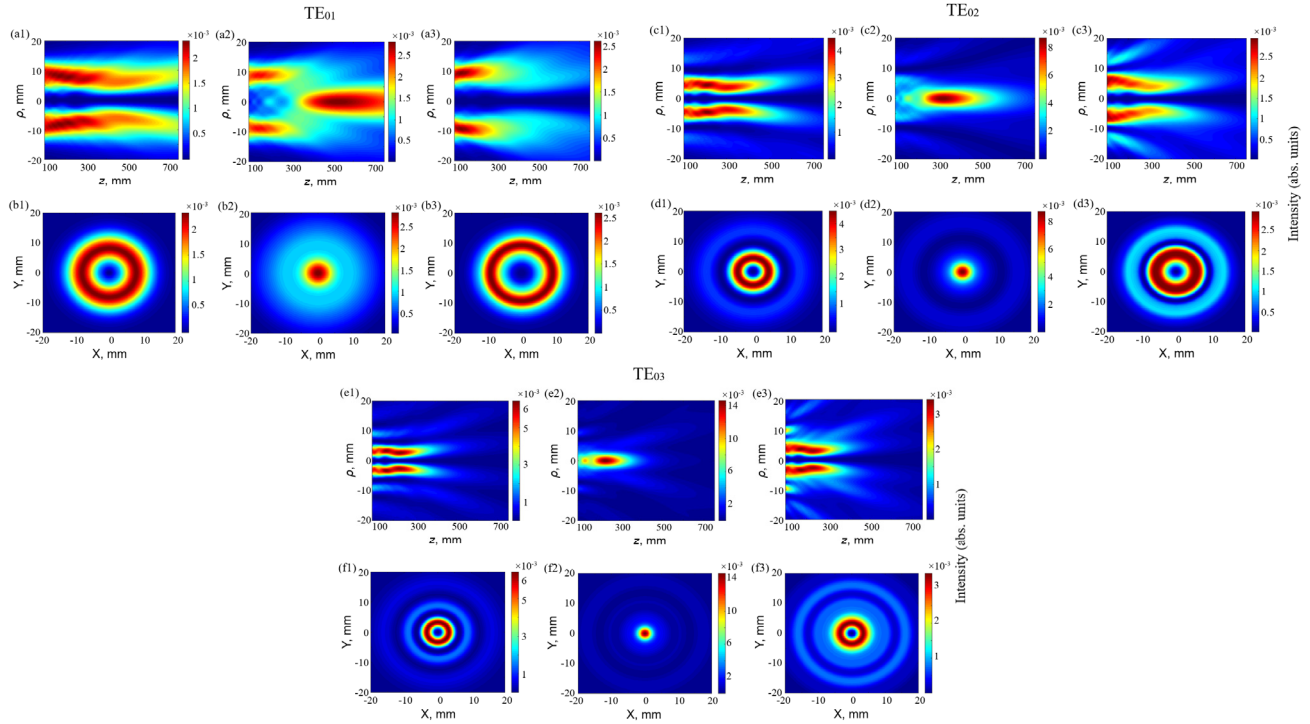


**Figure 2.** Calculated longitudinal (a1– a3, c1 – c3, e1 – e3) and transverse (b1 – b3, d1 – d3, f1 – f3) distributions of the total field intensity of laser beams excited by TE<sub>01</sub>, TE<sub>02</sub>, TE<sub>03</sub> modes in the Fresnel zone: in the absence of a phase plate (a1, b1, c1, d1, e1, f1), with a topological charge  $n = 1$  (a2, b2, c2, d2, e2, f2) and  $n = 2$  (a3, b3, c3, d3, e3, f3)

The values of the  $z$  coordinates at which the maximum field intensity is achieved and the magnitudes of these intensities as well as the beam diameters are given in Table 1. The diameters of the beams excited by the studied modes were calculated using the formula [36]

$$d = 2 \sqrt{\frac{2 \int_0^\infty \int_0^\infty \rho^2 I(\rho, \beta, z) \rho d\rho d\beta}{\int_0^\infty \int_0^\infty I(\rho, \beta, z) \rho d\rho d\beta}}. \quad (7)$$

Analysis of the obtained results shows that the installation of a spiral phase plate with a topological charge of  $n = 1$  compared to the case of its absence is accompanied by a noticeable increase in the beam diameter for all three modes. At  $n = 2$  for the TE<sub>01</sub> mode the beam diameter remains almost unchanged compared to the case without a phase plate, for the TE<sub>02</sub> mode it decreases, and for the TE<sub>03</sub> mode on the contrary it increases. The largest value of the beam diameter was obtained for the TE<sub>03</sub> mode at  $n = 1$  and it is  $d \approx 40$  mm.

**Table 1.** Parameters of the studied laser beams excited by TE<sub>0m</sub> modes in the regions of maximum field intensity at different topological charges.

Mode	$n$	$z$ (mm)	$I_{max} \times 10^{-3}$ (abs. units)	Beam diameter $d$ (mm)
TE <sub>01</sub>	0	176	2.33	29.54
	1	527	2.84	38.72
	2	132	2.61	29.87
TE <sub>02</sub>	0	208	4.48	32.87
	1	321	8.68	39.69
	2	100	2.98	30.42
TE <sub>03</sub>	0	167	6.44	34.27
	1	231	14.63	40.05
	2	172	3.43	37.79

Figure 3 shows the transverse distributions of the intensity and phase of the Cartesian  $E_x$  and  $E_y$  components of the electric field for the TE<sub>01</sub> mode in the Fresnel zone. Since the contribution of the  $E_z$  component to the total field intensity is insignificant, its intensity and phase distributions are not presented here or below. In the absence of SPP the field is localized in two areas. However, the phase distributions for the  $E_x$  and  $E_y$  components exhibit antiphase behavior: the phase changes by  $\pi$  between opposite half-planes according to the orientation of each component. At  $n = 1$



characteristic  $S$ -shaped curvatures appear in the field intensity. The phase distribution for these components in this case takes a spiral shape with two lobes. At  $n = 2$  the field is again localized in two regions and the phase distribution acquires a complex three-lobed structure with sharp phase transitions.

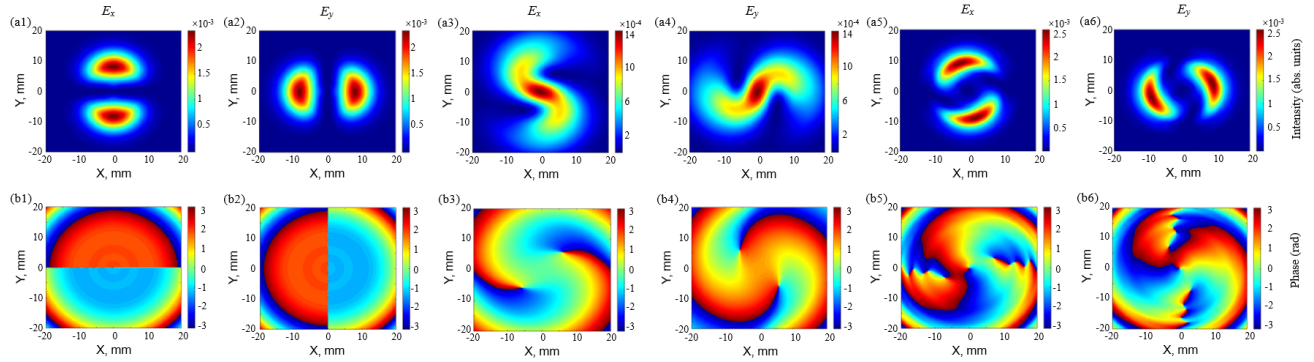


**Figure 3.** Calculated transverse distributions of intensity (a1 – a6) and phase (b1 – b6) for  $E_x$  and  $E_y$  components of the field of laser beams excited by the  $TE_{01}$  mode in the Fresnel zone: in the absence of a phase plate (a1, a2, b1, b2), with a topological charge of  $n = 1$  (a3, a4, b3, b4) and  $n = 2$  (a5, a6, b5, b6)

The transverse distribution of the field intensity and phase for the  $E_x$  and  $E_y$  components of laser beams excited by the  $TE_{02}$  mode in the Fresnel zone at different values of the topological charge is shown in Fig. 4. In the case of  $n = 0$  the localization of the field energy is observed in four regions. The phase distribution as for the  $TE_{01}$  mode exhibits antiphase behavior. At  $n = 1$  the maximum field intensity shifts toward the center, and the phase distribution takes on a spiral shape with a characteristic two-lobe structure. At  $n = 2$  localization of the field energy in four regions is again observed, but in this case the intensity of the side lobes increases. In this case the phase structure of the field demonstrates clearly defined three-lobe vortices with discontinuities in phase fronts.

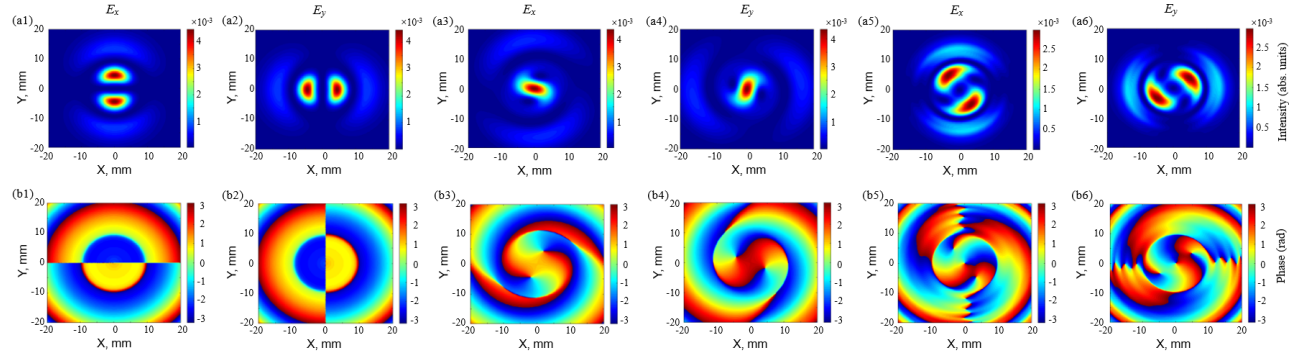


**Figure 4.** Calculated transverse distributions of intensity (a1 – a6) and phase (b1 – b6) for  $E_x$  and  $E_y$  components of the field of laser beams excited by the  $TE_{02}$  mode in the Fresnel zone: in the absence of a phase plate (a1, a2, b1, b2), with a topological charge of  $n = 1$  (a3, a4, b3, b4) and  $n = 2$  (a5, a6, b5, b6)

For the  $TE_{03}$  mode in the absence of SPP a further increase in the number of field localization regions is observed (Fig. 5). The phase distributions of the studied field components have antiphase symmetry. At  $n = 1$  a transformation of the intensity profile appears with energy localization in the central region and the phase distributions acquire a spiral shape. For  $n = 2$  a further increase in the energy localization regions is observed with two clearly defined regions of increased field intensity. In this case the phase distributions of the field acquire a multi-lobe spiral structure.

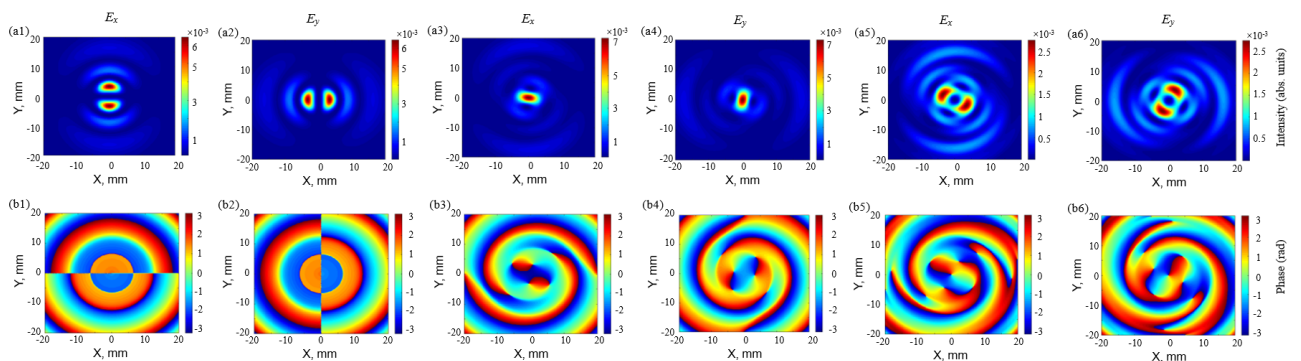


**Figure 5.** Calculated transverse distributions of intensity (a1 – a6) and phase (b1 – b6) for  $E_x$  and  $E_y$  components of the field of laser beams excited by the  $TE_{03}$  mode in the Fresnel zone: in the absence of a phase plate (a1, a2, b1, b2), with a topological charge of  $n = 1$  (a3, a4, b3, b4) and  $n = 2$  (a5, a6, b5, b6)

### 3. CONCLUSIONS

Analytical expressions are obtained to describe the nonparaxial diffraction of  $TE_{0m}$  modes ( $m = 1, 2, 3$ ) of a dielectric waveguide resonator of a terahertz laser during their interaction with a spiral phase plate with its different topological charges ( $n = 0, 1, 2$ ). The spatial structure of the intensity and phase of the electric field of formed vortex beams during their propagation in the Fresnel zone of free space is investigated.

It is shown that in the absence of a spiral phase plate, when the  $TE_{01}$  mode is excited in the resonator, a beam with a ring transverse intensity distribution is formed. The phase distributions for the transverse components of this mode, as well as for the other modes, have the opposite signs. The introduction of a SPP with a topological charge  $n = 1$  leads to the formation of an axial maximum in the transverse profile and an increase in the beam diameter at this maximum compared to the beam diameter in the absence of a plate by almost 10 mm. The phase distribution for a given topological charge takes on a spiral shape with two lobes for all modes. The restoration of the ring-shaped structure is observed at  $n = 2$  with a decrease in the beam energy localization region. In this case, the phase distribution acquires a three-lobe spiral structure.

In the case of the  $TE_{02}$  mode without SPP the beam has two pronounced rings in the cross section. At  $n = 1$  a significant increase in the field intensity at the center of the beam is observed and a shift in the localization of radiation energy to its source. For  $n = 2$  the spatial profile of the beam becomes more complex: additional zones of increased intensity appear and the phase exhibits a clear three-lobe structure with discontinuities in the phase fronts. For a given topological charge, the beam diameter has a minimum value.

The  $TE_{03}$  mode exhibits the most complex intensity distribution structure already at  $n = 0$  with three rings in the cross section. The introduction of SPP with  $n = 1$  leads to the localization of the field energy in the central region of the beam and a sharp increase in the maximum intensity in this region, which is accompanied by the largest increase in the beam diameter among the studied modes (up to 40 mm). The field structure becomes even more complex at  $n = 2$ . Several zones of increased intensity are formed, and the phase distribution acquires a distinct multi-lobe spiral configuration.

### ORCID

Andrey V. Degtyarev, <https://orcid.org/0000-0003-0844-4282>; Mykola M. Dubinin, <https://orcid.org/0000-0002-7723-9592>  
Vyacheslav O. Maslov, <https://orcid.org/0000-0001-7743-7006>; Konstantin I. Muntean, <https://orcid.org/0000-0001-6479-3511>  
Vladislav S. Senyuta, <https://orcid.org/0000-0001-6601-2379>

### REFERENCES

- [1] J. Freeman, E. Linfield, and A.G. Davies, "Terahertz frequency electronics and photonics: materials and devices," *Philosophical Transactions*, **383**(2296), 20230378 (2025). <https://doi.org/10.1098/rsta.2023.0378>
- [2] A. Rogalski, "Progress in performance development of room temperature direct terahertz detectors," *Journal of Infrared, Millimeter, and Terahertz Waves*, **43**(9), 709 (2022). <https://doi.org/10.1007/s10762-022-00882-2>
- [3] A. Leitenstorfer, A.S. Moskalenko, T. Kampfrath, et al., "The 2023 terahertz science and technology roadmap," *Journal of Physics D: Applied Physics*, **56**(22), 223001 (2023). <https://doi.org/10.1088/1361-6463/acbe4c>
- [4] D. Headland, Y. Monnai, D. Abbott, C. Fumeaux, and W. Withayachumnankul, "Tutorial: Terahertz beamforming, from concepts to realizations," *Apl Photonics*, **3**(5), 051101 (2018). <https://doi.org/10.1063/1.5011063>
- [5] A. Siemion, "Terahertz diffractive optics-smart control over radiation," *Journal of Infrared, Millimeter, and Terahertz Waves*, **40**(5), 477 (2019). <https://doi.org/10.1007/s10762-019-00581-5>
- [6] A. Forbes, "Advances in orbital angular momentum lasers," *Journal of Lightwave Technology*, **41**(7), 2079 (2022). <https://doi.org/10.1109/JLT.2022.3220509>
- [7] H. Hao, H. Xiaoxue, G. Liping, X. Sixing, and W. Xiaolei, "Research progress of terahertz vector beams," *Opto-Electronic Engineering*, **51**(8), 240071 (2024). <https://doi.org/10.12086/oee.2024.240071>
- [8] J. He, T. Dong, B. Chi, and Y. Zhang, "Metasurfaces for terahertz wavefront modulation: a review," *Journal of Infrared, Millimeter, and Terahertz Waves*, **41**(6), 607 (2020). <https://doi.org/10.1007/s10762-020-00677-3>
- [9] H. Wang, Q. Song, Y. Cai, Q. Lin, X. Lu, H. Shangguan, Y. Ai, and S. Xu, "Recent advances in generation of terahertz vortex beams and their applications," *Chin. Phys. B*, **29**(9), 097404 (2020). <https://doi.org/10.1088/1674-1056/aba2df>
- [10] J. Lamberg, F. Zarrinkhat, A. Tamminen, M. Baggio, J. Ala-Laurinaho, J. Rius, J. Romeu, E.E. Khaled, and Z. Taylor, "Wavefront-modified vector beams for THz cornea spectroscopy," *Optics Express*, **31**(24), 40293 (2023). <https://doi.org/10.1364/OE.494460>
- [11] S. Hu, L. Wei, Y. Long, S. Huang, B. Dai, L. Qiu, S. Zhuang, and D. Zhang, "Longitudinal polarization manipulation based on all-dielectric terahertz metasurfaces," *Optics Express*, **32**(5), 6963 (2024). <https://doi.org/10.1364/OE.514410>
- [12] H. Zhao, X. Wang, S. Liu, and Y. Zhang, "Highly efficient vectorial field manipulation using a transmitted tri-layer metasurface in the terahertz band," *Opto-Electronic Advances*, **6**(2), 220012 (2023). <https://doi.org/10.29026/oea.2023.220012>
- [13] J. Wätzel, J. Berakdar, and E.Y. Sherman, "Ultrafast entanglement switching and singlet-triplet transitions control via structured terahertz pulses," *New Journal of Physics*, **24**(4), 043016 (2022). <https://doi.org/10.1088/1367-2630/ac608a>
- [14] D. Bongiovanni, D. Li, M. Goutsoulas, H. Wu, Y. Hu, D. Song, and Z. Chen, "Free-space realization of tunable pin-like optical vortex beams," *Photonics Research*, **9**(7), 1204 (2021). <https://doi.org/10.1364/PRJ.420872>
- [15] G. Wang, X. Weng, X. Kang, Z. Li, K. Chen, X. Gao, and S. Zhuang, "Free-space creation of a perfect vortex beam with fractional topological charge," *Optics Express*, **31**(4), 5757 (2023). <https://doi.org/10.1364/OE.483304>
- [16] X. Wang, Z. Nie, Y. Liang, J. Wang, T. Li, and B. Jia, "Recent advances on optical vortex generation," *Nanophotonics*, **7**(9), 1533 (2018). <https://doi.org/10.1515/nanoph-2018-0072>

- [17] A.A. Paraipan, D. Gonzalez-Hernandez, I.V. Reddy, G. Balistreri, L. Zanotto, M. Shalaby, R. Morandotti, C. Liberale, and L. Razzari “Scanless spectral imaging of terahertz vortex beams generated by high-resolution 3d-printed spiral phase plates,” *Small Science*, **4**(12), 2400352 (2024). <https://doi.org/10.1002/smsc.202400352>
- [18] K. Miyamoto, K. Suizu, T. Akiba, and T. Omatu, “Direct observation of the topological charge of a terahertz vortex beam generated by a Tsurupica spiral phase plate,” *Applied Physics Letters*, **104**(26), 261104 (2014). <https://doi.org/10.1063/1.4886407>
- [19] D.T. Hodges, and T.S. Hartwick, “Waveguide laser for the far infrared (FIR) pumped by a CO<sub>2</sub> laser,” *Applied Physics Letters*, **23**(5), 252 (1973). <https://doi.org/10.1063/1.1654878>
- [20] P. Chevalier, A. Armizhan, F. Wang, M. Piccardo, S.G. Johnson, F. Capasso, and H.O. Everitt, “Widely tunable compact terahertz gas lasers,” *Science*, **366**(6467), 856 (2019). <https://doi.org/10.1126/science.aay8683>
- [21] A. Amirzhan, P. Chevalier, J. Rowlette, H.T. Stinson, M. Pushkarsky, T. Day, H.O. Everitt, and F. Capasso, “A quantum cascade laser-pumped molecular laser tunable over 1 THz,” *APL Photonics*, **7**(1), 016107 (2022). <https://doi.org/10.1063/5.0076310>
- [22] M.-H. Mammez, Z. Buchanan, O. Pirali, et al., “Optically pumped terahertz molecular laser: Gain factor and validation up to 5.5 THz,” *Adv. Photonics Res.*, **3**(4), 2100263 (2022). <https://doi.org/10.1002/adpr.202100263>
- [23] R.L. Abrams, and A.N. Chester, “Resonator theory for hollow waveguide lasers,” *Applied Optics*, **13**(9), 2117 (1974). <https://doi.org/10.1364/AO.13.002117>
- [24] G. Li, D. Wang, L. Fang, Z. Ran, and Q. Yan, “Improvement to beam quality of optically pumped terahertz gas lasers with hole-coupling resonators,” *Optical Engineering*, **58**(2), 026104 (2019) <https://doi.org/10.1117/1.OE.58.2.026104>
- [25] O.V. Gurin, A.V. Degtyarev, M.N. Legenkiy, V.A. Maslov, V.A. Svich, V.S. Senyuta, and A.N. Topkov, “Generation of transverse modes with azimuthal polarization in a terahertz band waveguide laser,” *Telecommunications and radio engineering*, **73**(20), 1819 (2014). <https://doi.org/10.1615/TelecomRadEng.v73.i20.30>
- [26] H. Zhou, X. Su, A. Minoofar, et al., “Utilizing multiplexing of structured THz beams carrying orbital-angular-momentum for high-capacity communications,” *Optics Express*, **30**(14), 25418 (2022). <https://doi.org/10.1364/OE.459720>
- [27] H. Wang, and R. Piestun, “Azimuthal multiplexing 3D diffractive optics,” *Scientific Reports*, **10**(1), 6438 (2020). <https://doi.org/10.1038/s41598-020-63075-8>
- [28] H. Ren, X. Li, and M. Gu, “Polarization-multiplexed multifocal arrays by a  $\pi$ -phase-step-modulated azimuthally polarized beam,” *Optics Letters*, **39**(24), 6771 (2014). <https://doi.org/10.1364/OL.39.006771>
- [29] V.V. Kotlyar, and A.A. Kovalev, “Nonparaxial propagation of a Gaussian optical vortex with initial radial polarization,” *J. Opt. Soc. Am. A*, **27**(3), 372 (2010). <https://doi.org/10.1364/JOSAA.27.000372>
- [30] B. Gu, and Y. Cui, “Nonparaxial and paraxial focusing of azimuthal-variant vector beams,” *Opt. Express*, **20**(16), 17684 (2012). <https://doi.org/10.1364/OE.20.017684>
- [31] Y. Zhang, L. Wang, and C. Zheng, “Vector propagation of radially polarized Gaussian beams diffracted by an axicon,” *J. Opt. Soc. Am. A*, **22**(11), 2542 (2005). <https://doi.org/10.1364/JOSAA.22.002542>
- [32] E.A.J. Marcatili, and R.A. Schmeltzer, “Hollow metallic and dielectric waveguides for long distance optical transmission and lasers,” *Bell Syst. Tech. J.*, **43**(4), 1783 (1964). <https://doi.org/10.1002/j.1538-7305.1964.tb04108.x>
- [33] J.F. Nye, and M.V. Berry, “Dislocations in wave trains,” *Proceedings of the Royal Society of London. A. Mathematical and Physical Sciences*, **336**(1605), 165 (1974). <https://doi.org/10.1098/rspa.1974.0012>
- [34] B. Gu, and Y. Cui, “Nonparaxial and paraxial focusing of azimuthal-variant vector beams,” *Opt. Express*, **20**(16), 17684 (2012). <https://doi.org/10.1364/OE.20.017684>
- [35] O.V. Gurin, A.V. Degtyarev, N.N. Dubinin, M.N. Legenkiy, V.A. Maslov, K.I. Muntean, V.N. Ryabykh, and V.S. Senyuta, “Formation of beams with nonuniform polarisation of radiation in a cw waveguide terahertz laser,” *Quantum Electron.*, **51**(4), 338 (2021). <https://doi.org/10.1070/QEL17511>
- [36] A.V. Degtyarev, M.M. Dubinin, O.V. Gurin, V.O. Maslov, K.I. Muntean, V.M. Ryabykh, V.S. Senyuta, and O.O. Svystunov, “Control over higher-order transverse modes in a waveguide-based quasi-optical resonator,” *Radio Physics and Radio Astronomy*, **27**(2), 49 (2022). <https://doi.org/10.15407/rpra22.02.49>

## ПОШИРЕННЯ АЗИМУТАЛЬНО ПОЛЯРИЗОВАНИХ ТЕРАГЕРЦОВИХ ЛАЗЕРНИХ ПУЧКІВ З ФАЗОВОЮ СИНГУЛЯРНІСТЮ

Андрій В. Дегтярьов, Микола М. Дубінін, Вячеслав О. Маслов, Костянтин І. Мунтян, Владислав С. Сенюта

*Харківський національний університет імені В.Н. Каразіна, майдан Свободи, 4, Харків, Україна, 61022*

Отримано аналітичні вирази для опису непараксильної дифракції мод діелектричного хвильовідного резонатора терагерцового лазера. Дослідження передбачає взаємодію між азимутально поляризованими  $TE_{0m}$  ( $m = 1, 2, 3$ ) модами та спіральною фазовою пластинкою (СФП) з урахуванням її різних топологічних зарядів ( $n$ ). За допомогою чисельного моделювання досліджено фізичні особливості вихрових пучків, що виникають, коли вони поширюються у вільному просторі. Векторні інтегральні перетворення Релея-Зоммерфельда використовуються для дослідження поширення у зоні Френеля вихрових лазерних пучків, збуджених  $TE_{0m}$  модами діелектричного хвильовідного квазіоптичного резонатора, при падінні на спіральну фазову пластину. Для досліджуванних мод за відсутності фазової пластини поле характеризується кільцевим поперечним розподілом інтенсивності на осі поширення. При цьому кількість кілець у поперечному перерізі відповідає азимутальному номеру мод, а розподіли фази для компонент даних мод мають протилежні знаки. Застосування СФП з топологічним зарядом  $n = 1$  змінює структуру поля пучків, формуючи осьовий максимум в поперечному профілі зі збільшенням діаметра пучка у даному максимумі у порівнянні з випадком відсутності фазової пластини. Водночас фазова структура для поперечних компонент набуває двопелюсткової симетрії. При використанні СФП з топологічним зарядом  $n = 2$  для  $TE_{01}$  моди спостерігається відновлення кільцеподібної структури поля, а для  $TE_{02}$  та  $TE_{03}$  мод – формування областей підвищеної інтенсивності. Фазовий розподіл для компонент поля в цьому випадку для  $TE_{01}$  і  $TE_{02}$  мод набуває трьохпелюсткової спіральної структури, а для  $TE_{03}$  моди – багатопелюсткової спіральної конфігурації.

**Ключові слова:** терагерцовий лазер; діелектричний хвильовідний резонатор; спіральна фазова пластинка; вихрові пучки; поляризація; поширення випромінювання



## PUSHING EFFICIENCY LIMITS: SCAPS-BASED ANALYSIS OF GaAs AND BAs SOLAR CELLS FOR NEXT-GENERATION PHOTOVOLTAICS

 Merad Laarej\*,  Mama Bouchaour<sup>§</sup>, Imane Bouazzaoui

University of Tlemcen, Faculty of Sciences, Department of Physics, Unity of Research "Materials and Renewable Energies", URMER  
BP : 119, Tlemcen, Nouveau Pôle, Mansourah, 13000, Algeria

\*Corresponding Author e-mail: [la\\_merad@yahoo.fr](mailto:la_merad@yahoo.fr) and [bouchaour.m@gmail.com](mailto:bouchaour.m@gmail.com)

Received May 2, 2025; revised July 8, 2025; accepted November 3, 2025

The present study utilizes SCAPS software to simulate and analyze the semiconductor materials gallium arsenide (GaAs) and boron arsenide (BAs) for photovoltaic applications. We outline the methodology, emphasizing critical factors considered during simulation. The performance of solar cells is investigated through quantum efficiency and photovoltaic performance curves. Additionally, the observed trends, key differences between GaAs and BAs, and their implications for advancing high-efficiency solar cells are discussed.

**Keywords:** GaAs; BAs; Photovoltaic; SCAPS Software; Conversion Efficiency ( $\eta$ )

**PACS:** 88.40.hj

### 1. INTRODUCTION

Gallium arsenide (GaAs) is a prominent material in the photovoltaic industry due to its direct bandgap and remarkable electronic transport properties. Its ability to efficiently absorb sunlight and convert photonic energy into electricity makes it a preferred material for high-performance solar cells.

Boron arsenide (BAs), while still in the development phase, has garnered attention for its promising properties in photovoltaic applications. With a wider bandgap compared to GaAs, BAs is potentially better suited for capturing high-energy photons in the solar spectrum. However, its practical implementation in photovoltaic cells remains a technical challenge.

The article solves the physical problem of designing next-generation solar cells by elucidating the trade-offs between light absorption, charge transport, recombination losses, and thermal stability, thereby guiding the practical optimization of both GaAs- and BAs-based devices for enhanced, stable photovoltaic performance.

This comprehensive approach not only advances our theoretical understanding but also has direct implications for developing efficient, robust solar cell technologies for real-world applications.

### 2. STATE OF THE ART FOR THE ANALYSIS OF SOLAR CELL PERFORMANCE

In recent years, high-efficiency solar cells have predominantly relied on III-V semiconductors, such as GaAs (Gallium Arsenide), due to their:

- Direct bandgap ( $\sim 1.42$  eV).
- High carrier mobility.
- Excellent performance under high radiation and temperature conditions (ideal for aerospace and concentrator photovoltaics).

To push efficiency beyond 30%, researchers have:

- Optimized multi-junction structures combining materials of varying bandgaps.
- Employed advanced transport layers (e.g., InGaP, AlGaInP).
- Used SCAPS-1D and other simulation tools to optimize layer thickness, doping, and interface quality.

Studies like those by [1] achieved efficiencies up to 30.88% in GaAs-based solar cells using complex heterojunctions. Other works, such as like [2], have used using pin-type GaAs cells in SCAPS simulations, reached efficiencies around 28.5%.

On the other hand, Boron Arsenide (BAs) is an emerging semiconductor, predicted to offer:

- A wide bandgap ( $\sim 2.45$  eV).
- Exceptional thermal conductivity.
- High ambipolar mobility.

These properties are promising for thermophotovoltaic and space applications, but its use in actual solar cells remains mostly theoretical or simulation-based due to fabrication challenges.

### 3. STRUCTURES STUDIED

To ensure an accurate comparison, the study evaluates two heterostructures based on BAs and GaAs under identical conditions (Figure 1). Both structures incorporate copper oxide (CuO) as the hole transport layer, facilitating

the collection of positive charge carriers generated in the photovoltaic device's active layer. Tungsten disulfide (WS<sub>2</sub>) serves as the electron transport layer, aiding in the collection of negative charge carriers.

A fluorine-doped tin oxide (FTO) layer is utilized as a transparent electrode in both configurations. This layer reduces voltage losses and enhances the efficiency of solar energy conversion into electrical power by providing a conductive interface between the active layer and the external circuit. This setup allows for a comprehensive comparison of the photovoltaic potential of GaAs and BAs under controlled and comparable conditions.

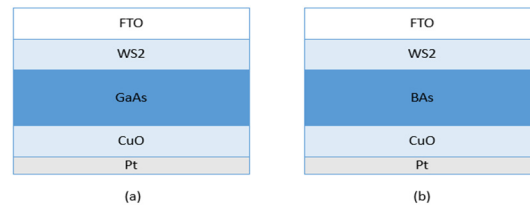


**Figure 1.** Structure of GaAs-based solar cells (a), BAs-based solar cells (b)

### 3.1. Physical and Optical Parameters of the Studied Cells

Table 1 displays the physical and optical parameters used in the SCAPS-1D simulations. The thickness of the CuO, WS<sub>2</sub>, and FTO layers were set to 0.1  $\mu\text{m}$ , 0.2  $\mu\text{m}$ , and 0.015  $\mu\text{m}$ , respectively, based on typical values reported for thin-film solar cell devices. The band gap of GaAs (1.42 eV) was taken from a standard semiconductor reference, while the band gap of BAs (2.45 eV) was obtained from theoretical calculations by Wentzcovitch and Cohen. The electron affinity and dielectric permittivity values for BAs were taken from Bushick et al. The electron mobility of GaAs was set to 8800  $\text{cm}^2/\text{Vs}$ , representing a high-quality single-crystal value, while the mobility of BAs was taken from experimental measurements on synthesized crystals.

**Table 1.** Parameters of the materials used in the simulation of the examined cells

Parameters	CuO	GaAs	WS2	FTO	BAs
Thickness ( $\mu\text{m}$ )	0.1	Variable	0.2	0.015	Variable
Band gap energy (eV)	2.17	1.42	1.870	3.5	1.46 [1] [2]
Electron affinity (eV)	3.2	4.07	4.3	4	4.495 [3]
Dielectric permittivity (relative)	7.110	13.8	11.9	9	9.02 [3]
Effective density of states of the conduction band ( $\text{cm}^{-3}$ )	$2.02 \times 10^{17}$	$2.2 \times 10^{18}$	$1 \times 10^{17}$	$2 \times 10^{18}$	$3.01 \times 10^{17}$ [3]
Effective density of states of the valence band ( $\text{cm}^{-3}$ )	$1.1 \times 10^{19}$	$1.8 \times 10^{19}$	$2.4 \times 10^{19}$	$1.8 \times 10^{19}$	$5.58 \times 10^{18}$ [3]
Electron mobility ( $\text{cm}^2/\text{Vs}$ )	200	8800 [4]	260	20	1400
Mobility of holes ( $\text{cm}^2/\text{Vs}$ )	81	400	51	10	2100
Doping concentration of donors ( $\text{cm}^{-3}$ )	0	0	$10^{17}$	$10^{19}$	0
Concentration of acceptor doping ( $\text{cm}^{-3}$ )	$10^{16}$	variable	0	0	variable
References	[5]	[6]	[7][8]	[9]	[10]

### 3.2. Evaluation of the simulated structures' baseline performance

The simulation results obtained using simplified models, which exclude variations in thickness, doping levels, and defect density, are presented in Table 2. This approach allows for a direct comparison of the baseline photovoltaic characteristics of each structure, providing an assessment of their initial performance under comparable and idealized conditions.

**Table 2.** Results of basic structure simulations

Structures	$V_{oc}$ (V)	$J_{sc}$ ( $\text{mA}/\text{cm}^2$ )	FF (%)	$\eta$ (%)
Pt/CuO/GaAs/WS <sub>2</sub> /FTO	1.0997	24.3669	83.71	22.43
Pt/CuO/BAs/WS <sub>2</sub> /FTO	1.2270	23.2075	83.91	23.89

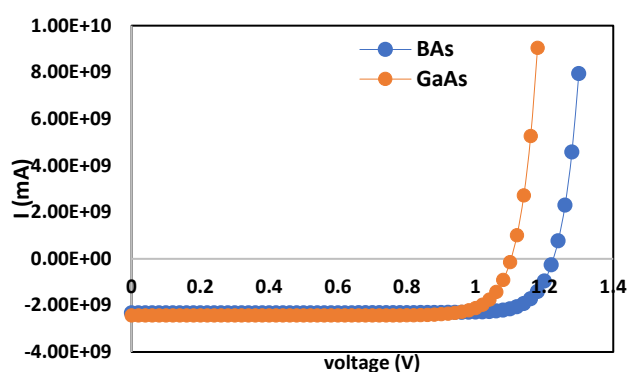


**Figure 2.** Variation of the current density  $I$  as a function of the voltage  $V$  for both GaAs and BAs

The results in Table 2 indicate that while GaAs achieved a slightly higher short-circuit current, BAs compensated with a superior fill factor, leading to greater overall photovoltaic conversion efficiency in this configuration. This suggests that, for this specific application, BAs may outperform GaAs in terms of charge management and minimizing internal losses.

Figure 2, present a current-voltage (I-V) characteristic comparison between two semiconductor materials: BAs (Boron Arsenide) and GaAs (Gallium Arsenide). In reverse bias, both materials exhibit very low leakage current, slightly lower for BAs,

indicating high-quality junctions. Under forward bias, GaAs starts conducting at a lower voltage ( $\sim 0.95$  V), while BAs requires a higher threshold ( $\sim 1.05$  V), suggesting a wider bandgap for BAs. The current rises more sharply for GaAs, reflecting better carrier injection at low voltages [11]. However, BAs demonstrates a more stable behavior, with lower recombination losses. Therefore, GaAs performs better at low voltages, while BAs shows greater stability and potential for high-voltage or harsh-environment applications.

### III. Comparative Study of GaAs and BAs-Based Solar Cells

This comparative study examines the performance of GaAs-based solar cells, a well-established material, and BAs, a promising emerging material for photovoltaic applications. By varying the active layer thickness, doping levels, and accounting for defects, we evaluate their effects on photovoltaic performance to gain deeper insights into the strengths and limitations of these materials in solar energy applications.

#### III.1. Effect of the active layer thickness

We explore thicknesses ranging from 0.25 to 3  $\mu\text{m}$  to determine the optimal level for light absorption, ensuring maximum efficiency. Additionally, we pinpoint the critical threshold beyond which efficiency declines as thickness increases, offering valuable insights for designing high-performance solar cells while minimizing material consumption.

##### III.1.1. Variation of $V_{oc}$ as a function of thickness

Figure 3 illustrates two distinct trends, one for GaAs and the other for BAs, highlighting the impact of active layer thickness on the open-circuit voltage ( $V_{oc}$ ) in solar cells. Notably, the  $V_{oc}$  decreases as the active layer thickness increases for both materials. Interestingly, however, the BAs curve consistently remains higher than that of GaAs at any given thickness.

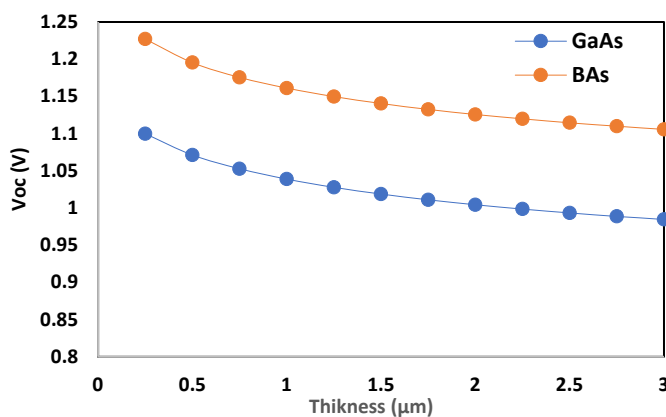


Figure 3. Variation of  $V_{oc}$  as a function of thickness

The decrease in  $V_{oc}$  with increasing active layer thickness can be explained as follows: As the thickness of the active layer increases, charge carriers (electrons and holes) must travel longer distances to reach the solar cell electrodes. This extended travel increases the likelihood of recombination before the carriers reach the electrodes, thereby reducing the voltage generated by the cell.

Increasing the active layer thickness can lead to greater light absorption within the layer itself, reducing the amount of light that reaches the p-n junction and thereby lowering the voltage generated by the cell. Additionally, BAs, with its wider bandgap compared to GaAs, requires higher energy for electrons and holes to recombine [12].

This characteristic reduces charge carrier recombination, resulting in a higher  $V_{oc}$  for BAs compared to GaAs.

##### III.1.2. Variation of $J_{sc}$ as a function of thickness

Figure 4 presents two different curves, one for GaAs and one for BAs, illustrating the relationship between short-circuit current density ( $J_{sc}$ ) and active layer thickness in solar cells. For both materials,  $J_{sc}$  increases as the active layer thickness grows. However, for GaAs, this increase is more pronounced between 0.25  $\mu\text{m}$  and 1.5  $\mu\text{m}$ , after which the  $J_{sc}$  begins to rise marginally or stabilizes. Notably, the GaAs curve consistently remains above the BAs curve for any given thickness.

The increase in  $J_{sc}$  with active layer thickness is due to more photons being absorbed and converted into electron-hole pairs as the layer becomes thicker. Beyond a certain thickness, light absorption reaches a saturation point, causing  $J_{sc}$  to stabilize as additional material no longer significantly enhances photon absorption.

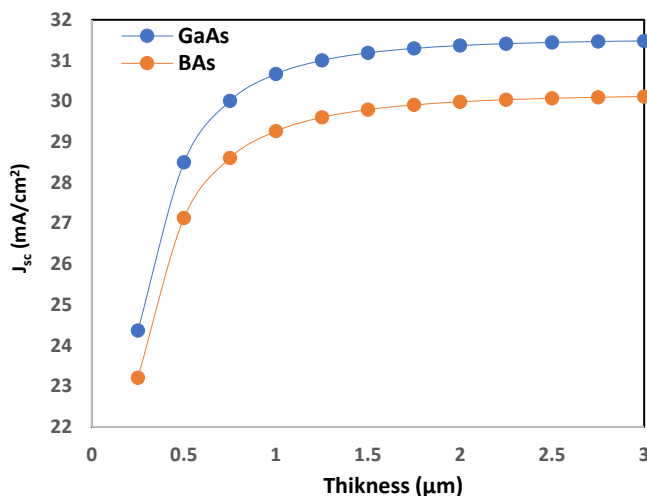


Figure 4.  $J_{sc}$  vs with thickness

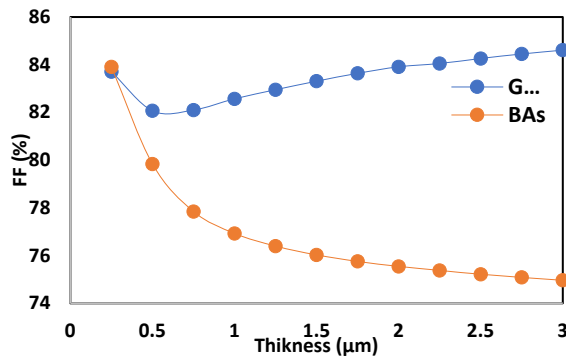


Figure 5. Variation of fill factor (FF) as a function of thickness

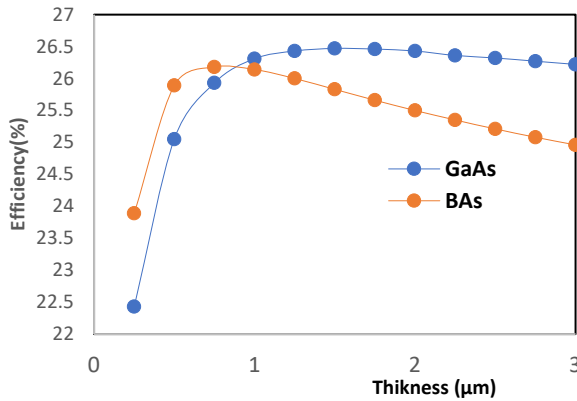


Figure 6. Variation of efficiency as a function of thickness

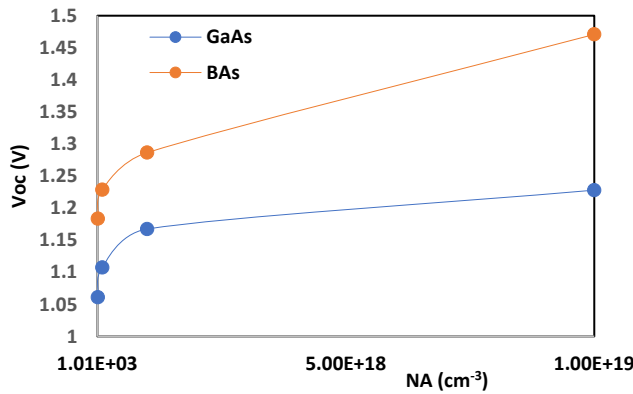


Figure 7. Variation of  $V_{oc}$  as a function of p-type doping

decline suggests the presence of adverse factors such as non-radiative recombination or structural imperfections, which diminish the overall efficiency of the solar cell.

### III. 2 Doping Effect of the Active Layer

We analyze the impact of varying doping concentrations, ranging from low levels ( $1 \times 10^{14} - 1 \times 10^{15}$ ) to high levels ( $1 \times 10^{18} - 1 \times 10^{19}$ ), on critical parameters such as  $J_{sc}$ ,  $V_{oc}$ , FF, and PCE. This analysis enables the identification of optimal doping levels to maximize the performance and efficiency of solar cells.

#### III.2.1. Variation of $V_{oc}$ as a function of doping in the active layer

Figure 7, presents two graphs illustrating the open-circuit voltage ( $V_{oc}$ ) as a function of p-type doping concentration for GaAs and BAS materials in a solar cell.  $V_{oc}$  increases with higher doping levels for both materials, but at every doping level, the BAS curve consistently remains above that of GaAs.

As the p-type doping concentration rises, the number of holes in the active layer increases [15]. This higher hole density reduces the depletion zone width within the p-n junction, decreasing charge carrier recombination losses in this region. Consequently, the open-circuit voltage ( $V_{oc}$ ) is enhanced, improving the overall performance of the solar cell.

The GaAs curve remains higher than the BAS curve throughout due to GaAs's superior electron mobility, which facilitates faster electron transport and minimizes recombination losses [13]. Consequently, while both materials exhibit an increase in  $J_{sc}$  with thickness, GaAs consistently generates higher current for a given thickness, benefiting from its more efficient charge transport properties.

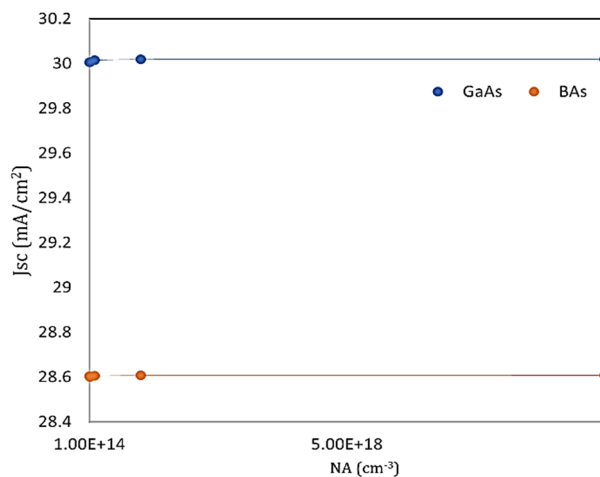
Figure 5 illustrates two graphs showing the fill factor (FF) of GaAs and BAS as a function of active layer thickness in a solar cell. Notably, the FF initially drops to around  $0.5 \mu\text{m}$  and then gradually increases as the thickness continues to rise. This behavior can be attributed to rising resistive losses at lower thicknesses, which initially reduce the FF. However, beyond this point, improved charge carrier separation and better control of recombination processes offset these losses, leading to an increase in the FF.

In contrast, the fill factor of BAS shows a significant decline with increasing active layer thickness, unlike GaAs. This reduction in FF suggests a potential decline in material quality as the active layer thickens, which may be attributed to an increase in charge carrier recombination. This difference highlights the challenges associated with maintaining optimal performance in BAS-based solar cells as layer thickness increases.

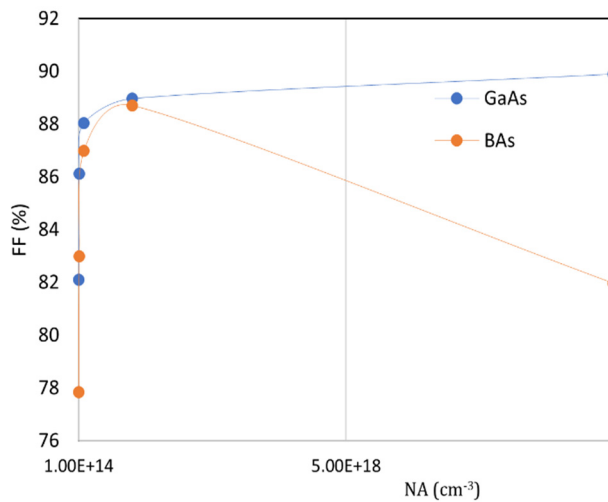
#### III.1.3. Variation of the efficiency ( $\eta$ ) versus the thickness

Figure 6 depicts the variation in efficiency as a function of active layer thickness. For GaAs, efficiency increases within the range of  $0.25$  to  $1.75 \mu\text{m}$ , reflecting improved light absorption and enhanced charge carrier management. Beyond this range, efficiency either stabilizes or slightly decreases, indicating that most incident photons have already been absorbed, and further gains are limited to marginal effects.

In contrast, BAS shows a similar trend to GaAs within the range of  $0.25$  to  $0.75 \mu\text{m}$ . However, beyond this point, the efficiency decreases more significantly [14]. This pronounced



**Figure 8.** Variation of  $J_{sc}$  versus p-type doping



**Figure 9.** Variation of the form factor (FF) as a function of P-type doping

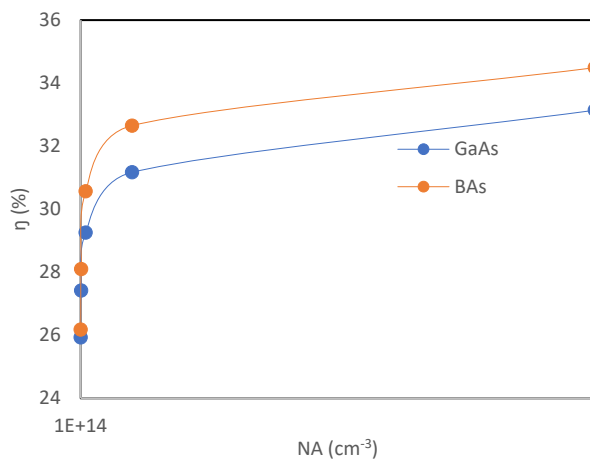


**Figure 10.** Variation of  $\eta$  as a function of P doping

concentrations of  $1 \times 10^{18}$  and  $1 \times 10^{19}$ . This trend suggests a potential saturation point, where further doping yields diminishing returns. This limitation could be attributed to effects such as charge carrier recombination or the saturation of available doping sites, indicating a practical upper limit to the benefits of p-type doping on photovoltaic conversion efficiency.

### III.2.2. Variation of $J_{sc}$ as a function of doping in the active layer

Figure 8 illustrates the variation of short-circuit current density ( $J_{sc}$ ) for GaAs and BAAs as a function of p-type doping concentration (NA). Despite an increase in NA from  $1 \times 10^{14}$  to  $1 \times 10^{19} \text{ cm}^{-3}$ , the  $J_{sc}$  for GaAs remains nearly constant at approximately  $30 \text{ mA}/\text{cm}^2$ , while for BAAs, it remains steady at around  $28.6 \text{ mA}/\text{cm}^2$  across the same doping range [11].

This stability indicates that the generation and accumulation of charge carriers are not significantly affected by higher doping concentrations. The consistency suggests that the solar cells are already optimized for photon absorption and charge carrier collection, and additional doping does not notably enhance their performance within this range.

### III.2.3. Variation of the fill factor (FF) as a function of doping of the active layer

Figure 9 illustrates the variation in the fill factor (FF) as a function of p-type doping concentration for GaAs and BAAs. In both materials, increasing the p-type doping concentration generally enhances the FF, indicating that charge carrier mobility in these semiconductors improves with higher doping levels.

For GaAs, the FF shows a steady increase with rising doping concentration, suggesting consistent improvements in conductivity. In contrast, BAAs initially exhibits a significant increase in FF; however, at very high doping concentrations, the FF begins to decline. This decline may result from saturation effects or increased recombination phenomena, indicating a threshold beyond which further doping becomes detrimental to the material's performance.

### III.2.4. Variation of efficiency ( $\eta$ ) as a function of doping of the active layer

Figure 10 presents two graphs showing the efficiency of GaAs and BAAs solar cells as a function of p-type doping concentration. For both materials, efficiency increases with higher doping levels. In GaAs, this increase is particularly pronounced, with the power conversion efficiency (PCE) rising from 27.42% to 33.14% as doping concentrations increase from  $1 \times 10^{14}$  to  $1 \times 10^{18}$ . This improvement reflects enhanced efficiency in converting light energy into electricity due to increased doping. The higher concentration of positive charge carriers (holes) resulting from p-type doping improves charge separation, thereby facilitating more efficient energy conversion.

Similarly, BAAs shows an efficiency increase with higher doping levels, but the rise in PCE is more gradual, from 32.65% to 34.49% between doping



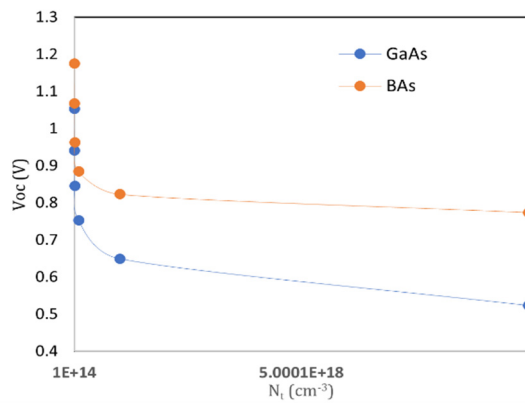


**Figure 11.** Variation of  $V_{oc}$  as a function of defect density  $N_t$

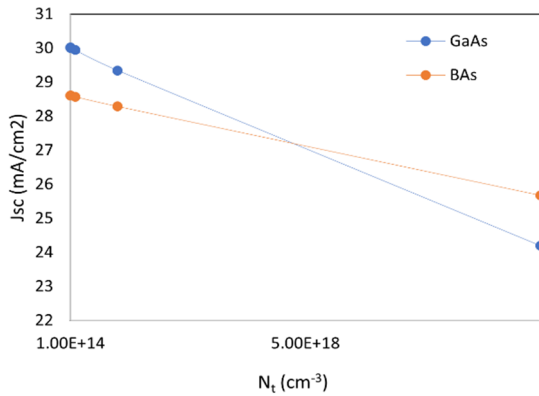


**Figure 12.** Variation of  $J_{sc}$  as a function of defect density  $N_t$

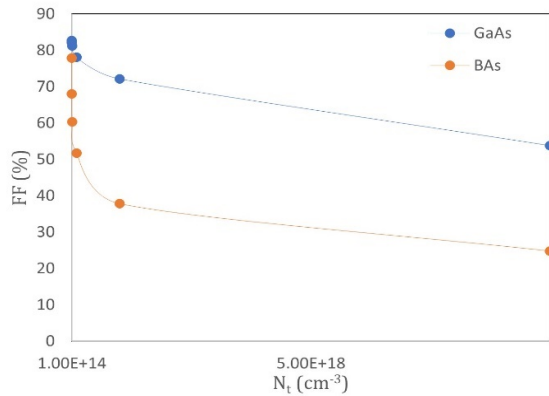


**Figure 13.** Variation of the fill factor (FF) as a function of defect density  $N_t$

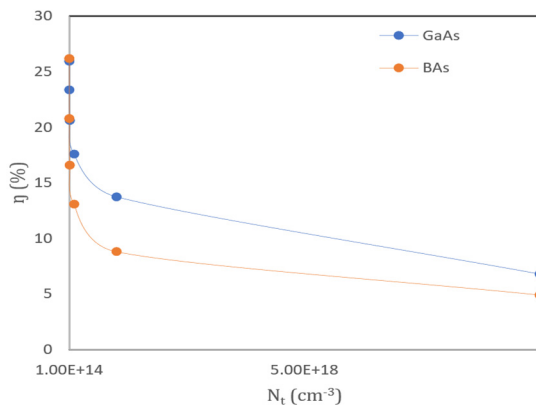


**Figure 14.** Variation of efficiency as a function of defect density  $N_t$

### III.2.5. Effect of defects in the active layer

Figure 11 illustrates the variation in the open-circuit voltage ( $V_{oc}$ ) as a function of defect density  $N_t$  for GaAs and Bas. By examining a range of defect density values, we can assess their impact on the electrical characteristics of the solar cell. This analysis shall enable us to identify the optimal defect density, contributing to enhanced overall performance and efficiency of the solar cell.

A gradual decline in the open-circuit voltage ( $V_{oc}$ ) is observed for both GaAs and BAS as the defect density in the crystalline layer increases. Initially, the decrease is mild, but it becomes more pronounced at higher defect levels.

Comparatively, while BAS may initially exhibit a slightly higher  $V_{oc}$  than GaAs, its drop at higher defect densities is more significant, indicating greater sensitivity to defects. This suggests that BAS may be more affected by disruptions in the crystalline structure.

For both materials, the decrease in  $V_{oc}$  aligns with the principle that defects disrupt the crystalline structure, reducing charge carrier mobility and ultimately impacting the open-circuit voltage.

### III.2.6. Variation of short-circuit current density ( $J_{sc}$ ) as a function of doping of the active layer

Figure 12 demonstrates that the short-circuit current density ( $J_{sc}$ ) gradually decreases as the defect density ( $N_t$ ) increases for both GaAs and BAS materials.

The decline in  $J_{sc}$  with increasing  $N_t$  is attributed to the rise in recombination centers within the material. These defects elevate the likelihood of electron-hole recombination before they can contribute to the current, thereby reducing  $J_{sc}$ . While GaAs initially exhibits higher efficiency, it shows greater sensitivity to defects at higher defect densities, highlighting its vulnerability under such conditions.

### III.2.7. Variation of the fill factor (FF) as a function of defect density

Figure 13 shows that GaAs initially exhibits a slightly higher fill factor (FF) compared to BAS; however, both materials experience a similar decline in FF as the defect density increases.

The reduction in FF with increasing defects in the crystalline layer can be attributed to enhanced charge carrier recombination, which decreases the number of carriers available to contribute to the output current. Additionally, some defects may obstruct or scatter incident light, limiting the generation of electron-hole pairs and further contributing to the decline in the fill factor (FF).

### III.2.8. Variation of the efficiency ( $\eta$ ) as a function of defect density

Figure 14 Initially, BAS exhibits a slightly higher Power Conversion Efficiency (PCE) compared to GaAs; however, both materials show similar declines in PCE as defect density increases.

The fill factor (FF) reflects the efficiency of converting light energy into electricity, accounting for material quality as well as ohmic and recombination

losses. A decrease in FF indicates reduced efficiency, which inevitably lowers the overall performance of the device. Consequently, when FF,  $J_{sc}$ , and  $V_{oc}$  decline due to crystalline defects, the overall Power Conversion Efficiency (PCE) of the photovoltaic device is significantly impacted.

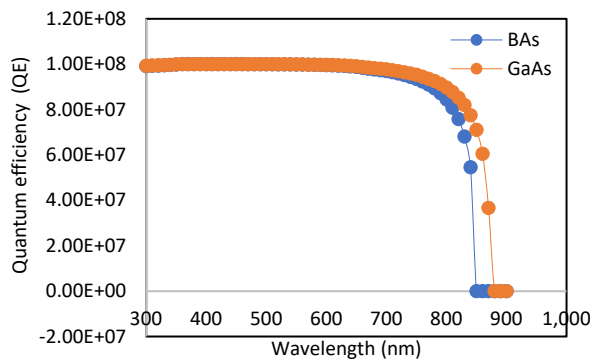


Figure 15. Quantum efficiency of the two structures

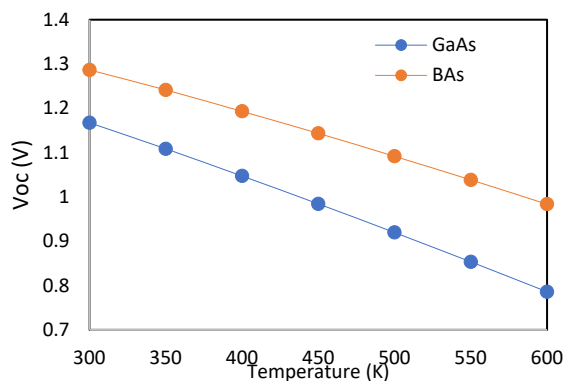


Figure 16. Variation of  $V_{oc}$  as a function of temperature

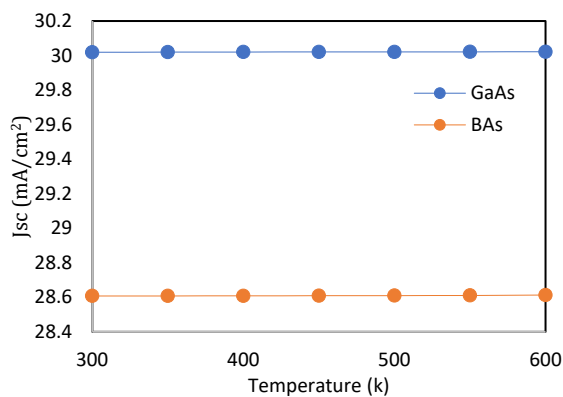


Figure 17. Variation of  $J_{sc}$  as a function of temperature

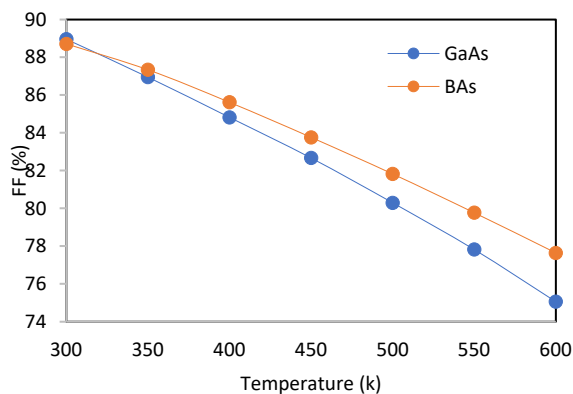


Figure 18. Variation of the fill factor (FF) as a function of temperature

## IV. Optimized Configuration

After conducting a series of in-depth analyses on thickness variations, doping, and defects; the optimized solar cell presents a thickness of  $0.75\mu\text{m}$ , a doping concentration of  $1\text{E}18\text{ cm}^{-3}$ , and a defect density of  $1\text{E}14\text{ cm}^{-3}$ . This optimization results in an efficiency of 31.17% for the GaAs-based structure and 32.65% for the BAs-based one.

### IV.1. Quantum Efficiency

According to Figure 15, GaAs shows a slightly higher quantum efficiency, but the difference is not significant. Both materials are effective over a wide range of wavelengths.

### IV. Effect of temperature

After optimizing the photovoltaic cell in terms of active layer thickness, doping, and defect management, it is crucial to study its behavior under extremely high temperature variations. This step allows for the identification of optimal operating conditions to ensure stable and maximum performance, which is essential, particularly for thermophotovoltaic applications, where materials must operate efficiently in extremely high-temperature environments.

#### IV.1. Effect of temperature on $V_{oc}$

Figure 16, illustrates a decrease in  $V_{oc}$  with increasing temperature for both materials, although BAs consistently maintains a higher value. This suggests superior thermal stability or reduced sensitivity to temperature variations compared to GaAs.

At elevated temperatures, charge carriers gain additional thermal energy, which increases their mobility within the material but reduces the open-circuit voltage. Furthermore, higher temperatures accelerate charge carrier recombination rates, shortening their average lifetime and contributing to the decline in  $V_{oc}$ .

#### IV.2. Effect of temperature on short-circuit current density ( $J_{sc}$ )

The observations of  $J_{sc}$  values as a function of temperature for the two materials (Figure 17) demonstrate a remarkable stability of the short-circuit current density ( $J_{sc}$ ) as the temperature increases. In the case of GaAs, the values of  $J_{sc}$  remain practically constant in the temperature range from 300 K to 500 K, with a slight variation of about  $0.0012\text{ mA/cm}^2$  over this temperature range. Similarly, for BAs, the  $J_{sc}$  values remain stable with a minimal variation of  $0.0012\text{ mA/cm}^2$  over the same temperature range.

The constancy of  $J_{sc}$  (short-circuit current density) shows that temperature does not have a significant impact on short-circuit current generation, confirming good stability in terms of photonic response.

#### IV.3. Effect of temperature on the fill factor (FF)

Figure 18 shows the evolution of FF as a function of temperature for the two materials: GaAs (Gallium



Arsenide) and BAs (Boron Arsenide). The FF decreases with the increase in temperature for both materials. This indicates that the energy conversion efficiency of devices based on these materials decreases at higher temperatures. This is typical for semiconductor devices because the non-radiative recombination of charge carriers increases with temperature.

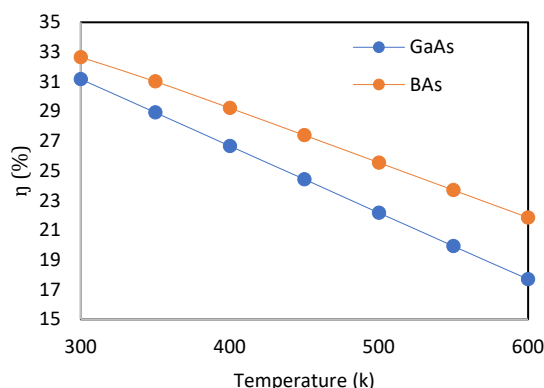


**Figure 19.** Variation of the efficiency as a function of temperature

#### IV.4. Effect of temperature on efficiency ( $\eta$ )

Figure 19, presents two graphs showing the efficiency of GaAs and BAs solar cells as a function temperature. The conversion efficiency decreases with the increase in temperature for both materials. Although the short-circuit current ( $I_{sc}$ ) remains almost stable, the conversion efficiency decreases. This decrease in efficiency can be mainly attributed to a drop in FF and the open-circuit voltage ( $V_{oc}$ ) with the increase in temperature. The stability of the  $I_{sc}$  suggests that photons are still effectively converted into charge carriers, but these charge carriers undergo more non-radiative recombination at higher temperatures. This reduces both  $V_{oc}$  and FF, leading to an overall decrease in conversion efficiency.

### V. Comparison

Finally, the performance of the two proposed structures, one based on GaAs and the other on BAs, was compared in terms of photovoltaic conversion efficiency (Table 2). This comparison evaluates the effectiveness of both semiconductor materials as active components in solar cells. To contextualize the findings and assess the advancements achieved in this study, the GaAs structure proposed here was also compared with results from previous research (see Table 3).

**Table 2.** Comparison of photovoltaic performance between GaAs and BAs as an active layer

structures	$V_{oc}$ (V)	$J_{sc}$ (mA/cm <sup>2</sup> )	FF (%)	$\eta$ (%)
Pt/CuO/GaAs/WS <sub>2</sub> /FTO	1.1738	30.6877	89.27	31.17
Pt/CuO/BAs/WS <sub>2</sub> /FTO	1.2805	29.2739	88.75	32.65

These results indicate that although GaAs is a high-performance material, BAs offers significant advantages in terms of thermal stability and conversion efficiency, which could make it a promising alternative for high-temperature applications, particularly thermophotovoltaic applications.

Table 3 compares the findings of this study with another similar published research on GaAs. The results demonstrate that our approach achieves strong performance using thinner layers, along with materials that are abundant, easy to fabricate, and less toxic. These attributes contribute to minimizing material waste and promoting environmental sustainability.

**Table 3.** Comparison of the performance of GaAs-based solar cells with similar studies.

Reference	$V_{oc}$ (V)	$J_{sc}$ (mA/cm <sup>2</sup> )	FF (%)	$\eta$ (%)
Ala'eddin A. Saif, M. Albishri et al (2023) [3]	1.02	47.96	87.48	30.88
This work (2024)	1.1738	30.6877	89.27	31.17

### VI. CONCLUSION

This comparative study evaluates the performance of two types of solar cells: one utilizing GaAs and the other BAs. By analyzing a range of performance parameters under comparable conditions, the study identifies the strengths and limitations of each material in photovoltaic applications, paving the way for advancements in solar energy, particularly in thermophotovoltaic technologies.

In this study, we compared the performance of solar cells based on GaAs and BAs using simulations conducted with SCAPS software. The results demonstrated that while GaAs is a well-established material for photovoltaic applications, BAs shows strong potential due to its greater thermal stability, reduced carrier recombination, and higher energy conversion efficiency under specific configurations.

The analysis of key parameters such as open-circuit voltage  $V_{oc}$ , short-circuit current  $J_{sc}$ , fill factor (FF), and conversion efficiency ( $\eta$ ) revealed that:

- BAs achieves a higher open-circuit voltage, indicating lower internal energy losses and better charge management.
- GaAs exhibits a slightly higher short-circuit current, likely due to more efficient absorption in the visible spectrum and superior electron mobility.

This study is the first to simulate and compare complete solar cell structures based on GaAs and Bas under an identical architecture, using CuO as the hole transport layer and WS<sub>2</sub> as the electron transport layer, with SCAPS software.

It highlights the promising photovoltaic potential of BAs, identifying optimized configurations (thickness, doping, and defect density) that achieve high efficiencies:

- 31.17% for GaAs
- 32.65% for BAs,

Demonstrating competitive or even superior performance compared to literature reports. The study shows that BAs outperforms GaAs in terms of thermal stability and energy conversion under high-temperature conditions, making it particularly suitable for thermophotovoltaic and space applications.

The analysis is comprehensive, evaluating the impact of multiple parameters on performance ( $\eta$ , Voc, J<sub>sc</sub>, FF, quantum efficiency), including:

- Active layer thickness
- Doping levels
- Defect density
- Operating temperature

Finally, the study provides practical recommendations for material selection based on target applications:

- GaAs for high-speed conduction solar cells.
- Bas for extreme thermal environments.

This work bridges theoretical insights with practical optimization, advancing the development of next-generation high-efficiency solar cells.

#### ORCID

Merad Laarej, <https://orcid.org/0000-0003-1753-7528>; Mama Bouchaour, <https://orcid.org/0009-0007-3204-0583>

#### REFERENCES

- [1] M. Tridane, A. Malaoui, and S. Belaaouad, "Numerical Simulation of pin GaAs Photovoltaic Cell Using SCAPS-1D», Biointerface Research in Applied Chemistry, **13**(4), 253 (2023). <https://doi.org/10.33263/BRIAC133.253>
- [2] A. Kumar, M.S. Thomas, G. Pareek, A. Jain, and N. Gupta, "Performance Evolution of GaAs-Based Solar Cell Towards 30% Efficiency for Space Applications," in: *2022 IEEE International Conference on Nanoelectronics, Nanophotonics, Nanomaterials, Nanobioscience & Nanotechnology (5NANO)*, (IEEE, India, 2022), pp. 1-3. <https://doi.org/10.1109/5NANO53044.2022.9828955>
- [3] M. Burgelman, P. Nollet, and S. Degraeve, "Modelling polycrystalline semiconductor solar cells," *Thin Solid Films*, **361**, 527-532 (2000). [https://doi.org/10.1016/S0040-6090\(99\)00825-1](https://doi.org/10.1016/S0040-6090(99)00825-1)
- [4] N. Khoshsirat, N.A.Md. Yunus, "Numerical simulation of CIGS thin film solar cells using SCAPS-1D," in: *2013 IEEE Conference on Sustainable Utilization and Development in Engineering and Technology (CSUDET)*, (Selangor, Malaysia, 2013), pp. 63-67. <https://doi.org/10.1109/CSUDET.2013.6670987>
- [5] R.M. Wentzcovitch, and M.L. Cohen, "Theory of structural and electronic properties of BAs," *J. Phys. C Solid State Phys.* **19**(34), 6791 (1986). <https://doi.org/10.1088/0022-3719/19/34/016>
- [6] A. Boudjemline, M.M. Islam, L. Louail, and B. Diawara, "Electronic and optical properties of BAs under pressure," *Phys. B: Condens. Matter*, **406**(22), 4272-4277 (2011). <https://doi.org/10.1016/j.physb.2011.08.043>
- [7] K. Bushick, K. Mengle, N. Sanders, and E. Kioupakis, "Band structure and carrier effective masses of boron arsenide: Effects of quasi-particle and spin-orbit coupling corrections," *Appl. Phys. Lett.* **114**(2), 022101 (2019). <https://doi.org/10.1063/1.5062845>
- [8] A. Saif, "High-Efficiency homojunction GaAs solar cell using InGaP as FSF and AlGaInP as BSF," *Results in Optics*, **12**, 100454 (2023). <https://doi.org/10.1016/j.rio.2023.100454>
- [9] K. Ajay, M. S. Thomas, P. Gulshan, A. Jain, et N. Gupta, "Performance Evolution of GaAs-Based Solar Cell Towards >30% Efficiency for Space Applications", *IEEE*, vol. 1, N° 978, p. 3728-6654. <https://doi.org/10.1109/5nano53044.2022.9828955>
- [9] N. Rono, A.E. Merad, J.K. Kibet, B.S. Martincigh, and V.O. Nyamori, "Optimization of Hole Transport Layer Materials for a Lead-Free Perovskite Solar Cell Based on Formamidinium Tin Iodide," *Energy Technol.* **9**(12), 2100859 (2021). <https://doi.org/10.1002/ente.202100859>
- [10] S.H. Zyoud, A.H. Zyoud, N.M. Ahmed, R.P. Anupama, S.N. Khan, A.F.I. Abdelkader, and S. Moyad, "Numerical modeling of high conversion efficiency FTO/ZnO/CdS/CZTS/MO thin film-based solar cells: Using SCAPS-1D software," *Crystals*, **11**(12), 1468 (2021). <https://doi.org/10.3390/cryst11121468>
- [11] J. Shin, G.A. Gamage, Z. Ding, K.E. Chen, F. Tian, X. Qian, J. Zhou, et al., "High ambipolar mobility in cubic boron arsenide," *Science*, **377**(6604), 437-440 (2022). <https://doi.org/10.1126/science.abn4290>
- [12] P.M. Oza, and N.H. Vasoya, "Modeling and simulation of TiO<sub>2</sub>/GaAs solar cell using SCAPS", *International Journal of Creative Research Thoughts (IJCRT)*, **10**(12), 2320-2882 (2022). [https://www.ijcrt.org/viewfull.php?&p\\_id=IJCRT2212610](https://www.ijcrt.org/viewfull.php?&p_id=IJCRT2212610)
- [13] Md.S. Shah, Md.K. Hasan, S.C. Barman, J.A. Bhuiyan, H. Mamur, and M.R. Amin Bhuiyan, "Enhancing PV performance of Al/ZnO/CdS/GaAs/NiO/Au solar cells through diverse layer combinations by SCAPS-1D", *Next Research*, **2**(1), 100143 (2025). <https://doi.org/10.1016/j.nexres.2025.100143>
- [14] X. Yu, H. He, Y. Hui, H. Wang, X. Zhu, S. Li, and T. Zhu, "Additive engineering for efficient wide-bandgap perovskite solar cells with low open-circuit voltage losses", *Frontiers in Chemistry*, **12**, (2024). <https://doi.org/10.3389/fchem.2024.1441057>
- [15] F.D. Silva, and D.N. Micha, "High-Efficiency GaAs Solar Cell Optimization by Theoretical Simulation", in: *34th Symposium on Microelectronics Technology and Devices (SBMicro)*, (IEEE, Sao-Paulo, Brazil, 2019). <https://doi.org/10.1109/SBMicro.2019.8919411>

## РОЗШИРЕННЯ МЕЖ ЕФЕКТИВНОСТІ: АНАЛІЗ СОНЯЧНИХ ЕЛЕМЕНТІВ GaAs ТА BAS ДЛЯ ФОТОЕЛЕКТРИКИ НАСТУПНОГО ПОКОЛІННЯ НА ОСНОВІ SCAPS

Мерад Лаарей, Мама Бушаур, Іман Буаззауї

*Університет Тлемсена, факультет природничих наук, кафедра фізики, дослідницьке об'єднання «Матеріали та відновлювані джерела енергії», URMER BP: 119, Тлемсен, Нуво-Поль, Мансура, 13000, Алжир*

У цьому дослідженні використовується програмне забезпечення SCAPS для моделювання та аналізу напівпровідникових матеріалів арсеніду галію (GaAs) та арсеніду бору (BAS) для фотоелектричних застосувань. Ми окреслюємо методологію, підкреслюючи критичні фактори, що враховуються під час моделювання. Продуктивність сонячних елементів досліджується за допомогою кривих квантової ефективності та фотоелектричної продуктивності. Крім того, обговорюються спостережувані тенденції, ключові відмінності між GaAs та BAS, а також їх значення для розвитку високоефективних сонячних елементів.

**Ключові слова:** *GaAs; BAS; фотоелектрична техніка; програмне забезпечення SCAPS; ефективність перетворення ( $\eta$ )*

## NUMERICAL INVESTIGATION OF LEAD-FREE PEROVSKITE SOLAR CELLS BASED ON FASnI<sub>3</sub>/ZrS<sub>2</sub> STRUCTURE USING SCAPS-1D SIMULATOR

 Hmoud Al-Dmour

Mutah University, Faculty of Science, Department of Physics, 61710, Jordan

Corresponding Author E-mail: [hmoud79@mutah.edu.jo](mailto:hmoud79@mutah.edu.jo)

Received August 8, 2025; revised September 28, 2025; accepted October 9, 2025

This study presents a numerical investigation and optimization of lead-free perovskite solar cells using SCAPS-1D simulation. The proposed device is composed of formamidinium tin iodide (FASnI<sub>3</sub>, absorptive layer), zirconium disulfide (ZrS<sub>2</sub>, electron transport material), gold (Au, the back contact), and Fluorine-doped tin oxide (SnO<sub>2</sub>:F, the front contact). The effects of varying the thickness, defect density, doping concentration, operating temperature, and back-contact work function on the photovoltaic performance were studied to determine the optimal device architecture with the highest power conversion efficiency (PCE). Results reveal that the initial performance of FASnI<sub>3</sub>/ZrS<sub>2</sub> solar cells was as follows: open-circuit voltage ( $V_{oc}$ ) = 0.99V, short-circuit current ( $J_{sc}$ ) = 20.7mA/cm<sup>2</sup>, Fill factor (FF) = 60.13%, and power conversion efficiency (PCE) = 12.4%. After optimization, the performance of FASnI<sub>3</sub>/ZrS<sub>2</sub> significantly improved, achieving a PCE of 23.3%, FF of 82.4%, and  $J_{sc}$  of 30.2mA/cm<sup>2</sup>. This remarkable improvement in these parameters is attributed to the increase in thickness and doping density of the FASnI<sub>3</sub> and ZrS<sub>2</sub> layers which lead to improved light absorption and charge generation. Additionally, the 5.3 eV work function of the back contact was found to provide better energy-level alignment with the FASnI<sub>3</sub> layer, thereby facilitating charge extraction. These findings offer valuable insights into the design of efficient, stable, and lead-free perovskite solar cells.

**Keywords:** FASnI<sub>3</sub>; ZrS<sub>2</sub>; SCAPS-1D; Lead-free perovskite solar cells; Electron transport layer; Photovoltaic modeling; Solar energy

**PACS:** 28.41.Ak, 88.40.H, 61.72.Vv, 71.55.-I, 73.30.+

### 1. INTRODUCTION

Over the last decade, human demand for energy has increased due to our growing reliance on technology, resulting in a corresponding rise in the use of fossil fuels [1]. They are non-renewable and take a long time to form. Additionally, burning fossil fuels releases CO<sub>2</sub> gas, which accumulates in the atmosphere [1]. Thus, considerable efforts have been made to replace fossil fuels with renewable energy sources, such as solar and nuclear energy. Solar energy is produced using solar cells, which offer a promising renewable energy source, providing an environmentally friendly way to curb CO<sub>2</sub> emissions and meet the growing demand for green energy [1,2]. This has led to an increasing demand for ecologically friendly photovoltaic devices, such as tin-based perovskite solar cells (PSCs) [2,3]. They have been considered promising alternatives to lead-based counterparts due to their remarkable optoelectronic properties, which include high absorption coefficients, adjustable bandgaps, and cost-effective manufacturing processes that together improve the utilization and potential of solar energy [3,4,5]. For example, Formamidinium (FA)-based lead-free perovskite solar cells exhibit higher efficiency, greater stability, and reduced toxicity [6]. In addition, tin (Sn)-based PSCs are gaining attention as promising alternatives to their lead (Pb)-based counterparts, offering similar optoelectronic properties such as high carrier mobility, strong light absorption, and long carrier diffusion lengths. Also, they offer significantly lower environmental and health hazards [7].

In recent years, considerable work has been conducted on lead-free PSCs by utilizing various ETL, HTL, and absorber layers. In this context, Ateeq et al used SCAPS simulation to improve performance of FTO/CeO<sub>2</sub>/FASnI<sub>3</sub>/CuI/Au for a lead-free solar cell by optimizing different values for bandgap, electron affinity, acceptor density, thickness, defect density, and back contact work function [8]. After optimization, the efficiency improved from 22.06% to 24.87%, and the current density increased from 26.03 to 30.68 mA/cm<sup>2</sup>. Various hole transport layers (HTLs), including PEDOT:PSS, Spiro-OMeTAD, PCBM, Cu<sub>2</sub>O, MoO<sub>3</sub>, and Si, have been investigated in perovskite solar cells. In another study, Almufarrij et al. optimized a lead-free n-i-p MASnI<sub>3</sub> device using graphene, ZnO:Al, and 3C-SiC interface layers, achieving a theoretical efficiency of 30.43% and highlighting MASnI<sub>3</sub> as a promising non-toxic material for sustainable energy [9].

On the other hand, ETL materials can be prepared from various materials, such as transition-metal dichalcogenides (TMDCs). ZrS<sub>2</sub> is a two-dimensional (2D) transition metal disulfide synthesized as a thin film for application in flexible transparent devices [10]. Various growth techniques can be employed to achieve tunability of bandgap energy, electronic, and optical properties for ZrS<sub>2</sub> thin films, such as Chemical Vapor Deposition (CVD) and Atomic Layer Deposition (ALD) [11]. It has a high electron mobility and a small energy gap, making it useful for solar cell applications [10]. In this study, we report the optimization of FASnI<sub>3</sub>/ZrS<sub>2</sub> solar cells using the SCAPS-1D software [12, 13]. The effects of absorber layer thickness, defect density states, doping density, and the work function of the back metal contact on the performance of FASnI<sub>3</sub>/ZrS<sub>2</sub> solar cells are investigated.

## 2. SIMULATION TOOL

Numerical simulation can play a vital role in optimizing various solar cell structures, such as those using SILVACO, COMSOL, SETFOS, and SCAPS-1D [14]. In this work, the SCAPS-1D simulation was employed to investigate the efficiency of solar cells comprising FASnI<sub>3</sub> and ZrS<sub>2</sub>. This program was developed by researchers at the University of Gent's Department of Electronics and Information Systems (ELIS), Belgium, for two reasons: to simulate the physical phenomena that occur within the solar cell and to predict how well the solar cell would operate under various conditions, such as differences in temperature, illumination angles, and sun radiation [12]. The program solves Poisson's and continuity equations for free electrons and holes in the conduction and valence bands, which are commonly used in different mechanisms of electronic devices. The equations are given below:

$$\frac{d^2\psi}{dx^2} + \frac{q}{\epsilon} [p(x) - n(x) + N_D - N_A + \rho_p - \rho_n] = 0 \quad (1)$$

$$\frac{1}{q} \frac{dJ_p}{dx} = G_{op} - R(x) \quad (2)$$

$$\frac{1}{q} \frac{dJ_n}{dx} = -G_{op} + R(x) \quad (3)$$

Where  $\epsilon$  is the dielectric constant,  $q$  is the electron charge,  $N_A$  and  $N_D$  are ionized acceptors and donor density,  $\Psi$  is the electrostatic potential,  $J_p$  is current density due to hole,  $J_n$  is current density due to electron,  $G_{op}$  is the carrier generation rate,  $R$  is the total recombination rate,  $p$  is free hole density,  $n$  is the free electron density,  $\rho_p$ , and  $\rho_n$  are the hole and electron distribution. The following drift-diffusion equations (2) and (3) represent the holes and electrons carrier transport properties of the semiconducting material. The structure of the HTL-free FASnI<sub>3</sub>-based perovskite solar cell is illustrated in Figure (1).

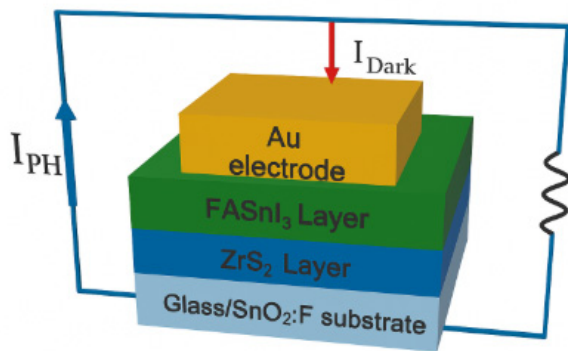


**Figure 1.** Schematic diagrams of SnO<sub>2</sub>:F/ZrS<sub>2</sub>/FASnI<sub>3</sub> Au solar cells

conduction band of these solar cells. For charge carrier behavior at the interfaces, we applied surface recombination velocities of  $1 \times 10^5$  cm/s for electrons and a slightly higher  $10^7$  cm/s for holes, reflecting common trends in perovskite materials.

**Table 1.** Simulation parameters of each layer of the proposed solar cell [11-15].

Parameters	ZrS <sub>2</sub>	FASnI <sub>3</sub>
Thickness (μm)	Varying 0.2 to 1.4	Varying 0.2 to 2.0
Bandgap (eV)	1.5	1.750
Electron affinity (eV)	4.7	4.125
Dielectric permittivity (relative)	16.4	8.2
CB effective density of states (cm <sup>-3</sup> )	$2.2 \times 10^{19}$	$1 \times 10^{18}$
VB effective density of states (cm <sup>-3</sup> )	$1.8 \times 10^{19}$	$1 \times 10^{18}$
Electron mobility (cm <sup>2</sup> /V·s)	300	22
Hole mobility (cm <sup>2</sup> /V·s)	30	22
Shallow uniform donor density $N_D$ (cm <sup>-3</sup> )	$1 \times 10^{19}$	0
Shallow uniform acceptor density $N_A$ (cm <sup>-3</sup> )	0	$1 \times 10^{16}$
Metal work function (eV)	Back contact (Au electrode) 5.1	Front contact (SnO <sub>2</sub> :F electrode) 4.4

## 3. RESULTS AND DISCUSSION

### 3.1. Effect of Thickness of ZrS<sub>2</sub> Layer and FASnI<sub>3</sub> Layer

The thickness of the components in solar cells plays a vital role in improving their efficiency, as it is a key factor in optimizing solar cells performance. The power conversion efficiency of solar cells depends on the efficiency of photon

The figure shows that the proposed solar cell is composed of these layers: FASnI<sub>3</sub> as absorber material, ZrS<sub>2</sub> as electron transport material (ETL), and two electrodes: gold (Au) as the back contact and fluorine-doped tin oxide (SnO<sub>2</sub>:F) as the front contact. The proposed device configurations are developed by modifying the properties of the materials used in this study. Table 1 summarizes the input parameters for HTL-free FASnI<sub>3</sub>-based perovskite solar cells, as obtained from the literature, to evaluate their performance [11,15]. To establish a stable reference frame for our analysis, we examined the most significant parameters that influence the performance of the tested device. In general, the main unchanged parameters based on published data are the effective density of states at  $1 \times 10^{18}$  cm<sup>-3</sup> for the valence band and  $10^{19}$  cm<sup>-3</sup> for the



absorption, exciton generation, and migration. Solar cells with a thicker layer enhance light absorption and increase charge generation, but they produce a longer path and affect the generation and migration of photo-generated charge carriers. On the other hand, the thinner layers in solar cells may decrease light absorption but facilitate charge-carrier movement. Figure 2 shows the parameters of the FASnI<sub>3</sub>/ZrS<sub>2</sub> solar cell when the thicknesses of the ZrS<sub>2</sub> and FASnI<sub>3</sub> layers were varied from 0.2  $\mu\text{m}$  to 1.4  $\mu\text{m}$  and 0.2  $\mu\text{m}$  to 2.0  $\mu\text{m}$ , respectively.

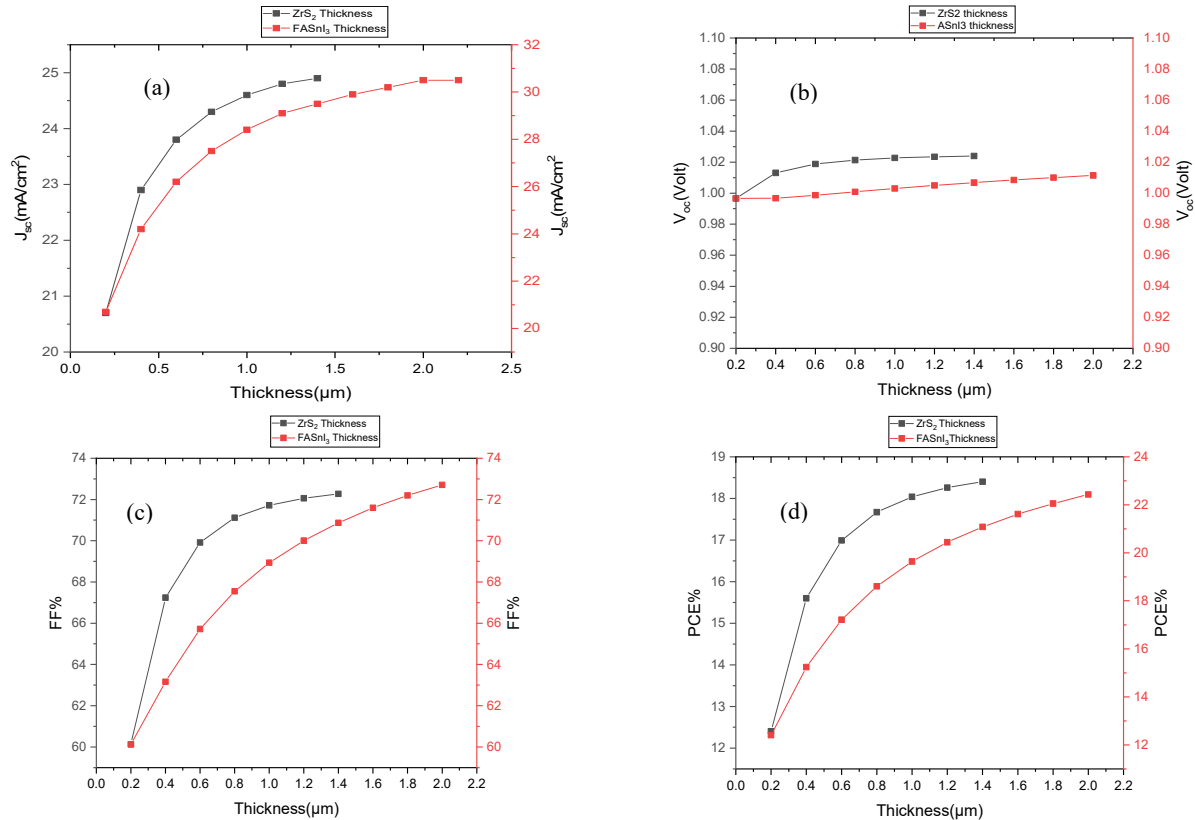


**Figure 2.** Effect of thickness of ZrS<sub>2</sub> and FASnI<sub>3</sub> on the parameters of ZrS<sub>2</sub>/FASnI<sub>3</sub> solar cells

The results reveal that thinner FASnI<sub>3</sub> and ZrS<sub>2</sub> layers produce lower fill factor and PCE compared to their thicker layers in FASnI<sub>3</sub>/ZrS<sub>2</sub> solar cells. Figures 2a and 2b show that the short-circuit current density increases ( $J_{sc}$ ) and reaches its peak value with an increase in thickness, while the open-circuit voltage ( $V_{oc}$ ) remains constant. However, the  $J_{sc}$  gets saturated with minor changes when the thickness of ZrS<sub>2</sub> and FASnI<sub>3</sub> changes from 0.8  $\mu\text{m}$  to 1.4  $\mu\text{m}$  and 1.2  $\mu\text{m}$  to 2  $\mu\text{m}$ , respectively. This saturation behavior suggests that beyond these thresholds, additional thickness does not contribute to further light absorption or current generation, likely because most incident photons are already absorbed. On the other hand, the open-circuit voltage ( $V_{oc}$ ) remained relatively constant across the thickness range studied, as it is more closely governed by the interface recombination rates and energy level alignment between the absorber and transport layers rather than by optical thickness [16]. Moreover, Figures 2c and 2d show that the efficiency (PCE) and fill factor (FF) were enhanced with increasing layer thickness, ranging from 12% to 21.32% and 60% to 72%, respectively. The above results are attributed to improved light absorption in the thicker active layers, which leads to enhancement of photogeneration of charge carriers. Similarly, the increase in FF indicates more efficient charge extraction and minimizes the effect of series resistance.

### 3.2. Effect of the Total Defect Density in Active Layers and Interfaces

Another essential factor that may significantly impact the device's efficiency is the defect density of the active layers. The level of defect density directly influences the quality of the interface and the bulk body of the solar cells, where the photo-generated charge is transported to the top and bottom electrodes [17,18]. As is known, the source of defect density in electronic devices comes from point defects, stacking faults, dislocations, and grain boundaries, which affect the performance of thin-film solar cells [18]. Additionally, different interfaces are formed in PSCs due to the use of various deposition techniques for each layer. The defects at the interface are influenced by the quality of the materials and the deposition methods, which occur due to interactions between the absorber precursor and the charge transport layer (CTL) solutions, leading to two main types of interface defects: those at the HTL/Perovskite and Perovskite/ETL interfaces. Figure 3 shows the fluctuation in device efficiency with varying defect densities in the ZrS<sub>2</sub> and FASnI<sub>3</sub> layers, as well as at the interface between ZrS<sub>2</sub> and FASnI<sub>3</sub>.

Figure 3-a illustrates the effect of varying the defect density in the ZrS<sub>2</sub> and FASnI<sub>3</sub> layers on the power conversion efficiency (PCE) of the FASnI<sub>3</sub>/ZrS<sub>2</sub> solar cell structure. The results show that efficiency remains unchanged when the

defect density is below  $1 \times 10^{16} \text{ cm}^{-3}$ , but then declines rapidly as the defect density increases from  $1 \times 10^{16} \text{ cm}^{-3}$  to  $10^{20} \text{ cm}^{-3}$ . These results are attributed to an increase in the carrier recombination rate in the bulk of the  $\text{ZrS}_2$  layer due to deep trap states, which affects the efficient extraction of photo-generated electrons. This leads to a reduction in the diffusion length and the carrier transport lifetime. On the other hand, PCE remains relatively stable with a slight decrease from  $\sim 12.5\%$  to  $\sim 11\%$  when the defect densities in  $\text{FASnI}_3$  were varied from  $1 \times 10^{12} \text{ cm}^{-3}$  to  $1 \times 10^{20} \text{ cm}^{-3}$ . That indicates the tendency of the  $\text{FASnI}_3$  layer to maintain its properties despite the presence of defects that do not affect its lifetimes and transport. That is attributed to defects usually or shallow states that minimally affect carrier recombination. These results align with the findings from the literature, indicating severe degradation in device performance when defect densities in ETLs exceed  $1 \times 10^{17} \text{ cm}^{-3}$ , while tin-based perovskites maintain reasonable efficiency even under high defect conditions [19]. Figure 3-b shows the fluctuation in device properties with defect density at  $\text{ZrS}_2/\text{FASnI}_3$  interface. As is known, the defects at the interface are influenced by the quality of the materials and the deposition methods occurred due to interactions between the absorber precursor and the charge transport layer (CTL) solutions, leading to two main types of interface defects: those at the HTL/Perovskite and Perovskite/ETL interfaces.

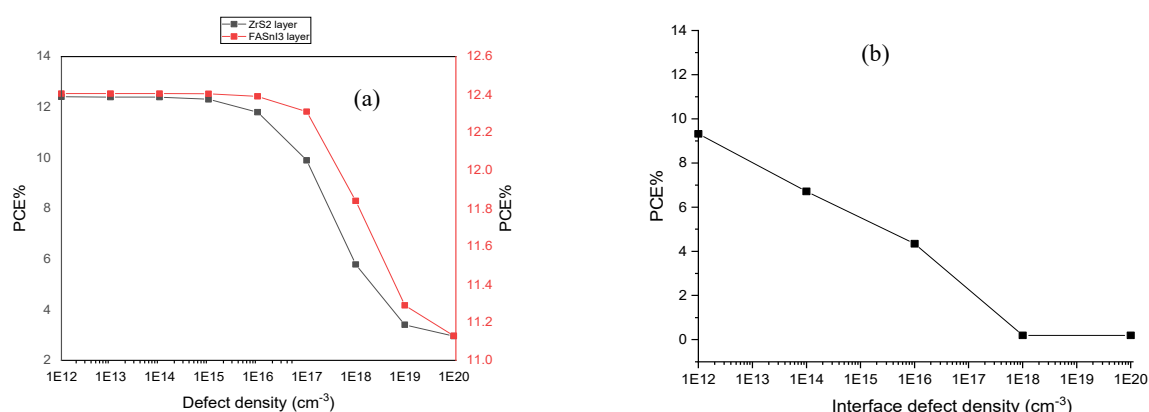


**Figure 3.** Effect of defect density in a)  $\text{ZrS}_2$  and  $\text{FASnI}_3$  layers and b)  $\text{ZrS}_2/\text{FASnI}_3$  interface on the parameters of  $\text{ZrS}_2/\text{FASnI}_3$  solar cells

### 3.3. Influence of Doping Densities in $\text{ZrS}_2$ and $\text{FASnI}_3$ Layers

The performance of perovskite and lead-free photovoltaic devices is significantly affected by the doping densities of the  $\text{ZrS}_2$  and  $\text{FASnI}_3$  layers. Figure 4 illustrates the parameters of the  $\text{ZrS}_2/\text{FASnI}_3$  solar cell as functions of the doping concentration varied from  $1 \times 10^{15}$  to  $1 \times 10^{21} \text{ cm}^{-3}$ .

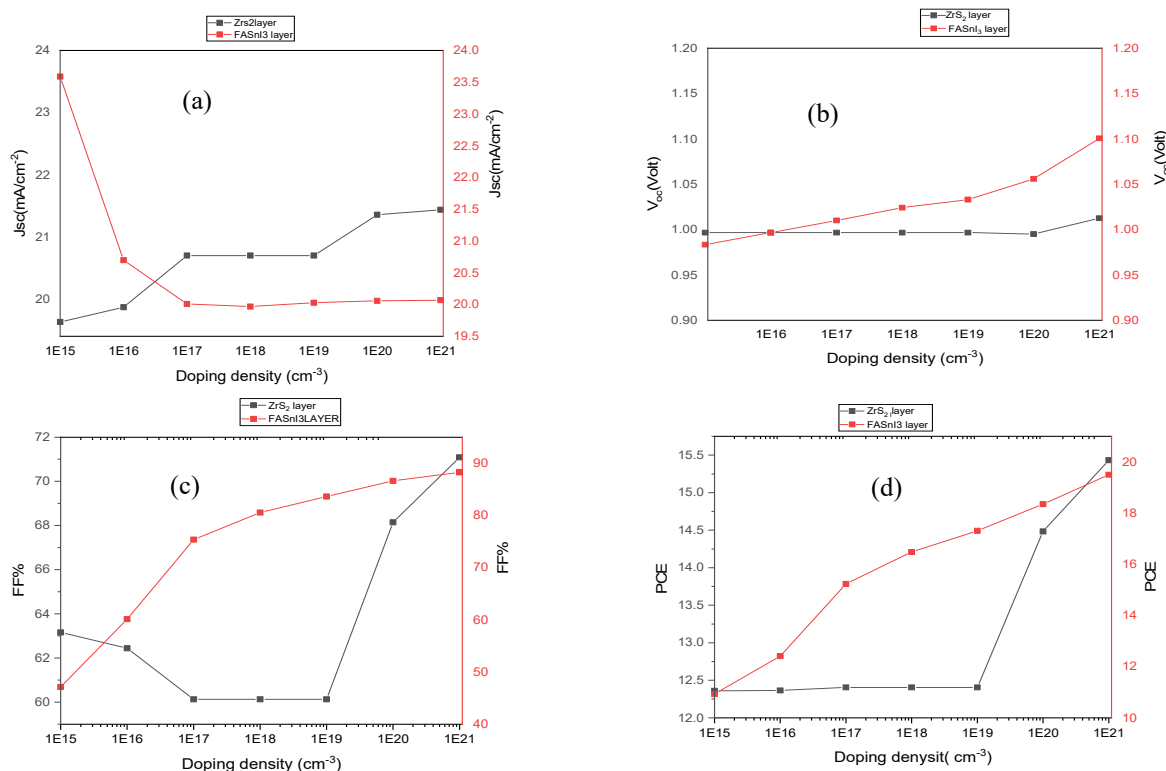


**Figure 4.** Effect of doping density in  $\text{ZrS}_2$  and  $\text{FASnI}_3$  layers on the parameters of  $\text{ZrS}_2/\text{FASnI}_3$  solar cells



Figures 4a and 4b show a slight enhancement in  $V_{oc}$  and  $J_{sc}$  as the doping concentration in the  $ZrS_2$  layer increases. For the  $ZrS_2$  layer, PCE increased from 12.4% to 16%, and FF from 54% to 73% (see figures 4c and 4d). These results suggest that heavy doping in the  $ZrS_2$  layer enhances conductivity and charge generation by decreasing the series resistance. On the other hand, the doping density in the  $FASnI_3$  absorber had a much more impact on the solar cell performance. The FF improved from 47.12% at the lowest doping level to 88.26% at the highest, while the PCE nearly doubled from 10.93% to 19.50%. That is attributed to several factors: (1) increased built-in electric field strength that facilitates charge separation and collection, (2) reduced carrier recombination due to higher quasi-Fermi level splitting, and (3) improved conductivity and reduced resistive losses in the absorber layer [20,21]. Unlike the  $ZrS_2$  layer, the  $FASnI_3$  doping had an immediate and continuous positive effect even at lower doping levels. This confirms that optimizing the absorber layer doping plays a more critical role in achieving high-efficiency solar cell performance.

### 3.4. Impact of the operating temperature

The operating temperature of perovskite solar cells (PSCs) affects their performance as they are typically installed outdoors and exposed to environmental conditions [22]. Table 2 summarizes the effect of different operating temperatures on the performance of the  $FASnI_3/ZrS_2$  solar cells under initial conditions. It is found that  $V_{oc}$  decreases from 0.99 to 0.82V while  $J_{sc}$  remains relatively constant when the temperature increases from 300K to 420K. The FF varies from 60 % to 64.9 %. Consequently, the power conversion efficiency decreases from approximately 12.2% at 300 K to 11% at 420 K.

**Table 2.** The parameter of  $FASnI_3/ZrS_2$  solar cells as a function of temperature

Temperature (K)	PCE (%)	FF (%)	$J_{sc}$ (mA/cm <sup>2</sup> )	$V_{oc}$ (V)
300	12.2	60.12	20.7	0.99
320	12.4	60.26	20.67	0.99
340	12.3	60.88	20.64	0.98
360	12.1	61.97	20.62	0.9
380	11.8	63.15	20.60	0.91
400	11.4	64.14	20.57	0.86
420	11.0	64.92	20.54	0.82

The results reveal that rising temperatures negatively affect solar cell performance, mainly by reducing  $V_{oc}$ ,  $J_{sc}$ , and PCE. This decline is caused by an increase in reverse saturation current density ( $J_0$ ) due to the increased thermal generation of charge carriers, as explained by the Shockley diode Equation [23]:

$$V_{oc} = \frac{nK_B T}{q} \left[ \ln \left( 1 + \frac{J_{sc}}{J_0} - \frac{V_{oc}}{J_s R_{sh}} \right) \right] \quad (4)$$

where  $V_{oc}$  is the open circuit voltage,  $n$  is the ideality factor,  $K_B$  is the Boltzmann constant,  $J_0$  is the reverse current,  $R_{sh}$  is the shunt resistance,  $T$  is the temperature (absolute), and  $q$  is the electric charge. The relationship between  $V_{oc}$  and  $J_0$  is inverse and logarithmic.

Additionally, high temperatures promote recombination by narrowing the semiconductor's energy bandgap, further reducing  $V_{oc}$ . According to the literature [23,24], higher temperatures change the properties of the materials used and reduce both the efficiency and  $V_{oc}$  of solar cells. This degradation is attributed to a change in the physical and chemical properties of the semiconductor materials used in solar cells. High temperatures break some of the bonds between atoms or molecules in solar cells. These effects reduce the energy gap of materials, change the mobility, and concentrations of charge carriers. Finally, there was a slight reduction in  $J_{sc}$ , as charge-separation processing at the interface was also reduced.

### 3.5 Effect of back-contact work function

In general, the performance of solar cells mainly depends on the alignment of energy levels at the interface between the materials used in fabrication. The properties of interfacial layers between the back and front contact electrodes, as well as the ETL and HTL, play a vital role in achieving high efficiency [25,26]. Figure 5 shows the PCEs of  $ZrS_2/FASnI_3$  solar cells as a function of different back-contact work functions. These metals are: Silver (Ag, 4.6 eV), Indium tin oxide (ITO, 4.7eV), Iron (Fe, 4.8eV), Cobalt (Co, 4.9C), Gold (Au, 5.1eV), Tungsten (W, 5.2ev), Nickel (Ni, 5.3) [27]. The PCE curve shows that increasing the back-contact work function from 4.6 eV to 5.3 eV increases PCE from 6.7% to 13.1%. That depends on the properties of the interfacial contact between the metals and the  $FASnI_3$  layers, which are determined by the chemical interaction between them. Metals with high work functions (W and Ni) form near-ohmic contacts with the  $FASnI_3$  layer, consequently facilitating hole extraction and producing high PCE. In contrast, metals with lower work functions, such as Ag and ITO, produce low PCE due to forming in Schottky barriers that hinder hole extraction. These results emphasize that better energy-level alignment at the metal (work function > 5eV) / $FASnI_3$  interface enhances charge-carrier extraction and overall solar cell efficiency.

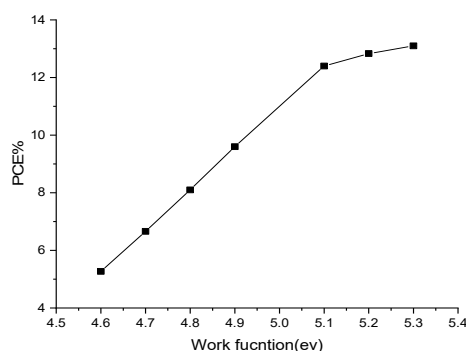


**Figure 5.** The PCE of  $\text{FASnI}_3/\text{ZrS}_2$  solar cells as a function of the work function of the back contact

### 3.6 Device optimization

Optimal device performance is achieved by optimizing various variables of the solar cells. Figure 6 illustrates the difference in the current-voltage characteristics of optimized and non-optimized solar cells. In this work, an optimization route is presented that significantly enhances the efficiency of  $\text{FASnI}_3/\text{ZrS}_2$  solar cells, offering an essential reference for further development of high-performance photovoltaic devices. After optimization, the open-circuit voltage (VOC) was adjusted from 0.99 V to 0.93 V, while the short-circuit current density (JSC) increased from 20.7  $\text{mA}/\text{cm}^2$  to 30.2  $\text{mA}/\text{cm}^2$ . This was accompanied by an improvement in the fill factor (FF) from 60.1% to 82.4%, leading to an enhancement in the power conversion efficiency (PCE) from 12.4% to 23.3%. These enhancements are attributed to increasing the thickness of the  $\text{FASnI}_3$  absorber layer from 0.2  $\mu\text{m}$  to 1.5  $\mu\text{m}$ , which improves photon absorption, generates more electron-hole pairs, and increases the short-circuit current density. Additionally, the  $\text{ZrS}_2$  electron transport layer thickness was modified to 1.0  $\mu\text{m}$ , which facilitated more efficient electron extraction and minimized recombination losses at the interface. A significant increase in the acceptor doping concentration of both  $\text{FASnI}_3$  and  $\text{ZrS}_2$  – from  $1 \times 10^{17} \text{ cm}^{-3}$  to  $1 \times 10^{21} \text{ cm}^{-3}$  – strengthened the built-in electric field across the junction, enhancing charge carrier separation and reducing resistive losses. Finally, increasing the back contact work function to 5.3 eV optimized the energy level alignment, improving hole collection and suppressing recombination at the rear interface.

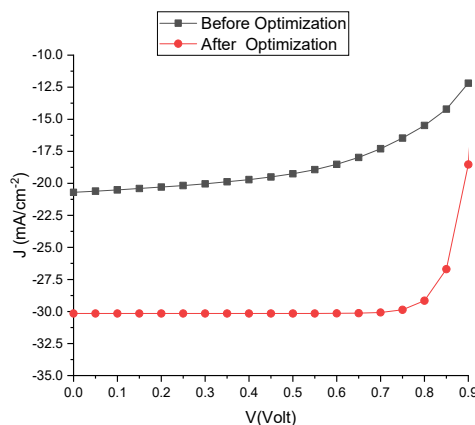


**Figure 6.** J-V curves before and after optimization

## 4. CONCLUSIONS

This study successfully demonstrated the numerical optimization of lead-free  $\text{FASnI}_3/\text{ZrS}_2$  perovskite solar cells using SCAPS-1D simulation. By systematically varying key parameters such as layer thickness, defect density, doping concentration, operating temperature, and back-contact work function, the device performance was significantly enhanced. The optimized solar cell achieved a remarkable power conversion efficiency of 23.3%, with improved open-circuit voltage, short-circuit current, and fill factor compared to the initial design. The improvements are mainly attributed to increased thickness and doping density of the absorber and electron transport layers, as well as better energy alignment through a higher back-contact work function. These results provide valuable guidance for developing efficient and environmentally friendly lead-free perovskite solar cells.

### Acknowledgements

The authors are thankful to Prof. Marc Burgelman of the University of Gent, Belgium, for providing the SCAPS 1D software for their studies.

### ORCID

©Hmoud Al-Dmour, <https://orcid.org/0000-0001-5680-5703>

## REFERENCES

- [1] J. Zhang, Geosci. Front. 15(5), 101873 (2024). <https://doi.org/10.1016/j.gsf.2024.101873>
- [2] M.S. Reza, A. Ghosh, N. Drissi, H. Al-Dmour, R.K. Prodhon, M.M. Islam, S. Begum, *et al.*, RSC Adv. **14**, 36675 (2024). <https://doi.org/10.1039/D4R07912D>
- [3] A.S. Abdulkarim, M. Srivastava, T. Ngulezhu, D. Singh, K. Strzałkowski, R.C. Singh, M.Z.A. Yahya, *et al.*, Curr. Appl. Phys. **71**, 190 (2025). <https://doi.org/10.1016/j.cap.2024.12.025>
- [4] A. Kojima, K. Teshima, Y. Shirai, and T. Miyasaka, J. Am. Chem. Soc. **131**(17), 6050 (2009). <https://doi.org/10.1021/ja809598r>
- [5] M. Tarekuzzaman, N. Shahadat, M. Montasir, O. Alsalmi, M.H. Mia, H. Al-Dmour, M. Rasheduzzaman, and M.Z. Hasan, RSC Adv. **15**, 13643 (2025). <https://doi.org/10.1039/D5RA01748C>
- [6] K. Sekar, L. Marasamy, S. Mayarambakam, H. Hawashin, M. Nour, and J. Bouclé, RSC Adv. **13**, 25483 (2023). <https://doi.org/10.1039/D3RA04617D>
- [7] A. Yadegarifard, H. Lee, H.-J. Seok, I. Kim, B.-K. Ju, H.-K. Kim, and D.-K. Lee, Nano Energy, **112**, 108481 (2023). <https://doi.org/10.1016/j.nanoen.2023.108481>
- [8] A. Rehman, S. Afzal, I. Naeem, D. Bibi, S.G. Sarwar, F. Nabeel, and R.M. Obodo, Hybrid Adv. **7**(2), 100301 (2024). <https://doi.org/10.1016/j.hybadv.2024.100301>
- [9] S.A.A. Jafri, R.S. Almufarji, A. Ashfaq, R.S. Alqurashi, L.G. Alharbe, A.R. Abd-Elwahed, O.A. Albeydani, *et al.*, Sol. Energy, **270**, 112391 (2024). <https://doi.org/10.1016/j.solener.2023.112391>
- [10] H. Al-Dmour, East Eur. J. Phys. (2), 445 (2024). <https://doi.org/10.26565/2312-4334-2024-2-58>
- [11] M. Abdelfatah, A. El-Sayed, W. Isamil, V. Sittinger, and A. El-Shaer, Sci. Rep. **13**, 4553 (2023). <https://doi.org/10.1038/s41598-023-31553-4>
- [12] M. Burgelman, P. Nollet, and S. Degraeve, Thin Solid Films, **361-362**, 527 (2000). [https://doi.org/10.1016/S0040-6090\(99\)00825-1](https://doi.org/10.1016/S0040-6090(99)00825-1)
- [13] B. Zaidi, N. Mekhaznia, M.S. Ullah, and H. Al-Dmour, J. Phys.: Conf. Ser. **2843**, 012012 (2024). <https://doi.org/10.1088/1742-6596/2843/1/012012>
- [14] A. Das, S.D. Peu, M.A.M. Akanda, M.M. Salah, M.S. Hossain, and B.K. Das, Energies, **16**, 2328 (2023). <https://doi.org/10.3390/en16052328>
- [15] A. Rehman, S. Afzal, I. Naeem, D. Bibi, S.G. Sarwar, F. Nabeel, and R.M. Obodo, Hybrid Adv. **7**, 100301 (2024). <https://doi.org/10.1016/j.hybadv.2024.100>
- [16] O.J. Sandberg, A. Sundqvist, M. Nyman, and R. Österbacka, Phys. Rev. Appl. **5**, 044005 (2016). <https://doi.org/10.1103/PhysRevApplied.5.044005>
- [17] H. Al-Dmour, and D.M. Taylor, J. Ovonic Res. **19**(5), 587 (2023). <https://doi.org/10.15251/JOR.2023.195.587>
- [18] L. Zhao, J. Schmidt, and A. Cuevas, Appl. Phys. Lett. **101**, 123904 (2012). <https://doi.org/10.1063/1.4754609>
- [19] H. Karmaker, A. Siddique, B.K. Das, and M.N. Islam, Results Eng. **22**, 102106 (2024). <https://doi.org/10.1016/j.rineng.2024.102106>
- [20] G.G. Njema, B.C. Mosonik, C.C. Ahia, and J.K. Kibet, Chem. Eur. J. **30**(71), e202403192 (2024). <https://doi.org/10.1002/chem.202403192>
- [21] H. Al-Dmour, AIMS Mater. Sci. **8**(2), 261 (2021). <https://doi.org/10.3934/matersci.2021017>
- [22] S. Wu, C. Li, S.Y. Lien, and P. Gao, Chemistry, **6**, 207 (2024). <https://doi.org/10.3390/chemistry6010010>
- [23] D.W. Husainat, P. Ali, J. Cofie, J. Attia, A. Fuller, and A. Darwish, AJOP, **8**(1), 6 (2020). <https://doi.org/10.11648/j.ajop.20200801.12>
- [24] T. Rahman, A.A. Mansur, M.S.H. Lipu, *et al.*, Energies, **16**(9), 3706 (2023). <https://doi.org/10.3390/en16093706>
- [25] G.G. Njema, J.K. Kibet, S.M. Ngari, Measurement: Energy, **2**, 100005 (2024). <https://doi.org/10.1016/j.meae.2024.100005>
- [26] M.A. Madanat, A.A. Al-Tabbakh, M. Alsaeed, H. Al-Dmour, and M.S. Mousa, Ultramicroscopy, **234**, 113479 (2022). <https://doi.org/10.1016/j.ultramic.2022.113479>
- [27] A. Kumar, N.P. Singh, A. Sundaramoorthy, Mater. Lett. X, **12**, 100092 (2021). <https://doi.org/10.1016/j.mblux.2021.100092>

**ЧИСЛОВЕ ДОСЛІДЖЕННЯ БЕЗСВИНЦЕВИХ ПЕРОВСКІТНИХ СОНЯЧНИХ ЕЛЕМЕНТІВ НА ОСНОВІ  
СТРУКТУРИ FASnI<sub>3</sub>/ZrS<sub>2</sub> ЗА ДОПОМОГОЮ СИМУЛЯТОРА SCAPS-1D**








**Хмуд Аль-Дмур**

*Університет Мута, факультет природничих наук, кафедра фізики, 61710, Йорданія*

У цьому дослідженні представлено чисельне дослідження та оптимізацію сонячних елементів на основі безсвинцевого перовскіту за допомогою моделювання SCAPS-1D. Запропонований пристрій складається з йодиду формамідінію-олова (FASnI<sub>3</sub>, поглинаючий шар), дисульфиду цирконію (ZrS<sub>2</sub>, матеріал для переносу електронів), золота (Au, задній контакт) та легованого фтором оксиду олова (SnO<sub>2</sub>:F, передній контакт). Було досліджено вплив зміни товщини, щільності дефектів, концентрації легування, робочої температури та роботи виходу заднього контакту на характеристики фотоелектричної системи з метою визначення оптимальної архітектури пристрою з найвищою ефективністю перетворення енергії (PCE). Результати показують, що початкова продуктивність сонячних елементів FASnI<sub>3</sub>/ZrS<sub>2</sub> була наступною: напруга холостого ходу (VOC) = 0,99 В, струм короткого замикання (JSC) = 20,7 мА/см<sup>2</sup>, коефіцієнт заповнення (FF) = 60,13% та коефіцієнт перетворення потужності (PCE) = 12,4%. Після оптимізації продуктивність FASnI<sub>3</sub>/ZrS<sub>2</sub> значно покращилася, досягнувши PCE 23,3%, FF 82,4% та JSC 30,2 мА/см<sup>2</sup>. Це помітне покращення цих параметрів пояснюється збільшенням товщини та щільності легування шарів FASnI<sub>3</sub> та ZrS<sub>2</sub>, що призводить до покращеного поглинання світла та генерації заряду. Крім того, було виявлено, що робота виходу зворотного контакту 5,3 еВ створює краще узгодження енергетичних рівнів із шаром FASnI<sub>3</sub>, що сприяє вилученню заряду. Ці результати пропонують цінну інформацію про розробку ефективних, стабільних та безсвинцевих перовскітних сонячних елементів.

**Ключові слова:** FASnI<sub>3</sub>; ZrS<sub>2</sub>; SCAPS-1D; безсвинцеві перовскітні сонячні елементи; шар електрон-транспорт; фотоелектричне моделювання; сонячна енергія

## ENHANCING AND OPTIMIZING OPTICAL PROPERTIES OF BIFACIAL SOLAR CELLS BY INCORPORATING METAL NANOPARTICLES

 Murodjon M. Komilov<sup>1</sup>,  Rayimjon Aliev<sup>1</sup>,  Avazbek A. Mirzaalimov<sup>2</sup>,  Suhrob R. Aliev<sup>4</sup>,  
 Murodjon K. Abduvohidov<sup>3</sup>,  Navruzbek A. Mirzaalimov<sup>1\*</sup>,  J. Ziyoidtinov<sup>1</sup>,  
 Sodiqjon I. Temirov<sup>1</sup>

<sup>1</sup>Andijan State University named after Z.M. Babur, 129, Universitet Str., 170100 Andijan, Uzbekistan

<sup>2</sup>Andijan State Pedagogical Institute, 4, Dostlik Str., 170100 Andijan, Uzbekistan

<sup>3</sup>Kokand University Andijan branch, 2-b, Boburshoh Str., 170100 Andijan, Uzbekistan

<sup>4</sup>Andijan State Technical Institute, 56, Boburshoh Str., 170100 Andijan, Uzbekistan

\*Corresponding Author e-mail: [mirzaalimov90@mail.ru](mailto:mirzaalimov90@mail.ru)

Received August 11, 2025; revised November 11, 2025; accepted November 15, 2025

In this study, the optical properties of a silicon-based bifacial solar cell with an  $n^+p-p^+$  structure were investigated using numerical simulation in the Sentaurus TCAD environment. Various metal nanoparticles were embedded in the emitter layer in a linear configuration to analyze their effects on light absorption and scattering. The study compared metal nanoparticles of platinum (Pt), gold (Au), silver (Ag), aluminum (Al), and copper (Cu). All nanoparticles were modeled with the same diameter (5 nm), and the current-voltage ( $I$ - $V$ ) characteristics were obtained for each configuration. The simulation results showed that platinum nanoparticles yielded the highest short-circuit current density of 13.8 mA/cm<sup>2</sup>, while silver nanoparticles yielded the lowest, at 5.027 mA/cm<sup>2</sup>. Optimal parameters were observed with nanoparticles of 5 nm in diameter. Furthermore, it was found that the photon absorption density for the most efficient metal type was 1.81 times greater than that of the reference structure without nanoparticles. Additionally, the spectral sensitivity of silicon shifted toward the ultraviolet region in the presence of metal nanoparticles. The study demonstrated enhanced utilization of the visible light spectrum, and due to the embedded nanoparticles, the overall absorption coefficient of the bifacial solar cell increased by a factor of 1.33, aligning more effectively with the visible spectral range.

**Keywords:** Silicon; Metal nanoparticles; Bifacial solar cell; Sentaurus TCAD; Nanoplasmonic effect

**PACS:** 85.60.Bt, 78.20.Bh, 84.60.Jt

### INTRODUCTION

Among renewable energy sources, solar energy is gaining an increasingly important role in the global energy system. This form of energy is environmentally friendly and represents an inexhaustible energy source [1]. Enhancing the efficiency of solar cells is currently one of the key research directions in science and technology. In particular, bifacial solar cells, distinguished by their ability to absorb light from both the front and rear sides, can increase their overall energy generation potential by up to 10–30% [2].

Silicon-based solar cells belong to the class of devices that are highly sensitive to environmental conditions. The effects of light intensity [3], temperature [4], and the angle of light incidence on solar cell performance has been widely investigated. It has been established that an increase in temperature leads to a slight rise in short-circuit current, while the open-circuit voltage decreases significantly, resulting in an overall reduction of the power conversion efficiency [5]. Numerous comprehensive studies have been conducted to enhance the efficiency of solar cells and minimize losses. In general, there are three primary loss mechanisms in solar cells: thermal [6], electrical [7], and optical [8]. In conventional silicon-based solar cells, more than 30% of the incident light is reflected from the surface [9]. To reduce this reflection coefficient, various anti-reflective coatings [10] and surface texturing techniques [11] have been developed. The surfaces of silicon-based solar cells are commonly coated with SiNx or SiO<sub>2</sub>, as these materials possess passivation properties and have refractive indices between those of air and silicon [12]. In practice, surface texturing is achieved using alkaline or acidic solutions, and silicon wafers with a (100) crystal orientation are typically employed [13]. Since the bandgap of silicon is 1.12 eV, it mainly absorbs photons in the visible spectral range. According to the quantum efficiency function, solar cell materials do not absorb photons with energies lower than the bandgap. If the photon energy is much greater than the bandgap, the excess energy is converted into hot electrons. These high-energy hot electrons quickly lose their excess energy through phonon emission, returning to the valence band and thus not contributing to the photocurrent. Therefore, to modify the absorption spectrum of solar cells, luminescent materials [14] or metallic nanoparticles [15] are often incorporated.

In converting solar energy into other forms, the device's optical properties play a crucial role. Surface texturing of various shapes on solar cells has been effectively employed to enhance light absorption [16]. Due to multiple refractions of sunlight at the surface, its energy is absorbed more efficiently. The presence of a  $p$ - $n$  junction near the surface requires maximizing light absorption in its vicinity [17]. Increased light absorption close to the  $p$ - $n$  junction results in a higher generation rate of charge carriers [18]. Therefore, surface textures with varying heights are fabricated on solar cells [19].

**Cite as:** M.M. Komilov, R. Alieva, A.A. Mirzaalimov, S.R. Aliev, M.K. Abduvohidov, N.A. Mirzaalimov, J. Ziyoidtinov, S.I. Temirov, East Eur. J. Phys. 4, 291 (2025), <https://doi.org/10.26565/2312-4334-2025-4-27>

© M.M. Komilov, R. Alieva, A.A. Mirzaalimov, S.R. Aliev, M.K. Abduvohidov, N.A. Mirzaalimov, J. Ziyoidtinov, S.I. Temirov, 2025; CC BY 4.0 license

These textures cause incident light rays to undergo multiple reflections within the structure, thereby increasing their interaction with the surface. Consequently, the degree of light absorption by the surface is significantly enhanced.

Currently, methods for generating additional charge carriers near the p–n junction are being continually improved. In particular, the use of metallic nanoparticles to enhance the optical and electrical properties of solar cells has emerged as a promising approach [20]. Metallic nanoparticles such as gold (Au), silver (Ag), and platinum (Pt) can enhance light scattering and absorption through the localized surface plasmon resonance (LSPR) phenomenon [21][22]. This effect leads to a localized enhancement of the electric field around the nanoparticles, thereby increasing the number of photons reaching the active layer [23]. Based on these mechanisms, numerous studies have confirmed that modifying solar cells with metallic nanoparticles can broaden the optical absorption spectrum, enhance scattering angles, and ultimately improve photogeneration efficiency [24][25]. For example, J. Zhu et al. demonstrated that the application of nanostructures could double the light absorption in illuminated solar cells **Error! Reference source not found..**

In this study, the optical and electrical properties of bifacial silicon-based solar cells were investigated by introducing metallic nanoparticles (Au, Pt, Cu, Al, Ag) into the emitter layer through numerical modeling using the Sentaurus TCAD software package. Based on the simulation results, the effects of nanoparticle radius and material type on the photocurrent density and current–voltage characteristics were determined. The results showed that the optimal selection of nanoparticle parameters can significantly improve light absorption, thereby enhancing the overall efficiency of the solar cell.

## MATERIALS AND METHODS

In this study, the effects of various metallic nanoparticles on the optical and electrical properties of a bifacial solar cell were investigated. The selected nanoparticles included silver (Ag), aluminum (Al), copper (Cu), gold (Au), and platinum (Pt). These materials were chosen due to their high nanoplasmonic activity as well as their strong light scattering and absorption capabilities, which play a crucial role in enhancing light–matter interactions within the solar cell. The device structure was based on a conventional n–p–p configuration, with both the front and rear sides designed to be light-absorbing. The top and bottom contacts consisted of metallic layers that efficiently received incident radiation through the intermediate layers. Metallic nanoparticles were embedded into the upper active emitter layer. In addition to the nanoparticle material, the radius (ranging from 1 to 25 nm) was considered as a variable parameter, and for each radius value, the optical and electrophysical characteristics of the solar cell were evaluated. During the optical simulations, the nanoparticle-specific surface plasmon resonance frequencies and absorption coefficients were taken into account. All numerical modeling procedures were performed using the Sentaurus TCAD software package.

During the simulation process, the following Sentaurus TCAD modules were employed as the primary tools:

*SDE (Sentaurus Structure Editor)* – used to design the geometric structure of the device, precisely defining the layers and positioning the nanoparticles;

*SProcess* – applied for adjusting dopant profiles and determining the exact placement of nanoparticles;

*SDevice* – used for electrophysical simulations of the device, including the calculation of current–voltage (I–V) and power–voltage (P–V) characteristics, electric field distribution, optical absorption levels, and photocurrent density;

*Sentaurus Visual* – employed for the visual analysis of the obtained results and for generating gradient maps of parameter distributions.

In the optical simulation stage, the complex absorption coefficients corresponding to each metallic nanoparticle were incorporated based on the optical models of the respective materials. The AM1.5G spectrum was adopted as the illumination source.

The primary photovoltaic parameters of the solar cell were determined using the current–voltage (I–V) characterization method, which enables the evaluation of output parameters for all types of solar cells. Fig. 1 presents the equivalent circuit of the device.

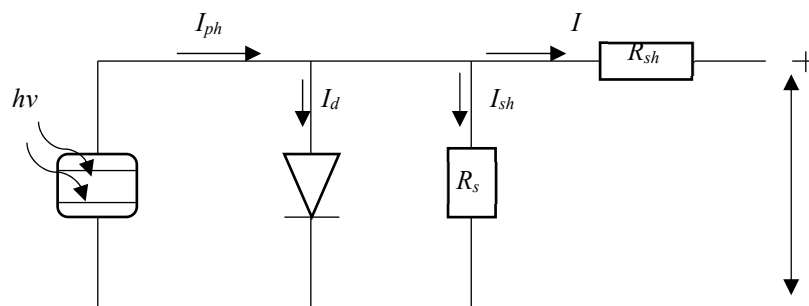


**Figure 1.** Equivalent circuit of a solar cell

Here,  $I_{ph}$  is the photocurrent,  $I$  is the total current in the circuit,  $I_d$  is the current flowing through the diode, and  $I_{sh}$  is the current passing through the shunt resistance. Applying Ohm's law to the entire circuit shown in Fig. 1, the total current can be expressed as:

$$I_{ph} = I + I_d + I_{sh} \quad (1)$$



The value of each current in the equation is determined separately. After that, the final working equation is obtained. The final equation can be seen in formula (2) below.

$$I_d = I_o \left[ \exp \left( \frac{U + IR_s}{nkT} q \right) - 1 \right], I_{sh} = \frac{U + IR_s}{R_{sh}}. \quad (2)$$

Here,  $I_o$  is the maximum current through the diode,  $R_s$  is the series resistance,  $U$  is the output voltage,  $q$  is the electron charge,  $n$  is the ideality factor,  $k$  is the Boltzmann constant, and  $T$  is the temperature.

Formula 2 represents the complete current equation of the solar cell during the circuit connection process [27]. By applying boundary conditions to this equation, modifications are introduced. For this purpose, the parameters at the maximum power point from the current–voltage characteristic graph are used. To determine the maximum power point, it is sufficient to take the product of the maximum current and voltage [28]. Fig. 2 shows the  $I$ – $V$  characteristic of the solar cell.

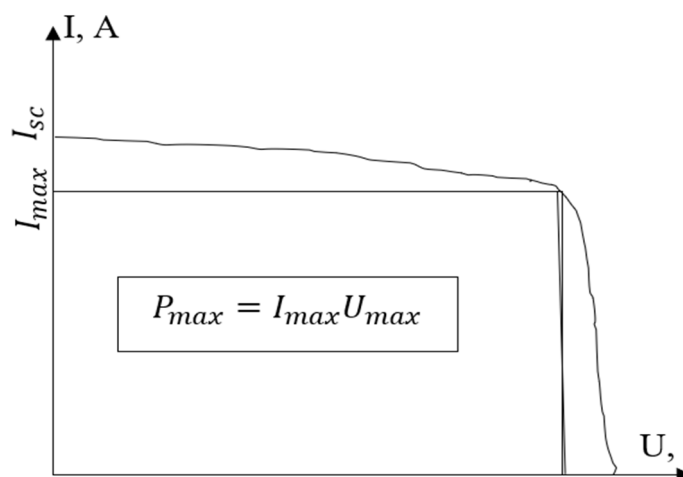


**Figure 2.** Current–voltage ( $I$ – $V$ ) characteristic of the solar cell.

By determining the  $I$ – $V$  characteristic of the solar cell, the short-circuit current and open-circuit voltage can be identified. If the initial conditions are set, when the short-circuit current in the  $I$ – $V$  characteristic approaches zero, the open-circuit voltage takes its maximum value. This can be seen below.

$$U = U_{oc}; I = I_{sc} = 0. \quad (3)$$

Through the condition in this 3rd formula, we obtain the following equation.

$$I_{ph} = 0 + I_o \left[ \exp \left( \frac{qU_{oc}}{nkT} \right) - 1 \right] + \frac{U_{oc}}{R_{sh}}, \quad (4)$$

$$I_{ph} = I_o \left[ \exp \left( \frac{qU_{oc}}{nkT} \right) - 1 \right] + \frac{U_{oc}}{R_{sh}}. \quad (5)$$

The 5th formula above clearly allows the determination of the photocurrent passing through the solar cell. Based on these formulas, the current–voltage characteristic of the bifacial solar cell with various metal nanoparticles introduced was determined.

## RESULTS AND DISCUSSION

Front-side illumination was applied to the bifacial solar cell with various metal nanoparticles introduced. For comparison purposes, the output parameters of the solar cell without nanoparticles were measured (Fig. 3).

As shown in the graph, all metal types yielded high current densities, with the solar cell without nanoparticles showing the lowest. Positive results were obtained for nanoparticles based on all tested materials. Among them, platinum showed the best performance, reaching a current density of 13.8 mA/cm<sup>2</sup>, while silver produced the lowest value of 5.027 mA/cm<sup>2</sup>. Based on these results, it was decided to continue the experiments with platinum.

The output parameters of the solar cell with platinum nanoparticles increased. These output parameters are significantly dependent on the shape and size of the nanoparticles. Therefore, in the experiment, platinum was taken in spherical form. The spherical particle shape is associated with its ability to generate a uniform field and wave propagation around itself. The sphere's radius was increased in steps of 1 nm. As a result, the dependence of current density on particle radius was obtained (Fig. 4). The introduction of an atom or particle into the solar cell changes its current density. At the same time, the open-circuit voltage depends only on the material type and environmental conditions.

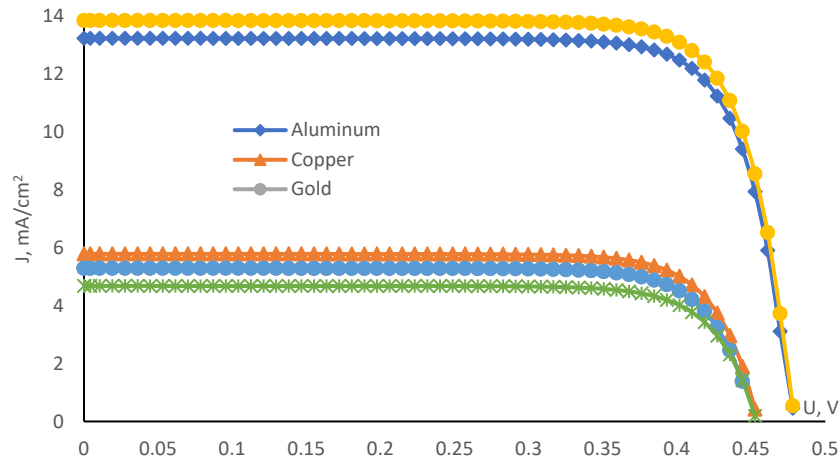


**Figure 3.**  $I$ - $V$  characteristics of the bifacial solar cell with various metal nanoparticles

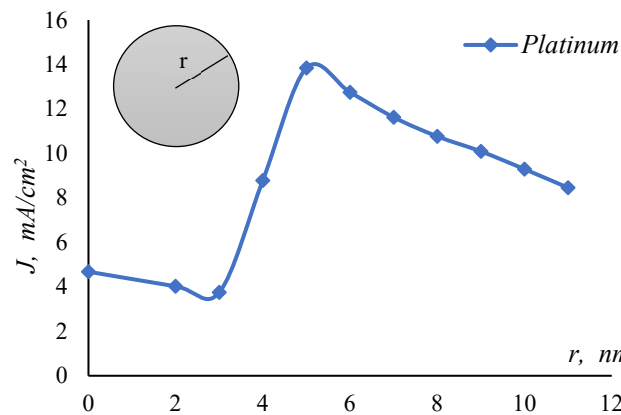


**Figure 4.** Dependence of the current density of the bifacial solar cell with platinum nanoparticles on the nanoparticle radius.

From the graph in Fig. 4, it can be seen that the current density of the bifacial solar cell with metal nanoparticles shows a significant dependence on the nanoparticle radius. In this case, the nanoparticle size causes the current density to increase in certain ranges and decrease in others. Accordingly, the optimal size of the metal nanoparticle was determined. For platinum nanoparticles, the optimal size was found to be 5 nm. According to the results, the optimal-size current density value was 2.96 times higher than that of the bifacial solar cell without nanoparticles. Measurements also showed that for sizes larger than 5 nm, a decrease in current density was observed. This decrease at sizes larger than the optimal radius is explained by the nanoplasmonic effect occurring in the structure. The occurrence of the nanoplasmonic effect first influences the local electric field, then affects the surface. The spatial extent of the generated electric field should be significantly larger than the nanoparticle size.

Below, the  $I$ - $V$  and  $P$ - $V$  characteristics of bifacial solar cells without and with nanoparticles are shown (Fig. 5).

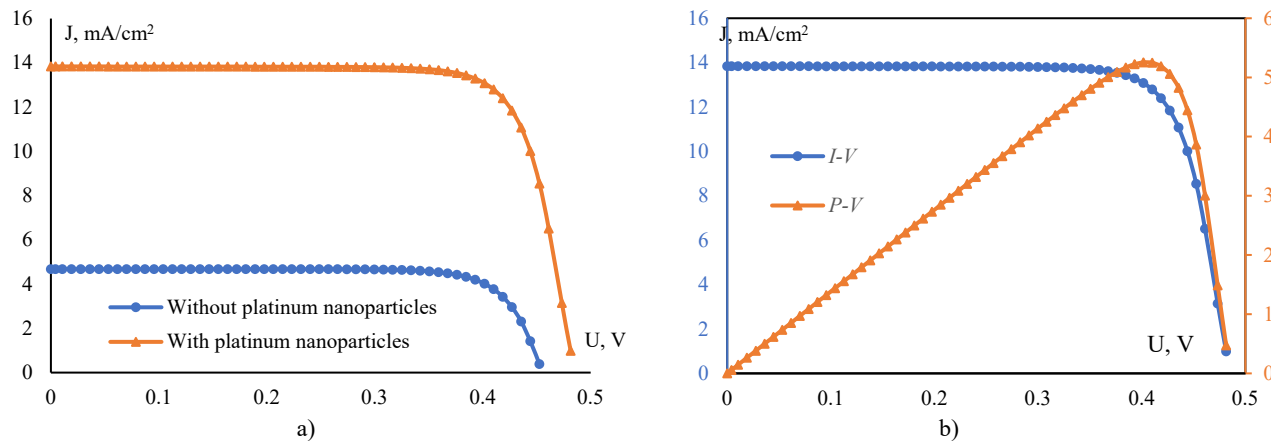


**Figure 5.** a)  $I$ - $V$  characteristics of bifacial solar cells with and without platinum nanoparticles, b)  $P$ - $V$  characteristics of the bifacial solar cell with platinum nanoparticles

From the above graphs, it can be seen that the current density generated by the solar cell with platinum nanoparticles is almost three times higher. Accordingly, the output power and the maximum power point were determined. The



maximum output power was found to be 5.25 mW, with the current density and voltage at this point being 13.08 mA/cm<sup>2</sup> and 0.401 V, respectively. The relatively small values of the output parameters indicate that the selected sample has a small size. This is because, at smaller sizes, the effect of metal nanoparticles on the selected sample becomes more significant.

The influence of nanoparticles is crucial in achieving higher output parameters. Since the nanoparticles are arranged in a straight line within the emitter layer of the solar cell, an additional light spectrum is generated in that layer. Metals, when exposed to incident light, perform the function of generating charge carriers through the light scattered back from them. The light scattered from the nanoparticles interacts with each other, producing high intensity in that region. As a result, the value of optical generation in that area increases.

The graph of optical generation as a function of solar cell thickness is shown in Fig. 6.

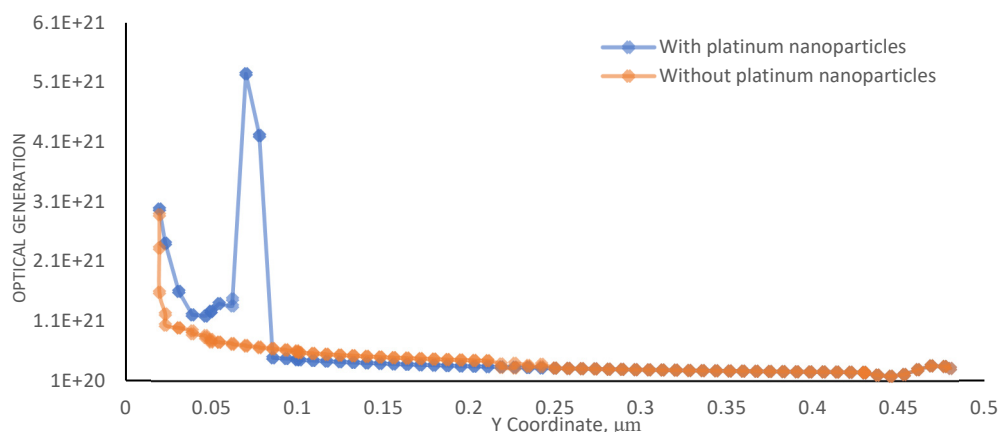


**Figure 6.** Optical generation of a bifacial solar cell as a function of its thickness

It can be seen from Figure 6 that the nanoparticle embedded in the emitter layer increased the optical generation of the solar cell by almost 1.81 times. In this graph, the optical generation of a solar cell without nanoparticles decreases exponentially. If nanoparticles are not embedded into the emitter layer, light intensity is more absorbed towards the base. Therefore, embedding nanoparticles into the emitter layer increases the light intensity in this layer, resulting in reduced absorption in the base region.

The absorption of light is directly related to its spectrum. Secondly, it is strongly dependent on the thickness of the solar cell. Thickness affects the internal interference process within the solar cell. The optical properties of light in a material are determined by its absorption, transmission, and reflection coefficients. By increasing absorption, it is possible to reduce the values of transmission and reflection coefficients. Therefore, in this research, the dependence of the absorption coefficient on the wavelength of light was determined (Fig. 7).

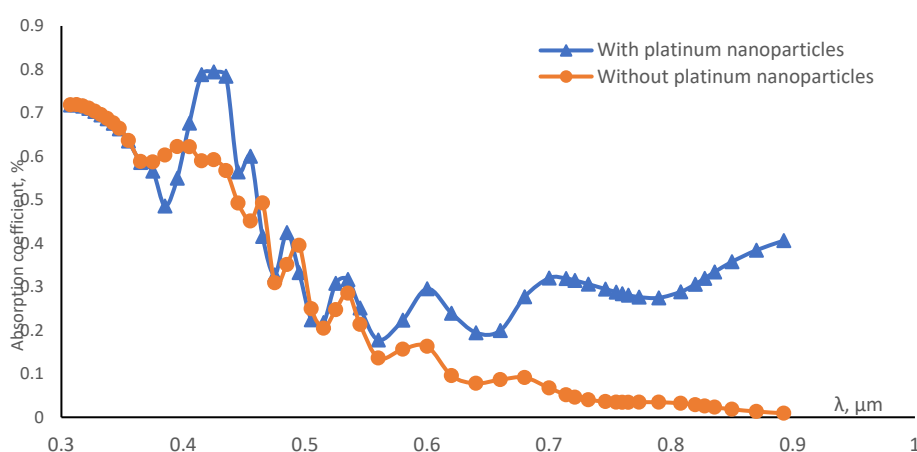


**Figure 7.** Dependence of the absorption coefficient of a bifacial solar cell on the wavelength of light

The above graph shows that the absorption coefficient of the solar cell with embedded nanoparticles is higher. It was determined that this value is 1.33 times greater than the absorption coefficient of the solar cell without nanoparticles, reaching 79.4%. For the silicon-based bifacial solar cell without nanoparticles, the absorption coefficient decreases as the wavelength of light increases, which leads to inefficient utilization of long-wavelength light. In contrast, the absorption coefficient of the nanoparticle-integrated solar cell shows good performance even at long wavelengths. Based on the obtained results, it can be concluded that the introduction of metal nanoparticles into the bifacial solar cell optimizes its optical properties.

## CONCLUSIONS

In this study, various types of metal nanoparticles were introduced into a bifacial solar cell. Among the embedded metal nanoparticles, platinum was identified as the most optimal type. Platinum, a high-efficiency metal, was selected, and its effect on the solar cell's optical properties was investigated. First, the optimal platinum nanoparticle radius for maximum performance was determined. For 5 nm platinum nanoparticles, a current density of 13.8 mA/cm<sup>2</sup> was achieved. This value was found to be 2.9 times greater than the current density of a solar cell without nanoparticles. Optimal-sized nanoparticles were embedded in the emitter layer of the solar cell, and they were observed to enhance optical generation.

In addition, the absorption coefficient values and corresponding graphs of the nanoparticle-integrated solar cell were obtained. The results showed that absorption increased in the nanoparticle-embedded region and remained effective at long wavelengths. It can be concluded that embedding metal nanoparticles into a bifacial solar cell is a promising approach, as it optimizes its optical properties. In the future, determining the thermal and electrical conductivities of the metal nanoparticles embedded in bifacial solar cells is expected to be even more promising.

## Conflict of Interests

The authors declare that they have no conflicts of interest.

## Acknowledgments

We would like to express our deepest appreciation to our colleague at the Renewable Energy Source Laboratory at Andijan State University, for their invaluable support throughout this research.

## ORCID

✉Murodjon M. Komilov, <https://orcid.org/0009-0006-2080-3371>; ✉Navruzbek A. Mirzaalimov, <https://orcid.org/0000-0002-9264-3710>;  
✉Rayimjon Aliev, <https://orcid.org/0000-0002-7375-727X>; ✉Avazbek A. Mirzaalimov, <https://orcid.org/0000-0003-2846-1901>;  
✉Murodjon K. Abduvohidov, <https://orcid.org/0000-0002-7598-8565>; ✉Suhrob R. Aliev <https://orcid.org/0000-0002-4494-8261>;  
✉J. Ziyoyitdinov, <https://orcid.org/0009-0007-6958-4074>

## REFERENCES

- [1] M.A. Green, *Third generation photovoltaics: Advanced solar energy conversion*. Springer Science & Business Media.
- [2] A. Cuevas, "The ultimate efficiency of bifacial solar cells," *Solar Energy*, **112**, 740-745 (2005).
- [3] R. Aliev, M. Komilov, N. Mirzaalimov, A. Mirzaalimov, S. Aliev, I. Gulomova, and J. Gulomov, "Textured Bifacial Silicon Solar Cells Under Various Illumination Conditions," *Journal of Nano and Electronic Physics*. **16**(5), 05025-05031 (2024). [https://doi.org/10.21272/jnep.16\(5\).05025](https://doi.org/10.21272/jnep.16(5).05025)
- [4] R. Aliev, M. Komilov, S. Aliev, and I. Gulomova, "Comparative analysis of conventional and bifacial solar cells under various illumination conditions," *Physics and Chemistry of Solid State*, **25**(4), 844-852 (2024). <https://doi.org/10.15330/pcss.25.4.844-852>
- [5] R. Aliev, M. Komilov, I. Gulomova, A. Mirzaalimov, N. Mirzaalimov, S. Aliev, and J. Gulomov, "Effect of temperature on the properties of a bifacial textured solar cell," *Vidnovluvana Energetika*, **81**(2), 97-105 (2025). [https://doi.org/10.36296/1819-8058.2025.2\(81\).97-105](https://doi.org/10.36296/1819-8058.2025.2(81).97-105)
- [6] N.A. Mirzaalimov, R. Aliev, A.A. Mirzaalimov, B.D. Rashidov, S. Qahramonova, and T. Abdulazizov, "Hybrid Solar-Wind Micro-Energy Systems in 3D Format for City Streets," in: *Sustainable Living Solutions: Renewable Energy and Engineering. EDMSET 2024. Advances in Science, Technology & Innovation*, edited by E. Dobjani, et al. (Springer, Cham. 2025). [https://doi.org/10.1007/978-3-031-76837-8\\_20](https://doi.org/10.1007/978-3-031-76837-8_20)
- [7] L. Xu, et al., "Heat generation and mitigation in silicon solar cells and modules," *Joule*, **5**(3), 631-645 (2021). <https://doi.org/10.1016/J.JOULE.2021.01.012>
- [8] Y.Q. Gu, C. R. Xue, and M. L. Zheng, "Technologies to Reduce Optical Losses of Silicon Solar Cells," *Advanced Materials Research*, **953-954**, 91-94 (2014). <https://doi.org/10.4028/WWW.SCIENTIFIC.NET/AMR.953-954.91>
- [9] B. Hoex, M. Dielen, M. Lei, T. Zhang, and C. Y. Lee, "Quantifying optical losses of silicon solar cells with carrier selective hole contacts," *AIP Conference Proceedings*, **1999**(1), 040010 (2018). <https://doi.org/10.1063/1.5049273>
- [10] B. Kumaragurubaran, and S. Anandhi, "Reduction of reflection losses in solar cell using Anti Reflective coating," in: *2014 International Conference on Computation of Power, Energy, Information and Communication, ICCPEIC*, pp. 155-157, (2014). <https://doi.org/10.1109/ICCPEIC.2014.6915357>
- [11] S.J. Jang, et al., "Antireflective property of thin film a-Si solar cell structures with graded refractive index structure," *Optics Express*, **19**(S2), A108-A117 (2011). <https://doi.org/10.1364/OE.19.00A108>
- [12] S.C. Baker-Finch, and K.R. McIntosh, "Reflection distributions of textured monocrystalline silicon: implications for silicon solar cells," *Progress in Photovoltaics: Research and Applications*, **21**(5), 960-971 (2013). <https://doi.org/10.1002/PIP.2186>
- [13] H. Park, S. Kwon, J.S. Lee, H.J. Lim, S. Yoon, and D. Kim, "Improvement on surface texturing of single crystalline silicon for solar cells by saw-damage etching using an acidic solution," *Solar Energy Materials and Solar Cells*, **93**(10), 1773-1778 (2009). <https://doi.org/10.1016/J.SOLMAT.2009.06.012>
- [14] X. Huang, S. Han, W. Huang, and X. Liu, "Enhancing solar cell efficiency: the search for luminescent materials as spectral converters," *Chemical Society Reviews*, **42**(1), 173-201 (2012). <https://doi.org/10.1039/C2CS35288E>
- [15] J. Gulomov, and R. Aliev, "The Way of the Increasing Two Times the Efficiency of Silicon Solar Cell," *Physics and Chemistry of Solid State*, **22**(4), 756-760 (2021). <https://doi.org/10.15330/pcss.22.4.756-760>
- [16] J. Frank, M. Rüdiger, S. Fischer, J.C. Goldschmidt, and M. Hermle, "Optical Simulation of Bifacial Solar Cells. *Energy Procedia*, **27**, 300-305 (2012). <https://doi.org/10.1016/j.egypro.2012.07.067>
- [17] I.A. Yuldoshev, M.Q. Sultonov, and F.M. Yuldashev, *Quyosh energetikasi" darslik*, (Bookany print, Toshkent, 2022).
- [18] A. Blakers, N. Zin, K.R. McIntosh, and K. Fong, "High Efficiency Silicon Solar Cells," *Energy Procedia*, **33**, (2013).

- [19] H.A. Atwater, and A. Polman, "Plasmonics for improved photovoltaic devices," *Nature materials*, **9**(3), 205–213 (2010). <https://doi.org/10.1038/nmat2629>
- [20] M.Z. Nosirov, *et al.*, "Photoemission current from metal nanoparticles in silicon," *J. Nano- Electron. Phys.* **16**(5) 05026 (2024). [https://doi.org/10.21272/jnep.16\(5\).05026](https://doi.org/10.21272/jnep.16(5).05026)
- [21] K.R. Catchpole, and A. Polman, "Plasmonic solar cells," *Optics Express*, **16**(26), 21793–21800 (2008). <https://doi.org/10.1364/OE.16.021793>
- [22] R.A. Pala, J. White, E. Barnard, J. Liu, and M.L. Brongersma, "Design of plasmonic thin-film solar cells with broadband absorption enhancements," *Advanced Materials*, **21**(34), 3504–3509 (2009). <https://doi.org/10.1002/adma.200900331>
- [23] V.E. Ferry, L.A. Sweatlock, D. Pacifici, and H.A. Atwater, "Plasmonic nanostructure design for efficient light coupling into solar cells," *Nano Letters*, **8**(12), 4391–4397 (2008). <https://doi.org/10.1021/nl8022548>
- [24] P. Spinelli, M.A. Verschuuren, and A. Polman, "Broadband omnidirectional antireflection coating based on subwavelength surface Mie resonators," *Nature Communications*, **3**, 692 (2012). <https://doi.org/10.1038/ncomms1691>
- [25] J. Zhu, C.M. Hsu, Z. Yu, S. Fan, and Y. Cui, "Nanodome solar cells with efficient light management and self-cleaning," *Nano Letters*, **10**(6), 1979–1984 (2009). <https://doi.org/10.1021/nl9034237>
- [26] S.L. Khrypko, and G.K. Zholudev, "Modeling of the Electric Characteristics of Photovoltaic Cell Based on Silicon," *J. Nano-Electron. Phys.* **3**(3), 90-99 (2011).
- [27] A.M. Laoufi, B. Dennai, O. Kadi, and M. Fillali, "Study of the Effect of Absorber Layer Thickness of CIGS Solar Cells with Different Band Gap Using SILVACO TCAD," *Journal of nano- and electronic physics*, **13**(4), 04018 (2021). [https://doi.org/10.21272/jnep.13\(4\).04018](https://doi.org/10.21272/jnep.13(4).04018)
- [28] R.V. Zaitsev, and M.V. Kirichenko. Improving the Physical Model of GaAs Solar Cells. *Journal of Nano- And Electronic Physics* **12**(6), 06015 (2020). [https://doi.org/10.21272/jnep.12\(6\).06015](https://doi.org/10.21272/jnep.12(6).06015)

#### ПОКРАЩЕННЯ ТА ОПТИМІЗАЦІЯ ОПТИЧНИХ ВЛАСТИВОСТЕЙ ДВУХФАЦІАЛЬНИХ СОНЯЧНИХ ЕЛЕМЕНТІВ ШЛЯХОМ ДОДАВАННЯ МЕТАЛЕВИХ НАНОЧАСТИНОК

Муроджон М. Комілов<sup>1</sup>, Райімжон Алієв<sup>1</sup>, Авазбек А. Мірзаалімов<sup>2</sup>, С.Р. Алієв<sup>4</sup>, Муроджон К. Абдувохидов<sup>3</sup>,  
Наврўзбек А. Мірзаалімов<sup>1</sup>, Дж. Зійотдінов<sup>1</sup>, Содікджон І. Теміров<sup>1</sup>

<sup>1</sup>Андижанський державний університет імені З.М. Бабура, Андижан, Узбекистан

<sup>2</sup>Андижанський державний педагогічний інститут, Андижан, Узбекистан

<sup>3</sup>Андижанська філія Кокандського університету, Андижан, Узбекистан

<sup>4</sup>Андижанський державний технічний інститут, Андижан, Узбекистан

У цьому дослідженні було досліджено зміни оптичних властивостей двостороннього сонячного елемента на основі кремнію зі структурою  $n^+-p-p^+$  за допомогою числового моделювання з використанням програмного середовища Sentaurus TCAD. Різні металеві наночастинки були вбудовані в шар емітера в лінійній конфігурації для аналізу їхнього впливу на процеси поглинання та розсіювання світла. У дослідженні порівнювалися металеві наночастинки платини (Pt), золота (Au), срібла (Ag), алюмінію (Al) та міді (Cu). Всі наночастинки були змодельовані з однаковим діаметром (5 нм), і для кожної конфігурації були отримані вольт-амперні (ВА) характеристики. Результати моделювання показали, що наночастинки платини дали найвищу щільність струму короткого замикання - 13,8 мА/см<sup>2</sup>, тоді як наночастинки срібла дали найнижчу - 5,027 мА/см<sup>2</sup>. Оптимальні параметри спостерігалися для наночастинок діаметром 5 нм. Крім того, було виявлено, що щільність поглинання фотонів для найефективнішого типу металу була в 1,81 рази більшою, ніж у еталонної структури без наночастинок. Крім того, спектральна чутливість кремнію змістилася в ультрафіолетову область у присутності металевих наночастинок. Дослідження продемонструвало покращене використання спектру видимого світла, і завдяки вбудованим наночастинкам загальний коефіцієнт поглинання двостороннього сонячного елемента збільшився в 1,33 рази, що ефективніше узгоджується з видимим спектральним діапазоном.

**Ключові слова:** кремній; металеві наночастинки; двосторонній сонячний елемент; TCAD Sentaurus; наноплазмонний ефект

## ENERGY TRANSPORT IN A MHD HYBRID NANOFLUID FLOW OVER A POROUS EXPONENTIALLY STRETCHING SHEET

 **Mahesh Joshi<sup>§</sup>**,  **G. Venkata Ramana Reddy<sup>\*</sup>**

*Department of Mathematics, Koneru Lakshmaiah Education Foundation,  
Green fields, Vaddeswaram, Guntur-522302, Andhra Pradesh, India*

*\*Corresponding Author: [gvrr1976@kluniversity.in](mailto:gvrr1976@kluniversity.in), <sup>§</sup>E-mail: [mjprince939@gmail.com](mailto:mjprince939@gmail.com)*

Received August 3, 2025; revised September 15, 2025; in final form September 17, 2025; accepted September 22, 2025

This study presents an in-depth analysis of the heat transfer mechanisms and fluid flow behavior associated with hybrid nanofluids in the presence of an exponentially stretching surface. Hybrid nanofluids, formed by dispersing more than one type of nanoparticle within a base fluid, exhibit superior thermophysical properties compared to conventional nanofluids. Their enhanced thermal conductivity, modified density, and tailored specific heat capacity make them highly suitable for advanced applications in nanotechnology, renewable energy systems, high-performance electronics cooling, and industrial-scale heat exchangers. The novelty of the present research lies in its attempt to explore the combined impact of hybrid nanoparticles and exponential stretching on boundary layer dynamics, thereby offering new insights into optimizing thermal systems. The core aim of this investigation is to maximize heat transfer efficiency under varying physical and operational conditions. To achieve this, the governing partial differential equations describing the conservation of mass, momentum, and energy are transformed into a set of nonlinear ordinary differential equations using similarity transformations and appropriate dimensionless parameters. This mathematical reformulation simplifies the complexity of the problem while preserving the essential physics of the flow. A computational framework is developed in MATLAB, where the coupled system of equations is solved using the fourth-order Runge–Kutta method integrated with a shooting technique to ensure accuracy and stability. The analysis highlights the roles of key parameters such as magnetic field intensity, Eckert number (viscous dissipation effects), Prandtl number (thermal diffusivity effects), and thermal radiation on velocity profiles, temperature distributions, and porous medium behavior. The results not only reveal the sensitivity of the flow and thermal fields to these controlling factors but also identify regimes where hybrid nanofluids significantly outperform traditional working fluids.

**Keywords:** Lorentz force; Dissipation; Magneto-hydro dynamics (MHD); Hybrid nanofluids; Exponential stretching sheet

**PACS:** 41.20.-q, 47.10.-g, 52.30.Cv, 47.10.A-, 47.65.-d

### Nomenclature

Notation	Definition	Units	Notation	Definition	Units
$u_1, u_2$	Velocity profiles along x, y directions	-	$Ec$	Eckert number	-
$U, V$	Exponential rate and Velocity rate	-	$Nu$	Nusselt number	-
$\mu$	Dynamic viscosity	$[M L^{-1} T^{-1}]$	$Pr$	Prandtl number	-
$\rho$	Fluid density	$[M L^{-3} T^0]$	$K$	Porosity parameter	-
$\eta$	Dimensionless distance	-	$B_0$	Magnetic field strength	$[L^{-1} A]$
$M$	Magnetic parameter	$[M T^{-2} I^{-1}]$	$q_r$	Radiative heat flux	$[W/m^2]$
$\dot{Q}$	Heat source	$[J/s]$ or $[W]$	$\beta$	Thermal expansion	$[K^{-1}]$
$C_p$	Specific heat	$[M^0 L^2 T^{-2} K^{-1}]$	$\nu$	Kinematic viscosity	$[M L^{-1} T^{-1}]$
$\alpha$	Thermal diffusivity	$[L^2 T^{-1}]$	$l$	Length	$[m]$
$\sigma$	Electrical conductivity	$[M^{-1} L^{-3} T^3 A^2]$	$\phi$	Volume fraction	-
$T$	Temperature	$[K]$	$\rho C_p$	Heat Capacitance	$[ML^2 T^{-2} K^{-1}]$
$T_w$	Wall stream temperature	$[K]$	$c_0$	Positive constant	-
$T_\infty$	Free stream temperature	$[K]$	$C_f$	Skin friction	-
$k$	Thermal conductivity	$[MLT^{-3} K^{-1}]$	$Re$	Reynolds number	-
$R$	Radiation parameter	-	$S$	Suction parameter	-

### INTRODUCTION

A fluid is a substance that encompasses both liquids and gases, characterized by its ability to deform and flow continuously when subjected to external forces such as pressure or shear stress. Unlike solids, fluids cannot resist shear stress and instead redistribute themselves until equilibrium is achieved. They exhibit key physical properties such as density, viscosity, temperature, and pressure, which determine their behavior under different flow conditions. The scientific study that deals with the motion and interaction of fluids is known as Fluid Dynamics, a core branch of Fluid Mechanics, which plays a vital role in understanding and predicting phenomena like turbulence, drag, lift, and flow stability. Such knowledge is crucial in applications ranging from aerodynamics and hydrodynamics to biomedical flows

and industrial processes. Recent advancements in this field include the incorporation of nanoparticles into conventional base fluids like water, ethylene glycol, or engine oil, creating nanofluids with enhanced thermal and flow characteristics. Heat transfer, a fundamental aspect of fluid flow, involves the exchange of energy driven by temperature differences and occurs mainly through conduction, convection, and radiation. In fluids, convection becomes particularly significant as the bulk motion of fluid particles aids in transferring thermal energy efficiently, making fluid dynamics essential for designing advanced cooling, heating, and energy conversion systems. Choi [1], one who initiated the concept of nanoparticles, which can incorporate into the base fluids to generate a nanofluid. The size of a nanoparticle varies anywhere between 1-100 nm. Nanofluids impart better properties, primarily thermal conductivity, also gives the abundant impact on velocity, temperature profiles. Nanofluids have a rich amount of research conducted within the last decades comprising preparation, characterization, modelling, convective, boiled heat transfer, and their applications [2-4].

A mixture of two nanoparticles into single base fluid is indicated as Hybrid nanofluids. Suresh [5] first proposed the theory of hybrid nanofluids to rise the valuable factors of normal nanomaterials. On extending more than two nanoparticles, consists the properties of thermophysical and chemical which lift the intensity in heat transfer [6]. Hybrid nanofluids come out with a promising result to enhance the attainment of heat transfer compared to traditional fluids and nanofluids with single nanoparticle [7]. There will be a high significant rate of thermal conductivity on applying two different nanoparticles to the fluid facilitating heat transfer [8]. Implementing two nanoparticles in the base fluid leads in prevention of particle sedimentation that ensures continuing stability of nanofluid and better their dispersion in the base fluid which can improve the heat transfer [9]. When the magnetic field is assigned in the hybrid nanofluid, Lorentz force acts on the particles that are charged inside the fluid heading to discrete effects and reactions. It exerts the substantial reference in the performance of hybrid nanofluids [10]. To make the transformation of heat strengthen, the flow patterns in the hybrid nanofluids are manipulated by managing the magnetic field [11]. Lorentz force helps in nanoparticle dispersion to make thermal conductivity and heat transfer more efficient [12]. During the flow of fluid, the K.E converts to thermal energy, this effects the friction behaviour of hybrid nanofluids and leads to viscous dissipation [13]. In enhancing the heat transfer rates, an increase in the fluid temperature is due to dissipation criteria [14]. The heat created from dissipation can alter the patterns of flow, changes in velocity profiles, and boundary layer thickness [15]. Thermal radiation, a form of heat transfer that includes the emission of electromagnetic waves, impact the thermal behaviour of fluid, mainly when combined with nanoparticles [16]. On adding excess heat source to the fluid, induces to a thicker thermal boundary layer, that increases the heat transfer [17]. Lorentz force, Viscous dissipation, Thermal radiation effects collectively considered to provide an absolute nanofluid behaviour [18]. The stretching surface along the flow is very much important and utilizes in spin forming, rolling, wire gathering, cultivating crystal, and production of fibre glass, plastic, rubber and more. Stretching sheet, a surface that moves continuously, immersed in a fluid, it produces a boundary layer flow. Stretching rate, properties of fluid, nanoparticle concentration are the points in which the thickness of boundary layer is depended [19]. The velocity gradients in the boundary layer are controlled by the stretching rate. The higher stretching rate results in high velocity gradient around the surface [20]. Magyari and Keller [21] were the first to pose the implementation of exponential stretching sheet to explore the circulation of wall temperature and heat transfer characteristics. Detailed explanation in boundary layer flow of MHD over an exponential stretching sheet on regarding thermal radiation was developed by Mabood [22]. The latest study on the influence of nanoparticles along the flow and heat transference through exponential shrinking sheet, gave the enhanced thermal boundary layer thickness as volume fraction of nanoparticle increased because of shrinking sheet [23].

Here, in this study the consideration of Lorentz force, thermal radiation, viscous dissipation are interacted to better the nanofluid nature. This combination will impact heat variation and flow features mainly in the plot involving magnetic fields and raised temperatures. Exploring all closely might provide a exact representation of nanofluid development [24]. Several outcomes are reported in the above literature, which are not reported to the whole. Accordingly, the main intention is to enquire the heat transfer and behaviour of fluid flow of Hybrid nanofluids forward to exponential stretching sheet with the Copper (Cu) and Titanium dioxide (TiO<sub>2</sub>) as nanoparticles merged in the Water (H<sub>2</sub>O) which is a base fluid. This appeal brings a novel perspective on shaping various forces that acts along the fluid flow. The results are shown both in tabulated and graphical form to the close extent compared to the previous works and conclusions are also clearly drafted.

### MATHEMATICAL MODEL

Let us consider a two-dimensional hybrid nanofluid flow that is independent of time, with Titanium dioxide (TiO<sub>2</sub>) and Copper (Cu) as nanoparticles, and Water (H<sub>2</sub>O) as the base fluid, to examine on an exponential stretching sheet. The x-axis is parallel and the y-axis is perpendicular to the surface, respectively (Fig. 1). The sheet elongates along the x-direction at an exponential rate of  $U = c_0 e^{x/l}$  and the velocity profile as  $V = c_0 e^{x/2l}$  (where  $l$  is length and  $c_0$  is the positive stretching constant). The sheet is placed at an exponentially varying temperature  $T_w = T_\infty + T_0 e^{x/2l}$  (where  $T_0, T_\infty$  are the reference value and the ambient value, respectively).

The vector notations for the fluid flow are

$$\nabla \cdot u = 0 \quad (1)$$



The above represents the vector form of equation of continuity that expresses the law of conservation of mass for incompressible fluids.

$$(u \cdot \nabla)u = \nu \nabla^2 u_1 - \frac{\sigma_{hnf}}{\rho_{hnf}} B_0^2(x) u_1 - \frac{\mu_{hnf}}{\rho_{hnf}} \frac{u_1}{K} \quad (2)$$

This equation is essentially the Navier-Stokes momentum equation for a hybrid nanofluid that flows through the porous medium under a magnetic field. The vector form unifies the inertia, viscous, magnetic, and porous drag.

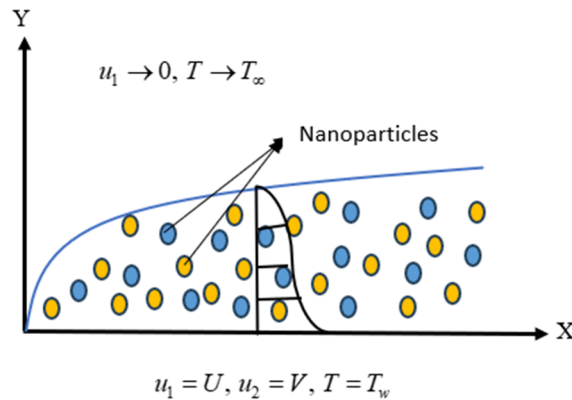


Figure 1. Model of the problem

$$(u \cdot \nabla)T = \alpha_{hnf} \nabla^2 T - \frac{1}{(\rho C p)_{hnf}} \nabla q_r + \frac{Q}{(\rho C p)_{hnf}} (T - T_\infty) + \frac{\mu_{hnf}}{(\rho C p)_{hnf}} \Phi \quad (3)$$

The above is the energy equation along a porous path for hybrid nanofluids with heat source, viscous dissipation, and radiative heat flux in vector form.

The governing equations that were modified from the vector form are [25,26].

*Continuity equation:*

This is the mathematical expression of conservation of mass in an incompressible fluid flow.

$$\frac{\partial u_1}{\partial x} + \frac{\partial u_2}{\partial y} = 0 \quad (4)$$

*Momentum equation:*

Equation (4) undergoes the principle of Newton's second law, where the change in momentum is directly proportional to the net forces acting on it and represents the convection flow change on the left side and viscous effects, magnetic forces, thermal conductivity respectively to the right of the equation.

$$u_1 \frac{\partial u_1}{\partial x} + u_2 \frac{\partial u_1}{\partial y} = \left( \frac{\mu_{hnf}}{\rho_{hnf}} \right) \frac{\partial^2 u_1}{\partial y^2} - \left( \frac{\sigma_{hnf}}{\rho_{hnf}} \right) B_0^2(x) u_1 - \left( \frac{\mu_{hnf}}{\rho_{hnf}} \right) \frac{u_1}{K} \quad (5)$$

*Energy equation:*

The change in total energy is equal to the summation of the rate of work done by force applied and change in heat quantity per unit time. The equation below describes the change of convection flow to the left and thermal diffusion, radiative heat flux gradient, heat generation with temperature differences, and viscous dissipation to the right accordingly in the equation.

$$u_1 \frac{\partial T}{\partial x} + u_2 \frac{\partial T}{\partial y} = \alpha_{hnf} \frac{\partial^2 T}{\partial y^2} - \frac{1}{(\rho C p)_{hnf}} \frac{\partial q_r}{\partial y} + \frac{Q}{(\rho C p)_{hnf}} (T - T_\infty) + \frac{\mu_{hnf}}{(\rho C p)_{hnf}} \left( \frac{\partial u_1}{\partial y} \right)^2 \quad (6)$$

Radiative heat flux  $q_r$  is possible to write by taking advantage of Rosseland approximation as [25]

$$q_r = -\frac{4\sigma^*}{3k^*} \left( \frac{\partial T^4}{\partial y} \right) \quad (7)$$

$\sigma^*$  is the Stephen Boltzmann constant and  $k^*$  is the absorption coefficient

$$T^4 \cong 4T_\infty^3 T - 3T_\infty^4 \quad (8)$$



Incorporating the value of  $T^4$  in the equation (7) we obtain

$$q_r = -\frac{16\sigma^* T_\infty^3}{3k^*} \left( \frac{\partial T}{\partial y} \right) \quad (9)$$

Equation (6) takes the form after including the Rosseland approximation  $q_r$  of equation (8)

$$u_1 \frac{\partial T}{\partial x} + u_2 \frac{\partial T}{\partial y} = \alpha_{hnf} \frac{\partial^2 T}{\partial y^2} + \frac{16\sigma^* T_\infty^3}{(\rho C p)_{hnf} 3k_1} \frac{\partial^2 T}{\partial y^2} + \frac{Q}{(\rho C p)_{hnf}} (T - T_\infty) + \frac{\mu_{hnf}}{(\rho C p)_{hnf}} \left( \frac{\partial u_1}{\partial y} \right)^2 \quad (10)$$

Boundary conditions are

$$\begin{aligned} u_1 = U, \quad u_2 = V, \quad T = T_w, \quad \text{at } y \rightarrow 0 \\ u_1 \rightarrow 0, \quad T \rightarrow T_\infty, \quad \text{as } y \rightarrow \infty \end{aligned} \quad (11)$$

Considered similarity transformations are [26,28]

$$\begin{aligned} \eta = y \sqrt{\frac{c_0}{2\nu l}} e^{\frac{x}{2l}}, \quad u_1 = c_0 e^{\frac{x}{l}} f'(\eta), \quad u_2 = -\sqrt{\frac{c_0 \nu}{2l}} e^{\frac{x}{2l}} [f(\eta) + \eta f'(\eta)], \\ T = T_\infty + T_0 e^{\frac{x}{2l}} \theta(\eta) \end{aligned} \quad (12)$$

Using relations of equation (8), equation (4) is satisfied and equation (5) & (6) respectively converted to

$$f''' - a_1 a_3 M f' - 2a_1 a_2 f'^2 - K f' + a_1 a_2 f f'' = 0 \quad (13)$$

$$a_1 \left( a_5 + \frac{4}{3} R \right) \theta'' + a_1 a_4 \text{Pr} f \theta' - a_1 a_4 \text{Pr} f' \theta + a_1 \text{Pr} \beta \theta + \text{Pr} \text{Ec} f''^2 = 0 \quad (14)$$

Boundary conditions are transferred to,

$$\begin{aligned} f'(0) = 1, \quad f(0) = S, \quad \theta(0) = 1, \quad \text{at } \eta = 0 \\ f'(\infty) \rightarrow 0, \quad \theta(\infty) \rightarrow 0, \quad \text{as } \eta \rightarrow \infty \end{aligned} \quad (15)$$

The dimensionless parameters are

$$\begin{aligned} M = \frac{2\sigma_f B_0^2 l}{(Cp)_f}, \quad \text{Pr} = \frac{\mu_f (Cp)_f}{k_f}, \quad \text{Ec} = \frac{U_w^2}{(Cp)_f (T_w - T_\infty)}, \\ R = \frac{4\sigma^* T_\infty^3}{k^* k_f}, \quad K = \frac{2l\nu_f}{c_0 K_0}, \quad \beta = \frac{2lQ_0}{c_0 (\rho C p)_f}, \quad S = -c_0 \sqrt{\frac{2l}{\nu_f c_0}} \end{aligned}$$

where M is the magnetic parameter, R is the radiation parameter, Pr is the Prandtl number, Ec is the Eckert number,  $\beta$  represents the thermal expansion, s is the suction parameter and K is the porosity parameter.

Quantities of engineering: Physical quantities known as skin friction and Nusselt number are mentioned as follows:

$$C_{fx} - \frac{\mu_{hnf}}{\rho_f U^2} \left( \frac{\partial u_1}{\partial y} \right)_{y=0} = 0$$

$$Nu_x + \frac{2l}{k_f (T_w - T_\infty)} \left( -k_{hnf} \left( \frac{\partial T}{\partial y} \right)_{y=0} + (q_r)_{y=0} \right) = 0$$

The dimensionless forms of Skin friction and Nusselt number

$$Cf_x \text{Re}_x^{\frac{1}{2}} = \left( \frac{f''(0)}{a_1} \right), \quad Nu_x \text{Re}_x^{\frac{-1}{2}} = -\left( a_4 + \frac{4}{3} R \right) \theta'(0)$$

**Table 1.** Thermophysical models for Hybrid nanofluids [26]

Properties	Hybrid nanofluid
Viscosity	$a_1 = \frac{\mu_{hnf}}{\mu_f} = (1 - \phi_1)^{2.5} (1 - \phi_2)^{2.5}$
Density	$a_2 = \frac{\rho_{hnf}}{\rho_f} = (1 - \phi_2) \left[ 1 - \phi_1 + \phi_1 \left( \frac{\rho_1}{\rho_f} \right) \right] + \phi_2 \left( \frac{\rho_2}{\rho_f} \right)$
Electrical conductivity	$a_3 = \frac{\sigma_{hnf}}{\sigma_f} = 1 + \frac{3 \left( \frac{\phi_1 \sigma_1 + \phi_2 \sigma_2}{\sigma_f} - (\phi_1 + \phi_2) \right)}{2 + \left( \frac{\phi_1 \sigma_1 + \phi_2 \sigma_2}{\sigma_f (\phi_1 + \phi_2)} \right) - \left( \frac{\phi_1 \sigma_1 + \phi_2 \sigma_2}{\sigma_f} - (\phi_1 + \phi_2) \right)}$
Specific heat	$a_4 = \frac{(\rho C_p)_{hnf}}{(\rho C_p)_f} = (1 - \phi_2) \left[ 1 - \phi_1 + \phi_1 \left( \frac{(\rho C_p)_1}{(\rho C_p)_f} \right) \right] + \phi_2 \left( \frac{(\rho C_p)_2}{(\rho C_p)_f} \right)$
Thermal conductivity	$a_5 = \frac{k_{hnf}}{k_f} = \frac{k_2 + 2k_{nf} - 2\phi_2(k_{nf} - k_2)}{k_2 + 2k_{nf} + 2\phi_2(k_{nf} - k_2)}, \text{ at } k_{nf} = \frac{k_1 + 2k_{nf} - 2\phi_1(k_{nf} - k_1)}{k_1 + 2k_{nf} + 2\phi_1(k_{nf} - k_1)} \times k_f$

**Table 2.** Thermal properties of Water, nanoparticles [26]

Property	Cu	TiO <sub>2</sub>	H <sub>2</sub> O
Density ' $\rho$ ' (kg/m <sup>3</sup> )	8933	4250	997.1
Specific heat 'Cp' (J/kg-K)	385	686.2	4179
Thermal conductivity 'k' (W/m-K)	400	8.9538	0.613
Electrical conductivity ' $\sigma$ ' (S/m)	$5.96 \times 10^7$	$2.38 \times 10^6$	$5 \times 10^{-2}$

### Methodology

This flowchart outlines the computational procedure for solving a boundary value problem (BVP) using MATLAB's bvp4c solver. It begins with variable declaration and initialization, followed by domain quantization to discretize the problem space. The core process starts by calling bvp4c, which requires defining a system of first-order ordinary differential equations (ODEs) and appropriate boundary conditions. Boundary conditions are either exactly known for the first solution or initially guessed for subsequent solutions. The process iteratively adjusts these guesses to match desired solutions, such as the second, third, or fourth, refining them to improve accuracy. Once the boundary conditions are properly set and the function is evaluated, the solver computes the numerical results, yielding the final solution of the BVP.

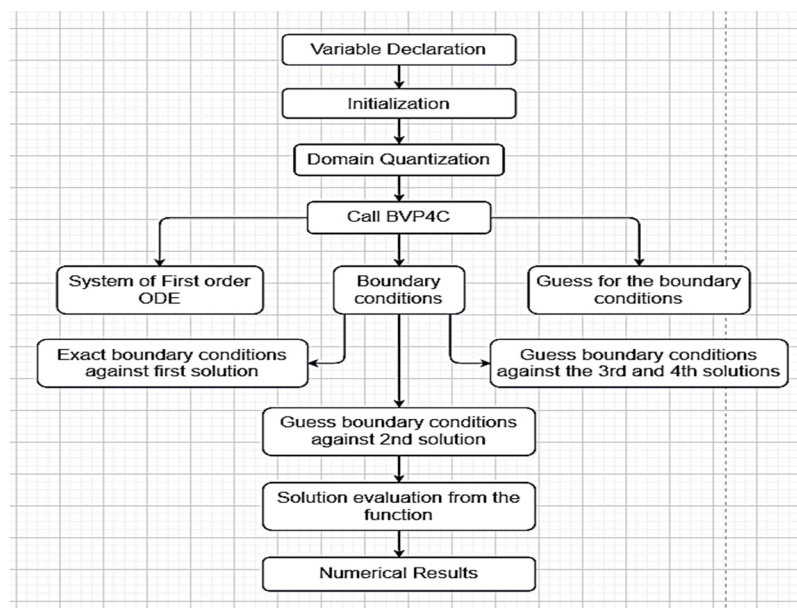


**Figure 2.** Flowchart of numerical solution

The system of Ordinary differential equations derived from equations (13) & (14), along with their respective boundary conditions given in equation (15), is solved numerically using the shooting method. To convert those equations into a first-order ODE, we initiate the variables as

$$f = f(1), f' = f(2), f'' = f(3), \theta = f(4), \theta' = f(5)$$

$$f''' = a_1 a_3 M f(2) + 2a_1 a_2 (f(2))^2 + K f(2) - a_1 a_2 f f(3)$$

$$\theta = f(5)$$

$$\theta'' = \frac{a_1 a_4 \Pr f(2) f(4) - a_1 \Pr \beta f(4) - \Pr Ec (f(2))^2 - a_1 a_4 \Pr f(1) f(5)}{a_1 \left( a_5 + \frac{4}{3} R \right)}$$

The corresponding dimensionless boundary conditions are

$$f(1) = S, f(2) = 1, f(4) = 1 \text{ at } \eta \rightarrow 0$$

$$f(2) \rightarrow 0, f(4) \rightarrow 0 \text{ at } \eta \rightarrow \infty$$

## RESULTS AND DISCUSSION

The non-linear differential equations are solved using Runge-Kutta method under boundary conditions lead to numerous changes in the velocity, temperature profiles and in the effects of skin friction and Nusselt number are represented in graphical and tabular forms.

**Table 3.** Comparison of  $-\theta'(0)$  with dissimilar values of  $R, M, Pr$

R	M	Pr	Ishak et al. [27]	Goud et al. [28]	Present work
0	0	1.0	0.9548	0.9547	0.9540
0	0	2.0	1.4715	1.4714	1.4573
0	0	3.0	1.8691	1.8690	1.7893
0	0	5.0	2.5001	2.5001	2.3195
0	0	10.0	3.6603	3.6603	3.2694

**Table 4.** Mutations of  $Cf_x \text{Re}_x^{\frac{1}{2}}$  by  $Pr = 6.2$ ;  $R = 1.0$ ;  $Ec = 0.3$ ;  $\beta = 0.1$

M	K	s	$\phi_1$	$\phi_2$	Zahid et al. [25]	Present work
0.5	1.0	0.1	0.1	0.1	-3.2211	-2.8553
1.0	1.0	0.1	0.1	0.1	-3.3551	-3.1546
1.5	1.0	0.1	0.1	0.1	-3.4836	-3.4277
2.0	1.0	0.1	0.1	0.1	-3.6073	-3.6805

**Table 5.** Changes of  $Nu_x \text{Re}_x^{\frac{-1}{2}}$  by  $Pr = 6.2$ ;  $K = 1.0$ ;  $s = 0.1$

M	Ec	R	$\beta$	$\phi_1$	$\phi_2$	Zahid et al. [25]	Present work
0.5	0.3	1.0	0.1	0.1	0.1	1.3487	1.3480
1.0	0.3	1.0	0.1	0.1	0.1	1.1466	1.1465
1.5	0.3	1.0	0.1	0.1	0.1	0.9518	0.9510
2.0	0.3	1.0	0.1	0.1	0.1	0.7570	0.7572

As the magnetic parameter increases, the Lorentz force intensifies, leading to a reduction in the fluid's drift velocity. When a magnetic field is applied to a fluid, it induces a resistive force known as the Lorentz force, which acts against the fluid's motion. Thus, the velocity is decreased in Figure 3.

From Figure 4 the temperature is raised on increasing the magnetic parameter due to the interaction between electrically conducting fluid and the magnetic field, called Lorentz force, generates the friction within the fluid converting the kinetic energy to thermal energy causes the temperature increment.

Figure (5), represents the increment in the porosity parameter leads to increase in the velocity, because a higher porosity means there are more interconnected void spaces allowing the fluid to flow easily with less resistance.

In Figure 6 it is observed that temperature is increased on increase in the porosity parameter, this is noticed mainly in the context of porous medium because higher porosity allows for greater penetration and an increased surface area for heat transport.

Figure 7 shows the impact of the velocity profile on increasing the suction parameter, particularly at the boundary layer. This is because suction effectively removes fluid from the boundary layer, reducing the momentum of the flow and repeatedly slowing it down.

Figure 8 elaborates the decrease in temperature with an increase in the suction parameter, due to a better cooling effect from the increased fluid being drawn into the boundary layer. This effect helps in removing the heat effectively, resulting in the temperature reduction.

Figure 9 depicts the variations in the temperature by increasing the radiation parameter, this is because the fluid is absorbing its own thermal radiation and increase heat transfer from heat surfaces. This showed the increase in the temperature on increasing in the radiation parameter.

Figure 10 shows the increase in the temperature while the values of Eckert number are increased. As Eckert number increases, the viscous dissipation in the fluid becomes more significant, which converts the kinetic energy to thermal energy, that results in the temperature increment.

Figures (11) & (12), separately shows the representation of variations in temperature profile on increasing the volume fractions of Copper and Titanium dioxide nanoparticles respectively. This result in the increase of temperature because increase in the particles can increase the surface areas for heat exchanging also can absorb excess heat leading to the high temperatures.

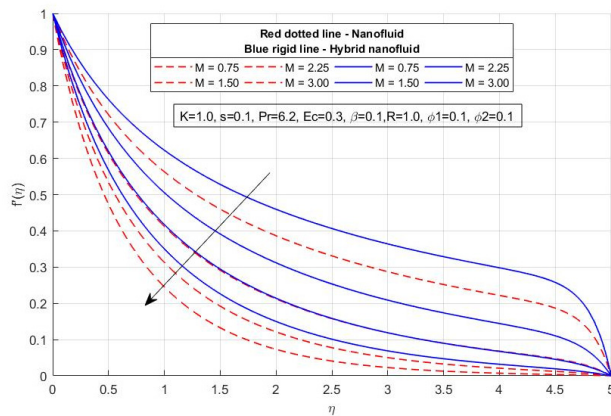


Figure 3. Difference in velocity profile for various values of M

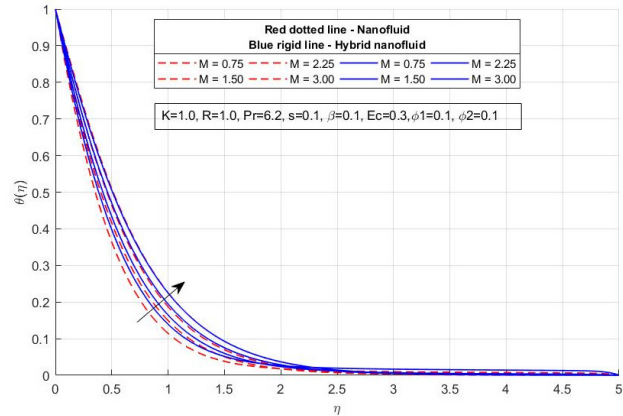


Figure 4. Variations of temperature profile for distinct values of M

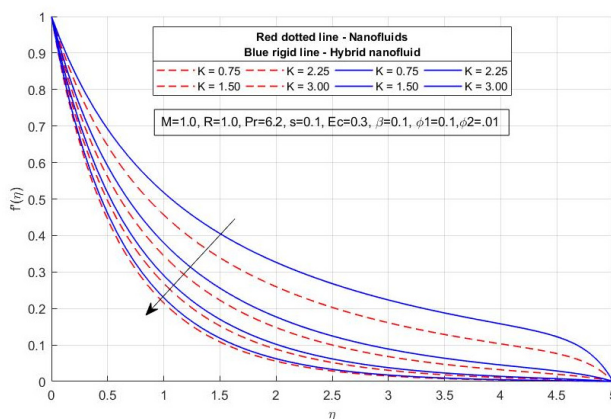


Figure 5. Difference in velocity profile with distinct values of K

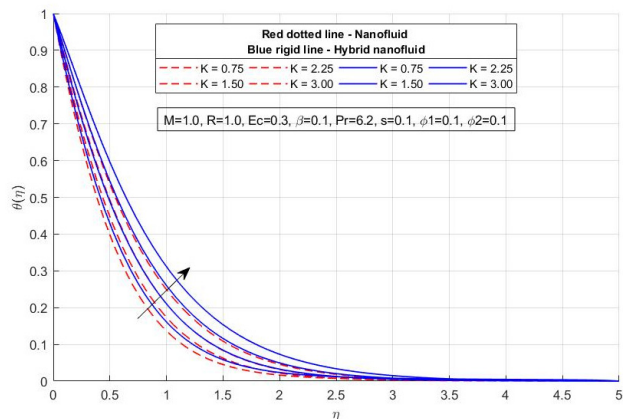


Figure 6. Variations in temperature profile for distinct values of K

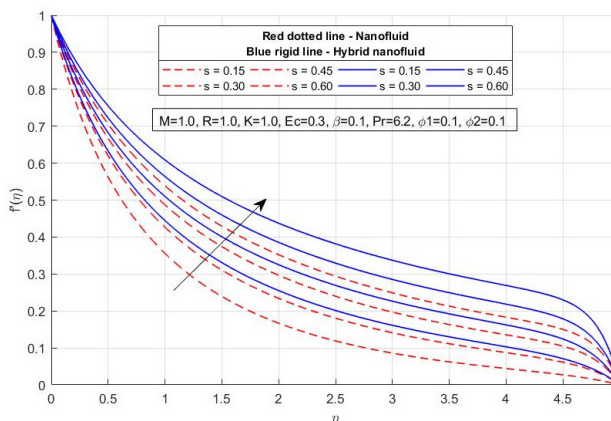


Figure 7. Difference in velocity profile for distinct values of s

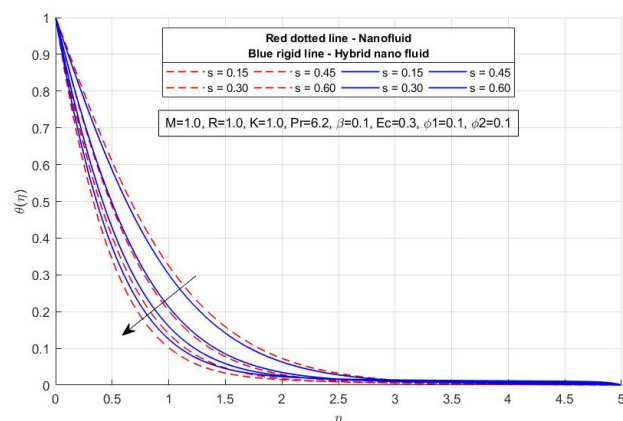
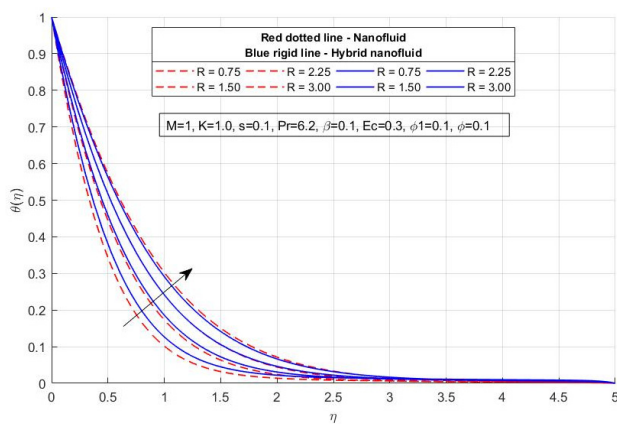
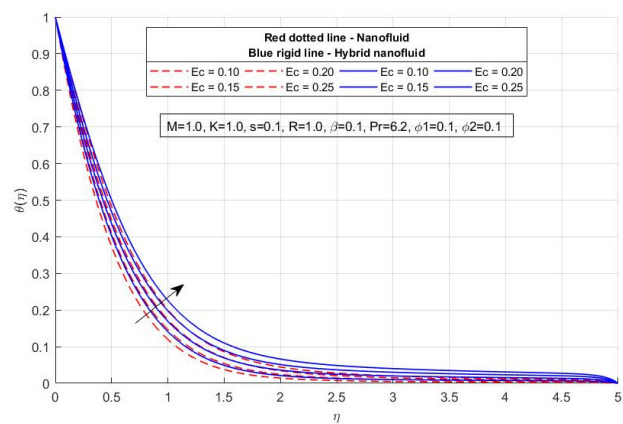


Figure 8. Variations in temperature profile for different values of s



**Figure 9.** Variances in temperature profile with distinct values of  $R$



**Figure 10.** Variances of temperature profile with distinct values of  $Ec$

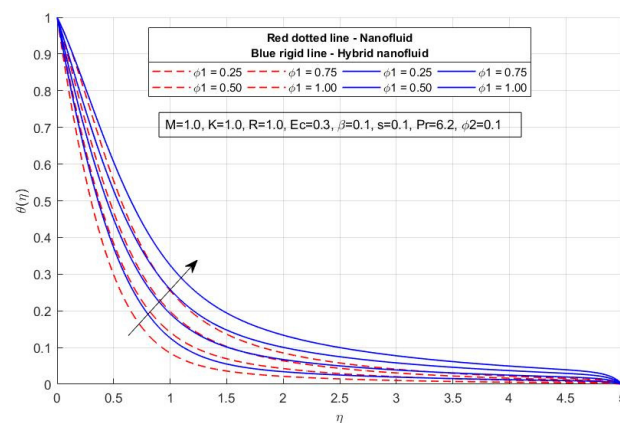


**Figure 11.** Variances of temperature profile for distinct values of  $\phi_1$

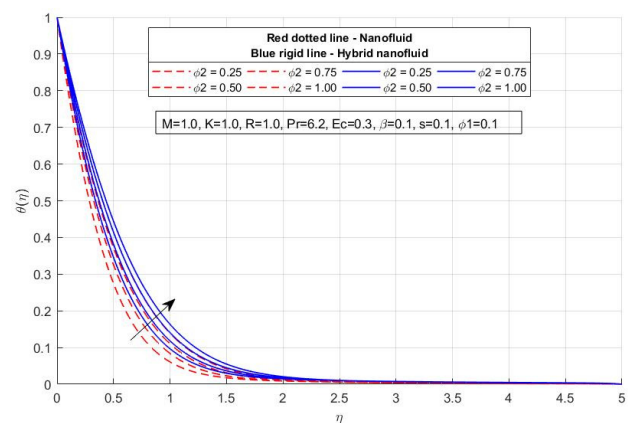


**Figure 12.** Variances in temperature profiles for distinct values of  $\phi_2$

## CONCLUSIONS

The outcomes of this research establish that the synergistic effect of hybrid nanoparticles and exponential surface stretching significantly advances heat transfer performance while offering deeper insights into boundary layer control. By integrating magnetohydrodynamic influences, viscous dissipation, and radiative effects, the study not only enhances the predictive accuracy of nanofluid-based thermal models but also identifies optimal operating conditions for engineering applications. These findings contribute novel perspectives toward the design of next-generation thermal management systems, particularly in energy, electronics, and advanced manufacturing sectors, where precise regulation of heat transfer is essential. A broad range of investigation is done on the Hybrid nanofluid flow and heat transfer which included two nanoparticles namely Titanium dioxide ( $\text{TiO}_2$ ) and Copper ( $\text{Cu}$ ) and the base fluid used is Water ( $\text{H}_2\text{O}$ ) on exponential stretching sheet. To validate, the present results are compared with the previously published articles, achieved good outcomes. On inclusion of the different parameters on the fluid velocity and temperature profiles were solved by attaining Runge-Kutta method of Shooting technique. The important disclosures are generalised here:

- The velocity component is decreased slightly on productivity of Magnetic parameter, Porosity parameter, Suction parameter.
- On increasing the Magnetic parameter, Porosity parameter there is an increase in the temperature profile in the both mentioned parameters.
- The values of temperature profiles and volume fractions are seen in proportional on increasing in the volume fractions.
- The magnetic parameter, suction parameter, porosity parameter are conversely related to the drag co-efficient of the volume fractions.
- By improving the suction parameter values there is an adequate downfall of velocity profile and temperature profile.
- The Radiation parameter consumes a productive association with rate of heat transfer whereas the magnetic parameter, viscous dissipation parameter, volume fractions of the nanoparticles all possess negative correlation.



In the coming research, the above work could be extended by engaging novel fluids and appropriate effects like space dependent heat sources.

#### ORCID

✉Mahesh Joshi, <https://orcid.org/0009-0005-7486-2361>; ✉G. Venkata Ramana Reddy, <https://orcid.org/0000-0002-6455-3750>

#### REFERENCES

- [1] S.U. Choi, and J.A. Eastman, *Enhancing thermal conductivity of fluids with nanoparticles* (No. ANL/MSD/CP-84938; CONF-951135-29). Argonne National Lab. (ANL), Argonne, IL (United States, 1995).
- [2] J. Sarkar, "A critical review of heat transfer correlations of nanofluids," *Renew Sustain Energy Rev.* **15**, 3271–3277 (2011). <https://doi.org/10.1016/j.rser.2011.04.025>
- [3] W. Yu, and H. Xie, "A review on nanofluids: preparation, stability mechanisms, and applications," *J. Nano mater.* **2012**, 435873 (2012). <https://doi.org/10.1155/2012/435873>
- [4] K.V. Wong, and O.D. Leon, "Applications of nanofluids: current and future," *Adv. Mech. Eng.* **2010**, 519659 (2010). <https://doi.org/10.1155/2010/519659>
- [5] S. Suresh, K. Venkataraj, P. Selvakumar, and M. Chandrasekar, "Experimental investigation of mixed convection with synthesis of Al<sub>2</sub>O<sub>3</sub> using two step method and its thermophysical properties," *Colloid. Surface.* **8**, 41–48 (2011). <https://doi.org/10.1016/j.colsurfa.2011.08.005>
- [6] J. Sarkar, P. Ghosh, and A. Adil, "A review on hybrid nanofluids: recent research, development, and applications," *Renew. Sustain. Energy Rev.* **43**, 164–177 (2015). <https://doi.org/10.1016/j.rser.2014.11.023>
- [7] I. Waini, A. Ishak, and I. Pop, "Unsteady flow and heat transfer past a stretching/shrinking sheet in a hybrid nanofluid," *International Journal of Heat and Mass Transfer*, **136**, 288–297 (2019). <https://doi.org/10.1016/j.ijheatmasstransfer.2019.02.101>
- [8] B. Yashkun, *et al.*, "Effect of thermal radiation and suction on MHD hybrid nanofluid flow and heat transfer over a stretching/shrinking sheet," *Journal of Molecular Liquids*, **315**, 113800 (2020).
- [9] G. Tharapatla, V.L. Garishe, N. Vijaya, S. Wuri, and G.V.R. Reddy, "MHD Hybrid Nanofluids Flow Through Porous Stretching Surface in the Presence of Thermal Radiation and Chemical Reaction," *East European Journal of Physics*, (3) 158–167 (2025). <https://doi.org/10.26565/2312-4334-2025-3-14>
- [10] M. Sheikholeslami, S. Zahir, S. Ahmad, K. Poom, and H. Babazadeh, "Lorentz force impact on hybrid nanofluid within a porous tank including entropy generation", *International Communications in Heat and Mass Transfer*, **116**, 104635 (2020). <https://doi.org/10.1016/j.icheatmasstransfer.2020.104635>
- [11] S.S.U. Devi, and S.A. Devi, "Numerical investigation of three-dimensional hybrid Cu–Al<sub>2</sub>O<sub>3</sub>/water nanofluid flow over a stretching sheet with effecting Lorentz force subject to Newtonian heating," *Can. J. Phys.* **94**, 490–496 (2016). <https://doi.org/10.1139/cjp-2015-0799>
- [12] D. Yadav, J. Wang, J. Lee, and H.H. Cho, "Numerical investigation of the effect of magnetic field on the onset of nanofluid convection," *Appl. Ther. Eng.* **103**, 1441–1449 (2016). <https://doi.org/10.1016/j.applthermaleng.2016.05.039>
- [13] R. Cortell, "Effects of viscous dissipation and radiation on the thermal boundary layer over a nonlinearly stretching sheet," *Phys. Lett. A*, **372**, 631–636 (2008). <https://doi.org/10.1016/j.physleta.2007.08.005>
- [14] A. Ali, A. Noreen, S. Saleem, A.F. Aljohani, and M. Awais, "Heat transfer analysis of Cu–Al<sub>2</sub>O<sub>3</sub> hybrid nanofluid with heat flux and viscous dissipation," *Journal of Thermal Analysis & Calorimetry*, **143**(3), 2367 (2021). <https://doi.org/10.1007/s10973-020-09910-6>
- [15] K.L. Hsiao, "Micropolar nanofluid flow with MHD and viscous dissipation effects towards a stretching sheet with multimedia feature," *Int. J. Heat Mass Transf.* **112**, 983–990 (2017). <https://doi.org/10.1016/j.ijheatmasstransfer.2017.05.042>
- [16] N.A. Zainal, R. Nazar, K. Naganthran, and I. Pop, "The Impact of Thermal Radiation on Maxwell Hybrid Nanofluids in the Stagnation Region," *Nanomaterials (Basel)*, **12**(7), 1109 (2022). <https://doi.org/10.3390/nano12071109>
- [17] H. Waqas, U. Farooq, D. Liu, M. Abid, M. Imran, and T. Muhammad, "Heat transfer analysis of hybrid nanofluid flow with thermal radiation through a stretching sheet: A comparative study," *Int. Commun. Heat Mass Transf.* **138**, 106303 (2022). <https://doi.org/10.1016/j.icheatmasstransfer.2022.106303>
- [18] T. Hayat, M.I. Khan, M. Waqas, A. Alsaedi, and M. Farooq, "Numerical simulation for melting heat transfer and radiation effects in stagnation point flow of carbon–water nanofluid," *Comput. Methods Appl. Mech. Eng.* **315**, 1011–1024 (2017). <https://doi.org/10.1016/j.cma.2016.11.033>
- [19] W. Khan, and I. Pop, "Boundary-layer flow of a nanofluid past a stretching sheet," *Int. J. Heat Mass Transf.* **53**, 2477–2483 (2010). <https://doi.org/10.1016/j.ijheatmasstransfer.2010.01.032>
- [20] N. Acharya, K. Das, K.P. Kumar, "Ramification of variable thickness on MHD TiO and Ag nanofluid flow over a slendering stretching sheet using NDM," *Eur. Phys. J. Plus*, **131**, 303 (2016). <https://doi.org/10.1140/epip/i2016-16303-4>
- [21] E. Magyari, and B. Keller, "Heat, and mass transfer in the boundary layers on an exponentially stretching continuous surface," *J. Phys. D Appl. Phys.* **32**, 577 (1999). <https://doi.org/10.1088/0022-3727/32/5/012>
- [22] F. Mabood, W. Khan, and A.M. Ismail, "MHD flow over exponential radiating stretching sheet using homotopy analysis method," *J. King Saud Univ.-Eng. Sci.* **29**, 68–74 (2017). <https://doi.org/10.1016/j.jksues.2014.06.001>
- [23] A. Zaib, K. Bhattacharyya, and S. Shafie, "Unsteady boundary layer flow and heat transfer over an exponentially shrinking sheet with suction in a copper–water nanofluid," *J. Cent. South Univ.* **22**, 4856–4863 (2015). <https://doi.org/10.1007/s11771-015-3037-1>
- [24] N.A. Haroun, S. Mondal, and P. Sibanda, "Hydromagnetic nanofluids flow through a porous medium with thermal radiation, chemical reaction and viscous dissipation using the spectral relaxation method," *Int. J. Comput. Methods*, **16**, 1840020 (2019). <https://doi.org/10.1142/S0219876218400200>
- [25] S. Rosseland, *Astrophysics and Atomic Theoretical Foundations*, (Springer: Berlin/Heidelberg, Germany, 1931).



- [26] M. Zahid, A. Basit, T. Ullah, B. Ali, and G. Liskiewicz, "Coupled Effects of Lorentz Force, Radiation, and Dissipation on the Dynamics of a Hybrid Nanofluid over an Exponential Stretching Sheet," *Energies*, **16**, 7452 (2023). <https://doi.org/10.3390/en16217452>
- [27] I. Waini, A. Ishak, and I. Pop, "Hybrid nanofluid flow induced by an exponentially shrinking sheet," *Chin. J. Phys.* **68**, 468–482 (2020). <https://doi.org/10.1016/j.cjph.2019.12.015>
- [28] A. Ishak, "MHD boundary layer flow due to an exponentially stretching sheet with radiation effect," *Sains Malaysiana*, **40**, 391–395 (2011). [http://www.ukm.edu.my/jsm/pdf\\_files/SM-PDF-40-4-2011/17%20Anuar%20Ishak.pdf](http://www.ukm.edu.my/jsm/pdf_files/SM-PDF-40-4-2011/17%20Anuar%20Ishak.pdf)
- [29] B.S. Goud, P. Srilatha, P. Bindu, and Y.H. Krishna, "Radiation effect on MHD boundary layer flow due to an exponentially stretching sheet," *Adv. Math. Sci. J.* **9**, 10755–10761 (2020). <https://doi.org/10.37418/amsj.9.12.59>

### ЕНЕРГЕТИЧНИЙ ТРАНСПОРТ У ПОТОЦІ МГД-ГІБРИДНОЇ НАНОРІДИНИ НАД ПОРИСТИМ ЛИСТОМ З ЕКСПОНЕНЦІАЛЬНИМ РОЗТЯГНЕННЯМ

Махеш Джоші, Г. Венката Рамана Редді

*Кафедра математики, Освітній фонд Конеру Лакшмаї, Зелені поля, Ваддесварам, Гунтур-522302, Андхра-Прадеш, Індія*

Це дослідження представляє поглиблений аналіз механізмів теплопередачі та поведінки потоку рідини, пов'язаних з гібридними нанорідинами за наявності поверхні, що експоненціально розтягується. Гібридні нанорідини, утворені шляхом диспергування кількох типів наночастинок в базовій рідині, демонструють кращі теплофізичні властивості порівняно зі звичайними нанорідинами. Їхня підвищена теплопровідність, модифікована щільність та спеціалізована питома теплоємність роблять їх дуже придатними для передових застосувань у нанотехнологіях, системах відновлюваної енергії, високопродуктивному охолодженні електроніки та теплообмінниках промислового масштабу. Новизна цього дослідження полягає в його спробі дослідити комбінований вплив гібридних наночастинок та експоненціального розтягування на динаміку пограничного шару, тим самим пропонує нові ідеї щодо оптимізації теплових систем. Основною метою цього дослідження є максимізація ефективності теплопередачі за різних фізичних та експлуатаційних умов. Для досягнення цієї мети керівні диференціальні рівняння з частинними похідними, що описують закон збереження маси, імпульсу та енергії, перетворюються на набір нелінійних звичайних диференціальних рівнянь за допомогою перетворень подібності та відповідних безрозмірних параметрів. Таке математичне переформулювання спрощує складність задачі, зберігаючи при цьому основну фізику потоку. У MATLAB розроблено обчислювальну базу, де зв'язана система рівнянь розв'язується за допомогою методу Рунге-Кутти четвертого порядку, інтегрованого з методом стрільби для забезпечення точності та стабільності. Аналіз підкреслює роль ключових параметрів, таких як напруженість магнітного поля, число Екерта (ефекти в'язкої дисипації), число Прандтля (ефекти температуропровідності) та теплове випромінювання, на профілі швидкості, розподіл температури та поведінку пористого середовища. Результати не тільки показують чутливість потоку та теплових полів до цих контролюючих факторів, але й визначають режими, в яких гібридні нанорідини значно перевершують традиційні робочі рідини.

**Ключові слова:** сила Лоренца; дисипація; магнітогідродинаміка (МГД); гібридні нанорідини; експоненціальне розтягування листа

# THREE-DIMENSIONAL MHD FLOW AND HEAT TRANSFER OF WATER-BASED NANOFLUIDS OVER A STRETCHING SURFACE WITH CORIOLIS FORCE AND THERMAL EFFECTS

 M.M. Bindu<sup>1,2</sup>,  Elliriki Mamatha<sup>2</sup>,  V. Nagaradhika<sup>3\*</sup>

<sup>1</sup>Government first grade college, Channapatna, 562160, India

<sup>2</sup>Department of Mathematics, GSS, GITAM Deemed to be University, Bengaluru-561203, India

<sup>3</sup>Department of Mathematics, Sir M. Visvesvaraya Institute of Technology, Bengaluru -562 157, India

\*Corresponding Author E-mail: [nagaradhika79@gmail.com](mailto:nagaradhika79@gmail.com)

Received July 9, 2025; revised September 9, 2025; accepted September 12, 2025

This study focuses on the thermal behavior and three-dimensional boundary layer flow of water-based nanofluids over a stretched surface, considering the combined effects of Coriolis and Lorentz forces. The model includes several important physical aspects such as surface convection, internal heat generation, Joule heating, viscous dissipation, and thermal radiation. Copper (Cu), aluminum oxide (Al<sub>2</sub>O<sub>3</sub>), and magnetite (Fe<sub>3</sub>O<sub>4</sub>) nanoparticles are dispersed in water to compare their effectiveness in enhancing heat transfer. By applying similarity transformations, the complex system of partial differential equations is reduced to a set of nonlinear ordinary differential equations, which are then solved numerically using the Runge-Kutta-Fehlberg method along with the shooting technique. The results show that nanofluids containing Cu nanoparticles provide the highest thermal performance, followed by those with Al<sub>2</sub>O<sub>3</sub> and Fe<sub>3</sub>O<sub>4</sub>. These findings highlight the importance of selecting appropriate nanoparticles to improve heat transfer efficiency in thermal management applications. Increasing rotation parameter  $\lambda$  suppresses the axial velocity while simultaneously reducing the temperature distribution, highlighting the damping influence of rotational effects on momentum and heat transport.

**Keywords:** Nonlinear thermal radiation; Nanofluid; Rotational Effects; Viscous dissipation; Joule heating

**PACS:** 44.30.+v, 44.05.+e, 66.10.cd, 47.11.-j

## INTRODUCTION

The integration of nanoparticles into traditional base fluids has opened new avenues in the domain of heat transfer enhancement. Nanofluids are highly developed fluids that have the potential to revolutionize several industrial processes. Their exceptional thermal conductivity and energy transfer characteristics make them ideal for electronic cooling, heat exchangers, and automotive systems, among many other uses. The foundational concept was introduced by Choi and Eastman [1], who demonstrated that suspending nanoparticles within a fluid significantly enhances its thermal performance. Subsequently, Buongiorno [2] arrived to the conclusion that the incorporation of nanoparticles causes an abnormal rise in the host fluid's thermal conductivity by presenting a theoretical framework that incorporates many slip processes to simulate nanofluid behavior.

A number of scholars have built upon this base via numerical and experimental investigations. As an example, Wang et al. [3] Sheikholeslami and Rokni studied vegetable oil nanofluid lubrication. [4] nanofluid flow was investigated in relation to magnetic fields. Khan and Pop [5] Computational techniques were used to study nanofluid boundary layer flow across a stretched surface. Krishnamurthy et al. also excelled. [6], who analyzed heat transfer in nanofluids over exponentially stretching surfaces, and Muqaddass et al. [7], Considering hybrid nanofluids under time-dependent thermal and external magnetic fields. Researchers like Nadeem et al. [8], Asadi et al. [9], and Das et al. [10] have also shed light on hybrid nanofluids, stability, and computational methods for difficult flow issues. Laila [11] investigated nanofluid flow in converging and diverging channels with rectangular and heated walls, demonstrating the strong influence of wall geometry on the velocity and temperature fields. Extending this line of research, Rehman et al. [12] examined nanofluid flow over an inclined cylindrical surface in a double-stratified medium. Complementarily, Makinde [13] developed computational models for nanofluid flow over a convectively heated unsteady stretching sheet, emphasizing the importance of transient effects and convective boundary conditions in thermal performance. Recent studies have also incorporated magnetic and hybrid nanofluid effects. Akbar et al. [14] analyzed magnetized Casson hybrid nanofluid flow in a converging-diverging channel with radiative heat transfer. Similarly, Khan et al. [15] investigated mixed convection hybrid nanofluid flow over a permeable, moving, and inclined flat plate, where thermophoresis and radiative heat flux were found to influence both momentum and energy transport significantly. Gireesha and Anitha [16] studied convective flow through a permeable microchannel, with irreversibility analysis demonstrating the thermodynamic implications of such fluids. Madhukesh et al. [17] introduced the concept of pollutant dispersion into nanofluid flows across a stretched disc-cone device, establishing the interplay between nanoparticle transport and environmental effects. Furthermore, Cheng et al. [18] performed nonsimilar forced convection simulations of water-copper nanofluid through a porous medium, considering thermal radiation, heat generation, and viscous dissipation, which added further realism to nanofluid modeling in porous environments. Sheikholeslami and Shehzad [19] studied magnetohydrodynamic (MHD) nanofluid

convection in a porous enclosure with heat flux boundary conditions, showing how porous media significantly alter convection patterns under magnetic influence. Jyoti et al. [20] analyzed kerosene-alumina nanofluid flow between parallel plates with nonlinear convection and radiative heat transfer, incorporating variable viscosity to highlight the sensitivity of transport processes to temperature-dependent properties.

The Coriolis force plays a pivotal role in rotating fluid systems and is relevant in geophysical, industrial, and mechanical contexts, such as rotating machinery, centrifuges, viscometers, and disk drives. The classic analysis of rotating flows began with the work of Kármán [21], who formulated similarity transformations for the rotating disk problem. This foundation was extended by Wang [22] and further advanced by Nazar et al. [23] through the application of numerical techniques. To ensure the reliability of the present analysis, our results have been compared with the findings reported in these studies, and an excellent level of agreement has been observed, thereby validating the accuracy of the current model. Rotating viscous flows in porous media were studied by Makinde et al. [24], while three-dimensional heat and mass transport in rotating nanofluids was studied by Sheikholeslami and Ganji [25]. Mustafa et al. [26], Archana et al. [27], and Sampath et al. [28] examined how Coriolis and Lorentz forces affect flow and heat transmission in rotating systems. Several other studies (Mabood et al. [29], Krishna and Chamkha [30], Kumar et al. [31] and Mustafa et al. [32]) have further explored rotational forces in fluid flow across a variety of physical scenarios. Moreover, the Coriolis force-arising from rotational effects-has been shown to influence flow direction and speed, especially in high-velocity or rotating systems, as discussed by several studies. However, a comprehensive study investigating the simultaneous influence of thermal radiation and Coriolis force on the flow of copper–alumina–water hybrid nanofluid over a rotating exponentially stretching surface is lacking in the literature. This research addresses that gap and aims to provide new insights relevant to both theoretical and applied sciences. Specifically, the study investigates the effects of increasing Coriolis force, magnetic field strength, inclination angle, and nanoparticle volume fraction on the skin friction, heat transfer rate, and overall behavior of the hybrid nanofluid flow.

In the pursuit of sustainable energy solutions, nanomaterials have emerged as key contributors due to their ability to enhance energy absorption and transfer efficiency. Among various renewable energy technologies, solar energy has gained prominence for its accessibility and environmental compatibility. Nanomaterials are well-suited to enhancing solar thermal systems due to their exceptional thermal diffusivity and large surface area, which enable them to absorb photons effectively. The importance of thermal radiation in enhancing heat transmission has been highlighted by recent research. Radioactive and magnetic field interactions in porous media were studied by Hayat et al. [33]. Radiative effects in nanofluid boundary layers were studied by Motsumi and Makinde [34] using the Runge-Kutta technique, and radiative MHD flow between rotating plates was studied by Sheikholeslami et al. [35]. Reddy et al. [36], Waqas et al. [37], Sreedevi et al. [38], and Gireesha et al. [40] demonstrate the growing interest in harnessing sun radiation to enhance fluid thermal performance.

The motivation for this study stems from the growing need for efficient heat transfer technologies in advanced engineering systems such as cooling of rotating machinery, electronic devices, solar collectors, and nuclear reactors. Although nanofluids have been extensively investigated, most existing works focus on limited physical effects, while a comprehensive analysis that simultaneously accounts for magnetic fields, rotation, nonlinear thermal radiation, viscous dissipation, Joule heating, and convective boundary conditions is remains limited. Therefore, the main objective of the present work is to analyze the three-dimensional magnetohydrodynamic flow and heat transfer of nanofluids under these combined influences. In addition, a comparative assessment of three different water-based nanofluids-copper, alumina, and ferrofluids-is carried out to highlight the distinct impact of nanoparticle type on the momentum and thermal fields, thereby providing useful insights into their relative performance for practical heat transfer applications.

#### Nomenclature

$B_0$	Applied magnetic field	$T$	Temperature
$T_f$	Surface temperature	$q_r$	radiative heat flux
$C_p$	Specific heat at constant pressure	$h_f$	heat transfer coefficient
$k_{nf}$	Thermal conductivity of nanofluid	$u_w$	Stretching velocity in x direction
$u, v, w$	The velocity components in the x,y,z directions(m/s)		
Greek words			
$\Omega$	Angular velocity	$\phi$	The particle volume fraction parameter of the nanoparticle
$\mu$	Dynamic viscosity of nanofluid	$\rho$	Density of nanofluid
$\sigma^*$	Stefan Boltzman constant	$\alpha$	Thermal diffusivity of nanofluid
$\rho C_p$	heat capacities	$k^*$	Mean absorption co-efficient
Subscripts			
nf	nanofluid	s	solid nanoparticles
f	base fluid		

#### MATHEMATICAL FORMULATION

Here we discuss the numerical simulation of a three-dimensional, incompressible, electrically conducting nanofluid flow across a stretched surface that is convectively heated and exposed to magnetic and rotating forces. To investigate

changes in thermophysical behavior, Cu, Al<sub>2</sub>O<sub>3</sub> and Fe<sub>3</sub>O<sub>4</sub> nanoparticles are added to water, which serves as the working fluid. For any given value of a constant stretching rate, the surface extends along the x-axis at a velocity  $u_w = ax$ . Researchers like Reddy et al. [36], Waqas et al. [37], Sreedevi et al. [38], and Gireesha et al. [40] are interested in harnessing sun radiation to enhance fluid thermal performance. This work investigates how Coriolis and Lorentz forces collectively influence the steady three-dimensional boundary layer flow of nanofluids generated by a stretching surface.

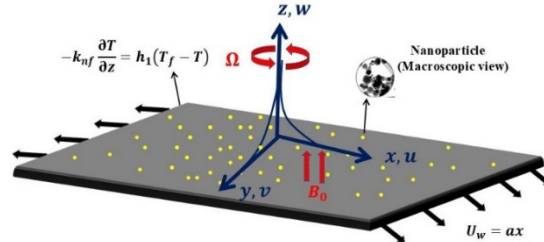


Figure 1. Geometry of the problem and coordinate system

Following the Tiwari-Das model's modifications for nanofluids and rotational effects, the flow is controlled by the continuity, momentum, and energy equations [41]. These equations are:

$$\frac{\partial u}{\partial x} + \frac{\partial v}{\partial y} + \frac{\partial w}{\partial z} = 0, \quad (2.1)$$

$$\rho_{nf} \left( u \frac{\partial u}{\partial x} + v \frac{\partial u}{\partial y} + w \frac{\partial u}{\partial z} - 2\Omega v \right) = \mu_{nf} \left( \frac{\partial^2 u}{\partial z^2} \right) - \sigma_{nf} B_0^2 u, \quad (2.2)$$

$$\rho_{nf} \left( u \frac{\partial v}{\partial x} + v \frac{\partial v}{\partial y} + w \frac{\partial v}{\partial z} + 2\Omega u \right) = \mu_{nf} \left( \frac{\partial^2 v}{\partial z^2} \right) - \sigma_{nf} B_0^2 v, \quad (2.3)$$

$$u \frac{\partial T}{\partial x} + v \frac{\partial T}{\partial y} + w \frac{\partial T}{\partial z} = \alpha_{nf} \left( \frac{\partial^2 T}{\partial z^2} \right) - \frac{1}{(\rho c_p)_{nf}} \frac{\partial q_r}{\partial z} + \frac{\mu_{nf}}{(\rho c_p)_{nf}} \left[ \left( \frac{\partial u}{\partial z} \right)^2 + \left( \frac{\partial v}{\partial z} \right)^2 \right] + \frac{\sigma_{nf} B_0^2}{(\rho c_p)_{nf}} [u^2 + v^2] + \frac{Q_T}{(\rho c_p)_{nf}} (T_f - T_\infty). \quad (2.4)$$

where  $q_r$  is the radiative heat flux modeled by the Rosseland approximation:

$$q_r = - \left( \frac{4\sigma^*}{3k^*} \right) \frac{\partial T^4}{\partial z}$$

The relevant boundary conditions for the present problem are;

$$\begin{aligned} u = u_w, \quad v = 0, \quad w = 0, \quad -k_{nf} \frac{\partial T}{\partial z} = h_f (T_f - T) \quad \text{at } z = 0, \\ u \rightarrow 0, \quad v \rightarrow 0, \quad T \rightarrow T_\infty \quad \text{as } z \rightarrow \infty, \end{aligned} \quad (2.5)$$

where  $u$ ,  $v$ , and  $w$  represents the standard velocity components.  $x$ ,  $y$ , and  $z$  directions respectively, while  $\Omega$  is the fluid's constant angular velocity,  $\rho_{nf}$  -density of the nanofluid,  $\mu_{nf}$  -dynamic viscosity of nanofluid,  $\alpha_{nf}$  -thermal diffusivity of nanofluid,  $C_p$  -specific heat at constant pressure,  $B_0$  -applied magnetic field strength,  $h_f$  -heat transfer coefficient,  $k_{nf}$  -thermal conductivity of nanofluid,  $T$  -temperature,  $q_r = - \left( \frac{4\sigma^*}{3k^*} \right) \frac{\partial T^4}{\partial z}$  is the Rosseland radiative heat flux and  $\sigma^*$  and  $k^*$  are the Stefan-Boltzman constant and the mean absorption coefficient.

## NANOFLUID PROPERTIES

According to Brinkman [42], nanofluid viscosity is dynamic.  $\mu_{nf}$  expressed as;

$$\mu_{nf} = \frac{\mu_f}{(1-\phi)^{2.5}}, \quad (2.6)$$

Effective density  $\rho_{nf}$  and effective heat capacity  $(\rho c_p)_{nf}$  are expressed as [41];

$$\rho_{nf} = (1 - \phi)\rho_f + \phi\rho_s, \quad (2.7)$$

$$(\rho c_p)_{nf} = (1 - \phi)(\rho c_p)_f + \phi(\rho c_p)_s, \quad (2.8)$$

Below is the base fluid's thermal conductivity, and the Maxwell-Garnett model for nanofluid effective thermal conductivity is  $k_{nf}$ .

$$\frac{k_{nf}}{k_f} = \frac{(k_s + 2k_f) - 2\phi(k_f - k_s)}{(k_s + 2k_f) + \phi(k_f - k_s)}, \quad (2.9)$$

moreover, the electrical conductivity of nanofluid  $\sigma_{nf}$  is given in the book by Maxwell [43] as;

$$\frac{\sigma_{nf}}{\sigma_f} = 1 + \frac{3(\sigma_s - \sigma_f)\phi}{(\sigma_s + 2\sigma_f) - (\sigma_s - \sigma_f)\phi}, \quad (2.10)$$

where  $(\rho C_p)_s$ -volumetric heat capacity of solid nanoparticles,  $(\rho C_p)_f$ ,  $(\rho C_p)_{nf}$ -are the base fluid's and the nanofluid's volumetric heat capacities, respectively.,  $\phi$  -a measure of nanoparticle volume fraction,  $\rho_f$ -density of base fluid,  $\mu_f$ -dynamic viscosity of base fluid,  $k_s$ - the thermal conductivity of solid nanoparticles; the subscripts  $s$  and  $f$  indicate the solid and base fluids, respectively. Thermophysical parameters of water and nanoparticles are listed in Table 1.

**Table 1.** Thermophysical Characteristics of Base Fluid and Nanoparticles

	$\rho(\text{kg/m}^3)$	$c_p(\text{J/kgK})$	$K(\text{W/mk})$	$\sigma(\Omega\text{m})^{-1}$
<b>Water</b>	997.1	4179	0.613	0.05
<b><math>\text{Fe}_3\text{O}_4</math></b>	5180	670	9.7	25000
<b>Cu</b>	8933	385	400	59.6
<b><math>\text{Al}_2\text{O}_3</math></b>	3970	765	40	16.7

Equations (2.1), (2.2), (2.3) and (2.4), subject to the boundary conditions (2.5) admit similarity solutions in terms of the similarity functions  $f, g, \theta$  and the similarity variable  $\eta$  and are defined as;

$$u = axf'(\eta), v = axg(\eta),$$

$$w = -\sqrt{\nu_f a} f(\eta), \theta(\eta) = \frac{T-T_\infty}{T_f-T_\infty}, \eta = \sqrt{\frac{a}{\nu_f}} z, \quad (2.11)$$

In view of the above quantities, the continuity Equation (2.1) is identically satisfied while Equations (2.2)–(2.5) become;

$$\frac{1}{(1-\phi)^{2.5} \left(1-\phi+\phi\frac{\rho_s}{\rho_f}\right)} f'''' - f'^2 + ff'' + 2\lambda g - \frac{\sigma_{nf}/\sigma_f}{\left(1-\phi+\phi\frac{\rho_s}{\rho_f}\right)} Mf' = 0, \quad (2.12)$$

$$\frac{1}{(1-\phi)^{2.5} \left(1-\phi+\phi\frac{\rho_s}{\rho_f}\right)} g'' + fg' - f'g - 2\lambda f' - \frac{\sigma_{nf}/\sigma_f}{\left(1-\phi+\phi\frac{\rho_s}{\rho_f}\right)} Mg = 0, \quad (2.13)$$

$$\frac{1}{\left(1-\phi+\phi\frac{(\rho c_p)_s}{(\rho c_p)_f}\right)} \left[ \frac{1}{Pr} \left( \left( \frac{K_{nf}}{k_f} + R(1+(\theta_w-1)\theta)^3 \right) \theta' \right)' \right] + f\theta' +$$

$$\frac{1}{\left(1-\phi+\phi\frac{(\rho c_p)_s}{(\rho c_p)_f}\right)} \left\{ \frac{1}{(1-\phi)^{2.5}} Ec(f'^2 + g'^2) + \frac{\sigma_{nf}}{\sigma_f} MEc(f'^2 + g^2) \right\} + \frac{Q_t\theta(\eta)}{\left(1-\phi+\phi\frac{(\rho c_p)_s}{(\rho c_p)_f}\right)} = 0 \quad (2.14)$$

The corresponding boundary conditions become;

$$f'(0) = 1, f(0) = 0, g(0) = 0, \theta'(0) = Bi(\theta(0) - 1) \text{ at } \eta = 0,$$

$$f'(\eta) \rightarrow 0, g(\eta) \rightarrow 0, \theta(\eta) \rightarrow 0 \text{ as } \eta \rightarrow \infty. \quad (2.15)$$

The magnetic parameter, radiation parameter, Prandtl number, heat source, Biot number, Eckert number, temperature ratio, and ratio of rotational rate to stretching rates are all examples of non-dimensional numbers.

$$M = \frac{\sigma_f B_0^2}{\rho_f a}, R = \frac{16\sigma^* T_\infty^3}{3k^* k_f}, Pr = \frac{(\mu c_p)_f}{k_f}, Q_t = \frac{Q_T}{\rho_f c_p f}, Bi = \frac{h_f}{k_{nf}} \sqrt{\frac{\nu_f}{a}}, Ec = \frac{u_w^2}{c_{pf}(T_f-T_\infty)}, \theta_w = \frac{T_f}{T_\infty}, \lambda = \frac{\Omega}{a}. \quad (2.16)$$

The quantities of practical interest are the skin friction coefficients  $C_{fx}, C_{fy}$  and the local Nusselt number  $Nu_x$  defined as follows;

$$C_{fx} = \frac{\tau_{wx}}{\rho_f u_w^2},$$

$$C_{fy} = \frac{\tau_{wy}}{\rho_f u_w^2},$$

$$Nu_x = \frac{xq_w}{k_f(T_f-T_\infty)}, \quad (2.17)$$

where  $\tau_{wx} = \tau_{zx}|_{z=0}$  and  $\tau_{wy} = \tau_{zy}|_{z=0}$  are the wall shear stresses and  $q_w$  is the wall heat flux given by,

$$\tau_{wx} = \mu_{nf} \frac{\partial u}{\partial z} \Big|_{z=0},$$

$$\tau_{wy} = \mu_{nf} \frac{\partial v}{\partial z} \Big|_{z=0},$$

$$q_w = -k_{nf} \left. \frac{\partial T}{\partial z} \right|_{z=0} + q_r|_{z=0}. \quad (2.18)$$

Using equations (2.11) and (2.18) in equation (2.17), one obtains,

$$\begin{aligned} \sqrt{Re_x} C_{fx} &= \frac{1}{(1-\phi)^{2.5}} f''(0), \\ \sqrt{Re_x} C_{fy} &= \frac{1}{(1-\phi)^{2.5}} g'(0), \\ \frac{Nu_x}{\sqrt{Re_x}} &= -\left(\frac{k_{nf}}{k_f} + R\theta_w^3\right) \theta'(0), \end{aligned} \quad (2.19)$$

where  $Re_x = \frac{u_w x}{\nu_f}$  is the local Reynolds number.

### NUMERICAL METHOD

The reduced system of Eqs. (2.12) -(2.14), together with the boundary conditions (2.15), is solved numerically by employing the Runge-Kutta-Fehlberg fourth–fifth order (RKF45) scheme combined with the shooting technique. For this purpose, the coupled nonlinear ordinary differential equations are first converted into an equivalent system of first-order equations. This transformation enables the implementation of the shooting method, in which the unknown initial conditions are iteratively adjusted until the prescribed boundary conditions at infinity are satisfied to the desired accuracy.

Set  $x_1 = f(\eta)$ ,  $x_2 = f'(\eta)$ ,  $x_3 = f''(\eta)$ ,  $x_4 = g(\eta)$ ,  $x_5 = g'(\eta)$ ,  $x_6 = \theta(\eta)$ ,  $x_7 = \theta'(\eta)$ . Accordingly, we have;

$$x'_1 = x_2, x'_2 = x_3, x'_4 = x_5, x'_6 = x_7,$$

$$\begin{aligned} x'_3 &= (1-\phi)^{2.5} \left(1 - \phi + \phi \frac{\rho_s}{\rho_f}\right) \left\{ f'^2 + f f'' + 2\lambda g - \frac{\frac{\sigma_{nf}}{\sigma_f}}{\left(1 - \phi + \phi \frac{\rho_s}{\rho_f}\right)} M f' \right\} \\ x'_5 &= -(1-\phi)^{2.5} \left(1 - \phi + \phi \frac{\rho_s}{\rho_f}\right) \left\{ f g' - f' g - 2\lambda f' - \frac{\frac{\sigma_{nf}}{\sigma_f}}{\left(1 - \phi + \phi \frac{\rho_s}{\rho_f}\right)} M g \right\} \\ x'_7 &= -\frac{1}{\left(\frac{K_{nf}}{k_f} + R(1 + (\theta_w - 1)\theta)^3\right)} \left\{ 3R(1 + (\theta_w - 1)\theta)^2(\theta_w - 1)\theta'^2 + \left(1 - \phi + \phi \frac{(\rho c_p)_s}{(\rho c_p)_f}\right) Pr f \theta' \right. \\ &\quad \left. + Pr \left[ \frac{1}{(1-\phi)^{2.5}} Ec(f''^2 + g'^2) + \frac{\sigma_{nf}}{\sigma_f} MEc(f'^2 + g^2) + Q_t \theta(\eta) \right] \right\} \end{aligned}$$

$$x_1(0) = x_2(0) - 1 = x_3 - a_1 = x_4(0) = 0, x_5(0) - a_2 = x_6(0) - a_3 = x_7(0) - Bi(x_6(0) - 1) = 0. \quad (2.19)$$

here  $a_1, a_2$  and  $a_3$  are estimated via shooting technique. Afterwards, the resultant initial value problem is solved numerically via RK-Fehlberg method. The convergence criteria and step size are chosen as  $10^{-6}$  and  $\nabla \xi = 0.001$ .

### RESULTS AND DISCUSSION

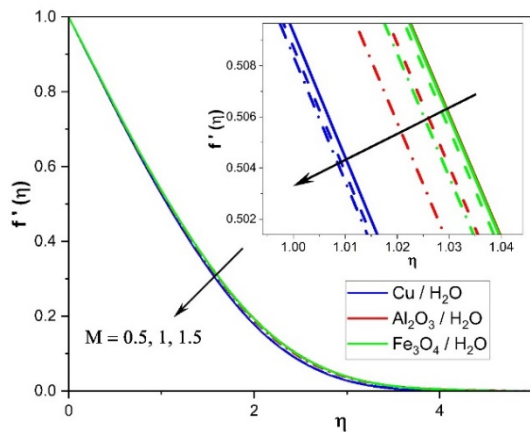
The Runge-Kutta-Fehlberg (RKF45) method, in conjunction with a shooting method, is used numerically to solve the system of transformed nonlinear ordinary differential equations produced by similarity transformations. To ensure accuracy and stability of the solution, the convergence criterion is fixed at  $10^{-6}$ , and a step size of  $\Delta \eta = 0.001$  is used. The computational domain is truncated at a sufficiently large value of the similarity variable  $\eta$ , beyond which the boundary layer effects are negligible. The correctness of the numerical model is verified by comparing generated skin friction coefficients  $f''(0)$  and  $g'(0)$  for specific rotation parameter  $\lambda$  to benchmark findings in literature. [22, 23]. Table 2 shows the results of the comparison, which prove that the numerical system is reliable since there is high agreement.

**Table 2.** Comparison of Present Results with Existing Studies ( $\phi = 0, M = 0$ )

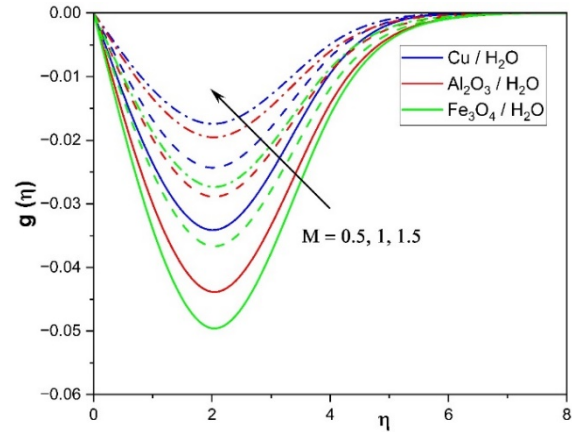
$\lambda$	Wang [22]		Nazar et al. [23]		Present results	
	$f''(0)$	$g'(0)$	$f''(0)$	$g'(0)$	$f''(0)$	$g'(0)$
0	-1	0	-1	0	-1.00006	0
0.5	-1.1384	-0.5128	-1.1384	-0.5128	-1.13837	-0.51276
1.0	-1.3250	-0.8371	-1.3250	-0.8371	-1.32503	-0.83710
2.0	-1.6523	-1.2873	-1.6523	-1.2873	-1.65235	-1.28726

Figures 2 and 3 demonstrate how the magnetic parameter  $M$  affects axial and transverse velocity profiles. As  $M$  increases, the axial velocity  $f'(\eta)$  decreases due to the opposing Lorentz force, which acts as a resistive drag on the fluid motion. In contrast, the transverse velocity  $g(\eta)$  shows an increasing trend with higher  $M$ , indicating enhanced secondary flow generated by the magnetic influence.



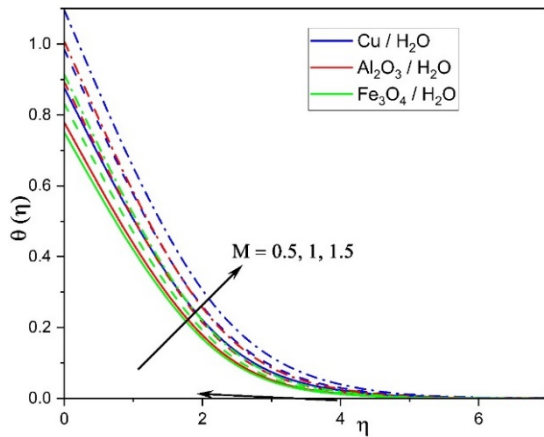


**Figure 02.** A study on the impact of a magnetic characteristic on speeds

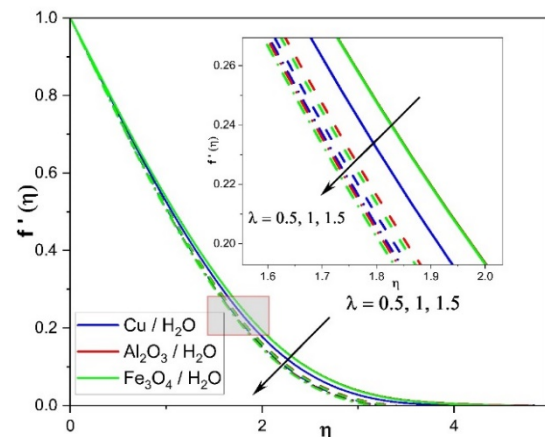


**Figure 03.** A study on the impact of a magnetic characteristic on speeds

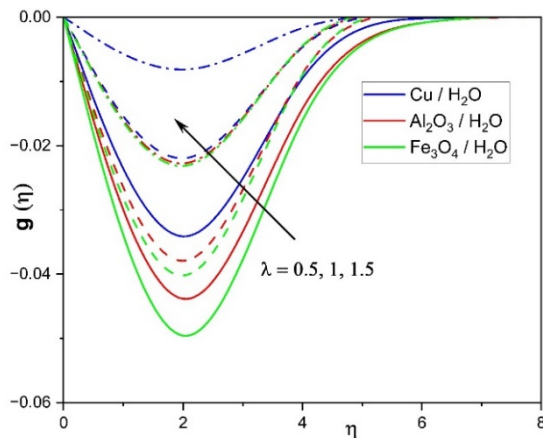
In Figure 4, the temperature profile ( $\eta$ ) increases with increasing  $M$ , mainly owing to ohmic heating effects from the magnetic field. Figures 5-7 illustrate how the rotation parameter  $\lambda$  affects the flow and heat fields. An increase in  $\lambda$  reduces the axial velocity while enhancing the transverse velocity, reflecting the rotational acceleration induced by the Coriolis force. The conversion of rotational energy into thermal energy causes a discernible increase in the temperature profile as  $\lambda$  values grow. This is because rotation introduces Coriolis acceleration, which diverts part of the momentum from the axial direction into the transverse direction. Consequently, energy is redistributed across velocity components, suppressing streamwise transport but enhancing lateral motion.



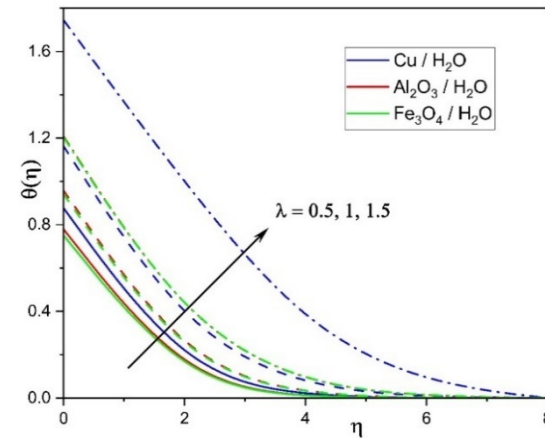
**Figure 04.** The impact of a magnetic parameter on a plot of temperatures



**Figure 05.** The velocity profile as a function of the stretching rate parameter and the ratio of the rotational speed to that parameter



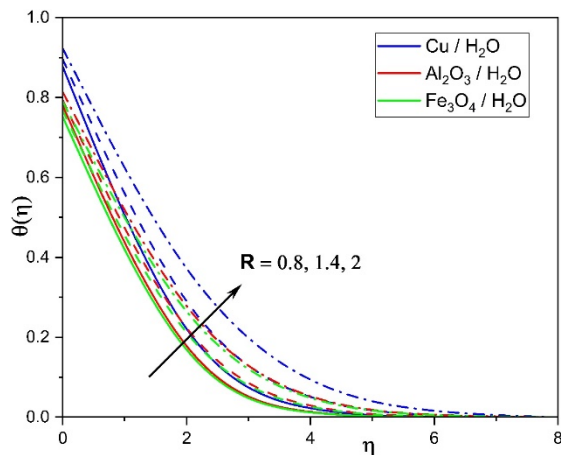
**Figure 06.** The impact on the velocity profile of the ratio of the stretching rate parameter to the rotation rate



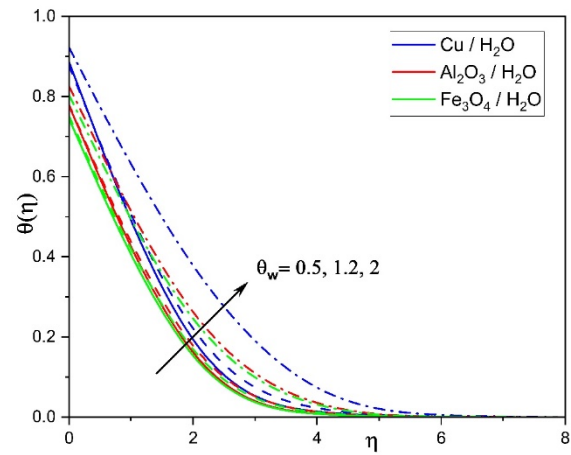
**Figure 07.** The influence of the ratio of rotation rate to the stretching rate parameter on the temperature profile

Figure 8 shows how the temperature distribution is affected by the nonlinear radiation parameter  $R$ . Nonlinear radiation augments energy transport by radiative diffusion, which enhances the effective thermal conductivity of the fluid,

thereby elevating the temperature profile. Figure 9 illustrates that increasing the temperature ratio parameter ( $\theta_w$ ) raises boundary layer temperatures and enhances thermal diffusion.

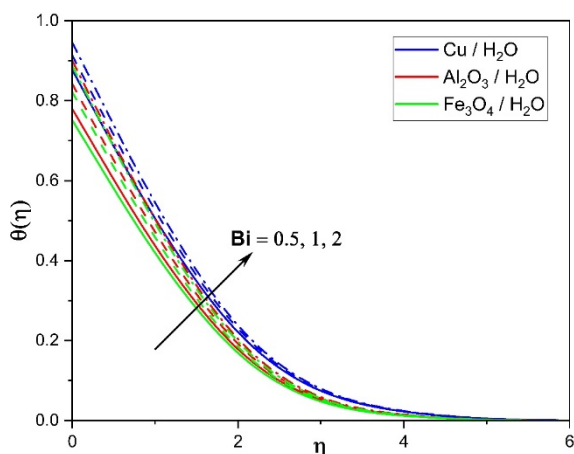


**Figure 08.** Heat profile as a function of radiation parameter

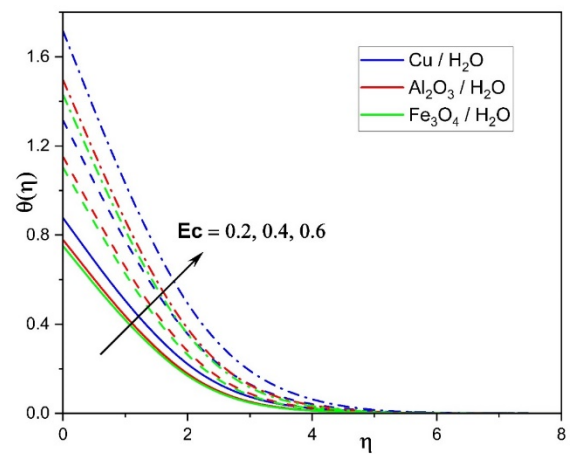


**Figure 09.** Changing the temperature profile according to a heat ratio parameter

In Figure 10, the Biot number ( $Bi$ ), which characterizes the convective heat exchange at the surface, is varied. As  $Bi$  increases, the temperature near the surface increases due to a higher rate of convective heating, which promotes more efficient heat transfer into the fluid. A larger  $Bi$  corresponds to stronger thermal interaction between the solid boundary and the fluid. The influence of viscous dissipation is depicted in Figure 11 via the Eckert number ( $Ec$ ).  $Ec$  values rise when internal fluid friction raises system temperature and thickens the thermal barrier layer, increasing thermal energy. Viscous dissipation converts mechanical work done by shear stresses into internal energy, while Joule heating transforms electromagnetic resistance into thermal energy. Both serve as internal heat generation mechanisms that elevate the fluid temperature.



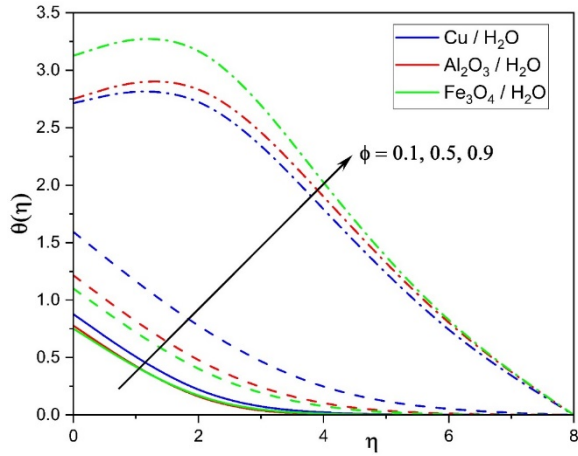
**Figure 10.** How the Biot number influences the temperature chart



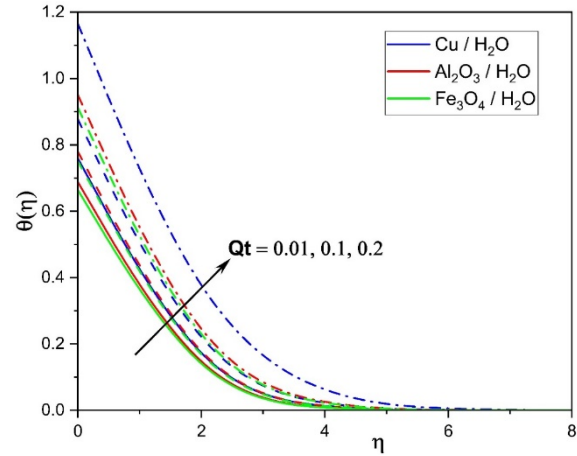
**Figure 11.** Understanding how the Eckert number influences the temperature profile

Figure 12 shows how the nanoparticle volume fraction  $\phi$  affects the temperature field. Due to the nanofluid's enhanced thermal conductivity and heat absorption capability, the temperature distribution becomes more noticeable as  $\phi$  grows. This increases thermal diffusion because the fluid can retain more heat. Figure 13 illustrates the effect of the internal heat source parameter. As  $Qt$  increases, the temperature within the boundary layer rises substantially, indicating a direct enhancement in internal energy generation which results in a thicker thermal boundary layer and stronger temperature in fluids. With regard to the parameters  $\lambda$  and  $M$ , Figures 14 and 15 show the fluctuation of the skin friction coefficients in  $x$  and  $y$  directions. It is observed that increasing  $\lambda$  and  $M$  leads to a reduction in axial skin friction, indicating a decrease in surface shear stress. However,  $C_{fy}$  increases with  $M$  due to enhanced resistance in the transverse direction caused by the Lorentz force, while it decreases with  $\lambda$ , as rotational motion reduces transverse shear. Figure 16 shows the variation of the local Nusselt number with respect to  $\lambda$  and  $M$ . Nusselt number decreases when either parameter rises, suggesting wall convective heat transmission decreases. The dampening effect of magnetic and rotating forces decreases the thickness of thermal boundary layer. Figure 17 demonstrates how Eckert number and nanoparticle concentration effect Nusselt number. A synergistic impact between thermal energy production and increased thermal

conductivity owing to nanoparticles is shown by the fact that raising either parameter boosts the heat transfer rate. Among the nanofluids considered, the Cu-based fluid consistently shows the highest heat transfer performance, followed by  $\text{Al}_2\text{O}_3$  and  $\text{Fe}_3\text{O}_4$ , respectively. These results underscore the significance of controlling magnetic, rotational, and thermal parameters to optimize heat and momentum transport in nanofluid-based systems. They also reinforce the crucial role of nanoparticle material selection in designing efficient thermal management technologies.



**Figure 12.** How the parameter for solid volume fraction affects the temperature profile



**Figure 13.** Heat source parameter influence on temperature profile

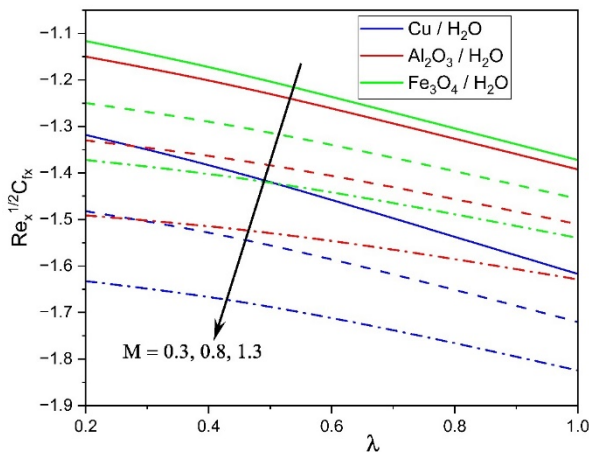


**Figure 14.** A study on the skin friction coefficient and its relationship to the magnetic parameter, rotation rate, and stretching rate

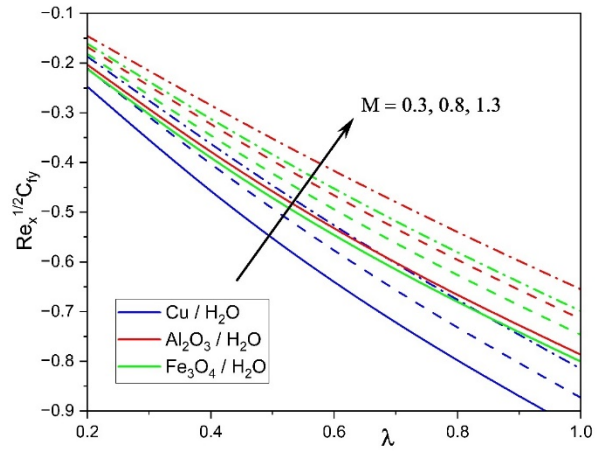


**Figure 15.** A study on the skin friction coefficient and its relationship to the magnetic parameter, rotation rate, and stretching rate

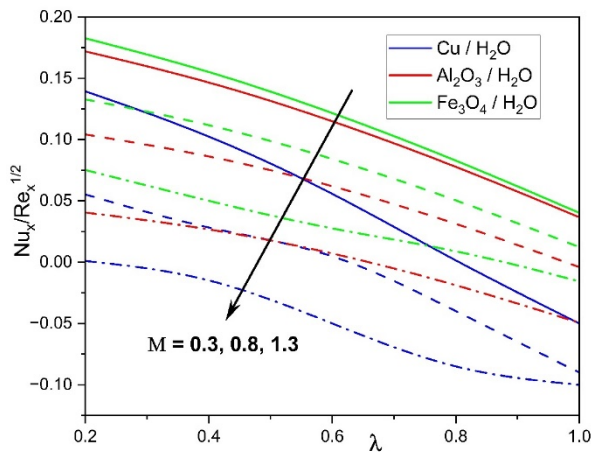


**Figure 16.** The skin friction coefficient as a function of the magnetic parameter and the ratio of the rotational speed to the stretching rate

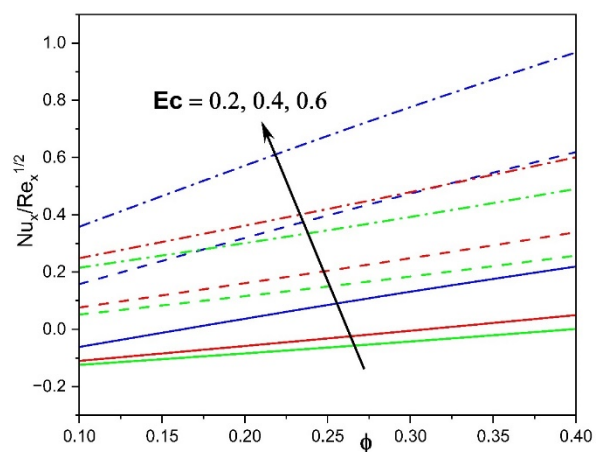


**Figure 17.** Nusselt number impacted by Eckert number v/s  $\phi$

Table 3 highlights the influence of nanoparticle concentration ( $\phi$ ), radiation parameter (R), Biot number (Bi), and Eckert number (Ec) on skin-friction coefficients and heat transfer for  $Fe_3O_4$ ,  $Al_2O_3$ , and  $Cu$  nanofluids.

**Table 3.** Variation of  $Re_x^{0.5} C_{fx}$ ,  $Re_x^{0.5} C_{fy}$  and  $Re_x^{-0.5} Nu$  for  $Fe_3O_4$ ,  $Al_2O_3$  and  $cu$  nanofluids with different values of  $\phi$ ,  $R$ ,  $Bi$  and  $Ec$

$\phi$	$R$	$Bi$	$Ec$	$Fe_3O_4$			$Al_2O_3$			$cu$		
				$\sqrt{Re_x} C_{fx}$	$\sqrt{Re_x} C_{fy}$	$\frac{Nu_x}{\sqrt{Re_x}}$	$\sqrt{Re_x} C_{fx}$	$\sqrt{Re_x} C_{fy}$	$\frac{Nu_x}{\sqrt{Re_x}}$	$\sqrt{Re_x} C_{fx}$	$\sqrt{Re_x} C_{fy}$	$\frac{Nu_x}{\sqrt{Re_x}}$
0.1				-2.57614	-1.12919	-0.1471	-2.51119	-1.0574	0.11598	-2.76735	-1.3362	-0.70944
0.4				-6.11419	-2.46404	0.762076	-5.81055	-2.11379	1.552431	-6.96659	-3.40968	-0.65158
0.8				-42.1525	-8.8709	-5.71607	-40.4565	-7.15531	-5.22018	-45.3067	-14.118	-5.20013
	1			-2.57614	-1.12919	-0.1471	-2.51119	-1.0574	0.11598	-2.76735	-1.3362	-0.70944
	2			-2.57614	-1.12919	0.12487	-2.51119	-1.0574	0.313545	-2.76735	-1.3362	-0.30353
	3			-2.57614	-1.12919	0.828804	-2.51119	-1.0574	1.04208	-2.76735	-1.3362	0.370026
		0.4		-2.57614	-1.12919	-0.1471	-2.51119	-1.0574	0.11598	-2.76735	-1.3362	-0.70944
		0.8		-2.57614	-1.12919	-0.22649	-2.51119	-1.0574	0.189343	-2.76735	-1.3362	-0.99507
		1.5		-2.57614	-1.12919	-0.30282	-2.51119	-1.0574	0.269242	-2.76735	-1.3362	-1.23501
			0.2	-2.57614	-1.12919	-0.1471	-2.51119	-1.0574	0.11598	-2.76735	-1.3362	-0.70944
			0.5	-2.57614	-1.12919	-0.74056	-2.51119	-1.0574	-0.00332	-2.76735	-1.3362	-1.76428
			0.7	-2.57614	-1.12919	-0.62222	-2.51119	-1.0574	-0.08866	-2.76735	-1.3362	-2.27411

Increasing  $\phi$  enhances both axial and transverse skin friction due to higher viscosity, with  $Cu$  showing the highest resistance, while the Nusselt number generally decreases, except for  $Al_2O_3$  which sustains better heat transfer. Larger  $R$  values intensify transverse skin friction through stronger Coriolis forces but improve heat transfer, where  $Al_2O_3$  performs best. Variation in  $Bi$  reveals that  $Al_2O_3$  nanofluid enhances convective heat exchange, whereas  $Fe_3O_4$  and  $Cu$  exhibit reduced Nusselt numbers. The Eckert number increases internal heating and suppresses cooling for  $Fe_3O_4$  and  $Cu$ , while  $Al_2O_3$  shows a mild positive response due to its superior thermal conductivity. Overall,  $Cu$  exhibits strong flow resistance,  $Fe_3O_4$  provides stability, and  $Al_2O_3$  consistently demonstrates the best heat transfer characteristics, making it the most efficient choice under varying conditions.

## CONCLUSIONS

This study provides new physical insights into the three-dimensional MHD nanofluid flow over a stretching surface under the combined influences of rotation, magnetic field, nonlinear radiation, Joule heating, and viscous dissipation. From a physics standpoint, the following key conclusions can be drawn:

- Rotation fundamentally redistributes momentum between the axial and transverse directions. While axial motion is suppressed, transverse velocity is enhanced, indicating that rotational energy is redirected into lateral flow, which modifies transport mechanisms across the boundary layer.
- The applied magnetic field resists fluid motion, thickening the momentum boundary layer, while simultaneously enhancing heat generation through Ohmic dissipation. This coupling shows how electromagnetic control can tune both fluid resistance and energy transport.
- Nonlinear radiation, internal heat generation, and convective surface effects act collectively to strengthen energy diffusion across the boundary layer. Their combined impact illustrates the importance of radiative and convective modes in enhancing nanoscale thermal transport.
- Viscous and Joule dissipation provide an internal energy feedback mechanism, where mechanical work against friction and electromagnetic resistance is directly converted into heat, raising the fluid temperature and altering thermal boundary layer dynamics.
- The comparative analysis of  $Cu$ ,  $Al_2O_3$ , and  $Fe_3O_4$  nanofluids demonstrates that nanoparticle type is a decisive factor in tuning flow and heat transfer.  $Cu$ -water nanofluid exhibits the strongest heat transfer enhancement due to its high thermal conductivity, whereas  $Fe_3O_4$ -water shows superior flow adaptability under magnetic control, making it advantageous for MHD applications.

**Acknowledgements:** The author would like to thank GITAM Deemed to be University for providing the MATLAB Software.

**Funding:** There is no funding received by any agency.

**Data Availability Statement:** This article contains all the pertinent data generated or analysed during this investigation; further material can be provided upon reasonable request to the authors.

**Declaration:** We, the authors of this manuscript, declare that this work is original and has not been published or submitted elsewhere for consideration.

**Conflict of Interest:** The author declares that there is no conflict of interest

## ORCID

©M.M. Bindu, <https://orcid.org/0009-0001-6250-8606>; ©Elliriki Mamatha, <https://orcid.org/0000-0002-1512-5063>

©V. Nagaradhika, <https://orcid.org/0000-0002-0927-7191>



## REFERENCE

- [1] S.U.Choi, and J.A. Eastman, *Enhancing thermal conductivity of fluids with nanoparticles* (No. ANL/MSD/CP-84938; CONF-951135-29), (Argonne National Lab. (ANL), Argonne, IL, United States), (1995).
- [2] J. Buongiorno, "Convective transport in nanofluids," *ASME J. Heat Transf.*, **128**, 240–250 (2006). <https://doi.org/10.1115/1.2150834>
- [3] Wang, Xiaoming, Changhe Li, Yanbin Zhang, Wenfeng Ding, Min Yang, Teng Gao, Huajun Cao, *et al.* "Vegetable oil-based nanofluid minimum quantity lubrication turning: Academic review and perspectives," *Journal of Manufacturing Processes*, **59**, 76-97 (2020). <https://doi.org/10.1016/j.jmapro.2020.09.044>
- [4] M. Sheikholeslami, and H.B. Rokni, "Nanofluid two phase model analysis in existence of induced magnetic field," *International Journal of Heat and Mass Transfer*, **107**, 288-299 (2017). <https://doi.org/10.1016/j.ijheatmasstransfer.2016.10.130>
- [5] W.A. Khan, and I. Pop, "Boundary-layer flow of a nanofluid past a stretching sheet," *International journal of heat and mass transfer*, **53**(11-12), 2477-2483 (2010). <https://doi.org/10.1016/j.ijheatmasstransfer.2010.01.032>
- [6] M.R. Krishnamurthy, B.J. Gireesha, R.S.R. Gorla, and B.C. Prasannakumara, "Suspended particle effect on slip flow and melting heat transfer of nanofluid over a stretching sheet embedded in a porous medium in the presence of nonlinear thermal radiation," *Journal of Nanofluids*, **5**(4), 502-510(2016). <https://doi.org/10.1166/jon.2016.1247>
- [7] N. Muqaddass, F. Mabood, S.A. Shehzad, F. Sahar, and I.A. Badruddin, "Analysis of heat transportation in a convectively heated time-dependent  $\text{CuAl}_2\text{O}_3\text{-H}_2\text{O}$  hybrid nanofluid with varying thermal conductivity," *Proceedings of the Institution of Mechanical Engineers, Part C: Journal of Mechanical Engineering Science*, **238**(6), 2513-2520 (2024). <https://doi.org/10.1177/09544062231187788>
- [8] S. Nadeem, N. Abbas, and M.Y. Malik, "Inspection of hybrid based nanofluid flow over a curved surface," *Computer methods and programs in biomedicine*, **189**, 105193 (2020). <https://doi.org/10.1016/j.cmpb.2019.105193>
- [9] A. Asadi, I.M. Alarifi, and L.K. Foong, "An experimental study on characterization, stability and dynamic viscosity of  $\text{CuO-TiO}_2$ /water hybrid nanofluid," *Journal of Molecular Liquids*, **307**, 112987 (2020). <https://doi.org/10.1016/j.molliq.2020.112987>
- [10] K. Das, P.R. Duari, and P.K. Kundu, "Nanofluid flow over an unsteady stretching surface in presence of thermal radiation," *Alex. Eng. J.* **53**(3), 737–745 (2014). <https://doi.org/10.1016/j.aej.2014.05.002>
- [11] L. Roohi, "Nanofluid flow in a converging and diverging channel of rectangular and heated walls," *Ain Shams Engineering Journal*, **12**(4), 4023-4035 (2021). <https://doi.org/10.1016/j.asej.2021.02.030>
- [12] K. Ur Rehman, M.Y. Malik, O.D. Makinde, and A.A. Malik, "A comparative study of nanofluids flow yields by an inclined cylindrical surface in a double stratified medium," *The European Physical Journal Plus*, **132**(10), 427 (2017). <https://doi.org/10.1140/epjp/i2017-11679-1>
- [13] O.D. Makinde, "Computational modelling of nanofluids flow over a convectively heated unsteady stretching sheet," *Current Nanoscience*, **9**(5), 673-678 (2013). <https://doi.org/10.2174/15734137113099990068>
- [14] N.S. Akbar, M.F. Hussain, M. Alghamdi, and T. Muhammad, "Thermal characteristics of magnetized hybrid Casson nanofluid flow in a converging-diverging channel with radiative heat transfer: A computational analysis," *Scientific Reports*, **13**(1), 21891 (2023). <https://doi.org/10.1038/s41598-023-49397-3>
- [15] U. Khan, I. Waini, A. Zaib, A. Ishak, and I. Pop, "MHD mixed convection hybrid nanofluids flow over a permeable moving inclined flat plate in the presence of thermophoretic and radiative heat flux effects," *Mathematics*, **10**(7), 1164 (2022). <https://doi.org/10.3390/math10071164>
- [16] B.J. Gireesha, and L. Anitha, "Convective flow of couple stress ternary nanoliquid flow through a permeable microchannel: irreversibility analysis," *International Journal of Modelling and Simulation*, 1-18 (2024). <https://doi.org/10.1080/02286203.2024.2388117>
- [17] J.K. Madhukesh, G.K. Ramesh, H.N. Fatima, G.S. Roopa, and S.A. Shehzad, "Influence of pollutant dispersion on nanofluid flowing across a stretched disc-cone device," *Journal of Molecular Liquids*, **411**, 125710 (2024). <https://doi.org/10.1016/j.molliq.2024.125710>
- [18] W. Cheng, M. Safeer, U. Farooq, S. Munir, J. Cui, and C.S.K. Raju, "Nonsimilar forced convection simulations of water-copper nanofluid flow through a porous medium in the presence of thermal radiations, heat generation and viscous dissipation," *Waves in Random and Complex Media*, **35**(1), 511-526 (2025). <https://doi.org/10.1080/17455030.2021.2023785>
- [19] M. Sheikholeslami, and S.A. Shehzad, "Magnetohydrodynamic nanofluid convection in a porous enclosure considering heat flux boundary condition," *International Journal of Heat and Mass Transfer*, **106**, 1261-1269 (2017). <https://doi.org/10.1016/j.ijheatmasstransfer.2016.10.107>
- [20] D.K. Jyoti, V. Nagaradhika, P.B.S. Kumar, and A.J. Chamkha, "Nonlinear Convection and Radiative Heat Transfer in Kerosene-Alumina Nanofluid Flow Between Two Parallel Plates with Variable Viscosity," *Journal of Nanofluids*, **13**(5), 1055-1062 (2024). <https://doi.org/10.1166/jon.2024.2193>
- [21] T.V. Karman, "Über laminar and turbulent Reibung," *ZAMM, J. App. Math. Mech.* **1**(4), 233–252 (1921).
- [22] C.Y. Wang, "Stretching a surface in a rotating fluid", *ZAMP*, **39**(2), 177–185 (1988). <https://doi.org/10.1007/BF00945764>
- [23] R. Nazar, N. Amin, and I. Pop, "Unsteady boundary layer flow due to a stretching surface in a rotating fluid," *Mech. Res. Commun.* **31**(1), 121–128 (2004). <https://doi.org/10.1016/j.mechrescom.2003.09.004>
- [24] O.D. Makinde, O.A. Bég, and H.S. Takhar, "Magnetohydrodynamic viscous flow in a rotating porous medium cylindrical annulus with an applied radial magnetic field," *Int. J. Appl. Math. Mech.* **5**(6), 68-81 (2009).
- [25] M. Sheikholeslami, and D.D. Ganji, "Three-dimensional heat and mass transfer in a rotating system using nanofluid," *Powder Technol.* **253**, 789–796 (2014). <https://doi.org/10.1016/j.powtec.2013.12.042>
- [26] M. Mustafa, A. Mushtaq, T. Hayat, and A. Alsaedi, "Rotating flow of magnetite-water nanofluid over a stretching surface inspired by non-linear thermal radiation," *PloS one*, **11**(2), e0149304 (2016). <https://doi.org/10.1371/journal.pone.0149304>
- [27] M. Archana, B.J. Gireesha, B.C. Prasannara, and R.S.R. Gorla, "Influence of nonlinear thermal radiation on rotating flow of Casson nanofluid, *Nonlinear Engineering*, **7**(2), 91-101 (2017). <https://doi.org/10.1515/nleng-2017-0041>
- [28] P.B. Sampath Kumar, B.J. Gireesha, B. Mahanthesh, and R.S.R. Gorla, "Radiative nonlinear 3D flow of ferrofluid with Joule heating, convective condition and Coriolis force," *Thermal Science and Engineering Progress*, **3**, 88-94 (2017). <https://doi.org/10.1016/j.tsep.2017.06.006>

- [29] F. Mabood, W.A. Khan, and O.D. Makinde, "Hydromagnetic flow of a variable viscosity nanofluid in a rotating permeable channel with Hall effects," *Journal of Engineering Thermophysics*, **26**(4), 553-566 (2017). <https://doi.org/10.1134/S1810232817040105>
- [30] M.V. Krishna, and A.J. Chamkha, "Hall and ion slip effects on MHD rotating boundary layer flow of nanofluid past an infinite vertical plate embedded in a porous medium," *Results in Physics*, **15**, 102652 (2019). <https://doi.org/10.1016/j.rinp.2019.102652>
- [31] S.S. Kumar, RV Prasad, S.U. Mamatha, C.S.K. Raju, and B.M. Rao, Dynamics of nonlinear-shaped solid particles occurrence of hydro-magnetic slip with comparative analysis of radiated ternary, hybrid and nanofluid flow in a rotating internally, *International Journal of Modern Physics B*, **37**(13), 2350127 (2023). <https://doi.org/10.1142/S0217979223501278>
- [32] Z. Mustafa, T. Hayat, T. Javed, and A. Alsaedi, "Unsteady MHD Casson fluid flow with Dufour and Soret's effects due to a rotating cone," *Waves in Random and Complex Media*, (2023). <https://doi.org/10.1080/17455030.2023.2188099>
- [33] T. Hayat, Z. Abbas, I. Pop, and S. Asghar, "Effects of radiation and magnetic field on the mixed convection stagnation-point flow over a vertical stretching sheet in a porous medium," *International Journal of Heat and Mass Transfer*, **53**(1-3), 466-474 (2010). <https://doi.org/10.1016/j.ijheatmasstransfer.2009.09.010>
- [34] T.G. Motsumi, and O.D. Makinde, "Effects of thermal radiation and viscous dissipation on boundary layer flow of nanofluids over a permeable moving flat plate," *Physica Scripta*, **86**(4), 045003 (2012). <https://doi.org/10.1088/0031-8949/86/04/045003>
- [35] M. Sheikholeslami, T. Hayat, and A. Alsaedi, "MHD free convection of Al<sub>2</sub>O<sub>3</sub>-water nanofluid considering thermal radiation: a numerical study," *International Journal of Heat and Mass Transfer*, **96**, 513-524 (2016). <https://doi.org/10.1016/j.ijheatmasstransfer.2016.01.059>
- [36] S.J. Reddy, P. Valsamy, and D.S. Reddy, "Thermal Radiation Impact on Nanofluid Boundary Layer Flow Towards a Moving Plate in Presence of Magnetic Field Using Numerical Solutions," *Journal of Nanofluids*, **13**(1), 199-206 (2024). <https://doi.org/10.1166/jon.2024.2144>
- [37] W. Hassan, U. Farooq, D. Liu, M. Abid, M. Imran, and T. Muhammad, "Heat transfer analysis of hybrid nanofluid flow with thermal radiation through a stretching sheet: A comparative study," *International Communications in Heat and Mass Transfer*, **138**, 106303 (2022). <https://doi.org/10.1016/j.icheatmasstransfer.2022.106303>
- [38] P. Sreedevi, P.S. Reddy, and A. Chamkha, "Heat and mass transfer analysis of unsteady hybrid nanofluid flow over a stretching sheet with thermal radiation," *SN Applied Sciences*, **2**(7), 1222 (2020). <https://doi.org/10.1007/s42452-020-3011-x>
- [39] R. Devi, S.V. Venkata, and M.G. Reddy, "Parametric analysis of MHD flow of nanofluid in stretching sheet under chemical sensitivity and thermal radiation," *Heat Transfer*, **51**(1), 948-975 (2022). <https://doi.org/10.1002/htj.22337>
- [40] B.J. Gireesha, G. Sowmya, M.I. Khan, and H.F. Öztop, "Flow of hybrid nanofluid across a permeable longitudinal moving fin along with thermal radiation and natural convection," *Computer methods and programs in biomedicine*, **185**, 105166 (2020). <https://doi.org/10.1016/j.cmpb.2019.105166>
- [41] R.K. Tiwari, and M.K. Das, "Heat transfer augmentation in a two-sided lid-driven differentially heated square cavity utilizing nanofluids," *Int. J. Heat Mass Transf.* **50**, 2002-2018 (2007). <https://doi.org/10.1016/j.ijheatmasstransfer.2006.09.034>
- [42] H.C. Brinkman, "The viscosity of concentrated suspensions and solutions," *J. Chem. Phys.* **20**, 571-581 (1952). <https://doi.org/10.1063/1.1700493>
- [43] J.C. Maxwell, *A treatise on electricity and magnetism*, Second Ed., (Cambridge, Oxford University Press, 1904). pp. 435-441.

# ТРИВИМІРНИЙ МГД-ПОТІК ТА ТЕПЛОПЕРЕНОС НАНОРІДИН НА ВОДНІЙ ОСНОВІ ЧЕРЕЗ ПОВЕРХНЮ ЩО РОЗТЯГУЄТЬСЯ ЗА ДОПОМОГОЮ СИЛИ КОРІОЛІСА ТА ТЕПЛОВИХ ЕФЕКТІВ

М.М. Бінду<sup>1,2</sup>, Еллірікі Маматха<sup>2</sup>, В. Нагарадхіка<sup>3</sup>

<sup>1</sup>Державний коледж першого ступеня, Чаннапатна, 562160, Індія

<sup>2</sup>Кафедра математики, GSS, GITAM Deemed to be University, Бенгалур-561203, Індія






<sup>3</sup>Кафедра математики, Технологічний інститут сера М. Вісвесварай, Бенгалур-562 157, Індія

Це дослідження зосереджено на тепловій поведінці та тривимірному пограничному шарі потоку нанорідина на водній основі на розтягнутій поверхні з урахуванням комбінованого впливу сил Коріоліса та Лоренца. Модель включає кілька важливих фізичних аспектів, таких як поверхнева конвекція, внутрішнє теплоутворення, джоулеве нагрівання, в'язка дисипація та теплове випромінювання. Наночастинки міді (Cu), оксиду алюмінію (Al<sub>2</sub>O<sub>3</sub>) та магнетиту (Fe<sub>3</sub>O<sub>4</sub>) диспергуються у воді для порівняння їхньої ефективності у посиленні теплопередачі. Застосовуючи перетворення подібності, складна система диференціальних рівнянь з частинними похідними зводиться до набору нелінійних звичайних диференціальних рівнянь, які потім розв'язуються чисельно за допомогою методу Рунге-Кутти-Фельберга разом з методом стрільби. Результати показують, що нанорідина, що містить наночастинки Cu, забезпечують найвищі теплові характеристики, далі йдуть ті, що містять Al<sub>2</sub>O<sub>3</sub> та Fe<sub>3</sub>O<sub>4</sub>. Ці результати підкреслюють важливість вибору відповідних наночастинок для покращення ефективності теплопередачі в застосуваннях для терморегуляції. Збільшення параметра обертання  $\lambda$  пригнічує осьову швидкість, одночасно зменшуючи розподіл температури, підкреслюючи вплив демпфування обертальних ефектів на імпульс та теплоперенос.

**Ключові слова:** нелінійне теплове випромінювання; нанорідина; обертальні ефекти; в'язка дисипація; джоулеве нагрів



# MAGNETOHYDRODYNAMIC CASSON HYBRID NANOFLUID DYNAMICS IN CIRCULATING BLOOD CONSIDERING THERMAL RADIATION AND CHEMICAL REACTIONS

 G. Durga Priyadarsini<sup>1</sup>,  Syeda Asma Kauser<sup>2</sup>,  Y. Hari Krishna<sup>3</sup>,  T. Nageswara Rao<sup>4</sup>,  
 G. Venkata Ramana Reddy<sup>5\*</sup>

<sup>1</sup>Department of Mathematics, Geethanjali College of Engineering and Technology, Cheeryal, Hyderabad, Telangana, India-501301

<sup>2</sup>Department of Mathematics, Global Institute of Engineering and Technology, Moinabad, Hyderabad, Telangana-501504, India

<sup>3</sup>Department of Mathematics, ANURAG Engineering College, Ananthagiri, Suryapet, Telangana-508206, India

<sup>4</sup>Department of Mathematics, Koneru Lakshmaiah Education Foundation, Vaddeswaram, India-522302

<sup>5</sup>Department of Integrated Research Discovery, Koneru Lakshmaiah Education Foundation, Vaddeswaram, India-522302

Email: priyadarsini.81@gmail.com, asmaxlnc1@gmail.com, yaraganihari@gmail.com, tnraothota@kluniversity.in

\*Corresponding Author Email: gvrr1976@kluniversity.in

Received September 2, 2025; revised October 24, 2025; accepted October 24, 2025

The purpose of this work is to investigate the relevance of thermal radiation and chemical reaction in the thermal and radiative analysis of hybrid Casson nanofluid dynamics. The physical model was based on the mixture of Gold and Silver hybrid nanoparticles (HN) which are suspended in a blood past a stretchable sheet. The dynamics of fluid past a stretchable sheet is a notable analysis for thermal and momentum boundary layers. It finds applications in various technological fields and in industries. The model equations were investigated using a system of partial differential equations (PDEs). Acceptable transformation was used to convert these PDEs into total differential equations (ODEs). Later, the system of equations was solved using the Runge-Kutta algorithm along with shooting. The analysis described in this paper explained that hybrid nanoparticles have high performance in radiative and thermal processes when compared with nanofluid. The fluid's velocity was observed to be repelled by an increasing magnetic value because of the Lorentz force. A comparison with previous work showed close agreement.

**Keywords:** Thermal analysis; Radiative analysis; Hybrid nanofluid; Thermal radiation; Magnetohydrodynamics

**PACS:** 47.65.-d, 47.56.+r, 44.40.+a, 66.20.-d, 47.85.mb

## Nomenclature

$f_d$ =	Clear fluid	$K$ =	thermal conductivity ( $Wm^{-1}K^{-1}$ )
$nf$ =	nano fluid	$T_w$ =	gradient of temperature at the wall (K)
$T$ =	Temperature	$HN$ =	hybrid nanofluid
$\mu$ =	dynamic viscosity ( $kgm^{-1}s^{-1}$ )	$\phi$ =	inclination angle
$C_{fx}$ =	Coefficient of skin friction	$T_\infty$ =	stream temperature
$c_p$ =	specific heat ( $JKg^{-1}K^{-1}$ )	$Q_c$ =	heat generation coefficient
$\phi_1$ =	Volume fraction of gold nanoparticle	$q_r$ =	heat flux
$u,v$ =	x and y-direction velocity ( $ms^{-1}$ )	$B_0$ =	magnetic strength
$\phi_2$ =	Volume fraction of silver nanoparticle	$\beta_t$ =	Volumetric capacity for temperature
$\rho$ =	fluid density	$g$ =	acceleration base on gravity
$\sigma$ =	electrical conductivity ( $sm^{-1}$ )		

## INTRODUCTION

The study of Magnetohydrodynamic (MHD) Casson hybrid nanofluids in circulating blood is a complex and interdisciplinary field that combines fluid dynamics, thermodynamics, and nanotechnology. These nanofluids, which are composed of blood as the base fluid and hybrid nanoparticles, have gained significant attention due to their potential applications in biomedical engineering, particularly in drug delivery, cancer treatment, and thermal management systems. The inclusion of thermal radiation and chemical reactions further complicates the dynamics, making it essential to understand their effects on flow, heat transfer, and mass transfer characteristics.

This comprehensive review aims to explore the current state of research on MHD Casson hybrid nanofluids in circulating blood, focusing on the effects of thermal radiation and chemical reactions. The review synthesizes findings from multiple studies to provide a detailed understanding of the physical phenomena involved and their implications for practical applications. Several parameters, including the magnetic field strength, nanoparticle volume fraction, and thermal radiation influence the flow characteristics of MHD Casson hybrid nanofluids. The Casson fluid model is particularly suitable for blood, as it accounts for its non-Newtonian behavior, which exhibits yield stress and shear-thinning properties. Recently, a lot of attention has been paid to the numerical analysis of heat transmission in hybrid nanofluids. The effective heat transmission of this type of nanofluid, along with radiative effects, has numerous applications in the pharmaceutical industry and engineering. Alqawasmi et al. [1] examined numerical simulation toward

hybrid nanofluid movement. Based on the morphology of nanoparticles and gyrotactic microorganisms, Raza et al. [2] investigated the effect of nanolayers on the movement of tri-hybrid nanofluid. Shamshuddin et al. [3] looked at the impact of radiation on the dissipative HN flow in a revolving disk. The term "nanofluids" describes a synthesis approach that utilizes nanometallics due to nano-scale formation and thermal design. Noreen and colleagues [4] conducted a comparative study of THN by analyzing the influence of Cattaneo-Christov heat flux in conjunction with the role of radiation. The combination of CNT-Gr-Fe<sub>3</sub>O<sub>4</sub> and MgO-Cu-Au hybrid nanoparticles of the kerosene oil type was investigated by Choudhary et al. [5] using a bidirectional stretching sheet. Rajamani and Reddy [6] examined MHD pulsating channel with Joule heating along with thermal radiation impacts. Nabwey et al. [7] studied heat transmission in MHD dynamics of Carreau HN past a curved surface that is exponentially stretched. In another study of Yu et al. [8], the optimisation of heat transmission with viscous nanofluid dynamics in a stretching and shrinking thin needle was discussed extensively.

Thermal radiation plays a significant role in the mechanisms that help bodies adjust their temperature to exchange energy. The analysis of thermal radiation on a moving fluid is explained by the variation of the material's internal energy. In thermal engineering and sectors where temperatures are extremely high, thermal radiation is important. A hybrid nanofluid's rotational dynamics were studied by Asghar et al. [9] in relation to the importance of heat radiation. Recently, Ramzan et al. [10] examined the thermal and theoretical study of hybrid nanofluid dynamics beyond a number of geometries that are not isothermal and non-isosolutal mechanisms. By looking at the internal heat generation, the function of HN in a dovetail fin's thermal process was investigated by Goud et al. [11]. Alrihieli and colleagues [12] investigated convective heating and radiative MHD nanofluid dynamics. Jayanthi and Niranjan [13] studied the effects of activation energy, joule heating, and viscous dissipation on the dynamics of nanofluids brought on by MHD in a vertical surface. Yaseen et al. [14] used two parallel plates to investigate how heat generation and thermal radiation affect the dynamics of hybrid and mono-hybrid nanofluids. Guedri and colleagues [15] examined the thermal dynamics of a radiative hybrid nanofluid across a nonlinear stretchy sheet. The mechanisms of Soret-Dufour and thermal radiation in unstable chemically reactive fluid dynamics were examined by Alao et al. [16]. The convective heat transfer in nanofluid flow via a stretching sheet was investigated by Manjunath et al. [17].

The flow of magnetohydrodynamics finds numerous uses in industries like heat exchangers, micro-electronics, and the modelling of combustion. In recent times, nanotechnology has been explained as the approach for thermal augmentation. Alsagri et al. [18] elucidated MHD simulation of nanofluid dynamics by utilizing viscous dissipation. Fatunmbi et al. [19] recently examined MHD micropolar nanofluid dynamics past an upright elongating sheet with temperature-dependent viscosity. Waqas et al [20] clarified the importance of MHD dynamics in a hybrid fluid type past a circulating disk. Eid et al. [21]. investigated the viscous nanofluid dynamics of micropolar magnetic on penetrable inclined surfaces. The machine learning method of Casson for hybrid nanofluid flow over a heat-stretched surface was recently investigated by Ramasekhar et al. [22]. Nayak et al. [23] investigated the function of dissipative viscous and radiation in a decreasing surface in MHD 3D dynamics and heat transfer analysis of nanofluid. Asjad et al. [24] investigated the bioconvection dynamics of the MHD viscous nanofluid. In their discussion of the importance of MHD, Idowu and Falodun [25] varied thermal conductivity and viscosity when two non-Newtonian fluids moved at the same time. Exponentially vertical surfaces with chemical reactions were used by Biswas et al. [26] to mimic Prandtl-nanofluid dynamics. Sitamahalakshmi and colleagues [27] investigated the impact of heat-mass transit on MHD Casson blood dynamics in a stretching permeable channel. A finite element description of paraffin wax nanoparticles and sand was investigated by Nagapayani et al. [28]. Gladys and Reddy [29] discussed the dynamics of non-Newtonian nanoparticles. Al-zabaidi et al. [30] studied flowing fluids past an inclined vicinity when there is significant of entropy generation, Lorentz force, and ohmic heating.

Many studies in the literature have considered the dynamics of nanofluids by ignoring the hybrid nanofluids. To our best knowledge, studies on hybrid nanofluids do not consider the thermal and radiative analysis through Casson fluid. The current research examined the thermal and radiative analysis of MHD Casson fluid with hybrid nanoparticles with viscous dissipation and magnetic field. Analysis of this nature has not been considered in the literature as far as we are concerned. This study finds application in engineering and many scientific domains. This model plays a significant role in the biomedical industry. This intricate computational framework intricately weaves MHD and thermal radiation scenarios through the dance of blood circulation, proving invaluable in medical interventions such as radiofrequency ablation, MRI (magnetic resonance imaging), and cancer chemotherapy. Within the Results and Discussion section, visual representations illuminate various crucial physical parameters. The application of gold and silver in the biomedical field with regard to blood demonstrates a variety of nanotechnological developments, from antimicrobial coatings and implanted devices to particular drug delivery and diagnostic equipment. Consequently, scholars are confident that the latest findings are distinctive and poised to significantly impact both engineering and medical fields, potentially igniting inspiration in future researchers.

### MATHEMATICAL ANALYSIS

A steady, incompressible, laminar flow of hybrid nanofluids, which contains gold and silver nanoparticles, was considered as shown in Figure 1. This nanoparticles based were taken into account along with base fluid blood incorporated. Mass and thermal radiative analysis over a moving surface with its velocity to be  $u_w = ax$  and free stream

temperature, and concentration  $T_\infty, C_\infty$  was considered. A transverse magnetic field  $B_0$  was impose in a perpendicular direction. The heat transmission analysis was elucidated with the viscous dissipation and heat generation along with chemical reaction on the hybrid nanofluids. Figure 1 shows the physical configuration. Priyadharshini et al. [22] state that the equations that apply become valid when the boundary layer is approximated.

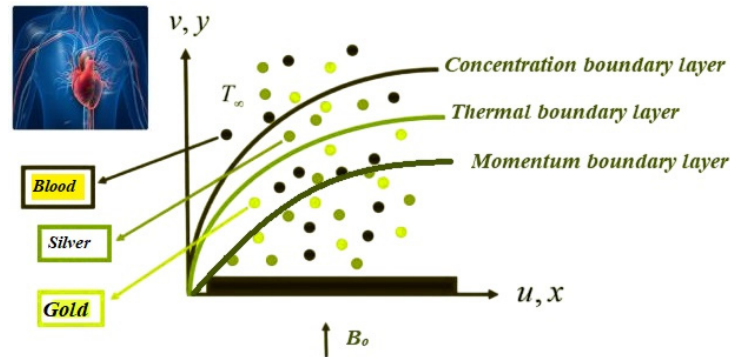


Figure 1. Physical model of the Problem

$$\frac{\partial u}{\partial x} + \frac{\partial v}{\partial y} = 0 \quad (1)$$

$$u \frac{\partial u}{\partial x} + v \frac{\partial u}{\partial y} = \frac{\mu_{hnf}}{\rho_{hnf}} \left(1 + \frac{1}{\beta}\right) \frac{\partial^2 u}{\partial y^2} - \frac{\sigma_{hnf}}{\rho_{hnf}} B_0^2 u - \frac{\mu_{hnf}}{K^*(c_p)_{hnf}} u \quad (2)$$

$$u \frac{\partial T}{\partial x} + v \frac{\partial T}{\partial y} = \frac{k_{hnf}}{(\rho c_p)_{hnf}} \frac{\partial^2 T}{\partial y^2} + \frac{Q_0}{(\rho c_p)_{hnf}} (T - T_\infty) - \frac{1}{(\rho c_p)_{hnf}} \frac{\partial q_r}{\partial y} - \frac{\sigma_{hnf}}{(\rho c_p)_{hnf}} B_0^2 u \quad (3)$$

$$u \frac{\partial C}{\partial x} + v \frac{\partial C}{\partial y} = D_B \frac{\partial^2 C}{\partial y^2} - Kr(C - C_\infty) \quad (4)$$

subject to the boundary conditions:

$$\left. \begin{aligned} u = ax, v = 0, T = T_w, C = C_w \text{ at } y = 0 \\ u \rightarrow 0, T \rightarrow T_\infty, C \rightarrow C_\infty \text{ as } y \rightarrow \infty \end{aligned} \right\} \quad (5)$$

The Rosseland diffusion approximation, which was employed by Reddy et al. [23], is utilized to describe the radiative heat flux that the flow faced.

$$q_r = -\frac{4\sigma_s}{3ke} \frac{\partial T^4}{\partial y} \quad (6)$$

With the use of Rosseland approximation, an optically thin fluid has been taken into consideration in the study's thermal and radiative analyses. Assume that the flow's temperature differential is negligible, so that equation (6) is linearized by simplifying  $T^4$  by utilizing Taylor's series in  $T_\infty$  and avoiding the higher order to obtain:

$$T^4 = 4T_\infty^3 T - 3T_\infty^4 \quad (7)$$

The energy equation becomes:

$$u \frac{\partial T}{\partial x} + v \frac{\partial T}{\partial y} = \frac{k_{hnf}}{(\rho c_p)_{hnf}} \frac{\partial^2 T}{\partial y^2} + \frac{Q_0}{(\rho c_p)_{hnf}} (T - T_\infty) + \frac{16\sigma_s T_\infty^3}{3ke(\rho c_p)_{hnf}} \frac{\partial^2 T}{\partial y^2} + \frac{\mu_{hnf}}{(\rho c_p)_{hnf}} B_0^2 u \quad (8)$$

The following are the definitions of the similarity variables used in this paper:

$$u = axf'(\eta), v = -(av)^{\frac{1}{2}}f(\eta), \theta = \frac{T-T_\infty}{T_w-T_\infty}, \phi = \frac{C-C_\infty}{C_w-C_\infty}, \eta = \left(\frac{a}{v}\right)^{\frac{1}{2}} y \quad (9)$$

Employing the equation (9) above on the governing equations to obtain:

$$\frac{\mu_{hnf}}{\mu_f} \left(1 + \frac{1}{\beta}\right) f''' + \frac{\rho_{hnf}}{\rho_f} (ff'' - (f')^2) - \frac{\sigma_{hnf}}{\sigma_f} Mf' - \frac{\mu_{hnf}}{K(c_p)_f} f' = 0 \quad (10)$$

$$\frac{k_{hnf}(\rho c_p)_f}{k_f(\rho c_p)_{hnf}} \left(\frac{1+R}{Pr}\right) \theta'' + \frac{(\rho c_p)_f}{(\rho c_p)_{hnf}} Q\theta + \frac{(\rho c_p)_f}{(\rho c_p)_{hnf}} Ec(f'')^2 - f\theta' = 0 \quad (11)$$

$$\phi'' + Scf\phi' - ScKr\phi = 0 \quad (12)$$

The transform boundary conditions are:

$$f(0) = 0, f'(0) = 1, \theta(0) = 1, \phi(0) = 1, f'(\infty) = 0, \theta(\infty) = 0, \phi(\infty) = 0 \quad (13)$$

where;

$M = \frac{\sigma_f B_0^2}{\alpha \rho_f}$ ,  $K = \frac{(c_p)_f a K^*}{(c_p)_{hnf}}$ ,  $R = \frac{16\sigma_s T_\infty^3}{3KeK}$ ,  $Pr = \frac{\nu_f}{\alpha_f}$ ,  $Q = \frac{Q_0}{(\rho c_p)_f a}$ ,  $Ec = \frac{B_0^2(ax)^2}{(c_p)_f(T_w - T_\infty)}$ ,  $Sc = \frac{\nu}{D_B}$ , are the Schmidt number, Eckert number, Prandtl number, heat generation a parameter, permeability parameter, magnetic parameter, and thermal radiation parameter.

The quantities of engineering interest for momentum and thermal boundary layer are described as follows:

$$C_{fx} = \frac{(\mu)_{hnf}}{\mu_f a x^2} \left( \frac{\partial u}{\partial y} \right)_{y=0}, \text{ and } Nu_x = -\frac{x k_{hnf}}{k_f (T_w - T_\infty)} \left( \frac{\partial T}{\partial y} \right)_{y=0}, Sh = D \left( \frac{\partial C}{\partial y} \right)_{y=0}$$

Skin friction, Nusselt number, and Sherwood number are obtained by applying the similarity variables as follows:

$$C_{fx} = \frac{(\mu)_{hnf}}{\mu_f} \frac{f''(0)}{\sqrt{Re_x}}, Nu_x = \frac{x k_{hnf}}{k_f} \theta'(0) \sqrt{Re_x}, Sh_x = \phi'(0)$$

### METHODOLOGY

Using the Runge-Kutta and shooting procedures, the nonlinear problems controlling ODEs in equations (10)–(12) subject to (13), were solved. Solving the BVP for even an extremely finite interval would be impractical, and it is not possible on an infinite interval. We will apply an infinite boundary condition in this study at a finite point  $\eta$  at  $\infty = 10$ . Care has been made to shoot in steps, improve shoots in stages, and avoid round off error by computing numerical values in order to integrate  $f''(0)$ , and  $\theta'(0)$ , which is an initial value problem. The collection of nonlinear equations is first transformed into first order ODEs in order to apply this technique:

$$f = y_1, \frac{df}{d\eta} = \frac{dy_1}{d\eta} = y_2, \frac{d^2 f}{d\eta^2} = \frac{d}{d\eta} \left( \frac{dy_1}{d\eta} \right) = \frac{dy_2}{d\eta} = y_3, \frac{d^3 f}{d\eta^3} = \frac{d}{d\eta} \left( \frac{dy_2}{d\eta} \right) = \frac{dy_3}{d\eta} \quad (14)$$

$$\theta = y_4, \frac{d\theta}{d\eta} = \frac{dy_4}{d\eta} = y_5, \frac{d^2 \theta}{d\eta^2} = \frac{d}{d\eta} \left( \frac{dy_4}{d\eta} \right) = \frac{dy_5}{d\eta} \quad (15)$$

$$\phi = y_6, \frac{d\phi}{d\eta} = \frac{dy_6}{d\eta} = y_7, \frac{d^2 \phi}{d\eta^2} = \frac{d}{d\eta} \left( \frac{dy_6}{d\eta} \right) = \frac{dy_7}{d\eta} \quad (16)$$

Substituting equations (14), (15) and (16) into the transformed equations to obtain:

$$\frac{\mu_{hnf}}{\mu_f} \frac{dy_3}{d\eta} + \frac{\rho_{hnf}}{\rho_f} (y_1 y_3 - (y_2)^2) - \frac{\sigma_{hnf}}{\sigma_f} M y_2 - \frac{\mu_{hnf}}{Ko(c_p)_f} y_2 = 0 \quad (17)$$

$$\frac{k_{hnf}(\rho c_p)_f}{k_f(\rho c_p)_{hnf}} \left( \frac{1+R}{Pr} \right) \frac{dy_5}{d\eta} + \frac{(\rho c_p)_f}{(\rho c_p)_{hnf}} Q y_4 + \frac{(\rho c_p)_f}{(\rho c_p)_{hnf}} Ec (y_3)^2 - y_1 y_5 = 0 \quad (18)$$

$$\frac{dy_7}{d\eta} + Sc y_1 y_7 - Sc K r y_6 = 0 \quad (19)$$

$$f(0) = 0, f'(0) = 1, \theta(0) = 1, f'(\infty) = 0, \theta(\infty) = 0, \phi(0) = 1, \phi(\infty) = 0 \quad (20)$$

Simplifying equations (16) and (17) to obtain:

$$\frac{dy_3}{d\eta} = \frac{\frac{\rho_{hnf}}{\rho_f} (y_1 y_3 - (y_2)^2) - \frac{\sigma_{hnf}}{\sigma_f} M y_2 - \frac{\mu_{hnf}}{Ko(c_p)_f} y_2}{\frac{\mu_{hnf}}{\mu_f}} \quad (22)$$

$$\frac{dy_5}{d\eta} = \frac{\frac{(\rho c_p)_f}{(\rho c_p)_{hnf}} Q y_4 + \frac{(\rho c_p)_f}{(\rho c_p)_{hnf}} Ec (y_3)^2 - y_1 y_5}{\frac{k_{hnf}(\rho c_p)_f}{k_f(\rho c_p)_{hnf}} \left( \frac{1+R}{Pr} \right)} \quad (23)$$

$$\frac{dy_7}{d\eta} = Sc K r y_6 - Sc y_1 y_7 \quad (24)$$

Subject to conditions:

$$y_1(0) = 0, y_2(0) = 1, y_4(0) = 1, y_6(0) = 1, y_2(\infty) = 0, y_4(\infty) = 0, y_6(\infty) = 0 \quad (21)$$

The outcomes are gotten by interchanging the scale factor up to a desired value by implementing an approximate solution. To obtain the solution, a guess for the initial assumptions are properly considered and the boundary thickness of the layer are taken into account.

## RESULTS AND DISCUSSION

The paper have discussed the thermal and radiative analysis of HN dynamics with impact of viscous dissipative and magnetic field. To explain the physical influence of pertinent dynamics parameters on velocity and temperature, hybrid numerical scheme called Runge-Kutta techniques along with the novel shooting method was utilized on the equations. The control parameters have been chosen as:  $Q=0.2$ ;  $Pr=21$ ;  $Ec=0.04$ ;  $M=0.2$ ;  $Kr=0.1$ ;  $Sc=0.22$ ;  $K=0.2$ ;  $R=0.5$ ;  $Kr=0.2$ ; The Prandtl number was chosen to be 21 based on the type of hybrid nanofluid considered in this study, while other parameters values are chosen based on experimental computations.

Figure 2 shows how the magnetic field affects fluid velocity when  $\phi_1 = 0.02$ ,  $\phi_2 = 0.01$ . The effect of magnetic in Figure 2 was plotted with nanocomposite particles Gold and Silver with base fluid blood. The depth of the boundary layer was shown to decrease with an increasing magnetic parameter value. The Lorentz force appears in the equation of momentum and gives all tendency of bringing down the motion of the tri-nanocomposite particles. This force is created due to the impose of magnetism field to the heat transmission analysis. Figure 3 illustrates how Eckert affects the fluid's temperature. The temperature profile is observed to increase with an increasing Eckert number value.

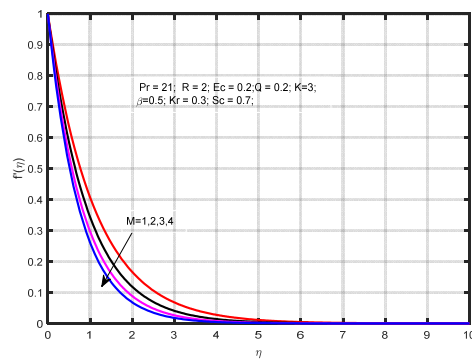


**Figure 2.** Significance of magnetism parameter in velocity distribution

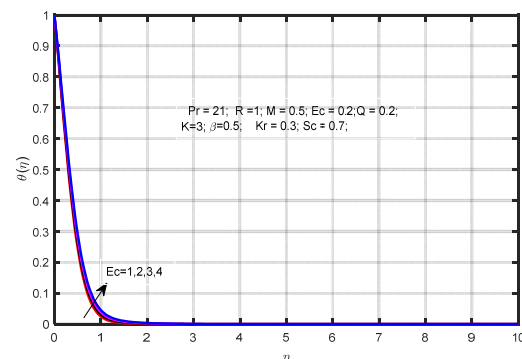


**Figure 3.** Eckert number significance in relation to temperature dispersion

The dissipative viscous term (Eckert number) transforms the kinetic into internal energy based on work done in anticipating viscous liquid stresses. This result indicates that increasing the Eckert value raises the temperatures and depth of the entire boundary layer. The boundary layer's enthalpy and the kinetic energy of the flow of nanofluids are represented by the Eckert number. Figure 4 showed how the fluid's temperature is affected by the heat generating parameter ( $Q$ ). The result in Figure 4 indicates that the fluid temperature increased as  $Q$  increased. This implies that, the heat generated reduces the thermal process within the boundary layer. Hence, the nanocomposite fluid enhances the temperature of fluid by generating heat more than a nanocomposite. Hence, the thermal and radiative analysis enriched the fluid temperature when heat generation parameter ascended.

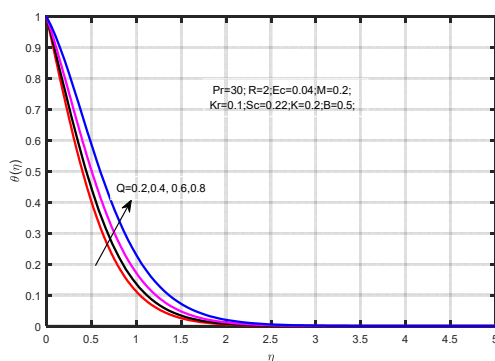


**Figure 4.** Significance of heat generation on the temperature distribution

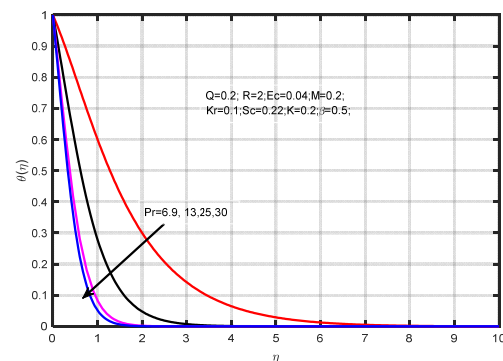


**Figure 5.** Prandtl number significance in relation to temperature dispersion

The effect of Prandtl number ( $Pr$ ) on fluid temperature is depicted in Figure 5. It was found that the temperature distribution descended with an increasing value of  $Pr$ . This indicates that the thermal boundary layer's thickness decreased.



This paper's thermal, radiative, and heat transfer analyses are governed by the dimensionless Prandtl number. The momentum to thermal diffusion ratio is denoted by  $Pr$ . Because the nanocomposite nanoparticles have better thermal conductivities, the temperature is dropping. The corresponding thickening of the thermal and momentum layer boundaries is implied by the current analysis, which is displayed in Figure 5.

The impact of thermal radiation ( $R$ ) on the temperature distribution is depicted in Figure 6. As  $R$  rises, the temperature profiles rise as well. The current research demonstrates how the temperature and depth of the thermal boundary layer are changed by the absorption of thermal radiation within the layer. Therefore, the thermal radiation improves the boundary layer's thermal and radiative analysis. Figure 7 shows how  $\beta$  affects the velocity profile. It claims that the velocity outline shrank as the  $\beta$  parameter increased. The improved Casson parameter's ability to limit the liquid's velocity by reducing the stress brought on by yield is crucial to achieving this objective.

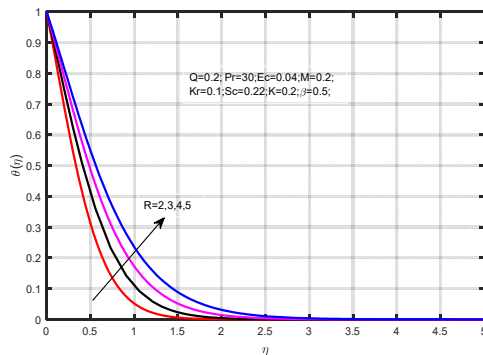


**Figure 6.** Thermal radiation's importance in relation to the temperature distribution

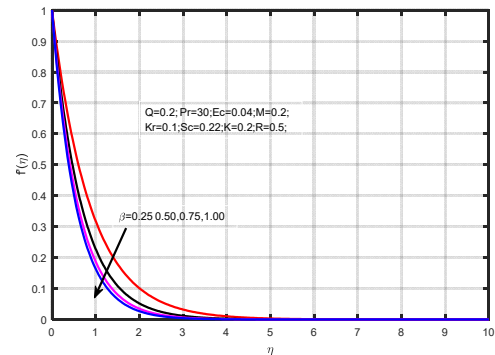


**Figure 7.** Effect of Casson fluid parameter on the velocity profiles

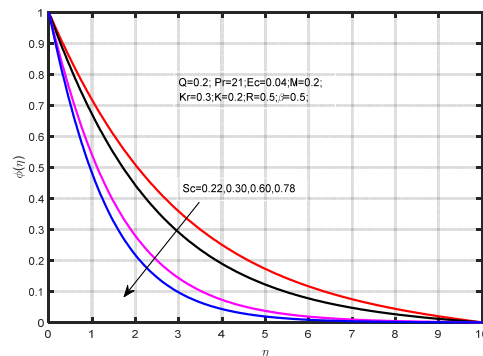


**Figure 8.** Schmidt number's impact on concentration profiles

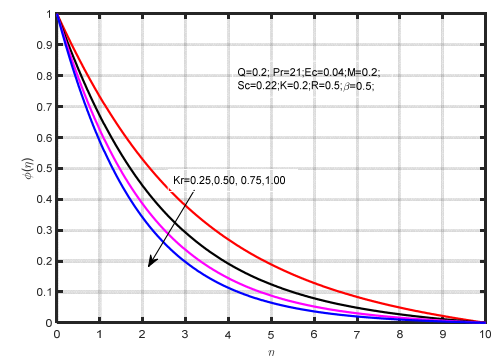


**Figure 9.** Chemical reactions' effects on concentration profiles

Figure 8 provides a clear illustration of how the Schmidt number affects the topography of concentration. It becomes evident that as the Schmidt number escalates, a notable reduction in the concentration field occurs. This phenomenon arises because the diffusion of solutes in fluids is inherently tied to the diffusion coefficient. Consequently, the observed decline in the concentration field correlates with a diminishing diffusion coefficient. Thus, a remarkable plunge in the concentration field in relation to the Schmidt number is clearly noted. As the parameter governing chemical reactions intensifies, the concentration profile diminishes, as illustrated in Figure 9, showcasing the significant impact of the chemical reaction parameter. Furthermore, the temperature profile follows a reversible trajectory.

Tables 1, 2, and 3 represents the fundamental thermal and comparative properties relevant to the hybrid nanofluid analysis. Table 1 lists the standard thermophysical properties of blood (as the base fluid) and nanoparticles such as gold (S1) and silver (S2), including density, specific heat, thermal conductivity, and dynamic viscosity. Table 2 outlines the mathematical formulation used to evaluate the effective thermophysical properties of the hybrid nanofluid, incorporating parameters such as density, viscosity, specific heat, thermal and electrical conductivities. Table 3 provides a comparison of the present numerical results with those reported by Manjunatha et al. [17] for various Prandtl number ( $Pr$ ) values, showing excellent agreement and thereby validating the accuracy of the current computational model.

**Table 1.** Thermal Properties(Standard Values)

Property	Symbol	Blood (Base fluid)	Gold (S <sub>1</sub> )	Silver (S <sub>2</sub> )
Density (kg/m <sup>3</sup> )	$\rho$	1060	19300	10500
Specific Heat (J/Kg)	$C_p$	3617	129	235
Thermal Conductivity (W/m)	$k$	0.52	318	429
Dynamic viscosity(Pa)	$\mu$	$3.5 \times 10^{-3}$	--	---



**Table 2.** Formulation of the effective thermophysical model of a hybrid nanofluid in mathematics:

Thermal property	Hybrid Nanofluids
Density	$\frac{\rho_{hnf}}{\rho_f} = (1 - \phi_2) \left[ 1 - \phi_1 - \phi_1 \left( \frac{\rho_{s1}}{\rho_f} \right) + \phi_2 \left( \frac{\rho_{s2}}{\rho_f} \right) \right]$
Dynamic viscosity	$\frac{\mu_{hnf}}{\mu_f} = (1 - \phi_1)^{2.5} (1 - \phi_2)^{2.5}$
Specific heat	$\frac{(\rho C_p)_{hnf}}{(\rho C_p)_f} = (1 - \phi_2) \left[ 1 - \phi_1 - \phi_1 \left( \frac{(\rho C_p)_{s1}}{\rho_f} \right) + \phi_2 \left( \frac{(\rho C_p)_{s2}}{\rho_f} \right) \right]$
Thermal conductivity	$\frac{k_{hnf}}{k_f} = \frac{k_{s2} + 2k_{hnf} - 2\phi_2(k_{hnf} - k_{s2})}{k_{s2} + 2k_{hnf} + 2\phi_2(k_{hnf} - k_{s2})} \cdot \frac{k_{s1} + 2k_{hnf} - 2\phi_1(k_{hnf} - k_{s1})}{k_{s1} + 2k_{hnf} + 2\phi_1(k_{hnf} - k_{s1})}$
Electrical conductivity	$\frac{\sigma_{hnf}}{\sigma_f} = \frac{3 \left[ \frac{\phi_1 \sigma_1 + \phi_2 \sigma_2}{\sigma_f} - (\phi_1 + \phi_2) \right]}{2 + \left[ \frac{\phi_1 \sigma_1 + \phi_2 \sigma_2}{\sigma_f (\phi_1 + \phi_2)} \right] - \left[ \frac{\phi_1 \sigma_1 + \phi_2 \sigma_2}{\sigma_f} - (\phi_1 + \phi_2) \right]}$

**Table 3.** Comparison results for  $(-\theta'(0))$  for different values of Pr

Pr	Manjunatha et al. [17]	Present work
2.0	0.9113	0.9113
7.0	1.8954	1.8953
20	3.3539	3.3538

## CONCLUSIONS

The thermal and radiation analysis of two-phase nanoparticles (*Gold + Silver*) suspended in blood base fluid has been solved numerically. The dynamics of suspended nanoparticles in blood were considered past a flexible sheet in the presence of a magnetic field, dissipative viscous and thermal radiation, along with chemical reaction. The main conclusions drawn from this investigation are:

- As the magnetic parameter increases, the heat and momentum profiles decrease. This is because an electrically conducting fluid moves more slowly when the Lorentz force is created. (ii) The speed and temperature distribution rose as the heat-generating parameter was increased. This demonstrates that greater heat is generated and that the volume percentage of nanoparticles is significantly enhanced;
- A higher Prandtl number results in a decrease in the thickness of the thermal and momentum boundary layers;
- The outcomes show that hybrid nanoparticles show a very high thermal and radiative performance compared to dual-phase nanoparticles.
- It was observed that increasing the Eckert number improved the temperature and velocity profiles.
- The concentration decreases as the chemical reaction and Schmidt number increase.

## ORCID

✉ G. Durga Priyadarsini, <https://orcid.org/0000-0001-8782-8836>; ✉ Syeda Asma Kauser, <https://orcid.org/0000-0003-2561-911X>

✉ Y. Hari Krishna, <https://orcid.org/0000-0002-6259-5228>; ✉ T. Nageswara Rao, <https://orcid.org/0000-0002-2841-530X>;

✉ G. Venkata Ramana Reddy, <https://orcid.org/0000-0002-6455-3750>

## REFERENCES

- [1] K. Alqawasm, K.A.M. Alharbi, U. Farooq, S. Noreen, M. Imran, A. Akgül, M. Kanan, and J. Asad, "Numerical approach toward hybrid nanofluid flow with nonlinear heat source-sink and Fourier heat flux model passing through a disk," *International Journal of Thermofluids*, **18**, 100367 (2023). <https://doi.org/10.1016/j.ijft.2023.100367>
- [2] Q. Raza, X. Wang, B. Ali, S.M. Eldin, H. Yang, and I. Siddique, "Role of nanolayer on the dynamics of trihybrid nanofluid subject to gyrotactic microorganisms and nanoparticles morphology vis two porous disks," *Case Studies in Thermal Engineering*, **51**, 103534 (2023). <https://doi.org/10.1016/j.csite.2023.103534>
- [3] M.D. Shamshuddin, N. Akkurt, A. Saeed, and P. Kumam, "Radiation mechanism on dissipative hybrid nanofluid flow through rotating disk encountered by Hall currents: HAM solution," *Alexandria Engineering Journal*, **65**, 543–559 (2023). <https://doi.org/10.1016/j.aej.2022.10.021>
- [4] S. Noreen, U. Farooq, H. Waqas, N. Fatima, M.S. Alqurashi, M. Imran, A. Akgül, and A. Bariq, "Comparative study of hybrid nanofluids with role of thermal radiation and Cattaneo-Christov heat flux between double rotating disks," *Scientific Reports*, **13**, 7795 (2023). <https://doi.org/10.1038/s41598-023-34783-8>
- [5] S. Choudhary, R. Mehta, N. Alessa, S. Jangid, and M.V. Reddy, "Thermal Analysis on Kerosene Oil-Based Two Groups of Hybrid Nanoparticles (CNT-Gr-Fe3O4 and MgO-Cu-Au) Mix Flow over a Bidirectional Stretching Sheet: A Comparative Approach," *Journal of Engineering*, **2023**, ID 8828300 (2023). <https://doi.org/10.1155/2023/8828300>
- [6] S. Rajamani, and A.S. Reddy, "Effects of Joule heating, thermal radiation on MHD pulsating flow of a couple stress hybrid nanofluid in a permeable channel," *Nonlinear Analysis: Modelling and Control*, **27**(4), (2022). <https://doi.org/10.15388/namc.2022.27.26741>

- [7] H.A. Nabwey, A.M. Rashad, W.A. Khan, S.M.M. El-Kabeir, and S.A. El Naem, "Heat transfer in MHD flow of Carreau -hybrid nanofluid over a curved surface stretched exponentially," *Front. Phys.* **11**, 1212715 (2023). <https://doi.org/10.3389/fphy.2023.1212715>
- [8] L. Yu, Y. Li, V. Puneeth, S. Znaidia, N.A. Shah, S. Manjunatha, M.S. Anwar, and M.R. Khan, "Heat transfer optimisation through viscous nanofluid flow over a stretching/shrinking thin needle," *Numerical Heat Transfer, Part A: Applications*, <https://doi.org/10.1080/10407782.2023.2267750>
- [9] A.S. Alsagri, A. Hassanpour, and A.A. Alrobaia, "Simulation of MHD nanofluid flow in existence of viscous dissipation by means of ADM," *Case Studies in Thermal Engineering*, **14**, 100494 (2019). <https://doi.org/10.1016/j.csite.2019.100494>
- [10] M. Ramzan, P. Kumam, S.A. Lone, T. Seangwattana, A. Saeed, and A.M. Galal, "A theoretical analysis of the hybrid nanofluid flows over a non-isothermal and non-isosolutal multiple geometries," *Heliyon*, **9**, e14875 (2023). <https://doi.org/10.1016/j.heliyon.2023.e14875>
- [11] J.S. Goud, P. Srilatha, R.S.V. Kumar, K.T. Kumar, U. Khan, Z. Raizah, H.S. Gill, *et al.* "Role of hybrid nanofluid in the thermal distribution of a dovetail fin with the internal generation of heat," *Case Studies in Thermal Engineering* **35**, 102113 (2022). <https://doi.org/10.1016/j.csite.2022.102113>
- [12] H. Alrihili, M. Alrehili, and A.M. Megahed, "Radiative MHD Nanofluid Flow Due to a Linearly Stretching Sheet with Convective Heating and Viscous Dissipation," *Mathematics*, **10**, 4743 (2022). <https://doi.org/10.3390/math10244743>
- [13] S. Jayanthi, and H. Niranjana, "Effects of Joule Heating, Viscous Dissipation, and Activation Energy on Nanofluid Flow Induced by MHD on a Vertical Surface," *Symmetry*, **15**, 314 (2023). <https://doi.org/10.3390/sym15020314>
- [14] M. Yaseen, S.K. Rawat, A. Shafiq, M. Kumar, and K. Nonlaopon, "Analysis of Heat Transfer of Mono and Hybrid Nanofluid Flow between Two Parallel Plates in a Darcy Porous Medium with Thermal Radiation and Heat Generation/Absorption," *Symmetry*, **14**, 1943 (2022). <https://doi.org/10.3390/sym14091943>
- [15] Guedri Kamel, Arshad Khan, Ndolane Sene, Zehba Raizah, Anwar Saeed, and Ahmed M. Galal, "Thermal Flow for Radiative Hybrid Nanofluid over Nonlinear Stretching Sheet Subject to Darcy–Forchheimer Phenomenon," *Mathematical Problems in Engineering*, **2022**, 3429439 (2022). <https://doi.org/10.1155/2022/3429439>
- [16] F.I. Alao, A.I. Fagbade, and B.O. Falodun, "Effects of thermal radiation, Soret and Dufour on an unsteady heat and mass transfer flow of a chemically reacting fluid past a semi-infinite vertical plate with viscous dissipation," *Journal of the Nigerian Mathematical Society*, **35**, 142–158 (2016). <https://doi.org/10.1016/j.jnnms.2016.01.002>
- [17] S. Manjunatha, V. Puneeth, B.J. Gireesha, and A.J. Chamkha, "Theoretical Study of Convective Heat Transfer in Nanofluid flowing past a Stretching Sheet," *J. Appl. Comput. Mech.* **8**, 1279–1286 (2021). <https://doi.org/10.22055/JACM.2021.37698.3067>
- [18] A. Asghar, L.A. Lund, Z. Shah, N. Vrinceanu, W. Deebani, and M. Shutaywi, "Effect of Thermal Radiation on Three-Dimensional Magnetized Rotating Flow of a Hybrid Nanofluid," *Nanomaterials*, **12**, 1566 (2022). <https://doi.org/10.3390/nano12091566>
- [19] E.O. Fatunmbi, A.S. Oke, and S.O. Salawu, "Magnetohydrodynamic micropolar nanofluid flow over a vertically elongating sheet containing gyrotactic microorganisms with temperature-dependent viscosity," *Results in Materials*, **19**, 100453 (2023). <https://doi.org/10.1016/j.rinma.2023.100453>
- [20] H. Waqas, U. Farooq, R. Naseem, S. Hussain, and M. Alghamdi, "Impact of MHD radiative flow of hybrid nanofluid over a rotating disk," *Case Studies in Thermal Engineering*, **26**, 101015 (2021). <https://doi.org/10.1016/j.csite.2021.101015>
- [21] M.R. Eid, W. Jamshed, B.S. Goud, Usman, R.W. Ibrahim, S.M. El Din, A. Abd-Elmonem, *et al.* "Mathematical analysis for energy transfer of micropolar magnetic viscous nanofluid flow on permeable inclined surface and Dufour impact," *Case Studies in Thermal Engineering*, **49**, 103296 (2023). <https://doi.org/10.1016/j.csite.2023.103296>
- [22] G. Ramasekhar, S. Alkarni, and N.A. Shah, "Machine learning approach of Casson hybrid nanofluid flow over a heated stretching surface," *AIMS Math.* **9**(7), 18746–18762 (2024). <https://doi.org/10.3934/math.2024912>
- [23] M.K. Nayak, "MHD 3D flow and heat transfer analysis of nanofluid by shrinking surface inspired with thermal radiation and viscous dissipation," *International Journal of Mechanical Sciences*, **124-125**, 185-193 (2017). <https://doi.org/10.1016/j.ijmecsci.2017.03.014>
- [24] Asjad Muhammad Imran, Muhammad Zahid, Fahd Jarad, and Abdullah M. Alsharif (2022), Bioconvection Flow of MHD Viscous Nanofluid in the Presence of Chemical Reaction and Activation Energy, *Mathematical Problems in Engineering* Volume 2022, Article ID 1707894, 9 pages <https://doi.org/10.1155/2022/1707894>
- [25] A.S. Idowu, and B.O. Falodun, "Variable thermal conductivity and viscosity effects on non-Newtonian fluids flow through a vertical porous plate under Soret-Dufour influence," *Mathematics and Computers in Simulation*, **177**, 358–384 (2020). <https://doi.org/10.1016/j.matcom.2020.05.001>
- [26] Biswas Rajib, B. O. Falodun, Nazmul Islam, Sarder Firoz Ahmmed, S. R. Mishra, Mohammad Afikuzzaman (2023), "Computational modeling of Prandtl-nanofluid flow using exponentially vertical surface in terms of chemical reaction," *Engineering Reports*, 2023, e12747, 1-23 <https://doi.org/10.1002/eng2.12747>
- [27] V. Sitamahalakshmi, G.V.R. Reddy, and B.O. Falodun, "Heat and Mass Transfer Effects on MHD Casson Fluid Flow of Blood in Stretching Permeable Vessel," *Journal of Applied Nonlinear Dynamics*, **12**(01), 87-97 (2023). <https://doi.org/10.5890/jand.2023.03.006>
- [28] M. Nagapavani, G.V.R. Reddy, H.F.M. Ameen, and H. Singh, "Finite element analysis for sand and paraffin wax nanoparticles in propylene glycol–water mixture-based hybrid nanofluid flow over a swirling cylinder with Arrhenius kinetics," *Numerical Heat Transfer, Part A: Applications*, **84**, 1518-1536 (2023). <https://doi.org/10.1080/10407782.2023.2177215>
- [29] T. Gladys, and G.V.R. Reddy, "Contributions of variable viscosity and thermal conductivity on the dynamics of non-Newtonian nanofluids flow past an accelerating vertical plate," *Partial Differential Equations in Applied Mathematics*, **5**, 100264 (2022). <https://doi.org/10.1016/j.padiff.2022.100264>
- [30] A. Al-Zubaidi, V.S. Sajja, R. Gadamsetty, G.R. Reddy, M.J. Babu, and I.L. Animasaun, "Dynamics over an inclined surface when entropy generation, Ohmic Heating, and Lorentz force are significant: Comparative analysis between water-copper nanofluid and water-copper-Iron (II, III) oxide hybrid nanofluid," *Waves in Random and Complex Media*, 1-23 (2022). <https://doi.org/10.1080/17455030.2022.2089368>

# МАГНІТОГІДРОДИНАМІЧНА ДИНАМІКА ГІБРИДНОЇ НАНОРІДИНИ КАССОНА В ЦИРКУЛЮЮЧІЙ КРОВІ З УРАХУВАННЯМ ТЕПЛОВОГО ВИПРОМІНЮВАННЯ ТА ХІМІЧНИХ РЕАКЦІЙ

Г. Дурга Пріядарсіні<sup>1</sup>, Сасда Асма Каузер<sup>2</sup>, Й. Харі Крішна<sup>3</sup>, Т. Нагешвара Рао<sup>4</sup>, Гуррампаті Венката Рамана Редді<sup>5</sup>

<sup>1</sup>Кафедра математики, Інженерно-технологічний коледж Гітанджалі, Чіріал, Хайдерабад, Телангана, Індія-501301

<sup>2</sup>Кафедра математики, Глобальний інститут інженерії та технологій, Мойнабад, Хайдерабад, Телангана-501504, Індія-

<sup>3</sup>Кафедра математики, Інженерний коледж ANURAG, Анантагірі, Сурьяпет, Телангана-508206, Індія-

<sup>4</sup>Кафедра математики, Освітній фонд Конеру Лакимаї, Ваддесварам, Індія-522302

<sup>5</sup>Кафедра комплексних дослідницьких відкриттів, Освітній фонд Конеру Лакимаї, Ваддесварам, Індія-522302

Метою цієї роботи є дослідження актуальності теплового випромінювання та хімічної реакції в тепловому та радіаційному аналізі динаміки гібридної нанорідина Кассона. Фізична модель базувалася на суміші гібридних наночастинок золота та срібла (HN), які суспендовані в крові повз розтяжний лист. Динаміка рідини повз розтяжний лист є визначним аналізом для теплових та імпульсних граничних шарів. Він знаходить застосування в різних технологічних галузях та промисловості. Модельні рівняння досліджувалися за допомогою системи диференціальних рівнянь з частковими похідними (PDEs). Для перетворення цих PDEs у повні диференціальні рівняння (ODEs) було використано прийнятне перетворення. Пізніше систему рівнянь було розв'язано за допомогою алгоритму Рунге-Кутти разом зі стрільбою. Аналіз, описаний у цій статті, пояснює, що гібридні наночастинок мають високу продуктивність у радіаційних та теплових процесах порівняно з нанорідиною. Спостерігалось, що швидкість рідини відштовхується зростаючим магнітним значенням через силу Лоренца. Порівняння з попередньою роботою показало близьку відповідність.

**Ключові слова:** термічний аналіз; радіаційний аналіз; гібридна нанорідина; теплове випромінювання; магнітогідродинаміка

## PERISTALTIC BILE FLOW IN PAPILLA AMPOULE OF POROUS WALLS AND INCLINED ECCENTRIC CATHETERIZED DUCT

 **D. Kumar**<sup>1\*</sup>,  **T.K. Rawat**<sup>2</sup>,  **M. Garvandha**<sup>1</sup>, **S. Kumar**<sup>3</sup>,  **S.K. Chaubey**<sup>1</sup>

<sup>1</sup>Sciences and Mathematics Unit, Department of Supportive Requirements,  
University of Technology and Applied Sciences-Shinas, Oman

<sup>2</sup>GLA University, Greater Noida, India

<sup>3</sup>Dr. Bhimrao Ambedkar University, Agra, India

\*Corresponding Author e-mail: [devendra.kumar@utas.edu.om](mailto:devendra.kumar@utas.edu.om)

Received September 1, 2025; revised October 4, 2025; accepted October 10, 2025

In this study, the combined effects of inclination and catheter on the biliary flow of a Carreau fluid through an eccentric catheterized duct with a porous material are mathematically investigated. The perturbation technique is employed to solve the governing equations, considering low Reynolds numbers, a long-wavelength approximation, and suitable small parameters. The surgical technique, when a catheter is inserted eccentrically into the duct, is connected to the outcomes of the investigation. Several parameters have been used to achieve the analytical solutions. Axial velocity, pressure gradient, flow rate, and wall shear stress are displayed in these data, together with the following emergent parameters: wall slip parameter, Weissenberg number, fluid behavior index, Darcy number, and angle of inclination. The pressure gradient is significantly altered by the angle of inclination and porosity parameter, and the catheter's axial velocity falls as the Weissenberg number rises. The physiological observations are consistent with these findings.

**Keywords:** Peristaltic bile flow; Papilla Ampoule; Porous Walls; Inclined Eccentric Catheterized Duct

**PACS:** 02.30.Jr, 02.30.Mv, 47.56.+r, 47.63.-b

### INTRODUCTION

The particular kind of pumping called peristaltic pumping makes it simple to move a range of rheological biofluids from one organ to another. The progressive wave of the duct wall's periodic contraction or relaxation causes the peristaltic motion. The catheter is essentially a long tube that is intended for use in ophthalmic, neurological, urological, cardiovascular, and gastrointestinal purposes. In addition to measuring several physiological flow characteristics like flow velocity, flow rate, pressure increase, and pressure gradient, the catheter is employed in clinical procedures to diagnose and treat illnesses. The initial hemodynamic conditions within the duct are disturbed when the catheter is introduced because it causes an annular zone to form between the catheter and the duct wall. Additionally, the catheter increased the flow's frictional resistance. Strasberg *et al.* [13] tested the accuracy of the results of the mathematical model by an experimental investigation. They establish the connection between biliary flow and canaliculi clearing. Additionally, the treatment of post-operative bile fistulas by internal endoscopic biliary drainage was investigated by Sauerbruch *et al.* [12]. James *et al.* [4] investigated orthotopic liver transplant recipients who had nasobiliary catheters inserted endoscopically, which aid in rerouting the flow of bile. According to Tripathi *et al.* [14], peristaltic transport via a finite channel, peristaltic heat flow creates a porous environment with greater resistance and enhanced as the Grashof number rises. By observing the effect of Weissenberg number and power index on axial velocity, Nadeem *et al.* [8] studied the unsteady peristaltic transport of Carreau fluid flow in an eccentric tube. It found that the axial velocity profile decreases as the values of the Weissenberg number and the power index increase. According to another mathematical model of papillary stenosis with stone developed by Kuchumov *et al.* [5], the permeability parameter, Weissenberg number, and amplitude ratio all affect the pressure that corresponds to the reflux state. Gudekote *et al.* [3] examined the Casson fluid moving through porous walls impacted by the wall slip parameter and elasticity. They discovered a correlation between rises in pressure and angle of inclination, noting that as the degree of inclination increases, so does the pressure. Nabil *et al.* [7] investigated the impact of heat and mass transfer on Casson fluid flow via two coaxial cylindrical tubes with peristalsis. Nurulaifa *et al.* [9] developed a mathematical model of Bingham fluid flow through an overlapping stenosed artery and discovered that when the plug core radius increased, the dispersion function decreased. It accounts for various leakage instances, such as leaking from the common bile duct lesion, choledochotomy, and cystic duct stump. The viscous flow between two sinusoidal deforming concentric tubes was analytically examined by McCash *et al.* [6]. It also discussed the applications, such as endoscopy of curved human organs and the maintenance and enhancement of intricately designed machinery. Moreover, by using a mathematical model of blood flow through a stenosed artery with post-stenotic dilatation, Dhange *et al.* [2] examined various physical attributes that affect fluid resistance to flow and noted that the surface shearing stress decreased with the upsurge of resistance. Moreover, a mathematical model of an eccentric catheterized artery with heat transfer was studied by Reima *et al.* [11]. They investigated the impact of temperature in the scenario where the artery is the outer tube, and the catheter is the inner tube. The results obtained are consistent with physiological observations as well as the causes and complications related to catheterization. They described how the model is applied to the

cardiovascular system and found that the viscosity of the peripheral layer reduces as the wall shear stress lowers. In the investigation of the fractional Oldroyd-B fluid between two coaxial cylinders loaded with gold nanoparticles, Cao *et al.* [1] observed that the inclusion of nanoparticles increased the base fluid's heat capacity. A model of nanolayer fluid flow over a porous surface in the presence of carbon nanotubes was proposed mathematically by Raza *et al.* [10]. They also examined the impact of increasing interfacial nanolayer thickness from 3 to 9 nm, which has a substantial effect on thermal performance and thermal conductivity.

Modern literature shows that bile is not strictly Newtonian: it commonly exhibits shear-thinning and viscoelastic features that vary with bile composition, pathology, and shear-rate range. We therefore justify the Carreau (shear-thinning). Experimental and review studies report shear thinning and viscoelastic features in bile depending on composition and disease state; thus, a shear rate-dependent viscosity model is appropriate for theoretical investigation. Recent reviews summarizing bile rheology, such as those by Kuchumov *et al.* [5], consider bile as a non-Newtonian fluid. These studies, along with related experimental reports, led to the selection of bile as a Carreau-type model.

In the present study, the combined effects of eccentric tubes, porosity, and angle of inclination on the peristaltic transport of Carreau fluid in an axisymmetric tube were examined. The findings might be beneficial in the various practical applications of medical science. The regular perturbation technique is used to solve the two-dimensional mathematical model in a cylindrical coordinate system. The Weissenberg number and eccentric parameter are involved in the solution of this investigation process. The resulting equations were solved analytically under the appropriate boundary conditions. With the help of influencing factors like the fluid behavior index, amplitude ratio, Darcy number, slip parameter, and angle of inclination, the expression has been derived for axial velocity, pressure gradient, wall shear stress, and flow rate. The obtained expressions were graphically represented in various combinations with emerging parameters. The results of the current model were evaluated and related to the intricate physiological flow of the bile through the diseased duct. It greatly aids in the investigation of bile flow in the duct in a much better way than earlier, especially in dialysis cases.

### MATHEMATICAL INTERPRETATION OF THE PROBLEM

The flow of bile is modeled by considering the peristaltic flow of an incompressible Carreau fluid flowing inside the eccentric tubes, in which the inner tube is uniform and rigid, representing a catheter placed in an eccentric position within the pancreatic duct. The pancreatic duct is filled with the porous medium of finite length  $L$  and inclined at an angle  $\alpha$  with the horizontal is taken into account as the outer tube. The relevant equations of momentum and continuity in vector form are as follows.

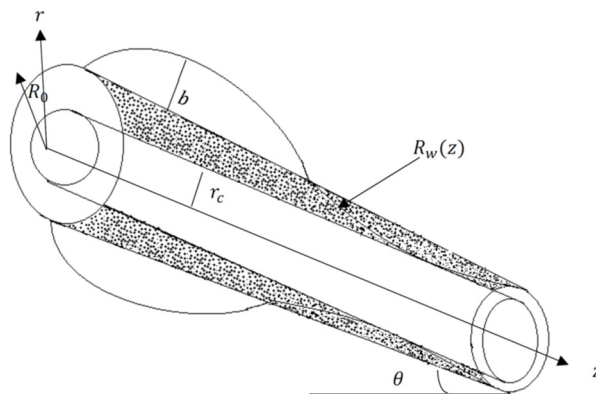


**Figure 1.** Geometrical representation of the problem

The fluid density  $\rho$  is uniform incompressibility conditions, the equation of continuity is:

$$\nabla \cdot V = 0 \quad (1a)$$

The equation governing the motion is:

$$\left( \frac{\partial V}{\partial t} + (\nabla \cdot V)V \right) = -\frac{1}{\rho} \nabla P + \frac{1}{\rho} \nabla \cdot \tau_{ln} \quad (1b)$$

Where,  $V = (u, v, w)$ , the velocity components in the  $r, \theta$  and  $z$  directions respectively,  $P$  is the pressure,  $\rho$  is the density and  $\tau_{ln}$  is the extra stress tensor.

The geometry of the non-uniform pancreatic duct with a catheter and the wall deformation due to an infinite sinusoidal wave propagating along the wall is mathematically described as

$$R_w(z) = R_0 - mz + z \tan \alpha + b \sin \frac{2\pi z}{\lambda} \quad (2a)$$

$$R_c(z) = r_c \quad (2b)$$

The constitutive equations for the non-Newtonian fluid are described by the Carreau equation



$$\check{C}_{ln} = -p\delta_{lm} + \check{\tau}_{ln} \quad (3a)$$

$$\check{\tau}_{ln} = \left[ \mu_\infty + (\mu_0 - \mu_\infty)(1 + ((I\check{\gamma})^2)^{\frac{m-1}{2}}) \right] \check{\gamma} \quad (3b)$$

here  $\check{\tau}_{ln}$  is the extra stress tensor,  $p$  stands for pressure,  $\delta_{ln}$  is the Kronecker delta,  $\mu_0$  and  $\mu_\infty$  are the zero and infinite shear rate viscosities,  $\Gamma$  is the time constant, and  $m$  is the dimensionless fluid behavior index. The shear rate  $\check{\gamma}$  is defined as follows:

$$\check{\gamma} = \sqrt{\frac{1}{2} \sum \sum \check{\gamma}_{ln} \check{\gamma}_{nl}} = \sqrt{\frac{1}{2} \Pi} \quad (3c)$$

Where,  $\Pi$  is the second invariant strain rate tensor. In case of  $\mu_\infty = 0$  and by using Taylor's expansion in equation (3c), we get:

$$\check{\tau}_{ln} = \mu_0 \left[ 1 + \frac{m-1}{2} ((I\check{\gamma}_{ln})^2) \right] \check{\gamma}_{ln} \quad (3d)$$

The biliary system, having stenosis, is assumed as a cylindrical elastic tube/model of the circular cross section containing an incompressible non-Newtonian fluid. The bile flow is modeled to be laminar, unsteady, two-dimensional, axially symmetric, and fully developed bile characterized by generalized Carreau model by considering an inclined non-uniform pancreatic duct filled with a porous medium. Under the assumptions, the governing equation may be written in the cylindrical coordinate system  $(\check{r}, \check{z}, \check{\theta})$  as

$$\frac{\partial \check{u}}{\partial \check{r}} + \frac{\check{u}}{\check{r}} + \frac{1}{\check{r}} \frac{\partial \check{v}}{\partial \check{\theta}} + \frac{\partial \check{w}}{\partial \check{z}} = 0 \quad (4a)$$

$$\rho \left( \frac{\partial \check{u}}{\partial \check{t}} + \check{u} \frac{\partial \check{u}}{\partial \check{r}} + \frac{\check{v}}{\check{r}} \frac{\partial \check{u}}{\partial \check{\theta}} - \frac{\check{v}^2}{\check{r}} + \check{w} \frac{\partial \check{u}}{\partial \check{z}} \right) = -\frac{\partial \check{p}}{\partial \check{r}} + \frac{1}{\check{r}} \frac{\partial}{\partial \check{r}} (\check{r} \check{C}_{rr}) + \frac{1}{\check{r}} \frac{\partial}{\partial \check{\theta}} (\check{C}_{r\theta}) + \frac{\partial}{\partial \check{z}} \check{C}_{rz} - \frac{\check{C}_{\theta\theta}}{\check{r}} - \rho g \cos \alpha \quad (4b)$$

$$\rho \left( \frac{\partial \check{v}}{\partial \check{t}} + \check{u} \frac{\partial \check{v}}{\partial \check{r}} + \frac{\check{v}}{\check{r}} \frac{\partial \check{v}}{\partial \check{\theta}} + \frac{\check{u}\check{v}}{\check{r}} + \check{w} \frac{\partial \check{v}}{\partial \check{z}} \right) = -\frac{1}{\check{r}} \frac{\partial \check{p}}{\partial \check{\theta}} + \frac{1}{\check{r}^2} \frac{\partial}{\partial \check{r}} (\check{r}^2 \check{C}_{r\theta}) + \frac{1}{\check{r}} \frac{\partial}{\partial \check{\theta}} (\check{C}_{\theta\theta}) + \frac{\partial}{\partial \check{z}} \check{C}_{\theta z} \quad (4c)$$

$$\rho \left( \frac{\partial \check{w}}{\partial \check{t}} + \check{u} \frac{\partial \check{w}}{\partial \check{r}} + \frac{\check{v}}{\check{r}} \frac{\partial \check{w}}{\partial \check{\theta}} + \check{w} \frac{\partial \check{w}}{\partial \check{z}} \right) = -\frac{\partial \check{p}}{\partial \check{z}} + \frac{1}{\check{r}} \frac{\partial}{\partial \check{r}} (\check{r} \check{C}_{rz}) + \frac{1}{\check{r}} \frac{\partial}{\partial \check{\theta}} (\check{C}_{\theta z}) + \frac{\partial}{\partial \check{z}} \check{C}_{zz} + \rho g \sin \alpha \quad (4d)$$

Here,  $\rho$  stands for density,  $\check{w}$  and  $\check{u}$  are the velocity components,  $\check{p}$  is the pressure,  $\sigma^2 = \frac{\epsilon}{Da}$ ,  $Da = \frac{k}{a^2}$ ,  $\epsilon$  is porosity,  $k$  is the permeability, and  $Da$  is the Darcy number.

From equation (3a) - (3c) and (3d) we get:

$$\frac{1}{2} \check{\gamma} \check{\gamma} = 2 \left\{ \left( \frac{\partial \check{w}}{\partial \check{r}} \right)^2 + \left( \frac{\check{w}}{\check{r}} \right)^2 + \left( \frac{\partial \check{u}}{\partial \check{z}} \right)^2 \right\} + \left( \frac{\partial \check{w}}{\partial \check{z}} + \frac{\partial \check{u}}{\partial \check{r}} \right)^2, \quad (5a)$$

$$\check{C}_{rr} = 2\mu_0 \left[ 1 + \frac{m-1}{2} ((I\check{\gamma}_{ln})^2) \right] \left( \frac{\partial \check{u}}{\partial \check{r}} \right), \quad (5b)$$

$$\check{C}_{rz} = \mu_0 \left[ 1 + \frac{m-1}{2} ((I\check{\gamma}_{ln})^2) \right] \left( \frac{\partial \check{w}}{\partial \check{r}} + \frac{\partial \check{u}}{\partial \check{z}} \right), \quad (5c)$$

$$\check{C}_{r\theta} = \mu_0 \left[ 1 + \frac{m-1}{2} ((I\check{\gamma}_{ln})^2) \right] \left( \frac{\partial \check{v}}{\partial \check{r}} + \frac{1}{\check{r}} \frac{\partial \check{u}}{\partial \check{\theta}} - \frac{\check{v}}{\check{r}} \right), \quad (5d)$$

$$\check{C}_{\theta\theta} = \mu_0 \left[ 1 + \frac{m-1}{2} ((I\check{\gamma}_{ln})^2) \right] \left( \frac{1}{\check{r}} \frac{\partial \check{v}}{\partial \check{\theta}} + \frac{\check{u}}{\check{r}} \right), \quad (5e)$$

$$\check{C}_{\theta z} = \mu_0 \left[ 1 + \frac{m-1}{2} ((I\check{\gamma}_{ln})^2) \right] \left( \frac{1}{\check{r}} \frac{\partial \check{w}}{\partial \check{\theta}} + \frac{\partial \check{v}}{\partial \check{z}} \right), \quad (5f)$$

$$\check{C}_{zz} = \mu_0 \left[ 1 + \frac{m-1}{2} ((I\check{\gamma}_{ln})^2) \right] \frac{\partial \check{w}}{\partial \check{z}}. \quad (5g)$$

Here,  $u(r, \theta, z, t)$ ,  $v(r, \theta, z, t)$  and  $w(r, \theta, z, t)$  represents the velocity components in  $r, \theta$  and  $z$  directions respectively,  $p$  is the pressure,  $\rho$  is the density of bile and  $\frac{\partial p}{\partial z}$  is the pressure gradient.

Assuming that the catheter is moving in the axial direction with velocity  $V_s$  and the catheter has a fixed radius  $r_s$ . Porous boundary (Darcy) models transmural leakage/permeation through the duct wall (e.g., in a fistula or diseased epithelium) and aggregate epithelial hydraulic permeability and lymphatic uptake. Inclination captures the gravitational contribution relevant to anatomical placement. Suitable boundary conditions are as follows

$$u(r, \theta, z, t) = v(r, \theta, z, t) = 0 \text{ at } r = R_w(z, t), \quad (6a)$$

$$-\frac{Knw}{\sqrt{Da}} = r_c \frac{\partial w}{\partial r} \text{ at } r = R_w(z, t), \quad (6b)$$

$$w(r, \theta, z, t) = V_c \text{ at } r = r_c. \quad (6c)$$



Assuming the system is at rest, i.e., no flow occurs.

$$u(r, \theta, z, t) = v(r, \theta, z, t) = w(r, \theta, z, t) = 0 \text{ at } t = 0, \quad (6d)$$

Let us introduce non-dimensional variables

$$z = \frac{\check{z}}{L_0}, r = \frac{\check{r}}{R_0}, v = \frac{\check{v}}{c}, u = \frac{\lambda \check{u}}{c R_0}, \varepsilon = \frac{R_0}{l_0}, p = \frac{R_0^2 \check{p}}{L_0 \eta_0 c}, Re = \frac{\rho c R_0}{\mu_0} \\ t = \frac{c \check{t}}{l_0}, R(z) = \frac{R(\check{z})}{R_0}, H_w(z) = \frac{H_w(\check{z})}{R_0}, C_{zz} = \frac{L_0}{c \mu_0} \check{C}_{zz}, C_{rr} = \frac{R_0}{c \mu_0} \check{C}_{rr}, \delta = \frac{R_0}{L_0}, We = \frac{c \Gamma}{R_0}, \check{\gamma} = \frac{c \dot{\gamma}}{R_0} \quad (7)$$

Reduced non-dimensional equations are

$$\varepsilon \left[ \frac{\partial u}{\partial r} + \frac{u}{r} + \frac{1}{r} \frac{\partial v}{\partial \theta} \right] + \frac{\partial w}{\partial z} = 0 \quad (8a)$$

$$Re \varepsilon^3 \left( \frac{\partial u}{\partial t} + u \frac{\partial u}{\partial r} + \frac{v}{r} \frac{\partial u}{\partial \theta} - \frac{v^2}{r} + w \frac{\partial u}{\partial z} \right) = - \frac{\partial p}{\partial r} + \varepsilon \frac{1}{r} \frac{\partial}{\partial r} (r C_{rr}) + \varepsilon \frac{1}{r} \frac{\partial}{\partial \theta} (C_{r\theta}) + \varepsilon^2 \frac{\partial}{\partial z} C_{rz} - \varepsilon \frac{C_{\theta\theta}}{r} - \frac{R_0^3 \rho g}{L_0 \mu_0 c} \cos \alpha \quad (8b)$$

$$Re \varepsilon^3 \left( \frac{\partial v}{\partial t} + u \frac{\partial v}{\partial r} + \frac{v}{r} \frac{\partial v}{\partial \theta} + \frac{uv}{r} + w \frac{\partial v}{\partial z} \right) = - \frac{1}{r} \frac{\partial p}{\partial \theta} + \varepsilon \frac{1}{r^2} \frac{\partial}{\partial r} (r^2 C_{r\theta}) + \varepsilon \frac{1}{r} \frac{\partial}{\partial \theta} (C_{\theta\theta}) + \varepsilon^2 \frac{\partial}{\partial z} C_{\theta z} \quad (8c)$$

$$Re \varepsilon \left( \frac{\partial w}{\partial t} + u \frac{\partial w}{\partial r} + \frac{v}{r} \frac{\partial w}{\partial \theta} + w \frac{\partial w}{\partial z} \right) = - \frac{\partial p}{\partial z} + \frac{1}{r} \frac{\partial}{\partial r} (r C_{rz}) + \frac{1}{r} \frac{\partial}{\partial \theta} (C_{\theta z}) + \varepsilon \frac{\partial}{\partial z} C_{zz} + \frac{R_0^2 \rho g}{L_0 \mu_0 c} \sin \alpha \quad (8d)$$

Where  $\eta = \frac{\rho g a^2}{\mu c}$ ,  $\eta' = \frac{\rho g a^3}{\mu c \lambda}$ ,  $\delta$  is the dimensionless wave number,  $We$  is the Weissenberg number,  $Re$  Reynolds number, and  $Kn$  Knudsen number.

The non-dimensional boundary conditions are

$$u(r, \theta, z, t) = v(r, \theta, z, t) = 0 \text{ at } r = R_w(z, t), \quad (9a)$$

$$- \frac{Knw}{\sqrt{Da}} = r_s \frac{\partial w}{\partial r} \text{ at } r = R_w(z, t) \quad (9b)$$

$$w(r, \theta, z, t) = V_c \text{ at } r = r_c, \quad (9c)$$

Let the system be at rest, i.e., no flow takes place.

$$u(r, \theta, z, t) = v(r, \theta, z, t) = w(r, \theta, z, t) = 0 \text{ at } t = 0, \quad (9d)$$

### SOLUTION OF THE PROBLEM

Considering a steady and laminar bile flow in an eccentric tube under the lubrication approach by neglecting the higher-order terms of  $\delta$  and  $Re$ . The equations of continuity, r-momentum,  $\theta$ -momentum and z-momentum become

$$\frac{\partial p}{\partial r} = \eta' \cos \alpha \quad (10a)$$

$$\frac{\partial p}{\partial z} - \eta \sin \alpha = \frac{1}{r} \frac{\partial}{\partial r} (r C_{rz}) + \frac{1}{r} \frac{\partial}{\partial \theta} (C_{\theta z}) \quad (10b)$$

$$\frac{\partial p}{\partial \theta} = 0 \quad (10c)$$

$$C_{rz} = \left[ 1 + \frac{m-1}{2} We^2 \left( \left( \frac{\partial w}{\partial r} \right)^2 + \left( \frac{1}{r} \frac{\partial w}{\partial \theta} \right)^2 \right) \right] \left( \frac{\partial w}{\partial r} \right) \quad (10d)$$

$$C_{\theta z} = \mu_0 \left[ 1 + \frac{m-1}{2} We^2 \left( \left( \frac{\partial w}{\partial r} \right)^2 + \left( \frac{1}{r} \frac{\partial w}{\partial \theta} \right)^2 \right) \right] \left( \frac{1}{r} \frac{\partial w}{\partial \theta} \right) \quad (10e)$$

We observe that equation (10b) cannot be solved analytically. The non-Newtonian behavior of bile is significant in small ducts at low shear rate, so we have assumed that the shear rate is low, i.e.,  $I\dot{\gamma} < 1$ . Linearizing the equation in terms of the Weissenberg number  $We^2$  by the regular perturbation technique.

$$w = w_0 + We^2 w_1 + \dots, \\ p = p_0 + We^2 p_1 + \dots, \\ q = q_0 + We^2 q_1 + \dots, \quad (11)$$

Using equations (5a)-(5g) into equation (10b) we obtain:

Zeroth-order system of  $We^2$  equations with boundary conditions

$$\frac{\partial^2 w_0}{\partial r^2} + \frac{1}{r} \frac{\partial w_0}{\partial r} = \frac{\partial p_0}{\partial z} - \eta \sin \alpha \quad (12a)$$

$$- \frac{Knw_0}{\sqrt{Da}} = r_c \frac{\partial w_0}{\partial r}, \text{ at } r = R_w(z, t), w_0 = V_c, \text{ at } r = r_c, \quad (12b)$$

A first-order system of  $We^2$  equations with boundary conditions

$$\frac{\partial^2 w_1}{\partial r^2} + \frac{1}{r} \frac{\partial w_1}{\partial r} = \frac{\partial p_1}{\partial z} - \frac{m-1}{2} \left( \frac{1}{r} \left( \frac{\partial w_0}{\partial r} \right)^3 + \frac{\partial}{\partial r} \left( \frac{\partial w_0}{\partial r} \right)^3 \right) \quad (12c)$$

$$w_0 = O_c, \text{ at } r = r_c, \quad -\frac{Knw_1}{\sqrt{Da}} = r_c \frac{\partial w_1}{\partial r} \text{ at } r = R_w(z, t) \quad (12d)$$

The slip boundary condition equation (12b), where  $Da$  is the Darcy number, which represents the porosity parameter, and  $Kn$  is the wall slip parameter, let  $\chi = \frac{dp_0}{dz} - \eta \sin \alpha$ .

The solution of the zeroth-order system

$$w_0 = \frac{1}{4} \chi r^2 + A_{11} \log r + A_{12} \quad (13a)$$

The solution of the first-order system

$$w_1 = \frac{1}{4} \left( \frac{dp_1}{dz} \right) r^2 - \frac{m-1}{2} \left[ \frac{1}{32} (\chi)^3 r^4 - \frac{(A_{11})^3}{2r^2} + \frac{3}{8} (\chi)^2 A_{11} r^2 \right] + A_{13} \log r + A_{14} \quad (6.13b)$$

The volumetric flow rate  $Q_o$  is given by

$$Q_o = \int_0^{R_w(z)} w_0 r dr = \int_0^{r_c} V_c r dr + \int_{r_c}^{R_w(z)} w_0 r dr \quad (14a)$$

$$Q_o = V_c r_c^2 + (\chi) \left( \frac{R_w^4 - r_c^4}{8} \right) + A_{11} (R_w^2 \log \sqrt{R_w} - r_c^2 \log \sqrt{r_c}) + A_{11} \left( \frac{r_c^2 - R_w^2}{4} \right) + A_{12} \left( \frac{R_w^2 - r_c^2}{2} \right) \quad (14b)$$

From equation (14b), we get

$$\frac{dp_0}{dz} = \left( \frac{8}{R_w^4 - r_c^4} \right) \left( Q_o - V_c r_c^2 - A_{11} (R_w^2 \log \sqrt{R_w} - r_c^2 \log \sqrt{r_c}) - A_{11} \left( \frac{r_c^2 - R_w^2}{4} \right) - A_{12} \left( \frac{R_w^2 - r_c^2}{2} \right) \right) + \eta \sin \alpha \quad (14c)$$

The volume flow rate  $Q_1$  is given by

$$Q_1 = \int_0^{R_w(z)} w_1 r dr = \int_0^{r_c} O_c r dr + \int_{r_c}^{R_w(z)} w_1 r dr \quad (15a)$$

$$Q_1 = \left( \frac{dp_1}{dz} \right) \left( \frac{R_w^4 - r_c^4}{16} \right) - \frac{m-1}{2} \left[ (\chi)^3 \left( \frac{R_w^6 - r_c^6}{192} \right) - \frac{(A_{11})^3}{2} \log \left( \frac{R_w}{r_c} \right) + 3(\chi)^2 A_{11} \left( \frac{R_w^4 - r_c^4}{32} \right) \right] \\ + A_{13} (R_w^2 \log \sqrt{R_w} - r_c^2 \log \sqrt{r_c}) + A_{13} \left( \frac{r_c^2 - R_w^2}{4} \right) + A_{14} \left( \frac{R_w^2 - r_c^2}{2} \right) \quad (15b)$$

From equation (15b), we get

$$\frac{dp_1}{dz} = \left( \frac{16}{R_w^4 - r_c^4} \right) \left( Q_1 + \frac{m-1}{2} \left[ (\chi)^3 \left( \frac{R_w^6 - r_c^6}{192} \right) - \frac{(A_{11})^3}{2} \log \left( \frac{R_w}{r_c} \right) + 3(\chi)^2 A_{11} \left( \frac{R_w^4 - r_c^4}{32} \right) \right] \right) \\ - \left( \frac{16}{R_w^4 - r_c^4} \right) A_{13} (R_w^2 \log \sqrt{R_w} - r_c^2 \log \sqrt{r_c}) - A_{13} \left( \frac{r_c^2 - R_w^2}{4} \right) - A_{14} \left( \frac{R_w^2 - r_c^2}{2} \right) \quad (15c)$$

Substituting in equation (11) we get

$$w = \frac{1}{4} (\chi) r^2 + A_{11} \log r + A_{12} + We^2 \left\{ \frac{1}{4} \left( \frac{dp_1}{dz} \right) r^2 - \frac{m-1}{2} \left[ \frac{1}{32} (\chi)^3 r^4 - \frac{(A_{11})^3}{2r^2} + \frac{3}{8} (\chi)^2 A_{11} r^2 \right] + A_{13} \log r + A_{14} \right\} \quad (16a)$$

$$Q = V_c r_c^2 + (\chi) \left( \frac{R_w^4 - r_c^4}{8} \right) + A_{11} (R_w^2 \log \sqrt{R_w} - r_c^2 \log \sqrt{r_c}) + A_{11} \left( \frac{r_c^2 - R_w^2}{4} \right) + A_{12} \left( \frac{R_w^2 - r_c^2}{2} \right) + \\ We^2 \left\{ \left( \frac{dp_1}{dz} \right) \left( \frac{R_w^4 - r_c^4}{16} \right) - \frac{m-1}{2} \left[ (\chi)^3 \left( \frac{R_w^6 - r_c^6}{192} \right) - \frac{(A_{11})^3}{2} \log \left( \frac{R_w}{r_c} \right) + 3(\chi)^2 A_{11} \left( \frac{R_w^4 - r_c^4}{32} \right) \right] \right\} \\ + We^2 \left\{ A_{13} (R_w^2 \log \sqrt{R_w} - r_c^2 \log \sqrt{r_c}) + A_{13} \left( \frac{r_c^2 - R_w^2}{4} \right) + A_{14} \left( \frac{R_w^2 - r_c^2}{2} \right) \right\} \quad (16b)$$

Similarly,

$$\frac{dp}{dz} = \left( \frac{8}{R_w^4 - r_c^4} \right) \left( Q_o - V_c r_c^2 - A_{11} (R_w^2 \log \sqrt{R_w} - r_c^2 \log \sqrt{r_c}) - A_{11} \left( \frac{r_c^2 - R_w^2}{4} \right) - A_{12} \left( \frac{R_w^2 - r_c^2}{2} \right) \right) + \\ \eta \sin \alpha + We^2 \left\{ \left( \frac{16}{R_w^4 - r_c^4} \right) \left( Q_1 + \frac{m-1}{2} \left[ (\chi)^3 \left( \frac{R_w^6 - r_c^6}{192} \right) - \frac{(A_{11})^3}{2} \log \left( \frac{R_w}{r_c} \right) + 3(\chi)^2 A_{11} \left( \frac{R_w^4 - r_c^4}{32} \right) \right] \right) \right\}$$

$$-We^2 \left\{ A_{13} (R_w^2 \log \sqrt{R_w} - r_c^2 \log \sqrt{r_c}) - A_{13} \left( \frac{r_c^2 - R_w^2}{4} \right) - A_{14} \left( \frac{R_w^2 - r_c^2}{2} \right) \right\} \quad (16c)$$

Where constants are

$$\begin{aligned} A_{11} &= \left[ 4V_c Kn + (\chi) (KnR_w^2 - Knr_c^2 + 2\sqrt{Da}R_w^2) \right] \left( \frac{-1}{4\sqrt{Da} + Kn \log \left( \frac{R_w}{r_c} \right)} \right) \\ A_{12} &= V_c - \frac{1}{4}(\chi)r_c^2 - A_{11} \log r_c \\ A_{13} &= \left( \frac{1}{\sqrt{Da} + Kn \log \left( \frac{R_w}{r_c} \right)} \right) \left[ \frac{1}{4} \frac{dp_1}{dz} (KnR_c^2 - KnR_w^2 - 2\sqrt{Da}R_w^2) \right] + \left( \frac{1}{\sqrt{Da} + Kn \log \left( \frac{R_w}{r_c} \right)} \right) \left( \frac{m-1}{2} \right) \\ &\quad \left\{ (\chi)^3 \frac{1}{32} (KnR_w^4 - Knr_c^4 + 4\sqrt{Da}R_w^4) + 16A_{11}^3 + \frac{3A_{11}}{8} (\chi)^2 (KnR_w^2 - Knr_c^2 + 2\sqrt{Da}R_w^2) \right\} \\ &\quad + \left( \frac{1}{\sqrt{Da} + Kn \log \left( \frac{R_w}{r_c} \right)} \right) \left( \frac{m-1}{2} \right) \frac{A_{11}^3 (KnR_w^2 - Knr_c^2 + 2\sqrt{Da}R_w^2)}{R_w^2 r_c^2} \\ A_{14} &= -A_{13} \log r_c - \frac{r_c^2}{4} \frac{dp_1}{dz} + \left( \frac{m-1}{2} \right) \left\{ \frac{r_c^4}{32} (\chi)^3 - \frac{A_{11}^3}{2r_c^2} + \frac{3A_{11}r_c^2}{8} (\chi)^2 \right\} \end{aligned}$$

## RESULTS AND DISCUSSION

In the present paper, the effect of various physiological parameters involved in the peristaltic flow of bile in an inclined eccentric tube filled with a porous medium is analyzed. The results of the present mathematical model are evaluated with the help of MATLAB 2021a. The range of physiological parameters to analyze the resulting expressions of axial velocity  $w$ , and pressure gradient  $\frac{dp}{dz}$  and the volumetric flow rate  $Q$  in this study, the porosity parameter  $Da$ , angle of inclination  $\alpha$ , Weissenberg number  $We$ , velocity of the catheter  $V_c$ , radius of catheter  $r_c$ , gravity parameter  $\eta$ , wall slip parameter  $Kn$  and fluid behavior index  $m$ .

The axial velocity profile with respect to radial distance has been made from Figures 2(a)–2(h) for several values to emerging parameters and the graphs shows that the axial velocity is maximum at the surface of the catheter (outer wall of catheter) and as we move towards the wall of duct axial velocity decreases and is minimum at the wall. Figure 2(a) shows the effect of the porosity parameter on axial velocity. The axial velocity increases with the porosity parameter; maximum velocity occurs at the highest value of porosity parameter because the number of pores increases with the increase of porosity parameter, so the fluid can easily move through the duct. In Figure 2(b), we see the effect of the angle of inclination on axial velocity. The axial velocity increases with the increase in angle of inclination. An inclined duct helps to pass fluid quickly through the duct, so inclination marks a positive impact on axial velocity. In Figure 2(c), we observe that the axial velocity falls as we increase the Weissenberg number. The high elasticity of fluid reduces the axial velocity. Figure 2(d) displays the axial velocity profile for different values of the radius of the catheter. It is noticed that axial velocity increases with the increase in catheter radius. In Figure 2(e), we see that the axial velocity increases with the velocity of the catheter and is justified by the nature of the curve. If we increase the velocity of the catheter, it helps to raise the velocity of the fluid. Figure 2(f) shows the effect of the gravity parameter on axial velocity. The axial velocity increases with the gravity parameter, because the bile flows from the upper body parts to the lower parts of the body, so gravity plays an important role in flow. In Figure 2(g), we see that the axial velocity falls with wall slip conditions as it produces a hindrance to flow at the duct wall of the duct, so velocity reduces for a higher wall slip parameter. Figure 2(h) shows the effect of fluid behavior index on axial velocity for large values of  $m$ . The fluid is in the shear-thinning condition and at  $m = 1$ . Fluid behaves like a Newtonian fluid, clearly showing axial velocity increases with the fluid behavior index.

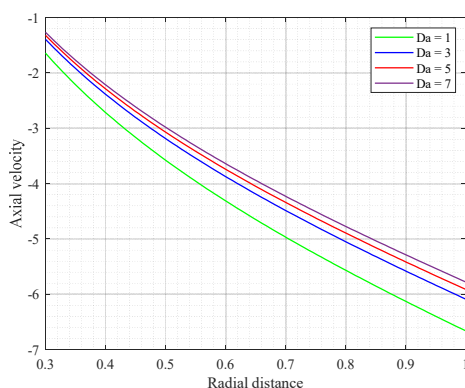


**Figure 2(a).** Profile of axial velocity  $w$  with  $r$  for different values of  $Da$  with  $\alpha = \frac{\pi}{4}$ ,  $We = 3$ ,  $r_c = 0.15$ ,  $V_c = 0.25$ ,  $\eta = 0.35$ ,  $Kn = 0.2$ ,  $b = 0.5$ ,  $m = 0.3685$

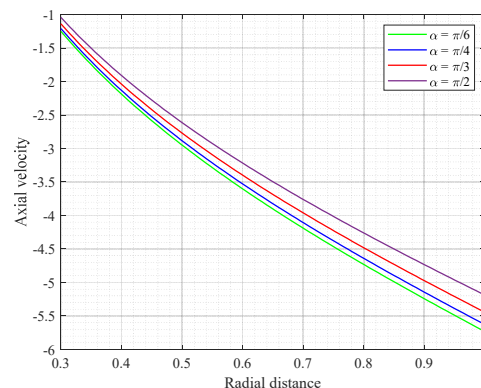


**Figure 2(b).** Profile of axial velocity  $w$  with  $r$  for different values of  $\alpha$  with  $Da = 3$ ,  $We = 3$ ,  $r_c = 0.15$ ,  $V_c = 0.25$ ,  $\eta = 0.35$ ,  $Kn = 0.2$ ,  $b = 0.5$ ,  $m = 0.3685$

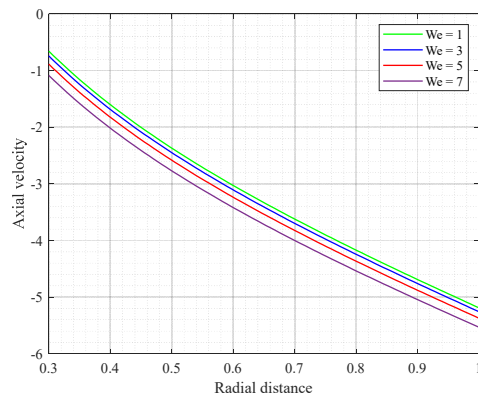


**Figure 2(c).** Profile of axial velocity  $w$  with  $r$  for different values of  $We$  with  $Da = 3, \alpha = \frac{\pi}{4}, r_c = 0.15, V_c = 0.25, \eta = 0.35, Kn = 0.2, b = 0.5, m = 0.3685$

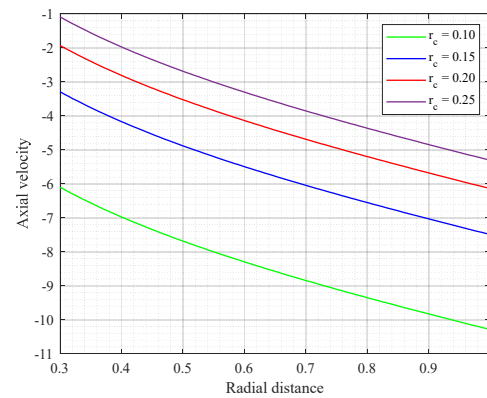


**Figure 2(d).** Profile of axial velocity  $w$  with  $r$  for different values of  $r_c$  with  $Da = 3, \alpha = \frac{\pi}{4}, We = 3, V_c = 0.25, \eta = 0.35, Kn = 0.2, b = 0.5, m = 0.3685$

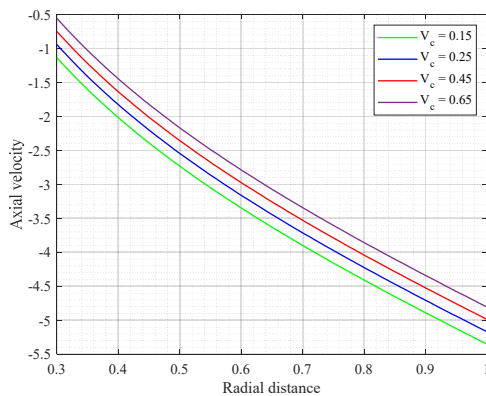


**Figure 2(e).** Profile of axial velocity  $w$  with  $r$  for different values of  $V_c$  with  $Da = 3, \alpha = \frac{\pi}{4}, We = 3, r_c = 0.15, \eta = 0.35, Kn = 0.2, b = 0.5, m = 0.3685$

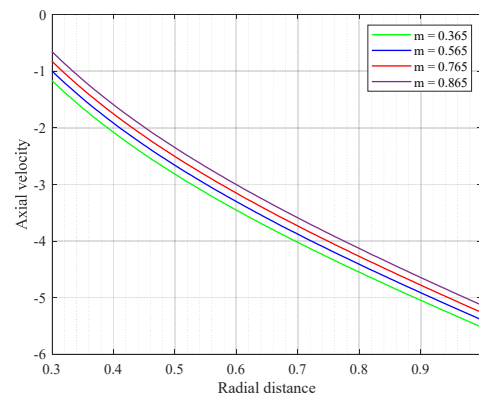


**Figure 2(h).** Profile of axial velocity  $w$  with  $r$  for different values of  $m$  with  $Da = 3, \alpha = \frac{\pi}{4}, We = 3, r_c = 0.15, V_c = 0.25, \eta = 0.35, Kn = 0.2, b = 0.5$

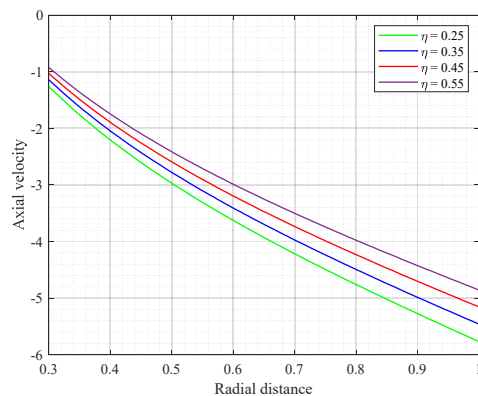


**Figure 2(f).** Profile of axial velocity  $w$  with  $r$  for different values of  $\eta$  with  $Da = 3, \alpha = \frac{\pi}{4}, We = 3, V_c = 0.25, r_c = 0.15, Kn = 0.2, b = 0.5, m = 0.3685$

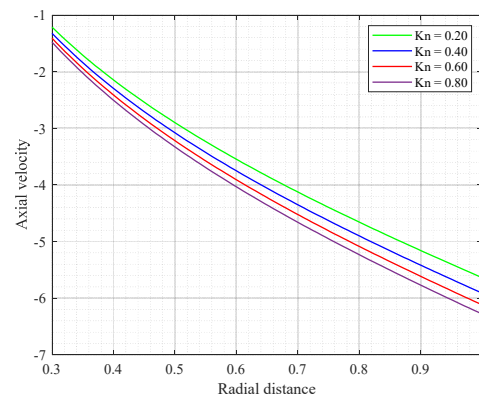


**Figure 2(g).** Profile of axial velocity  $w$  with  $r$  for different values of  $Kn$  with  $Da = 3, \alpha = \frac{\pi}{4}, We = 3, r_c = 0.15, \eta = 0.35, V_c = 0.25, b = 0.5, m = 0.3685$

Figures 3(a)–3(h) show pressure gradient distributions with respect to the axial distance of the various emerging parameters, and the graphs depict that more pressure is required to maintain the same flux in the narrow part of the duct due to the flexible wall, the duct contract or expand along the  $z$ -axis. Figure 3(a) shows the effect of the porosity parameter on the pressure gradient. The pressure decreases with increasing the porosity parameter. The minimum pressure is required to maintain the same flow rate at high porosity parameters, because porosity directly signifies the number of pores in a porous medium, so fluid passes easily through a porous duct for a high value of porosity parameter. Figure 3(b) shows the effect of angle of inclination on pressure gradient and observed that a lower pressure is required to maintain the same flux at a more inclined duct, i.e., the pressure gradient falls as we raise the value of inclination. Figure 3(c) shows the effect of Weissenberg number on the pressure gradient. More pressure is required to maintain the constant flux for an elastic fluid. Pressure gradient increases as we raise the Weissenberg number. In Figure 3(d), we see that low

pressure is required to pass through the duct with a large size of radius of the catheter, clearly indicating that the pressure decreases as we increase the radius of the catheter. Figure 3(e) shows that pressure reduces as the velocity of the catheter increases; the high catheter velocity helps in maintaining the flow so that the fluid can easily move in the duct. In Figure 3(f), we observe that the pressure gradient drops as the value of the gravity parameter increases. Figure 3(g) displays the pressure gradient distribution for distinct values of the wall slip parameter, as the wall slip parameter increases value of pressure also increases. The wall slip parameter shows a negative impact on the flow. In Figure 3(h), we see the effect of fluid behavior index on the pressure gradient. The low pressure is needed to maintain the same flow rate with the increment in the value of the fluid behavior index.

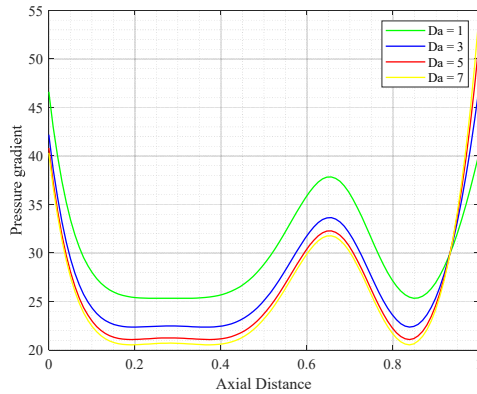


**Figure 3(a).** Profile of pressure gradient  $\frac{dp}{dz}$  with  $z$  for different values of  $Da$  with  $\alpha = \frac{\pi}{4}$ ,  $We = 3$ ,  $r_c = 0.15$ ,  $V_c = 0.25$ ,  $\eta = 0.35$ ,  $Kn = 0.2$ ,  $b = 0.5$ ,  $m = 0.3685$

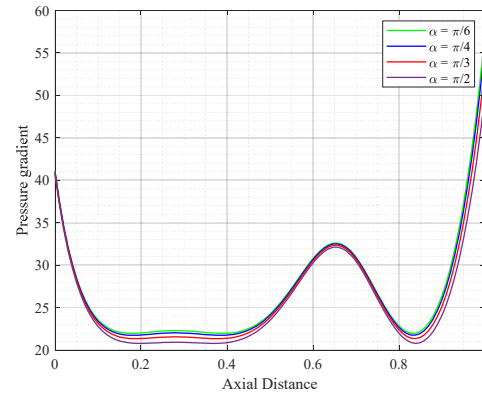


**Figure 3(b).** Profile of pressure gradient  $\frac{dp}{dz}$  with  $z$  for different values of  $\alpha$  with  $Da = 3$ ,  $We = 3$ ,  $r_c = 0.15$ ,  $V_c = 0.25$ ,  $\eta = 0.35$ ,  $Kn = 0.2$ ,  $b = 0.5$ ,  $m = 0.3685$

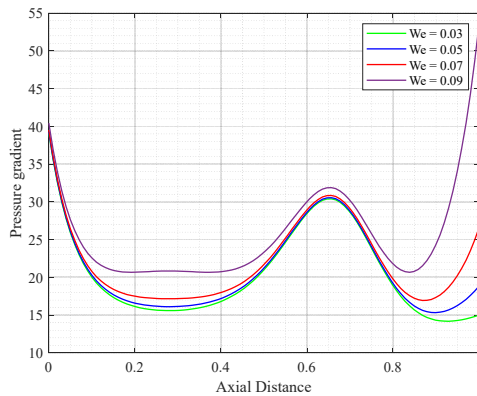


**Figure 3(c).** Profile of pressure gradient  $\frac{dp}{dz}$  with  $z$  for different values of  $We$  with  $Da = 3$ ,  $\alpha = \frac{\pi}{4}$ ,  $r_c = 0.15$ ,  $V_c = 0.25$ ,  $\eta = 0.35$ ,  $Kn = 0.2$ ,  $b = 0.5$ ,  $m = 0.3685$

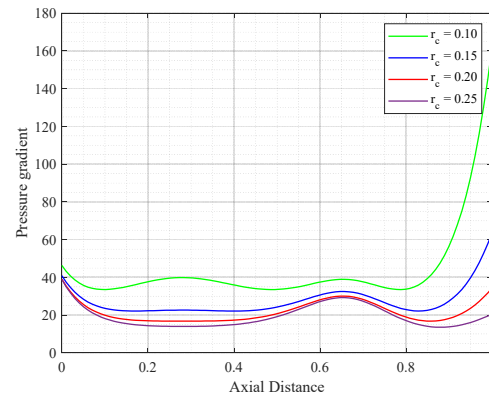


**Figure 3(d).** Profile of pressure gradient  $\frac{dp}{dz}$  with  $z$  for different values of  $r_c$  with  $Da = 3$ ,  $\alpha = \frac{\pi}{4}$ ,  $We = 3$ ,  $V_c = 0.25$ ,  $\eta = 0.35$ ,  $Kn = 0.2$ ,  $b = 0.5$ ,  $m = 0.3685$

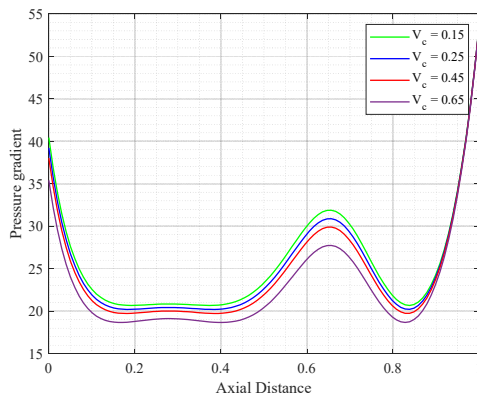


**Figure 3(e).** Profile of pressure gradient  $\frac{dp}{dz}$  with  $z$  for different values of  $V_c$  with  $Da = 3$ ,  $\alpha = \frac{\pi}{4}$ ,  $We = 3$ ,  $r_c = 0.15$ ,  $\eta = 0.35$ ,  $Kn = 0.2$ ,  $b = 0.5$ ,  $m = 0.3685$

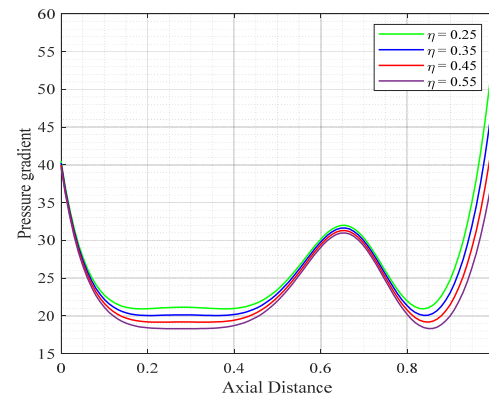


**Figure 3(f).** Profile of pressure gradient  $\frac{dp}{dz}$  with  $z$  for different values of  $\eta$  with  $Da = 3$ ,  $\alpha = \frac{\pi}{4}$ ,  $We = 3$ ,  $V_c = 0.25$ ,  $r_c = 0.15$ ,  $Kn = 0.2$ ,  $b = 0.5$ ,  $m = 0.3685$



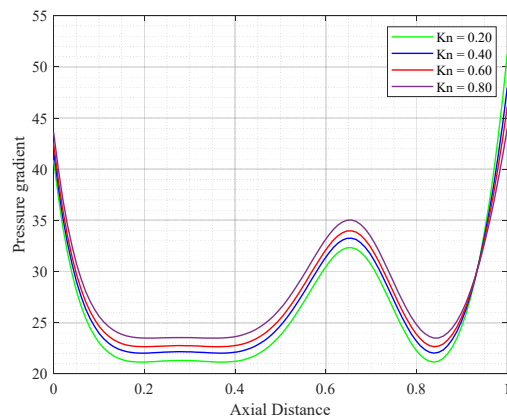


**Figure 3(g).** Profile of pressure gradient  $\frac{dp}{dz}$  with  $z$  for different values of  $Kn$  with  $Da = 3$ ,  $\alpha = \frac{\pi}{4}$ ,  $We = 3$ ,  $r_c = 0.15$ ,  $\eta = 0.35$ ,  $V_c = 0.25$ ,  $b = 0.5$ ,  $m = 0.3685$

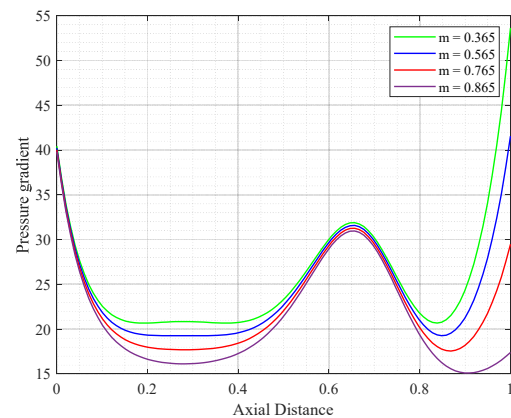


**Figure 3(h).** Profile of pressure gradient  $\frac{dp}{dz}$  with  $z$  for different values of  $m$  with  $Da = 3$ ,  $\alpha = \frac{\pi}{4}$ ,  $We = 3$ ,  $r_c = 0.15$ ,  $V_c = 0.25$ ,  $\eta = 0.35$ ,  $Kn = 0.2$ ,  $b = 0.5$

Figures 4(a)–4(h) display the flow rate concerning axial distance for numerous values of decisive parameters. The nature of the curves is the same along the  $z$ -axis; maximum flow occurs when the duct is expanded. Figure 4(a) shows the effect of the porosity parameter on the flow rate. The flow rate increases with the porosity parameter because the number of pores increases, which leads to flow rate. In Figure 4(b), we observe that the flow rate enhances with the angle of inclination. The flow of fluid is downwards, so inclination increases the flow rate. In Figure 4(c), we see that the flow rate decreases with Weissenberg number, which means a high elastic fluid will not be able to pass easily through the eccentric duct. An increase in the Weissenberg number ( $We$ ) and the wall slip parameter ( $Kn$ ) leads to a decrease in bile flow velocity because of the Weissenberg number (elasticity). The Weissenberg number measures the relative importance of elastic stresses to viscous stresses ( $We = \lambda U/L$ ). In a Carreau fluid, higher  $We$  implies stronger viscoelastic effects. Elastic normal stresses generated within the fluid resist deformation and act as an additional resistance to the pressure-driven flow. As a result, for the same driving pressure gradient, the axial velocity decreases because part of the input energy is stored elastically rather than converted into forward motion. Similar behavior has been reported in peristaltic transport of Carreau fluids in eccentric tubes, where velocity decreases with  $We$  (Nadeem et al., [8]; Reima et al., [11]). In Figure 4(d), we see that the flow rate falls as the radius of the catheter increases. It means maximum fluid passes through the inner tube with fixed velocity, and the rest of the fluid moves through the porous duct. In Figure 4(e), we observe that the flow increases with the increase in catheter velocity. The fluid is passed quickly through the catheter. Figure 4(f) shows the effect of the gravity parameter on flow rate, indicating clearly that the gravity parameter has a positive impact on the flow rate. From Figure 4(g), we noticed that the flow rate reduces with the wall slip parameter. Figure 4(h) displays the effect of fluid behavior index on flow rate. The flow rate increases as we increase the value of  $m$ , as the value of the fluid behavior index tends to 1, the flow rate increases.

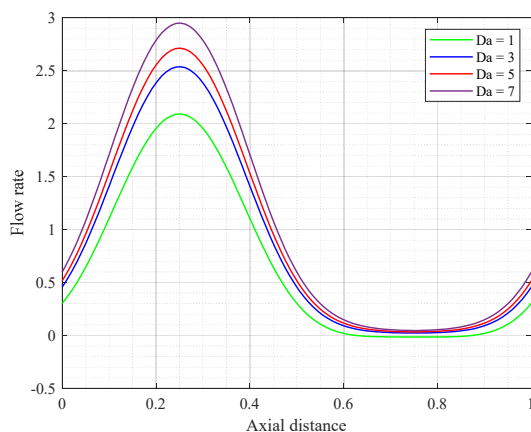


**Figure 4(a).** Profile of flow rate  $Q$  with  $z$  for different values of  $Da$  with  $\alpha = \frac{\pi}{4}$ ,  $We = 3$ ,  $r_c = 0.15$ ,  $V_c = 0.25$ ,  $\eta = 0.35$ ,  $Kn = 0.2$ ,  $b = 0.5$ ,  $m = 0.3685$

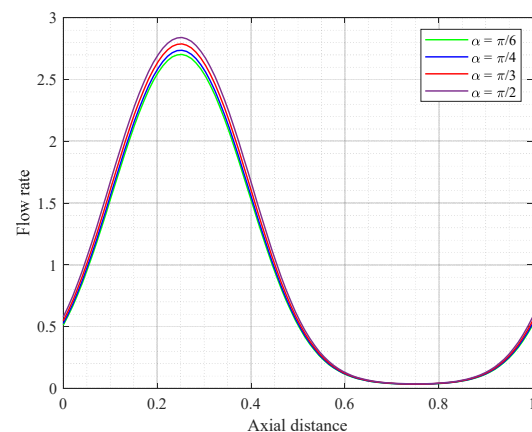


**Figure 4(b).** Profile of flow rate  $Q$  with  $z$  for different values of  $\alpha$  with  $Da = 3$ ,  $We = 3$ ,  $r_c = 0.15$ ,  $V_c = 0.25$ ,  $\eta = 0.35$ ,  $Kn = 0.2$ ,  $b = 0.5$ ,  $m = 0.3685$



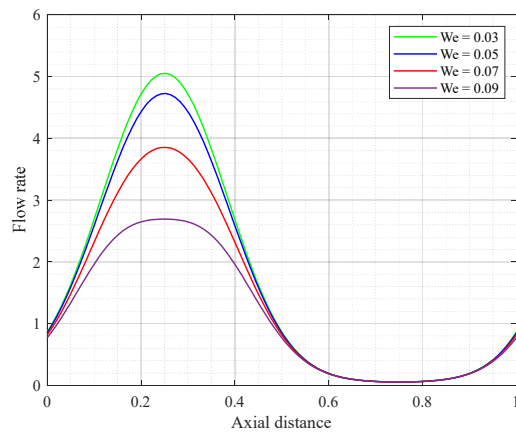


**Figure 4(c).** Profile of flow rate  $Q$  with  $z$  for different values of  $We$  with  $Da = 3, \alpha = \frac{\pi}{4}, r_c = 0.15, V_c = 0.25, \eta = 0.35, Kn = 0.2, b = 0.5, m = 0.3685$

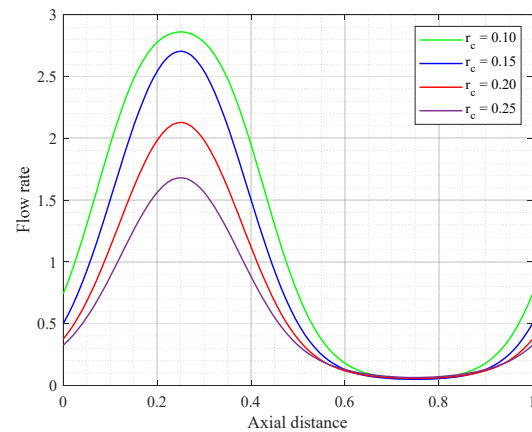


**Figure 4(d).** Profile of flow rate  $Q$  with  $z$  for different values of  $r_c$  with  $Da = 3, \alpha = \frac{\pi}{4}, We = 3, V_c = 0.25, \eta = 0.35, Kn = 0.2, b = 0.5, m = 0.3685$

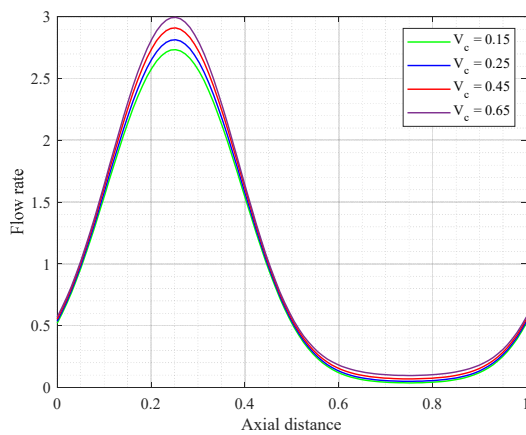


**Figure 4(e).** Profile of flow rate  $Q$  with  $z$  for different values of  $V_c$  with  $Da = 3, \alpha = \frac{\pi}{4}, We = 3, r_c = 0.15, \eta = 0.35, Kn = 0.2, b = 0.5, m = 0.3685$

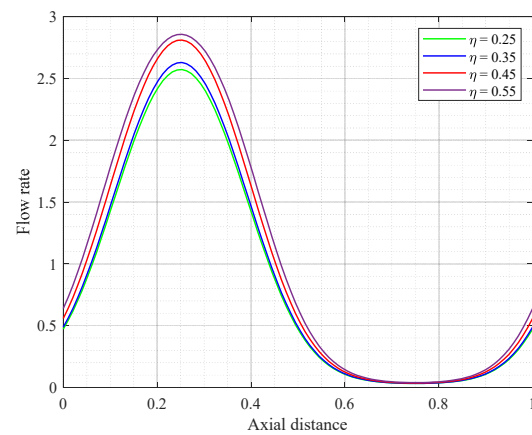


**Figure 4(f).** Profile of flow rate  $Q$  with  $z$  for different values of  $\eta$  with  $Da = 3, \alpha = \frac{\pi}{4}, We = 3, V_c = 0.25, r_c = 0.15, Kn = 0.2, b = 0.5, m = 0.3685$

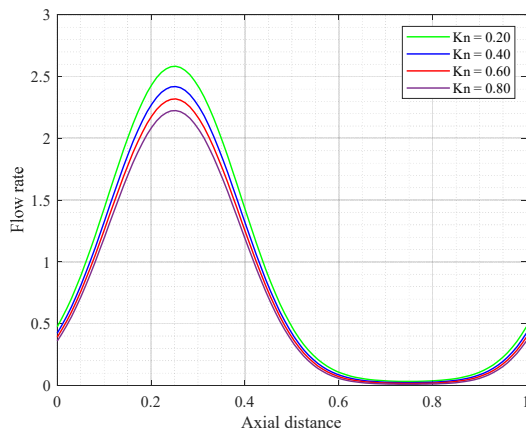


**Figure 4(g).** Profile of flow rate  $Q$  with  $z$  for different values of  $Kn$  with  $Da = 3, \alpha = \frac{\pi}{4}, We = 3, r_c = 0.15, \eta = 0.35, V_c = 0.25, b = 0.5, m = 0.3685$

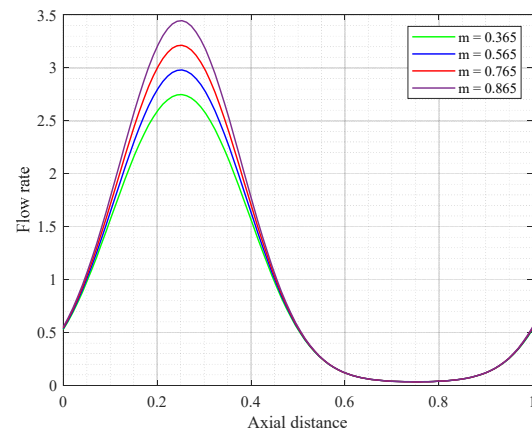


**Figure 4(h).** Profile of flow rate  $Q$  with  $z$  for different values of  $m$  with  $Da = 3, \alpha = \frac{\pi}{4}, We = 3, r_c = 0.15, V_c = 0.25, \eta = 0.35, Kn = 0.2, b = 0.5$

This discussion is consistent with representative studies (Nadeem et al. [8]; Reima et al. [11]) that report similar trends in velocity, shear, and flow rate with elasticity and catheterization. Reduction in axial velocity with increased elasticity and changes with catheter radius are consistent with previous Carreau/eccentric-catheter studies. The standard values of the parameters shown in the discussion are based on referenced or experimentally verified. These parameters correspond to the realistic situations.

## CONCLUSIONS

The bile is considered a non-Newtonian fluid. A comprehensive perturbation resolution has been discovered for Carreau fluid flow down an inclined eccentric catheterized duct with a porous wall containing bile. The obtained results in the case of Carreau fluid reveal that the flow characteristics are dependent on many parameters, such as catheter radius, catheter velocity, angle of inclination, gravity parameter, porosity parameter, Weissenberg number, fluid behavior index, and wall slip parameter. The key conclusions based on trends observed in the graphs are given as:

- Axial velocity and flow rate increase with an increased catheter velocity, angle of inclination, gravity parameter, porosity parameter, and fluid behavior index. It shows the positive impact on velocity and flux, which helps to move bile through the duct. Increase in axial velocity and flow rate at higher Darcy numbers in our simulations reflects that a more porous wall reduces resistance to flow, with clinical observations that bile escapes more readily when the duct wall loses its tight barrier function.
- Axial velocity and flow rate show a reverse nature with an increased Weissenberg number and wall slip parameter.
- Axial velocity is maximum at the outer surface of the catheter and is minimum at the wall of the duct.
- A catheter with a small radius increases the flow of bile. If the catheter size is large, it reduces the flow rate.
- In case of pressure gradient, more pressure is required to maintain the same flux with higher values of Weissenberg number, and for other parameters, low pressure is required to maintain the same flux.
- The reduction in wall shear stress due to shear-thinning also agrees with rheological observations of bile. Kuchumov et al. [5] analyzed the results of experiments, which relate well to the quantitative outcomes for bile. The present study is limited to theoretical outcomes considering the experimentally validated data. Even this analysis needs to be compared with clinical data in future work.

## Acknowledgement

This research project was funded by the University of Technology and Applied Sciences, Shinas, through the Internal Research Funding Program-2025, grant number (UTAS-Shinas-cy02-2025-005).

The authors are grateful to Prof. S.P. Singh, Department of Mathematics, Dayalbagh Educational Institute, Agra, Uttar Pradesh (India), for his valuable guidance and support in conducting this research.

## Conflict of Interests

There is no conflict of interest.

## Data Availability Statement

The data will be made available on request.

## Consent to Participate

There is no participation or involvement of any human/animal in this research article.

## ORCID

Devendra Kumar, <https://orcid.org/0000-0002-2346-8445>; Tanuj Kumar Rawat, <https://orcid.org/0009-0006-5907-1825>

Mahesh Garvandha, <https://orcid.org/0000-0002-4751-5840>; Sudhakar Kumar Chaubey, <https://orcid.org/0000-0002-3882-4596>

## REFERENCES

- [1] W. Cao, M.M. Kaleem, M. Usman, M. Imran Asjad, M.Y. Almusawa, and S.M. Eldin, "A study of fractional Oldroyd-B fluid between two coaxial cylinders containing gold nanoparticles," *Case Studies in Thermal Engineering*, **45**, 102949 (2023). <https://doi.org/10.1016/j.csite.2023.102949>
- [2] M. Dhange, G. Sankad, R. Safdar, W. Jamshed, M.R. Eid, U. Bhujakkanavar, S. Gouadri, and R. Chouikh, "A mathematical model of blood flow in a stenosed artery with post-stenotic dilatation and a forced field," *Plos one*, **17**(7), e0266727 (2022). <https://doi.org/10.1371/journal.pone.0266727>
- [3] M. Gudekote and R. Choudhari, "Slip Effects on Peristaltic Transport of Casson Fluid in an Inclined Elastic Tube with Porous Walls," *Journal of Advanced Research in Fluid Mechanics and Thermal Sciences*, **43**(1), 67–80 (2018).
- [4] J.W. Ostroff, J.P. Roberts, R.L. Gordon, R.L., E.J. Ring, and N.L. Ascher, "The management of T tube leaks in orthotopic liver transplant recipients with endoscopically placed nasobiliary catheters," *Transplantation*, **49**(5), 922-924 (1990). <https://doi.org/10.1097/00007890-199005000-00018>
- [5] A.G. Kuchumov, Y.L. Nyashin, V.A. Samartsev, "Modeling of Peristaltic Bile Flow in the Papilla Ampoule with Stone and in the Papillary Stenosis Case: Application to Reflux Investigation," in: *7th WACBE World Congress on Bioengineering, IFMBE Proceedings*, edited by J. Goh, and C. Lim, vol. **52**, (Springer, Cham. 2015). [https://doi.org/10.1007/978-3-319-19452-3\\_42](https://doi.org/10.1007/978-3-319-19452-3_42)
- [6] L.B. McCash, S. Akhtar, S. Nadeem, S. Saleem, and A. Issakhov, "Viscous flow between two sinusoidally deforming curved concentric tubes: advances in endoscopy," *Science Report*, **11**, 15124 (2021). <https://doi.org/10.1038/s41598-021-94682-8>
- [7] N.T. Eldabe, M.Y. Abouzeid, and H.A. Ali, "Effect of Heat and Mass Transfer on Casson Fluid Flow Between Two Co-Axial Tubes with Peristalsis," *Journal of Advanced Research in Fluid Mechanics and Thermal Sciences*, **76**, 54-75 (2020). <https://doi.org/10.37934/arfmts.76.1.5475>
- [8] S. Nadeem, A. Riaz, R. Ellahi, and N.S. Akbar, "Series solution of unsteady peristaltic flow of a Carreau fluid in eccentric cylinders," *Ain Shams Engineering Journal*, **5**, 293–304 (2014). <https://doi.org/10.1016/j.asej.2013.09.005>
- [9] S.M. Nurulaifa, Z. Ismail, and N.A. Jaafar, "Mathematical Modeling of Unsteady Solute Dispersion in Bingham Fluid Model of Blood Flow Through an Overlapping Stenosed Artery," *Journal of Advanced Research in Fluid Mechanics and Thermal Sciences*, **87**, 134-147 (2021). <https://doi.org/10.37934/arfmts.87.3.134147>

- [10] Q. Raza, X. Wang, M.Z. Qureshi, S.M. Eldin, A.A. Allah, B. Ali, and I. Siddique, "Mathematical modeling of nanolayer on biological fluids flow through porous surfaces in the presence of CNT," *Case Studies in Thermal Engineering*, **45**, 102958 (2023). <https://doi.org/10.1016/j.csite.2023.102958>
- [11] R.D. Alsemiry, H.M. Sayed, and N. Amin, "Mathematical analysis of Carreau fluid and heat transfer within an eccentric catheterized artery," *Alexandria Engineering Journal*, **61**, 523–539 (2022). <https://doi.org/10.1016/j.aej.2021.06.029>
- [12] T. Sauerbruch, M. Weinzierl, J. Holl, and E. Pratschke, "Treatment of Postoperative Bile Fistulas by Internal Endoscopic Biliary Drainage," *Gastroenterology*, **90**(6), 1998-2003 (1986). [https://doi.org/10.1016/0016-5085\(86\)90273-8](https://doi.org/10.1016/0016-5085(86)90273-8)
- [13] S.M. Strasberg, C.N. Petrunka, R.G. Ilson, and J.E. Paloheimo, "Characteristics of Inert Solute Clearance by the Monkey Liver," *Gastroenterology*, **76**(2), 259-266 (1978). [https://doi.org/10.1016/0016-5085\(79\)90331-7](https://doi.org/10.1016/0016-5085(79)90331-7)
- [14] D. Tripathi, "Study of transient peristaltic heat flow through a finite porous channel," *Mathematical and Computer Modeling*, **57**, 1270-1283 (2013). <https://doi.org/10.1016/j.mcm.2012.10.030>

# **ПЕРИСТАЛЬТИЧНИЙ ПОТІК ЖОВЧІ В АМПУЛІ СОСОЧКА З ПОРИСТИМИ СТІНКАМИ ТА ПОХИЛОЮ ЕКЦЕНТРИЧНОЮ КАТЕТЕРИЗОВАНОЮ ПРОТОКОЮ**

**Д. Кумар<sup>1</sup>, Т.К. Рават<sup>2</sup>, М. Гарванда<sup>1</sup>, С. Кумар<sup>3</sup>, С.К. Чаубей<sup>1</sup>**

<sup>1</sup>*Відділ наук та математики, кафедра допоміжних вимог, університет технологій та прикладних наук-Шинас, Оман*

<sup>2</sup>*Університет GLA, Велика Нойда, Індія*

<sup>3</sup>*Університет доктора Бхімрао Амбедкара, Агра, Індія*

У цьому дослідженні математично досліджується комбінований вплив нахилу та катетера на біліарний потік рідини Карро через ексцентричну катетеризовану протоку з пористим матеріалом. Технічне збурення використовується для розв'язання керівних рівнянь, враховуючи низькі числа Рейнольдса, довгохвильове наближення та відповідні малі параметри. Хірургічна техніка, коли катетер ексцентрично вводиться в протоку, пов'язана з результатами дослідження. Для досягнення аналітичних рішень було використано кілька параметрів. У цих даних відображаються осьова швидкість, градієнт тиску, швидкість потоку та напруження зсуву стінки, а також такі нові параметри: параметр ковзання стінки, число Вайсенберга, індекс поведінки рідини, число Дарсі та кут нахилу. Градієнт тиску значно змінюється кутом нахилу та параметром пористості, а осьова швидкість катетера падає зі збільшенням числа Вайсенберга. Фізіологічні спостереження узгоджуються з цими висновками.

**Ключові слова:** перистальтичний потік жовчі; цибулина сосочка; пористі стінки; похила ексцентрична катетеризована протока

## SORET AND DUFOUR EFFECTS ON Ag–TiO<sub>2</sub>/WATER IN A CASSON HYBRID NANOFLUID OVER A MOVING VERTICAL PLATE WITH CONVECTIVE BOUNDARY CONDITIONS

 K. Fatima<sup>1</sup>,  J.L. Rama Prasad<sup>2\*</sup>

<sup>1</sup>Department of Mathematics, Krishna University, Machilipatnam, AP, India

<sup>2</sup>Department of Mathematics, P.B. Siddhartha College of Arts & Science, Vijayawada, AP, India

Email: [bukharizulfa@gmail.com](mailto:bukharizulfa@gmail.com)

\*Corresponding Author e-mail: [jlrprasad@gmail.com](mailto:jlrprasad@gmail.com)

Received August 14, 2025; revised October 5, 2025; accepted November 1, 2025

This research presents a comprehensive investigation of the Soret and Dufour effects on Casson hybrid nanofluid (HNF) flow past a moving vertical plate, with silver (Ag) and titanium dioxide (TiO<sub>2</sub>) nanoparticles dispersed in water. The incorporation of Ag–TiO<sub>2</sub> hybrid nanoparticles combines the exceptional thermal conductivity of silver with the chemical stability and cost-effectiveness of TiO<sub>2</sub>, creating a fluid with superior transport properties compared to conventional single-component nanofluids. The governing partial differential equations describing momentum, heat and mass transfer are transformed into a set of nonlinear ordinary differential equations using similarity transformations. These equations are solved numerically via the Keller Box method, ensuring stability and accuracy in handling coupled highly nonlinear systems. In addition, an analysis was performed to examine the influence of nanoparticle morphology on velocity, temperature and concentration distributions, thereby validating and enriching the numerical outcomes. The results reveal that variable nanoparticle morphology and the combined Ag–TiO<sub>2</sub> dispersion significantly enhance heat transfer rates and mass transfer rates while reducing frictional losses near the plate surface. The inclusion of Soret and Dufour effects further amplifies cross-coupling between thermal and solutal fields leading to improved transport efficiency. These findings not only provide new insights into Casson hybrid nanofluid dynamics but also highlight the critical role of cross-diffusion in optimizing heat and mass transfer systems. The integration of Casson fluid rheology, hybrid nanoparticles and cross-diffusion effects under realistic boundary conditions has direct implications for industrial cooling, metallurgical processing, biomedical drug delivery and energy system optimization. By demonstrating the synergistic performance of Ag–TiO<sub>2</sub> nanofluids, this study establishes a pathway for designing next-generation thermal management and biomedical transport technologies.

**Keywords:** Convective Boundary Conditions; MHD; Casson Hybrid Nanofluid; Shape of Nanoparticles; Soret and Dufour effects

**PACS:** 47.20.Bp, 44.40.+a, 47.52.+j, 47.11.Bc

### INTRODUCTION

The development of advanced heat-transfer fluids has become imperative as industries demand higher thermal management performance across applications ranging from electronic cooling and energy systems to biomedical devices and chemical processing. Nanofluids are base fluids loaded with suspended nanoparticles offer a promising route for enhancing thermal transport because the inclusion of high-conductivity particles increases the effective thermal conductivity of the mixture. More recently, hybrid nanofluid suspensions containing two or more distinct nanoparticle species have attracted attention because they combine complementary thermal, chemical and rheological attributes of different particles to yield superior heat-transfer and stability characteristics compared with single-component nanofluids. Among hybrid combinations, systems that pair noble metals (e.g., silver, Ag) with metal oxides (e.g., titanium dioxide, TiO<sub>2</sub>) are particularly attractive. Silver imparts exceptionally high thermal and electrical conductivity, while TiO<sub>2</sub> contributes chemical stability, corrosion resistance and cost-effectiveness. The Ag–TiO<sub>2</sub>/water hybrid therefore represents a practical formulation for applications where both enhanced heat transfer and operational robustness are required. However, realistic performance prediction of such fluids requires more than bulk-averaged property estimates. It requires capturing the coupled interaction between momentum, heat and mass transport under operating conditions that often involve large temperature and concentration gradients.

The Casson fluid model, which characterizes yield-stress behavior and shear-thinning dynamics, is widely used to represent fluids whose microstructural deformation affects macroscopic flow examples include blood, polymeric suspensions, and certain high-viscosity industrial fluids. Combining Casson rheology with hybrid nanoparticle suspensions introduces rich, nonlinear coupling between flow resistance, particle transport and thermal behavior that cannot be captured by Newtonian assumptions. Therefore, investigations of Casson hybrid nanofluids are both theoretically significant and practically necessary.

When coupled heat and mass transfer occur, two cross-diffusion phenomena may become important. Soret effect induces mass flux i.e., particles or solutes migrate from hot to cold or vice versa, depending on species specifics. In practical terms, the Soret effect alters concentration fields in the presence of thermal gradients, thereby changing local thermophysical properties and feeding back on flow and heat transfer. Dufour effect induces a heat flux i.e., variations in species concentration drive thermal energy transport. Though often smaller than the direct conductive heat flux, the Dufour effect can modify temperature distributions in systems with strong concentration gradients or significant solutal fluxes.

The two effects are reciprocal manifestations of cross-coupled transport: Soret describes heat driving mass flux; Dufour describes mass flux driving heat. Their relative importance depends on fluid properties, particle size and concentration and the magnitudes of temperature and concentration gradients. In nanoparticle-laden systems especially hybrid formulations with differing particle diffusivities and thermal conductivities Soret and Dufour coupling can appreciably affect Nusselt and Sherwood numbers, boundary-layer structure, and ultimately system performance.

The literature on nanofluid heat and mass transfer is extensive, covering experimental measurements, empirical correlations for effective properties and numerous numerical investigations. Foundational models such as Buongiorno's two-component approach accounted for key microscale transport mechanisms (Brownian diffusion and thermophoresis), and many studies have extended these ideas to hybrid nanofluids, magnetic fields, viscous dissipation and slip conditions. However, several gaps and limitations remain. While there is growing work on hybrid nanofluids, relatively few studies integrate non-Newtonian Casson rheology with hybrid particle systems, particularly with combinations such as Ag–TiO<sub>2</sub> that present strong contrasts in conductivity and diffusivity. Although some investigations account for Soret/Dufour in Newtonian nanofluids or single-particle Casson fluids, the combined influence of both cross-effects in Casson hybrid nanofluids is underexplored. Given the differing particle mobilities and interaction potentials in hybrid suspensions, cross-diffusion coupling may be amplified or altered compared with single-component systems.

Numerical studies frequently assume idealized spherical particles and homogeneous dispersion yet particle morphology (e.g., platelets, rods, aggregates) and real dispersion quality critically affect effective thermal conductivity and viscosity. Experimental efforts that systematically examine the interplay of particle shape, hybrid mixing ratios and cross-diffusion under flowing conditions are limited. Many existing analyses focus on canonical problems do not combine moving boundaries, convective boundary conditions and mixed convection with non-Newtonian rheology conditions typical in industrial processes such as coating, extrusion, and vertical heat exchangers. There is a paucity of system-level analysis that quantifies the trade-off between enhanced heat transfer and increased pumping or process complexity specifically for Casson hybrid formulations with Soret/Dufour effects.

Abdul Aziz [1] derived similarity solution in laminar boundary layer flow over flat plate with convective surface. Yahyaee [2] explored how different nanoparticle shapes affect film boiling on vertical cylinders using numerical simulations. Azad Hussain et al. [3] investigated flow, heat transfer characteristics in magneto hydro dynamic bioconvective carbon nanotubes flow across stretched surface incorporating Dufour and Soret effects. Bhavanam Naga Lakshmi et al. [4] examined three-dimensional rotating HNF flow across linearly stretchable surface including Ag, CuO nano particles with H<sub>2</sub>O as base fluid considering Soret, Dufour effects. Cebeci and Bradshaw [5] described Keller Box implicit finite difference system. RamReddy et al. [6] examined mixed convective heat, mass transport in semi-infinite vertical flat plate within nanofluid taking Soret effect into account. Chundru Maheswari [7] examined MHD hybrid nanofluid, namely MgO – Ag/H<sub>2</sub>O in laminar and steady-state flow over a horizontally positioned thin needle that can move same or opposite direction to free stream, employing shooting method, taking into account thermophoresis parameter, Brownian motion effects. Eleni Seid et al. [8] conducted mathematical investigation of combined slip, Soret, Dufour effects in electrically conducting nanofluid flow across vertically extending sheet.

Isa et al. [9] analyzed water-based hybrid nanofluid, including alumina (Al<sub>2</sub>O<sub>3</sub>), copper (Cu) nanoparticles in two-dimensional mathematical model. Iskandar Waini [10] investigated consistent mixed convection flow along vertical porous surface containing hybrid nanoparticles. J. Jayaprakash et al. [11] elucidated Maxwell nanofluid flow across linearly stretched porous sheet accounting for interactions with mixed convection, Dufour, Soret numbers. Kavita Jat et al. [12] examined Soret and Dufour impacts on magnetohydrodynamic hybrid nanofluids across nonlinear stretched sheet. Balamurugan et al. [13] examined convective electrically conducting Newtonian fluid flow over inclined heated porous plate. Minea Alina [14] proposed numerical assessment on three oxide-based nanofluids and their hybrids. Mansour and Bakier [15] conducted an experiment on mixed convection heat, mass transfer utilizing finite difference approach within porous saturated cavity influenced by dual-moving lid and heat sources.

Sheikholeslami [16] studied nanoparticle shape effects in forced convective nanofluid in constant magnetic field. Sreedhar et al. [17] examined convective heat, mass transfer effects in wedge-shaped flows inside nanofluids. Veera Krishna et al. [18] studied radiative unsteady non-Newtonian Casson hybrid nanofluid across porous surface with infinite exponential acceleration, driven by slip velocity in rotating frame. Nor Alifah Rosaidi et al. [19] examined aligned magnetohydrodynamic nanofluid convective flow across plate moving vertically. Norsyasya Zahirah et al. [20] investigated nanoparticle influence morphologies on Casson hybrid nanofluid flow across moving vertical plate. Noreen and Adil [21] considered Cu–water nanofluid flow with different shaped nanoparticles. Zainal et al. [22] examined steady MHD stagnation point nanofluid flow along flat convective plate. P. Chandrakala [23] studied hybrid nanofluid flow across sheet that expands exponentially, using heat source, sink. Ruchi Jain et al. [24] investigated on Williamson hybrid fluid flow utilizing single, multi-wall carbon nanotubes combined with CuO and water examining effects of Hall effect, Soret, Dufour effect over porous stretching or shrinking lamina with suction, injection. Sahar Goudarzi et al. [25] examined how Brownian motion, thermophoresis affect nanoparticles movement in Ag-MgO/Water hybrid nanofluid. S.A.M. Mehryan et al. [26] examined Aluminium Oxide - Copper water nanofluid within free convective heat transport porous cavity. S. Hussain et al. [27] statistically explored entropy production resulting from partly heated square double lid-driven cavity filled with Aluminium Oxide -water nano fluid under inclined magnetic field. Anwar et al [28]



formulated two various fractional models to explain flow patterns, thermal behavior in sodium alginate (NaAlg/SA) based hybrid nanofluid. Khaleque [29] studied convective flow in mixed power-law fluid over continuously stretched surface.

This study examines Soret, Dufour effects on Casson hybrid nanofluid (Ag-TiO<sub>2</sub>/Water) in relation to moving vertical plate. Silver (Ag) and titanium dioxide (TiO<sub>2</sub>) were incorporated into water-based fluid for this study. Similarity transformation techniques are employed to translate PDE's into ODE's subsequently solved numerically using Keller Box method. This study also examines several nanoparticle geometries impact on velocity, temperature, concentration profiles. Furthermore, quantitative results are examined, tabulated, graphically represented considering various non-dimensional parameters. By analyzing the role of nanoparticle morphology and thermal conductivity, the study aims to provide insights into how hybrid nanofluids can be used for optimal performance in industrial applications.

## MATHEMATICAL FORMULATION

Rheological formula for Casson hybrid nanofluids with isotropic and incompressible flow is:

$$\tau_{ij} = \begin{cases} (\mu_B + p_y/\sqrt{2\pi})2e_{ij} & , \pi > \pi_c \\ (\mu_B + p_y/\sqrt{2\pi_c})2e_{ij}, & \pi < \pi_c \end{cases}$$

where  $\mu_B$  is non-Newtonian fluid's dynamic viscosity,  $p_y$  is yield stress,  $\pi_c$  is critical value based on non-Newtonian model, Plate is assumed to move at constant velocity  $U_w = \lambda U_\infty$ , where  $U_w$ ,  $\lambda$  being plate velocity, its parameter respectively.

Aligned magnetic field with acute angle,  $\alpha$  as shown in Figure 1 is applied to flow. It is recognized as origin function, expressed by  $B(x) = \frac{B_0}{\sqrt{x}}$  with  $B_0 \neq 0$ .

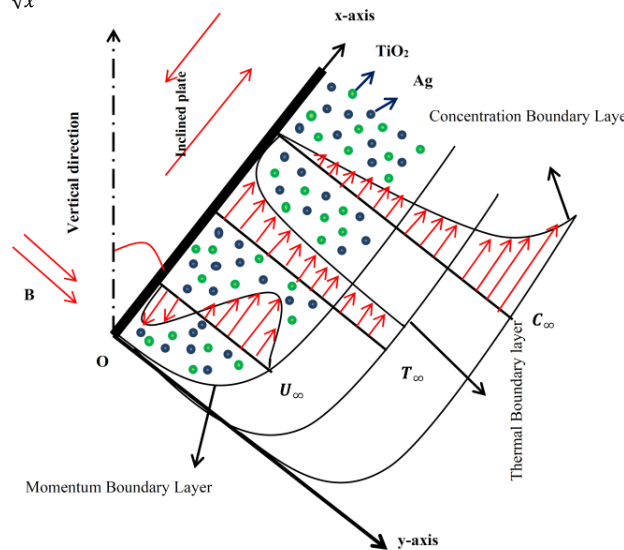


Figure 1. Physical model of Problem

Magnetic field intensity is denoted by  $B_0$ , (x,y) represents coordinates along plate. Assuming stable two-dimensional boundary layer flow, following governing equations developed as:

$$u_x + v_y = 0 \quad (1)$$

$$uu_x + vv_y = \frac{\mu_{hnf}}{\rho_{hnf}} \left(1 + \frac{1}{\beta}\right) \frac{\partial^2 u}{\partial y^2} + \frac{(\rho\beta)_{hnf}}{\rho_{hnf}} g(T - T_\infty) + \frac{(\rho\beta)_{hnf}}{\rho_{hnf}} g(C - C_\infty) - \frac{\sigma B_0^2(x) \sin^2 \alpha (u - U_\infty)}{\rho_{hnf}} \quad (2)$$

$$uT_x + vT_y = \alpha_{hnf} T_{yy} - \frac{1}{(\rho C_p)} (q_r)_y + \tau \left[ D_B C_y T_y + \frac{D_T}{T_\infty} (T_y)^2 \right] + \frac{D_T K_T}{C_s C_p} C_{yy} \quad (3)$$

$$uC_x + vC_y = D_m C_{yy} + \frac{D_T K_T}{T_\infty} T_{yy} \quad (4)$$



**Boundary conditions:**

$$\left. \begin{aligned} u = u_w = \lambda U_\infty, v = 0, k_{hnf} \frac{\partial T}{\partial y} = h_f (T - T_\infty), D_m \frac{\partial C}{\partial y} = h_m (C - C_\infty) \text{ at } y = 0, \\ u \rightarrow 0, T \rightarrow T_\infty, C \rightarrow C_\infty \text{ as } y \rightarrow \infty \end{aligned} \right\} \quad (5)$$

where  $u, v$  indicates velocity components along  $x, y$ -axis,  $\alpha$  is inclined magnetic field,  $T, T_f$  is the temperature of fluid, nanofluid,  $U_\infty, T_\infty, C_\infty$  denotes free stream velocity, temperature, concentration respectively.  $g$  is gravity,  $\rho_{hnf}$  is effective density,  $\sigma$  is electrical conductivity,  $(\rho\beta)_{hnf}$  is thermal expansion coefficient,  $\mu_{hnf}$  is effective dynamic viscosity,  $\alpha_{hnf}$  is fluid's thermal diffusivity,  $(\rho C_p)_{hnf}$  is fluid's heat capacity,  $k_{hnf}$  is thermal conductivity (hybrid nanofluids),  $M$  is magnetic parameter,  $h_f$  is heat transfer coefficient ( $h_f = \frac{c}{\sqrt{x}}$ ,  $c$  is a constant),  $h_m$  is mass transfer coefficient of fluid,  $D_B$  is Brown dissemination coefficient,  $D_T$  is heat dispersion coefficient,  $D_m$  is mass diffusivity and  $\beta$  is the Casson hybrid nanofluid parameter.

Rosseland approximation for radiative heat flow  $q_r = -\frac{4\sigma^*}{3k^*} \frac{\partial T^4}{\partial y}$  where  $(\sigma)$ ,  $k^*$  being Stefan-Boltzman constant, absorption coefficient respectively.

Considering temperature function as  $T^4$  given by  $T^4 \cong 4T_\infty^3 T - 3T_\infty^4$ , the equation (3) becomes

$$uT_x + vT_y = \alpha T_{yy} - \frac{16\sigma T_\infty^3}{3(\rho C_p)_{hnf} k^*} T_{yy} + \tau \left[ D_B C_y T_y + \frac{D_T}{T_\infty} (T_y)^2 \right] + \frac{D_T K_T}{C_s C_p} C_{yy} \quad (6)$$

Introducing stream function  $\psi(x, y)$  as shown below

$$u = \frac{\partial \psi}{\partial y}, v = -\frac{\partial \psi}{\partial x}$$

Following similarity variables are introduced as in Zukri et al. [20] to solve above equations

$$\left. \begin{aligned} \zeta = \frac{y}{x} \sqrt{\text{Re}_x}, \psi(x, y) = v_f \sqrt{\text{Re}_x} f(\zeta), \\ \theta = \frac{T - T_\infty}{T_w - T_\infty}, \phi = \frac{C - C_\infty}{C_w - C_\infty} \end{aligned} \right\} \quad (7)$$

where  $\zeta$  is similarity variable,  $\text{Re}_x = \frac{U_\infty x}{\nu_f}$  refers to Reynolds number,  $\nu_f = \frac{\mu_f}{\rho_f}$  is kinematic viscosity.

Various forms possess distinct numerical shape factors. This shape factor ascertains suitability of shape concerning the nanoparticles. The shape factor, denoted as  $m$  in Table 1, together with its numerical values for various forms, is shown in Table 3. The shape factor,  $m=3/Z$ , should be acknowledged, where  $Z$  represents sphericity. Sphericity being sphere's surface area ratio to particles' surface area with equivalent volumes. Sphericity values for sphere, platelet, cylinder, brick are 1.000, 0.526, 0.625, 0.811, respectively.

**Table 1.** Thermophysical Relation in Nanoparticles Shape of Hybrid Nanofluids





Properties	Hybrid Nanofluids
Density	$\rho_{hnf} = (1 - \phi_2)[(1 - \phi_1)\rho_f + \phi_1\rho_{s1}] + \phi_2\rho_{s2}$
Heat Capacity	$(\rho C_p)_{hnf} = (1 - \phi_2)[(1 - \phi_1)(\rho C_p)_f + \phi_1(\rho C_p)_{s1}] + \phi_2(\rho C_p)_{s2}$
Viscosity	$\mu_{hnf} = \frac{\mu_f}{(1 - \phi_1)^{2.5}(1 - \phi_2)^{2.5}}$
Electrical Conductivity	$\sigma_{hnf} = \frac{(\sigma_{s2} + 2\sigma_{nf}) - 2\phi_2(\sigma_{nf} - \sigma_{s2})}{(\sigma_{s2} + 2\sigma_{nf}) + \phi_2(\sigma_{nf} - \sigma_{s2})} \times \frac{(\sigma_{s1} + 2\sigma_f) - 2\phi_1(\sigma_f - \sigma_{s1})}{(\sigma_{s1} + 2\sigma_f) + \phi_1(\sigma_f - \sigma_{s1})} (\sigma_f)$

Properties	Hybrid Nanofluids
Thermal Conductivity	$\frac{k_{hnf}}{k_{bf}} = \frac{k_{s2} + (m-1)k_{bf} - (m-1)\phi_2(k_{bf} - k_{s2})}{k_{s2} + (m-1)k_{bf} - \phi_2(k_{bf} - k_{s2})}$
	$\frac{k_{bf}}{k_f} = \frac{k_{s1} + (m-1)k_f - (m-1)\phi_1(k_f - k_{s1})}{k_{s1} + (m-1)k_f - \phi_1(k_f - k_{s1})}$
	$k_{bf} = \frac{k_{s1} + (m-1)k_f - (m-1)\phi_1(k_f - k_{s1})}{k_{s1} + (m-1)k_f - \phi_1(k_f - k_{s1})} \times k_f$
	$\frac{k_{hnf}}{k_f} = \frac{k_{hnf}}{k_{bf}} \times \frac{k_{bf}}{k_f} = \frac{k_{s2} + (m-1)k_{bf} - (m-1)\phi_2(k_{bf} - k_{s2})}{k_{s2} + (m-1)k_{bf} - \phi_2(k_{bf} - k_{s2})} \times \frac{k_{s1} + (m-1)k_f - (m-1)\phi_1(k_f - k_{s1})}{k_{s1} + (m-1)k_f - \phi_1(k_f - k_{s1})}$

**Table 2.** Thermophysical Properties of Base Fluid and Nanoparticles

Properties	Base Fluid (Water)	Ag (Silver)	TiO <sub>2</sub> (Titanium Oxide)
$\rho(\text{kg/m}^3)$	997.1	10500	4250
$C_p(\text{J/kgK})$	4179	235	686.2
$k(\text{W/mk})$	0.613	429	8.9538

**Table 3.** Nanoparticles Shape Factors (m)

Nanoparticles Shape	Shapes	Shape Factor (m)	Sphericity (Z)
Spherical		3.0	1.000
Platelets		5.7	0.526
Cylindrical		4.8	0.625
Bricks		3.7	0.811

Following non-linear ODE's result from substituting Eq. (7) into Eqs. (2),(4)

$$\left(1 + \frac{1}{\beta}\right) f''' + A_1 (ff'' + \gamma\theta + \delta\phi) - A_6 A_4 M \sin^2 \alpha (f' - 1) = 0, \quad (8)$$

$$\left(A_5 + \frac{4}{3} Rd\right) \theta'' + Pr A_3 (N_b \theta' \phi' + N_t \theta'^2 + Du \phi'' + f \theta') = 0, \quad (9)$$

$$\phi'' + ScSr \theta'' + Scf \phi' = 0. \quad (10)$$

Transformed boundary conditions:

$$\left. \begin{aligned} f(0) = 0, f'(0) = \lambda, \theta'(0) = \frac{-k_f}{k_{hnf}} \Omega (1 - \theta(0)), \phi'(0) = -Bs (1 - \phi(0)) \text{ as } \zeta = 0, \\ f'(\zeta) \rightarrow 1, \theta(\zeta) \rightarrow 0, \phi(\zeta) \rightarrow 0 \text{ as } \zeta \rightarrow \infty \end{aligned} \right\} \quad (11)$$

where:

$$\gamma = \text{Thermal Buoyancy parameter} = \frac{Gr_x}{Re_x^2}, \quad Gr_x = \frac{g \beta_{hnf} (T_w - T_\infty) x^3}{\nu_f^2}$$

$$\delta = \text{Solutal Buoyancy parameter} = \frac{G_{cx}}{Re_x^2}, \quad G_{cx} = \frac{g\beta_{hnf}(C_w - C_\infty)x^3}{v_f^2}$$

$$M = \text{Magnetic parameter} = \frac{B_0^2 \sigma_f}{U_\infty \rho_f}$$

$$Pr = \text{Prandtl number} = \frac{v_f(\rho C_p)_f}{k_f}$$

$$Rd = \text{Radiation parameter} = \frac{4\sigma T^3}{k_f k^*}$$

$$N_b = \text{Brownian motion Parameter} = \frac{\tau D_B(C_w - C_\infty)}{v_f}$$

$$N_t = \text{Thermophoresis Parameter} = \frac{\tau D_B(T_w - T_\infty)}{v_f T_\infty}$$

$$Du = \text{Dufour number} = \frac{D_T K_T (C_w - C_\infty)}{v_f C_S C_p (T_w - T_\infty)}$$

$$Sr = \text{Soret number} = \frac{D_T K_T (T_w - T_\infty)}{v_f T_\infty (C_w - C_\infty)}$$

$$\Omega = \text{Thermal Biot number} = \frac{h_f}{k_f} \sqrt{\frac{v_f}{U_\infty}}$$

$$Bs = \text{Solutal Biot number} = \frac{h_s}{(D_m)_f} \sqrt{\frac{v_f}{U_\infty}}$$

$$Sc = \text{Schmidt number} = \frac{v_f}{D_m}$$

$$A_1 = \left( \frac{\rho_{hnf}}{\rho_f} \right) = \left( (1-\phi_2) \left[ (1-\phi_1) + \phi_1 \frac{\rho_{s1}}{\rho_f} \right] + \phi_2 \frac{\rho_{s2}}{\rho_f} \right) * \left( (1-\phi_1)^{2.5} (1-\phi_2)^{2.5} \right)$$

$$A_2 = \left( \frac{\rho_{hnf}}{\rho_f} \right) = \left( (1-\phi_2) \left[ (1-\phi_1) + \phi_1 \frac{\rho_{s1}}{\rho_f} \right] + \phi_2 \frac{\rho_{s2}}{\rho_f} \right)$$

$$A_3 = \left( \frac{(\rho C_p)_{hnf}}{(\rho C_p)_f} \right) = \left( (1-\phi_2) \left[ (1-\phi_1) + \phi_1 \frac{(\rho C_p)_{s1}}{(\rho C_p)_f} \right] + \phi_2 \frac{(\rho C_p)_{s2}}{(\rho C_p)_f} \right),$$

$$A_4 = \left( \frac{\mu_f}{\mu_{hnf}} \right) = \left( (1-\phi_1)^{2.5} (1-\phi_2)^{2.5} \right)$$

$$A_5 = \frac{k_{hnf}}{k_f} = \left( \frac{k_{s2} + (m-1)k_{bf} - (m-1)\phi_2(k_{bf} - k_{s2})}{k_{s2} + (m-1)k_{bf} - \phi_2(k_{bf} - k_{s2})} * \frac{k_{s1} + (m-1)k_f - (m-1)\phi_1(k_f - k_{s1})}{k_{s1} + (m-1)k_f - \phi_1(k_f - k_{s1})} \right)$$

$$A_6 = \frac{\sigma_{hnf}}{\sigma_f} = \left( \frac{\sigma_{s2}(1+2\phi_2) + 2\sigma_f(1-\phi_2)}{\sigma_{s2}(1-\phi_2) + \sigma_f(2+\phi_2)} * \frac{\sigma_{s1}(1+2\phi_1) + 2\sigma_f(1-\phi_1)}{\sigma_{s1}(1-\phi_1) + \sigma_f(2+\phi_1)} \right)$$

Skin friction coefficient  $Cf_x$ , Heat Transfer Coefficient  $Nu_x$ , Sherwood number  $Sh_x$  defined as

$$Cf_x = \frac{\tau_w}{\rho_f u_w^2}, \quad Nu_x = \frac{xq_w}{k_f(T_w - T_\infty)}, \quad Sh_x = \frac{xq_m}{D_B(C_w - C_\infty)}$$

$$\tau_w = \mu_{hnf} \left( 1 + \frac{1}{\beta} \right) \left( \frac{\partial u}{\partial y} \right)_{y=0}, \quad q_w = -k_{hnf} \left( \frac{\partial T}{\partial y} \right)_{y=0} + (q_r)_{y=0}, \quad q_m = -D_B \left( \frac{\partial C}{\partial y} \right)_{y=0}$$

$$q_w = -k_{mf} \left( \frac{\partial T}{\partial y} \right)_{y=0} + \frac{4\sigma}{3k^*} \frac{\partial T^4}{\partial y},$$

$$Re_x^{1/2} Cf_x = \left( 1 + \frac{1}{\beta} \right) \left( \frac{f''(0)}{A_4} \right) \quad (12)$$

$$Re_x^{-1/2} Nu_x = - \left( A_5 + \frac{4}{3} Rd \right) \theta'(0) \quad (13)$$

$$Re_x^{-1/2} Sh_x = -\phi'(0) \quad (14)$$

where  $Re_x$  is local Reynold's number given by  $Re_x = \frac{U_\infty x}{\nu_f}$

### NUMERICAL PROCEDURE

To numerically solve the equations according to the boundary conditions, Cebeci and Bradshaw [5] devised an implicit finite difference approach. The necessary actions are as follows:

1. First order equation is created from the converted equations.
2. Central differences are used to write difference equations.
3. Consequently, an algebraic equation is formulated, linearized using Newton's method which is represented as matrix equation.
4. Using Block tri-diagonal elimination approach linear systems is resolved.

Introducing  $f' = p$ ,  $p' = q$ ,  $\theta' = t$ ,  $\phi' = n$

Equations (8),(9), (10) reduced to

$$q' + \left( \frac{\beta}{1+\beta} \right) \left( A_1 (fq + \gamma\theta + \delta\phi) - A_6 A_4 M \sin^2 \alpha (p-1) \right) = 0 \quad (15)$$

$$\theta'' + \left( \frac{3Pr A_3}{3A_5 + 4Rd} \right) \left( N_b t n + N_t t^2 + Duf n' + ft \right) = 0 \quad (16)$$

$$n' + Sc Srt' + Scfn = 0 \quad (17)$$

Boundary conditions:

$$\left. \begin{aligned} f = 0, p = \lambda, \Omega(1-\theta) = -A_5 t, Bs(1-\phi) = -nas\zeta \rightarrow 0 \\ p \rightarrow 1, \theta \rightarrow 0, \phi \rightarrow 0 as \zeta \rightarrow \infty \end{aligned} \right\} \quad (18)$$

### RESULTS AND DISCUSSION

Keller Box Method in Matlab numerically enumerates solutions to non-linear ordinary differential equations. To achieve most precise results, it is essential to select and meticulously tune proper initial assumptions optimal boundary layer thickness and various parameter values inside the coding function which covers several variable ranges, including Casson fluid, magnetic fields, buoyancy, thermophoresis, Brownian motion, radiation parameters and Prandtl numbers.

**Table 4.** Comparing  $\theta(0)$ ,  $-\theta'(0)$  results for different Biot number values when  $M = 0$ ,  $\gamma = 0.5$

$\Omega$	Pr = 0.1				Pr = 0.72			
	Aziz[1]		Present study		Aziz[1]		Present study	
	$\theta(0)$	$-\theta'(0)$	$\theta(0)$	$-\theta'(0)$	$\theta(0)$	$-\theta'(0)$	$\theta(0)$	$-\theta'(0)$
5	0.9714	0.1430	0.9703	0.1421	0.9441	0.2791	0.9301	0.2672
10	0.9855	0.1450	0.9848	0.1446	0.9713	0.2871	0.9699	0.2821
20	0.9927	0.1461	0.9928	0.1467	0.9854	0.2913	0.9846	0.2905

To establish the accuracy of our numerical scheme, we first validated our results against the benchmark similarity solution of Aziz [1] for convective boundary-layer flow with constant fluid properties. Table 4 compares surface

temperature  $\theta(0)$  and wall heat transfer rate  $-\theta'(0)$  for varying Biot numbers at  $M = 0, \gamma = 0.5$ . Excellent agreement is obtained across all cases, thereby confirming the reliability of the Keller Box method employed in this study.

While Aziz [1] restricted attention to Newtonian fluids with constant viscosity and thermal conductivity, the present work extends the formulation in several crucial directions. Unlike Newtonian models, our framework accounts for yield-stress behavior, which is essential in biological and industrial fluids. The combined effects of metal and metal-oxide nanoparticles on transport properties are explored for the first time under cross-diffusion conditions. Our model includes coupled heat-mass transfer phenomena, absent in Aziz's baseline study, which significantly modify thermal and solutal boundary-layer structures. The inclusion of Joule heating, chemical reaction, Brownian motion and variable viscosity/thermal conductivity enables a more realistic representation of actual industrial and biomedical processes.

Certain nanoparticle shapes alter the effective viscosity and flow micro-structure, reducing the momentum boundary layer shear at the surface. The Casson fluid model's shear-thinning property means that with more aligned or elongated nanoparticle shapes, the local resistance to flow can decrease under shear, reducing skin friction.

Increase in heat transfer coefficient depends on thermal conductivity and convective heat transport near wall. Nanoparticle shapes that increase surface area and thermal pathways (e.g., TiO<sub>2</sub> platelets or Ag elongated particles) enhance effective thermal conductivity of nanofluid. Combined with fluid motion either opposing or aiding flow, this increases temperature gradient at wall, raising heat transfer rates.

Figures 2, 3 show skin friction coefficient decreases due to reduction in effective wall shear stress caused by nanoparticle shapes altering the fluid's microstructure and shear-thinning behavior of Casson hybrid nanofluid, especially under relative motion of plate, while heat transfer coefficient increases because these nanoparticle shapes enhance effective thermal conductivity and thermal gradients, improving convective heat transfer despite moving plate conditions.

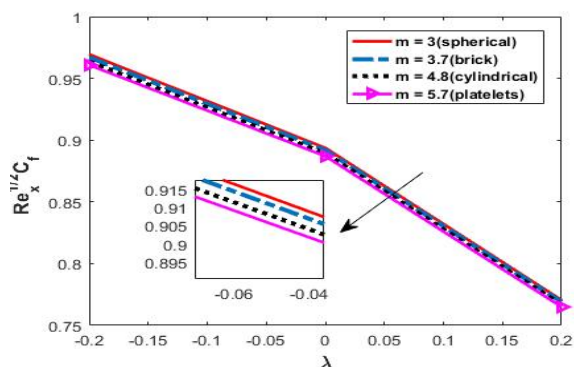


**Figure 2.** Skin friction coefficient distribution with variations in  $m$  and  $\lambda$

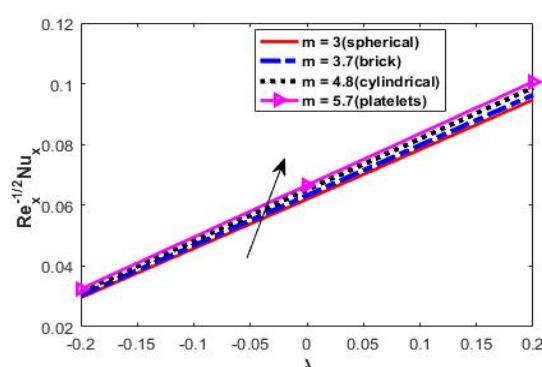


**Figure 3.** Heat transfer coefficient distribution with variations in  $m$  and  $\lambda$

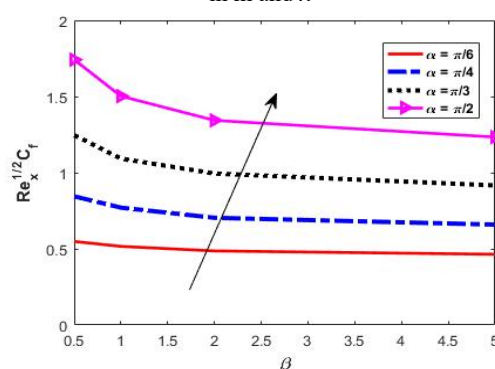


**Figure 4.** Skin friction coefficient distribution with variations in  $\alpha$  and  $\beta$

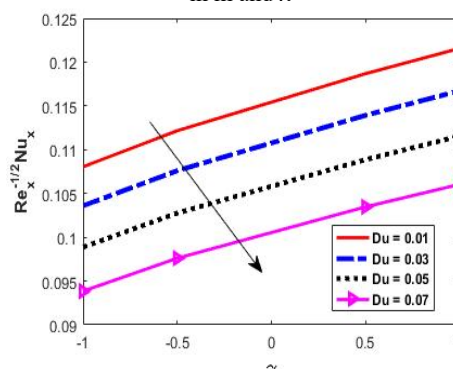


**Figure 5.** Heat transfer coefficient distribution with variations in  $\gamma$  and  $Du$

In Casson hybrid nanofluids containing silver (Ag) and titanium dioxide (TiO<sub>2</sub>) in water, combined effect of an inclined magnetic field, Casson parameter on skin friction coefficient is significant. Figure 4 shows that both parameters contribute to increasing the skin friction. Magnetic field, through Lorentz force, enhances resistance to flow, while Casson parameter, by altering the fluid's rheological properties towards a more Newtonian-like behavior, also increases shear stress at the wall. Numerical studies on Casson hybrid nanofluids often show that the skin friction coefficient increases as these parameters rise. This combined effect underscores the intricate relationship between external fields, fluid rheology and nanoparticle properties in determining the flow characteristics of such complex fluids.

Increasing thermal buoyancy ( $\gamma$ ) or Dufour number adds extra velocity into the boundary layer, making it thicker and less steep near the wall, thereby lowering the wall temperature gradient and reducing the heat transfer coefficient distribution as shown in Figure 5.

When buoyant forces resulting from heat or concentration gradients are substantial, the inclined magnetic field can interact with these forces to augment flow velocity. Tilt of magnetic field can modify direction, intensity of buoyancy-driven flows, occasionally resulting in enhanced convective currents and elevated velocity profiles as shown in Figure 6. Figure 7 shows that temperature profiles diminish with a rise in the inclined magnetic field, since the magnetic field inhibits fluid mobility, hence decreasing convective heat transfer and leading the fluid to retain less thermal energy at heated surface. Inclined magnetic field often inhibits nanoparticle motion, diminishing thickness of concentration boundary layer and decreasing concentration profiles shown in Figure 8.

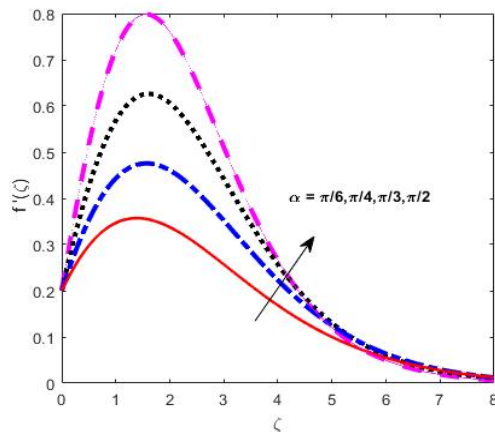


Figure 6. Velocity  $f'(\zeta)$  versus  $\alpha$

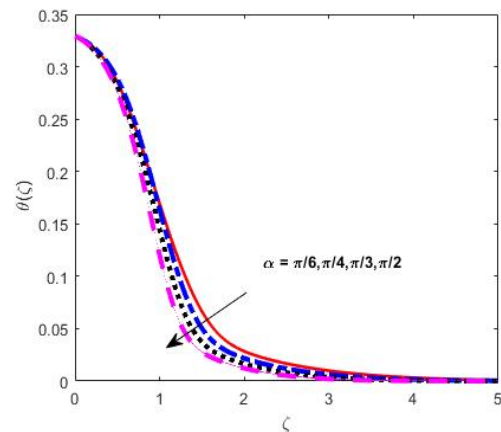


Figure 7. Temperature  $\theta(\zeta)$  versus  $\alpha$

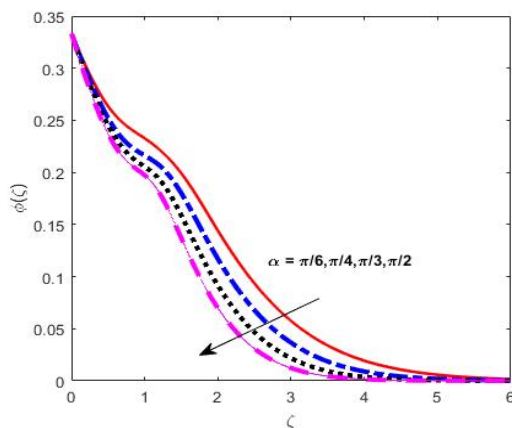


Figure 8. Concentration  $\phi(\zeta)$  versus  $\alpha$

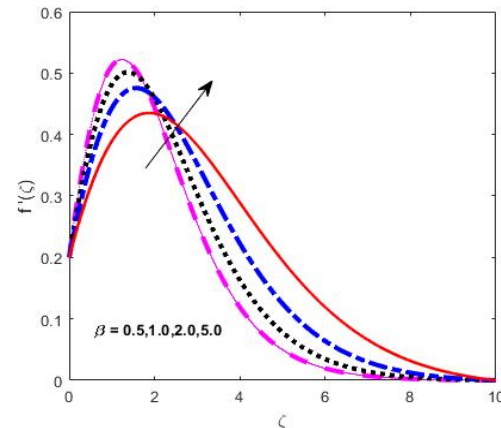


Figure 9. Velocity  $f'(\zeta)$  versus  $\beta$

Figure 9 demonstrates that elevating Casson parameter often diminishes fluid velocity next to the channel walls, owing to the augmented fluid yield stress that impedes flow start and lessens velocity gradients at the boundaries. The reduction in temperature profiles with an increasing Casson parameter as shown in Figure 10, is mostly attributed to augmented flow resistance and diminished convective heat transfer caused by the fluid's non-Newtonian rheology. Figure 11 shows the diminished nanoparticle concentration profiles adjacent to the walls, as the fluid's augmented resistance to flow restricts mass transfer and curtails nanoparticle movement into boundary layers.

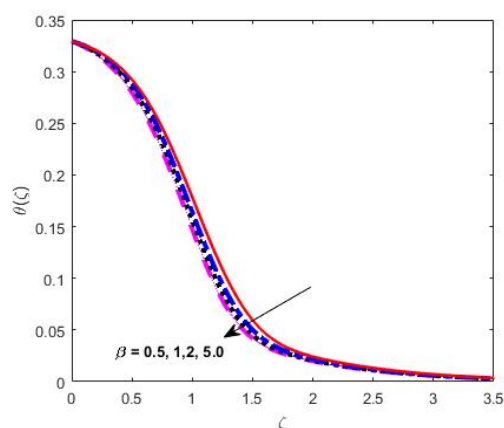


Figure 10. Temperature  $\theta(\zeta)$  versus  $\beta$

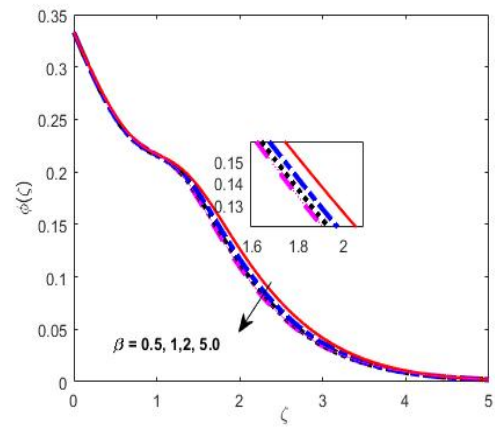


Figure 11. Concentration  $\phi(\zeta)$  versus  $\beta$



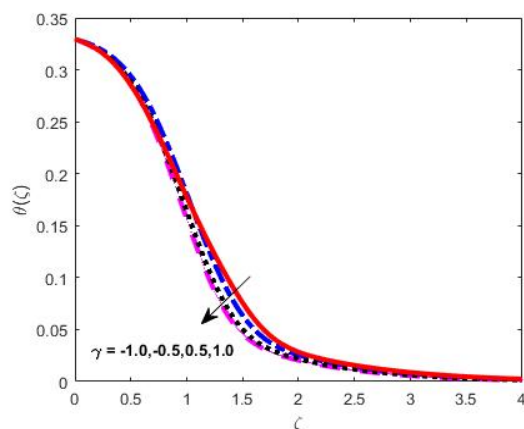
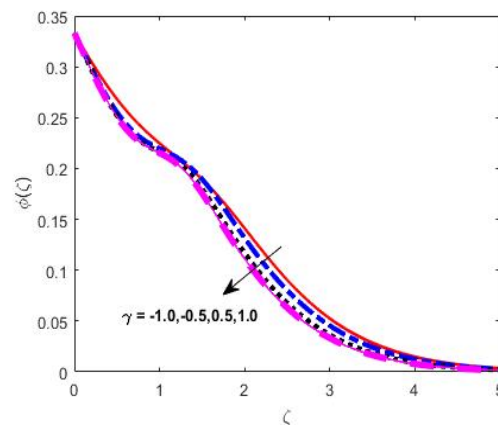
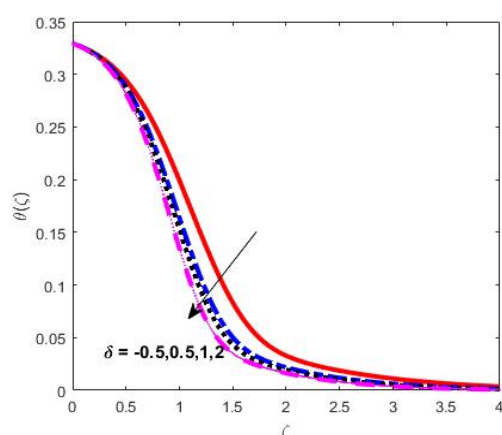
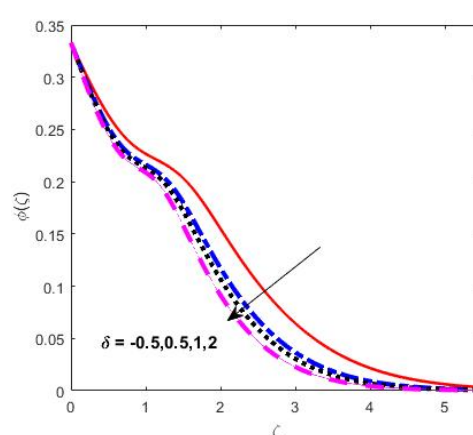
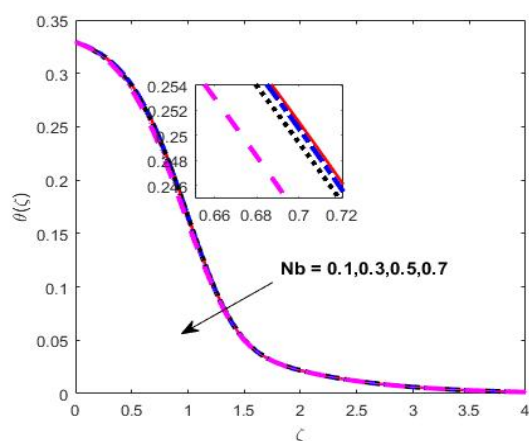
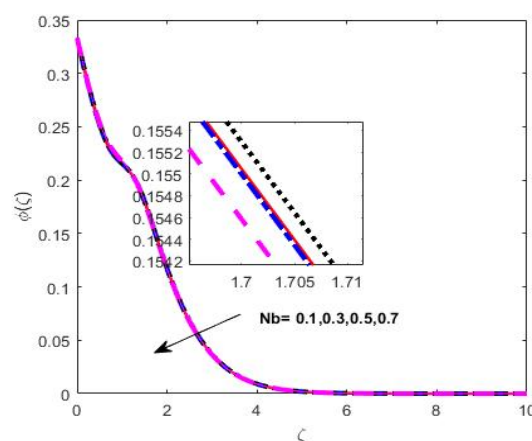
Figure 12. Temperature  $\theta(\zeta)$  versus  $\gamma$ Figure 13. Concentration  $\phi(\zeta)$  versus  $\gamma$ Figure 14. Temperature  $\theta(\zeta)$  versus  $\delta$ Figure 15. Concentration  $\phi(\zeta)$  versus  $\delta$ 

Figure 12 shows a counterintuitive decrease in temperature profile with higher thermal buoyancy parameter in Casson hybrid nanofluids with Ag and TiO<sub>2</sub> arises mainly due to enhanced natural convection and fluid mixing that accelerate heat removal from heated surfaces, thinning the thermal boundary layer and reducing local temperatures near those surfaces. The concentration profile typically shows a decrease as shown in Figure 13, with increasing thermal buoyancy parameter as the enhanced upward movement of fluid transports nanoparticles and dissolved substances away from heated surfaces, thinning the concentration boundary layer.

The temperature profile typically declines as the solutal buoyancy parameter increases, since enhanced solutal buoyancy intensifies mixing and convective transport, hence diminishing heat gradients near the surface, the reduction in concentration profiles with an increasing solutal buoyancy parameter as shown in Figures 14 and 15, results from intensified buoyancy forces that augment convective mass transfer away from wall, thereby diminishing nanoparticle concentration in boundary layer of the Casson hybrid nanofluid comprising silver and TiO<sub>2</sub> in water.

Figure 16. Temperature  $\theta(\zeta)$  versus NbFigure 17. Concentration  $\phi(\zeta)$  versus Nb

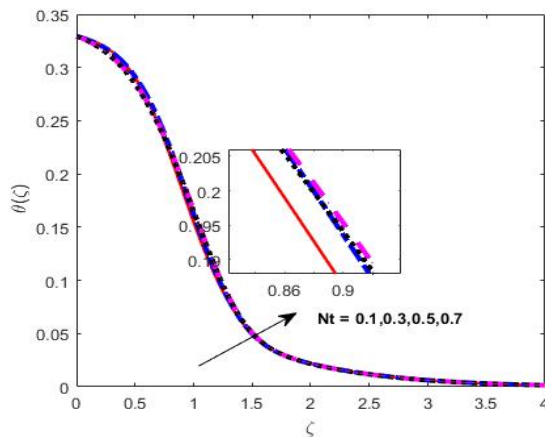


Figure 18. Temperature  $\theta(\zeta)$  versus  $Nt$

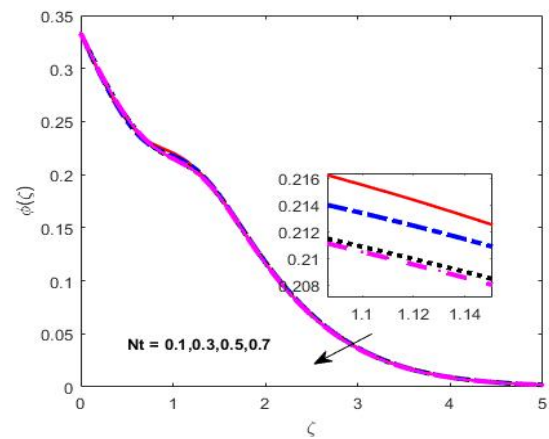


Figure 19. Concentration  $\phi(\zeta)$  versus  $Nt$

Figure 16, 17 demonstrates temperature, concentration profiles decrease with increasing Brownian motion parameter as its enhancement intensifies nanoparticle diffusion, which reduces the concentration gradient by dispersing nanoparticles more effectively. This also disturbs thermal boundary layer by increasing heat dispersion, decreasing effective nanoparticle concentration near the surface, leading to thinner thermal, concentration boundary layers in Casson hybrid nanofluid containing Ag and  $\text{TiO}_2$  nanoparticles suspended in water.

Figure 18 shows that as the thermophoresis parameter increases, temperature profiles rise due to enhanced thermal transport mechanisms within the hybrid nanofluid. This increase in temperature promotes greater kinetic energy among the particles. Conversely, the concentration profiles decrease because thermophoretic effect causes particles to migrate away from higher temperature regions leading to reduction in concentration as shown in Figure 19.

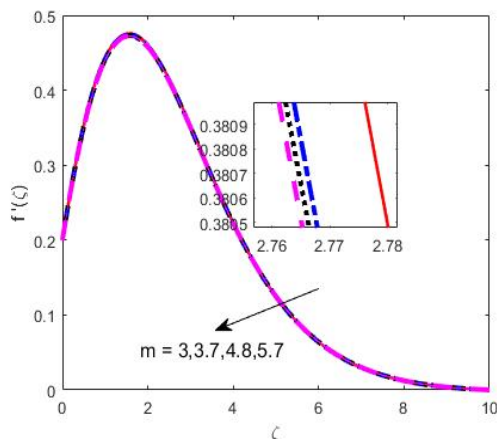


Figure 20. Velocity  $f'(\zeta)$  versus  $m$

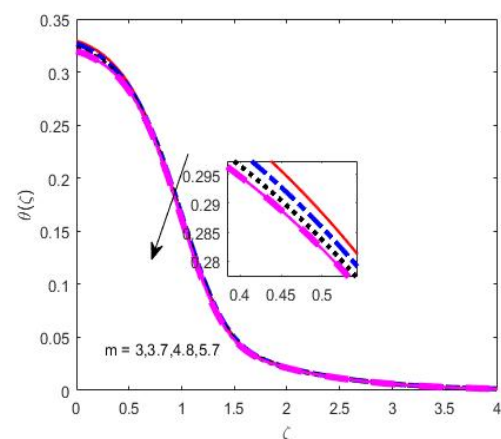


Figure 21. Temperature  $\theta(\zeta)$  versus  $m$

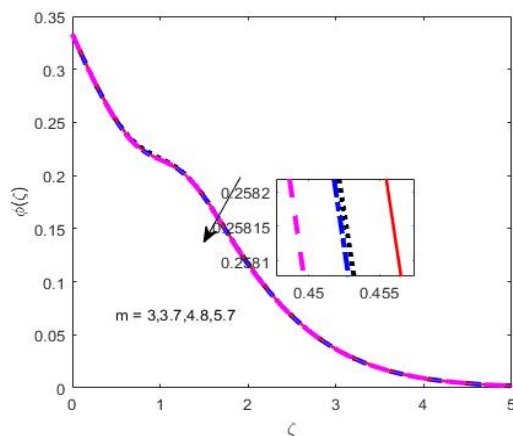


Figure 22. Concentration  $\phi(\zeta)$  versus  $m$

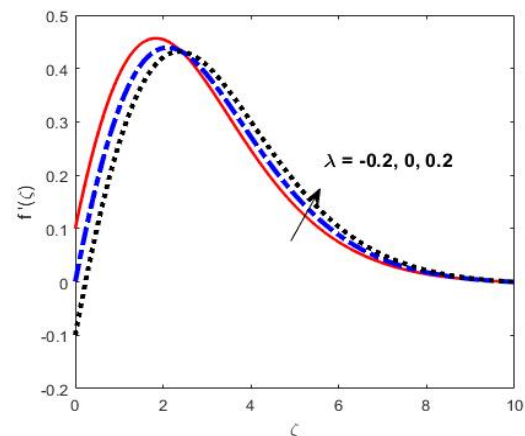


Figure 23. Velocity  $f'(\zeta)$  versus  $\lambda$

Figures 20, 21 and 22 demonstrates the influence of nanoparticle shape factor. Increasing nanoparticle shape factor in Ag- $\text{TiO}_2$  hybrid nanofluids increases viscosity and flow resistance. These effects lower fluid velocity profiles,

especially at solid boundaries or surfaces where particle-fluid interactions and viscous forces are most significant. Complex flow dynamics, such as magnetic field impacts and boundary layer alterations, further reduce velocity. Hybrid nanofluid temperature profiles drop as nanoparticle shape factor rises, reaching a minimum and then slightly rising for disk nanoparticles. Thermal disturbance and heat transmission are better in spherical nanoparticles. Blade-shaped nanoparticles transmit heat fastest, followed by cylindrical, platelet, brick, and spherical forms. Because nanoparticle morphology improves dispersion and convective mass transfer, Ag-TiO<sub>2</sub> hybrid nanofluid concentration profiles drop with nanoparticle shape factor. More uniform nanoparticle dispersion, thinner boundary layer, and smaller local concentration peaks result. This behavior is governed by micro-convection, fluid mixing, viscosity variations, and shape-factor-driven thermophoretic mass flow.

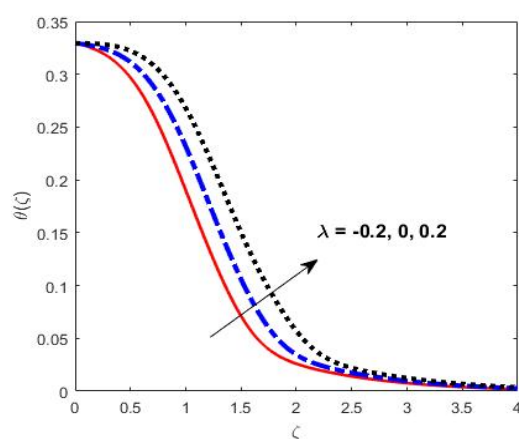


Figure 24. Temperature  $\theta(\zeta)$  versus  $\lambda$

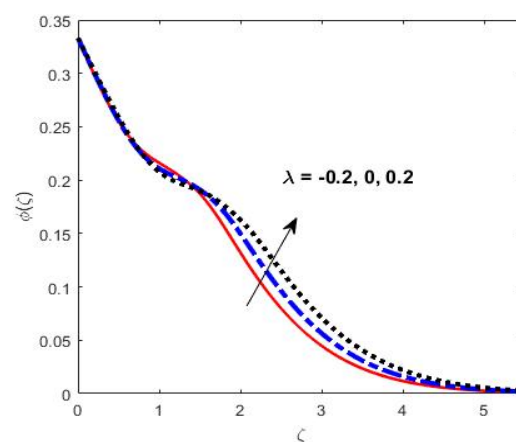


Figure 25. Concentration  $\phi(\zeta)$  versus  $\lambda$

Figures 23, 24 and 25 demonstrates the effect of moving plate parameter. The momentum boundary layer thickens as the plate moves in the flow direction, while velocity profiles drop as it goes against the flow. Convective heat transfer from the moving plate raises nearby temperatures. Increasing nanoparticle dispersion with parameters like thermophoresis raises temperature. Nanoparticle transport increases mass diffusion and thins the concentration boundary layer with plate motion in the flow direction. This reduces nanoparticle concentration near the plate as particles are swept downstream, enhancing distribution uniformity.

Figure 26 shows that with elevation in the solutal Biot number often improves the temperature distribution in the hybrid nanofluid. This arises from the solutal Biot number, which quantifies convective to diffusive mass transfer resistance. Concentration profiles of nanoparticles or solutes in the hybrid nanofluid escalate with the solutal Biot number. A greater solutal Biot number signifies improved convective mass movement at the surface, which decreases concentration boundary layer thickness and increases solute or nanoparticle concentration near boundary. Consequently, concentration boundary layers diminish in thickness and concentration gradients intensify as solutal Biot number increases as shown in figure 27.

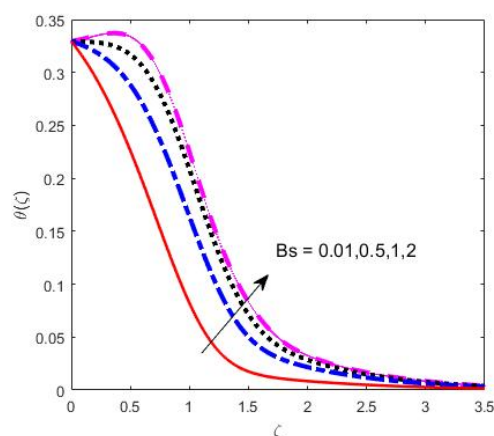


Figure 26. Temperature  $\theta(\zeta)$  versus  $B_s$

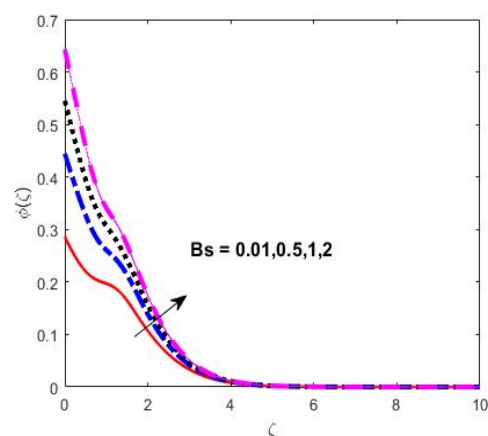


Figure 27. Concentration  $\phi(\zeta)$  versus  $B_s$

Temperature profile improves with higher thermal Biot numbers as shown in figure 28. The thermal Biot number is surface convective to fluid conductive heat transfer ratio. Higher Biot numbers imply more convective heat exchange between fluid, its surroundings resulting in thicker thermal boundary layers, higher fluid temperatures near surface. Better heat transfer and local Nusselt values indicate more efficient thermal energy delivery. The hybrid nanofluid system's thermal radiation, heat source intensity, and Brownian motion boost temperature distribution. The heat

transmission coefficient increases with Biot number, creating a greater temperature differential and higher fluid temperatures near the heated surface. Figure 29 shows thermal Biot number increases concentration dispersion, however Schmidt number and chemical reaction rates can mitigate this impact. The concentration boundary layer thickness and form depend on this interaction.

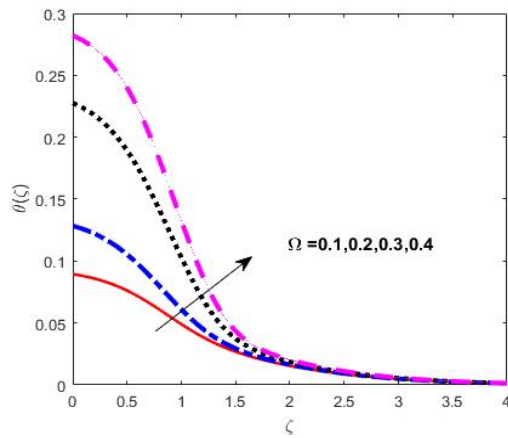


Figure 28. Temperature  $\theta(\zeta)$  versus  $\Omega$

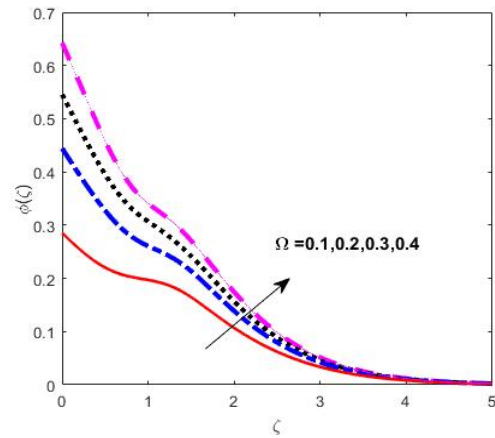


Figure 29. Concentration  $\phi(\zeta)$  versus  $\Omega$

Dufour effect represents the heat flux generated by concentration gradients within fluid. In Casson hybrid nanofluids with Ag and TiO<sub>2</sub> nanoparticles, this effect leads to increase in temperature profile near surface because heat transfer is augmented by mass diffusion processes. As the Dufour number increases, more heat is transported into the fluid from concentration gradients, thereby elevating the fluid temperature as shown in Figure 30.

The Soret effect causes species within the nanofluid to migrate from colder to hotter regions due to temperature gradients, resulting in enhanced concentration gradients. In Casson hybrid nanofluids with Ag and TiO<sub>2</sub> nanoparticles, this leads to an increase in nanoparticle concentration near the heated surfaces as shown in Figure 31 enriching the solute distribution in the fluid.

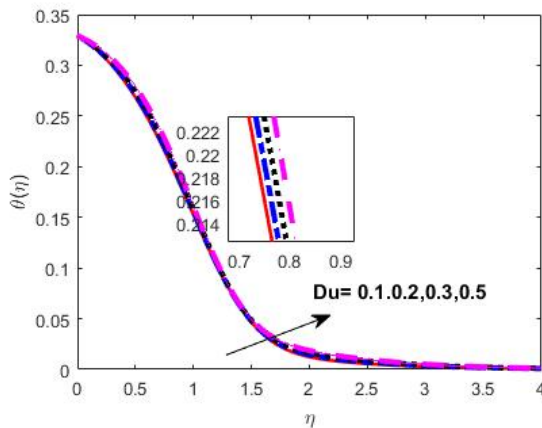


Figure 30. Temperature  $\theta(\zeta)$  versus  $Du$

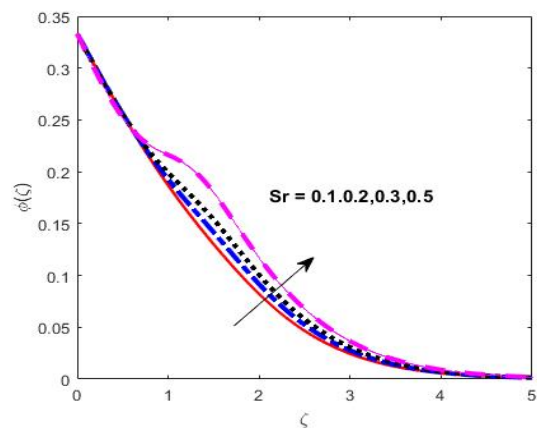


Figure 31. Concentration  $\phi(\zeta)$  versus  $Sr$

Tables 5, 6 and 7 below shows variation in skin friction coefficient, Nusselt number, Sherwood number for various nanoparticle shapes when plate moves in accordance with flow. From tabulated values, spherical shape shows highest skin friction, Sherwood number for all parameters whereas platelet shape has highest nusselt number for increasing Biot number.

Table 5. Variation in Skin Friction Coefficient  $f'(0)$

$\alpha$	M	$\phi_1$	$\phi_2$	$\beta_c$	Skin Friction $f'(0)$			
					Shapes of nanoparticles			
					Spherical	Bricks	Cylindrical	Platelets
0°	1	0.1	0.1	2	0.400115	0.393619	0.385249	0.379654
30°					0.623173	0.615313	0.605506	0.599195
60°					1.338845	1.331604	1.322577	1.316769
90°					1.831634	1.824847	1.816386	1.810939
90°	0				0.400115	0.393619	0.385249	0.379654
	1				1.831634	1.824847	1.816386	1.810939
	2				4.500536	4.495191	4.488521	4.484220
	3				8.017072	8.012569	8.006946	8.003315

$\alpha$	<b>M</b>	$\varphi_1$	$\varphi_2$	$\beta_c$	Skin Friction $f''(0)$			
					Shapes of nanoparticles			
					Spherical	Bricks	Cylindrical	Platelets
	1	0	0	1.213740	1.213740	1.213740	1.213740	
0		0.1	1.606387	1.604808	1.602760	1.601382		
0.1		0	1.280598	1.277597	1.273458	1.270503		
0.05		0.05	1.406770	1.404328	1.400976	1.398591		
0.1		0.1	1	2.034106	2.028023	2.020232	2.015055	
			2	1.831634	1.824847	1.816386	1.810939	
			5	1.684668	1.678128	1.669972	1.664721	
			100	1.579132	1.572756	1.564803	1.559681	

Table 6. Variation in Nusselt number  $\theta'(0)$ 

Rd	N <sub>b</sub>	N <sub>t</sub>	Du	γ	Ω	Nusselt Number θ'(0)			
						Shapes of nanoparticles			
						Spherical	Bricks	Cylindrical	Platelets
1	0.3	0.3	0.1	0.5	0.1	0.090411	0.089705	0.088655	0.087842
2						0.138606	0.137220	0.135167	0.133588
3						0.180374	0.178423	0.175541	0.173327
5						0.251698	0.248818	0.244566	0.241304
1	0.1	0.3	0.1	0.5	0.1	0.090398	0.089692	0.088642	0.087830
	0.3					0.090411	0.089705	0.088655	0.087842
	0.5					0.090424	0.089719	0.088668	0.087855
	0.7					0.090438	0.089733	0.088682	0.087869
	0.3	0.1	0.3	0.5	0.1	0.090409	0.089703	0.088653	0.087841
		0.3				0.090411	0.089705	0.088655	0.087842
		0.5				0.090412	0.089707	0.088657	0.087844
		0.7				0.090414	0.089709	0.088658	0.087846
		0.01	0.3	0.5	0.1	0.114346	0.113732	0.112819	0.112114
		0.03				0.109277	0.108642	0.107699	0.106948
		0.05				0.104057	0.103402	0.102429	0.101676
		0.07				0.098705	0.098030	0.097026	0.096249
	0.3	0.3	0.5	0.1	-0.5	0.089477	0.088785	0.087756	0.086958
					-1.0	0.089000	0.088316	0.087297	0.086508
					0.5	0.090411	0.089705	0.088655	0.087842
					1.0	0.090857	0.090145	0.089085	0.088265
		0.5	0.5	0.315639	0.315791	0.315988	0.316117		
			1	0.411254	0.412808	0.415106	0.416874		
			5	0.515960	0.520103	0.526355	0.531266		
			10	0.529210	0.533793	0.540726	0.546186		

Table 7. Variation in Sherwood number  $\phi'(0)$ :

$\beta_c$	$\delta$	Bs	Sc	Sr	Sherwood Number $\phi'(0)$					
					Shapes of nanoparticles					
					Spherical	Bricks	Cylindrical	Platelets		
1	0.5	0.5	1.0	0.5	0.181278	0.181111	0.180871	0.180694		
2					0.184588	0.184427	0.184197	0.184027		
5					0.186499	0.186348	0.186132	0.185973		
100					0.187395	0.187253	0.187053	0.186906		
1	-0.5	0.5	1.0	0.5	0.172397	0.172250	0.172041	0.171886		
	0.5				0.181278	0.181111	0.180871	0.180694		
	1				0.185024	0.184848	0.184597	0.184411		
	2				0.188765	0.188596	0.188354	0.188175		
	0.5	0.5	0.5	1.0	0.5	0.181278	0.181111	0.180871	0.180694	
		1				0.292474	0.292205	0.291813	0.291516	
		2				0.403236	0.402890	0.402382	0.401994	
		10				0.563659	0.563238	0.562617	0.562140	
		0.5	0.5	1.0	0.5	1.0	0.127680	0.127661	0.127638	0.127624
			1.0				0.181278	0.181111	0.180871	0.180694
			1.5				0.227563	0.227176	0.226614	0.226192
			2.0				0.272782	0.272107	0.271122	0.270376
1.0	0.1	0.190251	0.190201	0.190128	0.190073					
	0.2	0.188187	0.188108	0.187994	0.187909					



$\beta_c$	$\delta$	Bs	Sc	Sr	Sherwood Number $\phi'(0)$			
					Shapes of nanoparticles			
					Spherical	Bricks	Cylindrical	Platelets
					0.3	0.186013	0.185905	0.185750
				0.5	0.181278	0.181111	0.180871	0.180694

### CONCLUSIONS

Casson hybrid nanofluid flow along plate moving vertically with Soret, Dufour effects considering nanoparticles shapes were investigated in this study. Convective boundary conditions were also considered. Following are findings of this research:

- Temperature and concentration distribution drop and velocity outline rises with increase in inclination parameter.
- Velocity increases while temperature and concentration show an opposite trend, as Casson parameter rises,
- Mass diffusion and fluid energy decrease by boosting the Brownian motion factor.
- Temperature profile is elevated by thermophoresis factor, while concentration is lowered.
- Temperature and concentration also increase, with rise in Bs and  $\Omega$ ,
- Temperature and concentration show a fall in their profiles, when thermal buoyancy and solutal buoyancy parameters are modified,
- Platelet shaped nanoparticle was shown to have highest velocity, temperature, concentration profiles followed by cylindrical, bricks, spherical shape.
- Skin friction coefficient increases with increase in  $\beta$  values when magnetic field is applied perpendicularly.
- Platelet shaped nanoparticle has highest skin friction when plate moves against flow, while plate moving in accordance with flow gives highest Nusselt number.

### Conflict of Interest & Acknowledgement

Authors declare that there is no conflict of interests regarding this paper publication. The Authors thank SAGTE for their encouragement and financial support.

### Nomenclature

U	Characteristic velocity of the moving plate(m/s)
x,y	Cylindrical coordinates (m)
k	Thermal conductivity of the fluid (W/mK)
$T_w$	Plate temperature (K)
$T_\infty$	Ambient temperature (K)
$C_w$	Plate concentration(kg/m <sup>3</sup> )
$C_\infty$	ambient concentration(kg/m <sup>3</sup> )
$Nu_x$	Nusselt Number
$Re_x$	Reynolds number
$Sh_x$	Sherwood number
$C_{fx}$	skin friction coefficient
$\Omega$	Thermal Biot number
Bs	SolutalBiot number
Sr	Soret effect
Du	Dufour effect
M	Magnetic field parameter
Pr	Prandtl number
K	Porosity parameter
Rd	Radiation parameter
$N_b$	Brownian motion Parameter
$N_t$	Thermophoresis Parameter
Sc	Schmidt number

### Greek Symbols

$\beta$	Casson Parameter
$\lambda$	Moving plate parameter
$\gamma$	Thermal Buoyancy parameter
$\delta$	Solutal Buoyancy parameter
$\zeta$	Similarity variable
$\tau_w$	Wall shear stress (kg/ms <sup>2</sup> )
$\rho$	Density of the fluid (kg/m <sup>3</sup> )
$C_p$	Specific heat at constant pressure (J/kgK)
$\rho C_p$	Heat capacitance of fluid (J/Km <sup>3</sup> )
$\alpha$	Thermal diffusivity(m <sup>2</sup> /s)
$\sigma$	Electrical conductivity(S/m)
$\mu$	Dynamic viscosity of the fluid (kg/ms)
$\nu_f$	Kinematic viscosity of the fluid (m <sup>2</sup> /s)

### Superscripts

' differentiation with respect to h

### Subscripts

f	fluid
nf	nanofluid
hnf	Hybrid nanofluid

### ORCID

©K. Fatima, <https://orcid.org/0009-0007-5459-1773>; ©J.L. Rama Prasad, <https://orcid.org/0000-0003-3604-5182>

### REFERENCES

- A. Aziz, "A similarity solution for laminar thermal boundary layer over a flat plate with a convective surface boundary condition," Commun. Nonlinear Sci. Numer. Simulat. **14**, 1064-1068 (2009). <https://doi.org/10.1016/j.cnsns.2008.05.003>
- A. Yahyaee, "Influence of nanoparticle shapes in nanofluid film boiling on vertical cylinders: A numerical study," International Journal of Thermofluids, **22**, 100631 (2024). <https://doi.org/10.1016/j.ijft.2024.100631>
- A. Hussain, S. Raiz, A. Hassan, A.M. Hassan, H. Karamti, and G. Bognár, "Analysis of Soret and Dufour effects on radiative heat transfer in hybrid bioconvective flow of carbon nanotubes," Scientific Reports, (2024). <https://doi.org/10.1038/s41598-024-62647-2>



- [4] B.N. Lakshmi, V.S. Bhagavan, M.R. Ravuri, and G.V.R. Reddy, "Contribution of Soret and Dufour aspects on Hybrid Nanofluid over 3D Magneto Radiative Stretching Surface with Chemical Reaction," *CFD Letters*, **17**(5), 131-151 (2025). <https://doi.org/10.37934/cfdl.17.5.131151>
- [5] Cebeci and Bradshaw, *A Physical and Computational Aspects of Convective Heat transfer*, (Springer-Verlag, New York, 1988).
- [6] Ch. RamReddy, P.V.S.N. Murthy, A.J. Chamkha, and A.M. Rashad, "Soret effect on mixed convection flow in a nanofluid under convective boundary condition," *International Journal of Heat and Mass Transfer*, **64**, 384-392 (2013). <https://doi.org/10.1016/j.ijheatmasstransfer.2013.04.032>
- [7] C. Maheswari, R.M. Ramana, G.B. Prakash, D. Ramesh, and D.V. Kumar, "Influence of Thermophoresis and Brownian Motion on MHD Hybrid Nanofluid MgO - Ag/H<sub>2</sub>O Flow along Moving Slim Needle," *Journal of Advanced Research in Applied Sciences and Engineering Technology*, **36**(2), 67-90 (2024). <https://doi.org/10.37934/araset.36.2.6790>
- [8] E. Seid, E. Haile, and T. Walelign, "Multiple slip, Soret and Dufour effects in fluid flow near a vertical stretching sheet in the presence of magnetic nanoparticles," *International Journal of Thermofluids*, **13**, 100136 (2022). <https://doi.org/10.1016/j.ijft.2022.100136>
- [9] S.S.P.M. Isa, S. Parvin, N.M. Arifin, F.M. Ali, and K. Ahmad, "Soret-Dufour Effects on The Water based Hybrid Nanofluid Flow with Nanoparticles of Alumina and Copper," *Malaysian Journal of Mathematical Sciences*, **17**(3), 283–304 (2023). <https://doi.org/10.47836/mjms.17.3.04>
- [10] I. Waini, A. Ishak, T. Groşan, and I. Pop, "Mixed convection of a hybrid nanofluid flow along a vertical surface embedded in a porous medium," *International Communications in Heat and Mass Transfer*, **114**, 104565 (2020). <https://doi.org/10.1016/j.icheatmasstransfer.2020.104565>
- [11] J. Jayaprakash, V. Govindan, S.S. Santra, S.S. Askar, A. Foul, S. Nandi, S.M. Hussain, "Thermal radiation, Soret and Dufour effects on MHD mixed convective Maxwell hybrid nanofluid flow under porous medium: a numerical study," *International Journal of Numerical Methods for Heat & Fluid Flow*, **34**(10), 3924-3952 (2024). <https://doi.org/10.1108/HFF-03-2024-0229>
- [12] K. Jat, K. Sharma, P. Soni and P. Choudhary, "Numerical analysis of heat and mass transport of hybrid nanofluid over a nonlinear stretchable sheet with magnetic field in presence of Soret and Dufour Effect," *Journal of Physics: Conference Series*, **2844**, 012019 (2024). <https://doi.org/10.1088/1742-6596/2844/1/012019>
- [13] K.S. Balamurugan, J.L. Ramaprasad, D. Gurram, and V.C.C. Raju, "Influence of Radiation Absorption, Viscous and Joules dissipation on MHD free Convection Chemically Reactive and Radiative Flow in a Moving Inclined Porous Plate with Temperature Dependent Heat Source," *International Refereed Journal of Engineering and Science*, **5**(12), 20-31 (2016).
- [14] M.A. Adriana, "Hybrid nanofluids based on Al<sub>2</sub>O<sub>3</sub>, TiO<sub>2</sub> and SiO<sub>2</sub>: Numerical evaluation of different approaches," *International Journal of Heat and Mass Transfer*, **104**, 852–860 (2017). <https://doi.org/10.1016/j.ijheatmasstransfer.2016.09.012>
- [15] M.A. Mansour, and M.A.Y. Bakier, "Magnetohydrodynamic mixed convection of TiO<sub>2</sub>-Cu/water between the double lid-driven cavity and a central heat source surrounding by a wavy tilted domain of porous medium under local thermal non-equilibrium," *S.N. Applied Sciences*, **5**, 51 (2023). <https://doi.org/10.1007/s42452-022-05260-0>
- [16] M. Sheikholeslami, M.M. Bhatti, "Forced convection of nanofluid in presence of constant magnetic field considering shape effects of nanoparticles," *International Journal of Heat and Mass Transfer*, **111**, 1039–1049 (2017). <https://doi.org/10.1016/j.ijheatmasstransfer.2017.04.070>
- [17] M.S. Babu, V.V. Ramana, G.R. Shankar, and C.S.K. Raju, "Mixed convective flow of heat and mass transfer of nanofluids over a static wedge with convective boundary conditions," *Journal of Thermal Engineering*, **7**(14), 1958–1969 (2021). <https://doi.org/10.18186/thermal.1051302>
- [18] M.V. Krishna, N.A. Ahammad, and A.J. Chamkha, "Radiative MHD flow of Casson hybrid nanofluid over an infinite exponentially accelerated vertical porous surface," *Case Studies in Thermal Engineering*, **27**, 101229 (2021). <https://doi.org/10.1016/j.csite.2021.101229>
- [19] N.A. Rosaidi, N.H. AbRaji, S.N. Hidayatu, A. Ibrahim, and M.R. Ilias, "Aligned Magnetohydrodynamics Free Convection Flow of Magnetic Nanofluid over a Moving Vertical Plate with Convective Boundary Condition," *Journal of Advanced Research in Fluid Mechanics and Thermal Sciences*, **93**(2), 37-49 (2022). <https://doi.org/10.37934/arfm.93.2.3749>
- [20] N.Z.M. Zukri, M.R. Ilias, S.S. Ishak, R. Osman, N.A.M. Makhatar, and M.N. AbdRahman, "Magnetohydrodynamic Effect in Mixed Convection Casson Hybrid Nanofluids Flow and Heat Transfer over a Moving Vertical Plate," *CFD Letters*, **15**(7), 92-111 (2023). <https://doi.org/10.37934/cfdl.15.7.92111>
- [21] N.S. Akbar, and A.W. Butt, "Ferromagnetic effects for peristaltic flow of Cu–water nanofluid for different shapes of nanosize particles," *Applied Nanoscience*, **6**, 379–385 (2016). <https://doi.org/10.1007/s13204-015-0430-x>
- [22] N.A. Zainal, R. Nazar, K. Naganthran, and I. Pop, "MHD mixed convection stagnation point flow of a hybrid nanofluid past a vertical flat plate with convective boundary condition," *Chinese Journal of Physics*, **66**, 630–644 (2020). <https://doi.org/10.1016/j.cjph.2020.03.022>
- [23] P. Chandrakala, and V.S. Rao, "Effect of Heat and Mass Transfer over Mixed Convective Hybrid Nanofluids past an Exponentially Stretching Sheet," *CFD Letters*, **16**(3), 125-140 (2024). <https://doi.org/10.37934/cfdl.16.3.125140>
- [24] R. Jain, R. Mehta, A. Bhatnagar, H. Ahmad, Z.A. Khan, and G.M. Ismail, "Numerical study of heat and mass transfer of Williamson hybrid nanofluid (CuO/CNT's-water) past a permeable stretching/shrinking surface with mixed convective boundary condition," *Case Studies in Thermal Engineering*, **59**, 104313 (2024). <https://doi.org/10.1016/j.csite.2024.104313>
- [25] S. Goudarzi, M. Shekaramiz, A. Omidvar, E. Golab, A. Karimipour, and A. Karimipour, "Nanoparticles migration due to thermophoresis and Brownian motion and its impact on Ag-MgO/Water hybrid nanofluid natural convection," *Powder Technology*, **375**, 493–503 (2020). <https://doi.org/10.1016/j.powtec.2020.07.115>
- [26] S.A.M. Mehryan, F.M. Kashkooli, M. Ghalambaz, and A.J. Chamkha, "Free convection of hybrid Al<sub>2</sub>O<sub>3</sub>-Cu water nanofluid in a differentially heated porous cavity," *Advanced Powder Technology*, **28**(9), 2295-2305 (2017). <https://doi.org/10.1016/j.appt.2017.06.011>
- [27] S. Hussain, K. Mehmood, and M. Sagheer, "MHD mixed convection and entropy generation of water–alumina nanofluid flow in a double lid driven cavity with discrete heating," *Journal of Magnetism and Magnetic Materials*, **419**, 140–155 (2016). <https://doi.org/10.1016/j.jmmm.2016.06.006>

- [28] T. Anwar, P. Kumam, and P. Thounthong, "A comparative fractional study to evaluate thermal performance of NaAlg-MoS<sub>2</sub>-Co hybrid nanofluid subject to shape factor and dual ramped conditions," *Alexandria Engineering Journal*, **61**, 2166–2187 (2022). <https://doi.org/10.1016/j.aej.2021.06.085>
- [29] T.S. Khaleque, A. Hossain, M.D. Shamsuddin, M. Ferdows, S.O. Salawu, and S. Sun, "Soret and Dufour impacts on radiative power-law fluid flow via continuously stretchable surface with varying viscosity and thermal conductivity," *Scientific Reports*, **14**, 23152 (2024). <https://doi.org/10.1038/s41598-024-73426-4>

## ЕФЕКТИ СОРЕ ТА ДЮФУРА НА Ag–TiO<sub>2</sub>/ВОДА В ГІБРИДНІЙ НАНОРІДИНІ КЕССОНА НАД РУХОМОЮ ВЕРТИКАЛЬНОЮ ПЛАСТИНКОЮ З КОНВЕКТИВНИМИ ГРАНИЧНИМИ УМОВАМИ

К. Фатіма<sup>1</sup>, Дж.Л. Рама Прасад<sup>2</sup>

<sup>1</sup>Кафедра математики, Університет Крішні, Мачіліпатнам, АР, Індія

<sup>2</sup>Кафедра математики, Коледж мистецтв і наук ім. П.Б. Сіддхартхи, Віджаявада, АР, Індія

Це дослідження представляє комплексне дослідження ефектів Соре та Дюфура на потік гібридної нанорідини Кассона (HNF) повз рухому вертикальну пластину з наночастинками срібла (Ag) та діоксиду титану (TiO<sub>2</sub>), диспергованими у воді. Включення гібридних наночастинок Ag–TiO<sub>2</sub> поєднує виняткову теплопровідність срібла з хімічною стабільністю та економічною ефективністю TiO<sub>2</sub>, створюючи рідину з чудовими транспортними властивостями порівняно зі звичайними однокомпонентними нанорідинами. Визначальні диференціальні рівняння в частинних похідних, що описують імпульс, тепло- та масообмін, перетворюються на набір нелінійних звичайних диференціальних рівнянь за допомогою перетворень подібності. Ці рівняння розв'язуються чисельно за допомогою методу Келлер-Бокса, що забезпечує стабільність і точність при роботі зі зв'язаними високонелінійними системами. Крім того, було проведено аналіз для вивчення впливу морфології наночастинок на розподіл швидкості, температури та концентрації, що підтверджує та збагачує числові результати. Результати показують, що змінна морфологія наночастинок та комбінована дисперсія Ag–TiO<sub>2</sub> значно підвищують швидкість теплопередачі та масообміну, одночасно зменшуючи втрати на тертя поблизу поверхні пластини. Включення ефектів Соре та Дюфура ще більше посилює перехресний зв'язок між тепловими та розчинними полями, що призводить до підвищення ефективності переносу. Ці результати не тільки дають нове розуміння динаміки гібридних нанорідин Кассона, але й підкреслюють критичну роль перехресної дифузії в оптимізації систем тепло- та масообміну. Інтеграція реології рідини Кассона, гібридних наночастинок та ефектів перехресної дифузії в реалістичних граничних умовах має прямі наслідки для промислового охолодження, металургійної обробки, доставки біомедичних ліків та оптимізації енергетичних систем. Демонструючи синергетичну ефективність нанорідин Ag–TiO<sub>2</sub>, це дослідження встановлює шлях для розробки технологій терморегуляції та біомедичного транспорту наступного покоління.

**Ключові слова:** конвективні граничні умови; МГД; гібридна нанорідина Кассона; форма наночастинок; ефекти Соре та Дюфура